Télédétection SAR interférométrique de zones urbaines en bande L à partir de l'utilisation des techniques d'analyse spectrale polarimétriques et multi-bases

Stefan Sauer

N° d'ordre : 3726

Thèse

présentée devant
l'UNIVERSITÉ DE RENNES I
pour obtenir le grade de
Docteur de l'Université de Rennes I
Mention : *Traitement du Signal et Télécommunications*

par
Stefan Sauer

Équipe d'accueil : Institut d'électronique et de télécommunications de Rennes
École doctorale : Matisse
Composante universitaire : UFR Structure et Propriétés de la Matière

Télédétection SAR interférométrique de zones urbaines en bande L à partir de l'utilisation des techniques d'analyse spectrale polarimétriques et multi-bases

Soutenue le 19 Mars 2008 devant la commission d'examen

Composition du jury

Président du jury

Alberto Moreira	Professeur et Directeur - DLR, Oberpfaffenhofen, Allemagne

Rapporteurs

Jordi J. Mallorquí	Professeur - UPC, Barcelone, Espagne
Fabrizio Lombardini	Professeur - Université de Pise, Italie

Examinateurs

Florence Tupin	Maître de Conférences - Telecom ParisTech, Paris
Andreas Reigber	Ingénieur - DLR, Oberpfaffenhofen, Allemagne
Laurent Ferro-Famil	Maître de Conférences - Université de Rennes 1

Directeur de thèse

Eric Pottier	Professeur - Université de Rennes 1

Acknowledgments

My cordial gratitude goes to Prof. Eric Pottier for his constant advice and encouragement during the PhD thesis. He ensured the funding and gave me the opportunity to attend international conferences. This allowed me to become familiar with the current developments in Synthetic Aperture Radar and to present my research results. I highly appreciate his numerous advices in professional matters, and also his suggestion where to buy sage in Rennes.

I wish to thank Dr. Laurent Ferro-Famil who guided me throughout the entire PhD work. In particular, he suggested a new look at the MUSIC algorithm in order to adapt it to the polarimetric scenario. Laurent recommended important papers and regularly mentioned the significance of coherent scatterers in urban areas. This encouraged me to extend the stochastic signal model by taking point-like targets into account.

I am greatly indebted to Dr. Andreas Reigber who offered me the chance to start working in the field of Synthetic Aperture Radar by giving me a four week introduction to SAR: It included raw data processing, interferometry, polarimetry, and POL-InSAR. During the years Andreas welcomed me many times in his Remote Sensing Lab at TU Berlin where we had wonderful discussions.

I would like to thank all the members of the jury: Prof. Alberto Moreira accepted to preside over the examination board. Prof. Jordi Mallorquí and Prof. Fabrizio Lombardini agreed to evaluate the manuscript as rapporteurs and proposed some changes to improve the thesis. Thanks also to Prof. Florence Tupin for showing interest in my PhD work.

Thanks to Prof. Jean-Pierre Le Cadre for his kind aid in signal processing techniques.

A special thanks goes to Joëlle for her considerate assistance concerning administrative issues.

It is a pleasure to thank my friend Shaharyar to whom I could turn in all professional and private matters.

I should also thank the members of the SAPHIR team, Maxim, Sandrine, Nicolas, Sangun, Yue, Sophie, Franck, Tadashi, Stéphane, Paul, Carlos, Stéphane, Frédéric, Olivier, Audrey, Cyril, and Gianfranco.

Thanks to all other people working at I.E.T.R., in particular Dominique,

Hung, Franck, Olivier, Ludovic, Sylvain, Anne-Claude, Noëlle, and Prof. Kouroch Mahdjoubi, and in the Remote Sensing Lab at TU Berlin, Marc and Stéphane.

Finally, I would like to express my profound gratitude to my parents for their continuing support.

Contents

List of Figures

List of Tables

Chapter 1

Introduction

Radar imaging is based on emitting electromagnetic waves in the direction of an examined scene and measuring the echo of the backscattered field to generate a reflectivity map. Synthetic Aperture Radar (SAR) constitutes an extension of imaging radar leading to an increased resolution.

Compared to optical and infrared systems, SAR sensors possess some advantages: Since the radar antennas are active and provide their own illumination source, they operate equally well during day and night in contrast to passive sensors. As microwaves with wavelengths longer than one centimeter permeate nearly undisturbedly small water drops, radar imaging techniques can be used under unfavorable weather conditions such as in the presence of clouds and rain. The large frequency diversity permits the measurement of different characteristics of the studied area. For instance at L-band the electromagnetic waves penetrate partially the forest canopy resulting in backscattering contributions from the ground, the tree trunks and the tree cover.

Over urban areas, the analysis of SAR data is a very difficult task due to three main reasons: Radar images are geometrically distorted by layover and shadow effects. The layover yields a superposition of different reflection components. Scattering patterns are very complex with various contributions within one resolution cell. In urban scenes, particular phenomena like single bounce reflection from surfaces such as building roofs and sport fields, double bounce scattering generated by building wall-ground and tree trunk-ground interaction arise. It may occur also higher-order reflection processes. Lastly, SAR images are affected by the speckle effect that is normally modeled as a multiplicative noise.

To overcome these problems some extensions of single-channel Synthetic Aperture Radar have been proposed:

SAR Polarimetry studies how the polarization of an electromagnetic wave is modified by interacting with a target or natural media [8,46]. These modifications are significantly associated with geometric characteristics and

physical properties of the examined object such as its shape, orientation, and dielectric features. Hence, polarimetric information coupled with the knowledge of electromagnetic reflection behavior offers an additional dimension to describe targets using SAR data. This allows the separation and identification of scattering mechanisms of natural media employing differences in the polarization signature for purposes of classification and parameter inversion [12, 13, 32].

SAR interferometry is an established technique to measure terrain topography [6, 69, 91]. This approach is based on the generation of an interferogram using two complex SAR images of the same area acquired from two slightly different look angles. The phase difference contains information related to the scene topography and permits the determination of the scatterer height in order to generate high resolution digital elevation models (DEMs). The interferometric coherence, which is sensitive to changes in the arrangement of reflectors inside the resolution cells, can be used to monitor changing processes. Differential SAR interferometry enables accurate mapping of elevation changes to detect small surface deformations [25,26,81,86].

In the past, two advanced multi-channel SAR approaches have been studied:

While SAR interferometry permits the retrieval of the topographic height of reflectors, the physics of scattering processes can be investigated via SAR polarimetry. In polarimetric SAR interferometry both techniques are combined to estimate the vertical location of scattering mechanisms [14]. To extract physical parameters from single-baseline POL-InSAR observations a coherent model describing the reflection processes has been designed [75]. Schemes to inverse the electromagnetic model for retrieving forest parameters such as tree height and underlying ground topography have been introduced [15, 75]. Processing polarimetric single-baseline InSAR signals by means of the ESPRIT algorithm has been proposed to investigate forested areas [114] and applied to analyze urban scenes [42].

An extension of conventional two-dimensional SAR imaging is SAR tomography that allows the reconstruction of a three-dimensional scatterer distribution [84,85]. An airborne multibaseline interferometric SAR configuration including fourteen parallel tracks has been used to form a synthetic aperture in elevation. This set-up permits to achieve focusing in height direction and to generate a three-dimensional SAR image [84, 85]. The tomographic SAR imaging approach has been applied to forested areas where both the ground level and the tree canopy have been distinguished resulting in an estimation of tree height and ground topography. Since the tomographic processing preserves the phase information the scattering pattern inside the studied volume has been examined using polarization diversity [84, 85]. A three-dimensional radar imaging technique of vegetation using single and dual-baseline polarimetric interferometric SAR observations called polarization coherence tomography has been developed recently [16, 17].

Lately, spectral analysis techniques have been analyzed in detail to process single polarization multibaseline interferometric SAR data [37, 39, 63]. These algorithms serve two main purposes. Firstly, they retrieve the parameters of signals such as their spatial frequency and reflectivity (estimation problem). The estimate of the spatial frequency or phase allows the calculation of the height of scatterers. Thus, high resolution methods resolve the layover problem by extracting the characteristics of multiple backscattering sources inside the same range-azimuth resolution cell [37]. The reflectivity estimates result in three-dimensional images [63]. Secondly, spectral analysis techniques determine the number of sources (detection problem).

Several nonparametric and parametric array signal processing techniques for the analysis of single polarization MB interferometric signals have been scrutinized: Classical beamforming [45] and Capon [11,37] are nonparametric methods to determine simultaneously phase and amplitude. They do not make any assumption about the statistical properties of the received signal. The MUSIC [37, 100] and least squares methods [63] are model-based algorithms for frequency and reflectivity estimation, respectively. Multilook RELAX [37, 63] is a parametric joint frequency and reflectivity estimator. In the InSAR scenario, they operate under modeling error, since they do not take the speckle phenomenon into account. Despite this fact, model-based algorithms produce generally better results than nonparametric techniques. They refine the resolution and reduce considerably the influence of sidelobes. The second major purpose of spectral analysis techniques is to extract the number of sources, called the detection or model order selection problem. Although this problem is severely aggravated in the case of InSAR data due to speckle, common information theoretic criteria like the minimum description length and the efficient detection criteria are utilized to solve it [38,65].

Recently, spectral analysis techniques have been utilized for three-dimensional imaging from single polarization dual-baseline observations [67, 90] and polarimetric tomographic measurements [43, 44, 64]. The number of backscattering sources has been estimated using model order selection methods on single polarization dual-baseline InSAR data [66].

In this work, a new way of analyzing polarimetric multibaseline InSAR data is conceived by adapting the above described array signal processing algorithms to this configuration. Until now, these techniques have been developed for the special case of polarization diversity in the receive channel [23, 118]. Since in the SAR context sensors are active, wave polarimetry comprising two polarization states has to be extended to scattering polarimetry including four polarizations channels. In a first step the single polarization MB InSAR signal model is generalized to the fully polarimetric set-up. In this situation, the polarimetric MB interferometric steering vector is a linear combination of four vectors each of them being associated with one specific polarization. The coefficients of this combination form a polarimetric scattering vector that allows to extract the physical features

of reflectors. Subsequently, polarimetric spectral estimation algorithms are formulated in a rigorous mathematical way and their features are explained. These new algorithms enhance the phase estimation of scatterers not merely by increasing the dimension of the observation space, but also via calculating optimal polarization combinations. Furthermore, they permit the retrieval of some physical characteristics of the reflectors by performing a polarimetric analysis of the estimated scattering mechanisms. Additionally, the polarimetric reflectivity can be determined. To specify the number of sources, the information theoretic criteria have to be adapted to the polarimetric MB InSAR configuration as the degrees of freedom increase compared to the single polarization case. Finally, a joint estimation and detection approach is presented for the single polarization [113] and fully polarimetric case.

To demonstrate the performance of the conceived spectral analysis techniques, they are applied to fully polarimetric dual-baseline InSAR observations of an urban environment. First, the number of backscattering sources is estimated by the model order selection techniques. Using single-baseline POL-InSAR measurements, scatterer height and reflection mechanisms are determined to produce a three-dimensional model of an urban scene. Subsequently, the building layover is analyzed by means of polarimetric dual-baseline interferometric SAR data. Finally, three-dimensional images are generated that include polarimetric information about the reflection processes.

The proposed array signal processing methods are applied to fully polarimetric and repeat pass dual-baseline interferometric SAR images at L-band acquired by DLR's experimental SAR (E-SAR) system on August 1st, 2000, over the city of Dresden in Germany.

The structure of the thesis is as follows:

A short introduction to basic and advanced techniques of Synthetic Aperture Radar (SAR) is given in chapter 2. First, fundamental concepts of Synthetic Aperture Radar are described. Subsequently, two established extensions of single-channel SAR are presented: SAR polarimetry and SAR interferometry. Finally, two advanced multi-channel SAR approaches are outlined, namely polarimetric SAR interferometry and multibaseline SAR interferometry.

Classical spectral analysis methods to process single polarization multibaseline interferometric SAR data are presented in chapter 3. First, an established signal model for sensor array processing and models of MB InSAR point-like targets and extended sources are described. Model order selection algorithms are explained that rely on information theoretic criteria to estimate the number of sources. Spectral estimation techniques are elaborated to retrieve the signal parameters such as the scatterer height and their reflectivity from single polarization MB InSAR observations. Finally, a maximum likelihood estimator is introduced that solves the combined

detection-estimation problem.

Spectral analysis methods are adapted to the polarimetric multibaseline interferometric SAR scenario in chapter 4. First, signal models are extended to include polarization diversity yielding the multibaseline polarimetric interferometric steering vector. The model order selection techniques to estimate the number of sources from MB POL-InSAR observations are elaborated in the second section. Subsequently, the spectral estimation algorithms are adapted to process polarimetric MB InSAR data. They permit the retrieval of the spatial frequencies, the associated optimal scattering vectors, and the polarimetric reflectivities. Finally, the polarimetric maximum likelihood estimator is developed for solving simultaneously the detection-estimation problem.

The performance of the developed array signal processing algorithms is demonstrated in chapter 5 by applying them to fully polarimetric dual-baseline InSAR observations over an urban environment. First, the number of backscattering sources is determined by the model order selection techniques. By means of single-baseline POL-InSAR measurements the reflector height and scattering mechanisms are extracted to provide a three-dimensional model of an urban scene. Subsequently, the building layover is analyzed from polarimetric dual-baseline interferometric SAR data. Finally, three-dimensional images are generated that include polarimetric information about the reflection processes.

Finally, the results are summarized and some perspectives are outlined.

Chapter 2

Synthetic Aperture Radar

This chapter gives a short introduction to basic and advanced techniques of Synthetic Aperture Radar (SAR). First, fundamental concepts of Synthetic Aperture Radar are described. Subsequently, two established extensions of single-channel SAR are presented: While SAR polarimetry is sensitive to the shape, orientation, and dielectric properties of scatterers, SAR interferometry allows to estimate their height. Finally, two advanced multi-channel SAR approaches are outlined: Polarimetric SAR interferometry and multi-baseline SAR interferometry.

2.1 Synthetic Aperture Radar

The fundamental concepts of Synthetic Aperture Radar (SAR) are presented in this section. First, SAR image resolution is explained and subsequently the properties and a basic processing approach of SAR raw data are introduced. Finally, some important characteristics of SAR images are described.

2.1.1 SAR Image Resolution

Synthetic Aperture Radar (SAR) is a coherent, microwave imaging technique to produce a two-dimensional reflectivity map of a studied scene with high spatial resolution. A monostatic radar system comprises a microwave transmitter and receiver mounted on a moving platform such as an air-plane or a satellite. As the radar moves along its flight direction, called azimuth or along-track dimension, the antenna beam is pointed sidewards to the ground. The direction perpendicular to the sensor trajectory is referred to as slant-range or across-track dimension. The antenna emits consecutively short radar pulses to objects on the ground that scatter off part of the energy to the receiver. The reflected signals reach the receiver after the time delay

$$\Delta t = \frac{2d}{c} \tag{2.1}$$

that depends on the distance d between the scatterer and the sensor. The propagation velocity of electromagnetic waves is denoted by c. Two reflectors with different distances to the radar can be separated due to the different time delays of their echoes. The slant-range resolution δ_{sr} is a function of the transmitted pulse duration τ, or the signal bandwidth BW [21, 85]

$$\delta_{sr} = \frac{c\tau}{2} = \frac{c}{2BW}. \tag{2.2}$$

Very short pulse lengths are required to obtain fine range resolution, whereas high energy pulses have to be emitted to achieve sufficient signal-to-noise ratios (SNRs). To overcome this contradiction, a linearly frequency modulated pulse (chirp) is transmitted. The energy which is distributed over a longer duration is compressed by applying a matched filter to the returned signal.

The azimuth resolution of a conventional side-looking radar is related to the size of the antenna footprint on the ground. The angular spread α_{ra} is given by

$$\alpha_{ra} = \frac{\lambda}{L} \tag{2.3}$$

where λ is the wavelength and L the antenna length in the along-track direction. At range r_0, the spatial resolution in azimuth is obtained as

$$\delta_{az} = \alpha_{ra} r_0 = \frac{\lambda r_0}{L}. \tag{2.4}$$

For long distances between the sensor and the target the resolution in flight direction degrades. To yield high along-track resolution the synthetic aperture principle is employed: The response of a reflector on the ground is contained in several radar echoes leading to a phase history over the illumination time. By coherently combining pulses, a synthetically enlarged antenna is constructed. An artificial antenna array is built up using the movement of a single sensor.The beam spread of the synthetic antenna of length L_{sa} is given by

$$\alpha_{sa} = \frac{\lambda}{2L_{sa}} \tag{2.5}$$

where the factor two accounts for the phase shift induced by the two-way path between the antenna and the scatterer. The maximum length of the synthetic aperture for an object at range distance r_0 is limited by the flight path length during which the reflector is illuminated, i.e., the size of the antenna footprint on the ground

$$L_{sa} = \alpha_{ra} r_0 = \frac{\lambda r_0}{L}. \tag{2.6}$$

Finally, the spatial resolution in azimuth using a synthetic aperture results in [6, 22]

$$\delta_{az} = \alpha_{sa} r_0 = \frac{L}{2}. \tag{2.7}$$

In contrast to other imaging techniques utilizing a telescope or microscope [21], the achievable resolution in SAR does not depend on the sensor-target distance since the effective antenna length increases with longer range distances. Moreover, the smaller the real antenna, the better the resolution in along-track.

2.1.2 SAR Raw Data Characteristics

During the SAR data acquisition the observed scene on the ground is projected into the recorded raw data by a special transfer function. The basic SAR signal features are explained, making the following simplifying assumptions: The sensor moves along a straight line in azimuth direction with a constant velocity v. The along- and cross-track coordinates are given by $x = vt_{az}$ and $r = 0$, respectively. It is assumed that the radar is transmitting a single frequency signal.

The reflection processes on the ground can be described by a reflectivity function $\rho(x, r) \in \mathbb{C}$. It models the ground as a superposition of δ-like point scatterers

$$\rho(x, r) = \sum_n \rho_n \delta(x - x_n, r - r_n) \tag{2.8}$$

where $\rho_n \in \mathbb{C}$ is the complex backscattering amplitude related to the nth scatterer, and $\delta(x, r)$ the two-dimensional Dirac delta-function.

The antenna transmits radar pulses to the ground with the pulse repetition frequency PRF and receives the backscattered echoes after a short time-delay. The transmitted pulses of the sensor at position x is written as

$$s_{tr}(x, t) = p(t) \exp(j\omega t) = \delta(t) \exp(j\omega t) \tag{2.9}$$

where $p(t)$ represents a pulse envelope being a delta-function in this case, and ω the radar carrier frequency.

As the velocity of electromagnetic wave propagation c and the platform speed v differ by several orders of magnitude, the distance between the emitting and receiving positions are ignored. When the radar pulse is sent at time $t = 0$ for each azimuth location x, the echo of a target positioned at (x_n, r_n) is received by the sensor after the time delay

$$\Delta t_n(x, x_n, r_n) = \frac{2d(x - x_n, r_n)}{c} \tag{2.10}$$

where $d(x - x_n, r_n)$ denotes the distance between the sensor at the position x and the reflector at (x_n, r_n). Apart from a phase-shift of $\omega \Delta t_n$, that encodes the travelled path the echo of a scatterer has the same shape as the transmitted pulse. The received echo at position x after demodulation is a coherent superposition of all echoes from the reflectors inside the illuminated

scene [85]

$$
\begin{aligned}
s_r^{tot}(x,t) &= \sum_n \rho_n \delta\left(t - \frac{2d(x-x_n,r_n)}{c}\right) \exp\left(-\frac{2j\omega d(x-x_n,r_n)}{c}\right) \exp(j\omega t) \\
&= \exp(j\omega t) \iint \rho(x_n,r_n) \cdot \delta(t-\Delta t_n) \\
&\qquad \cdot \exp\left(-\frac{2j\omega d(x-x_n,r_n)}{c}\right) \mathrm{d}x_n \mathrm{d}r_n. \qquad (2.11)
\end{aligned}
$$

The exponential contribution in front of the integral in equation (2.11) is removed by coherent quadratic demodulation. The time delay Δt_n and hence $d(x-x_n,r_n)$ determine both the scatterer phase and its location in the raw data.

The range history of the nth scatterer is

$$
d(x-x_n,r_n) = \sqrt{r_n^2 + (x-x_n)^2}. \qquad (2.12)
$$

The hyperbolic curve with center at x_n and curvature depending on r_n describes the echoes of a target received from different azimuth locations x. This phenomenon is called range cell migration.

For SAR sensors with moderate to low resolution ($r_n \gg L_{sa}$), the range history can be rewritten using the Taylor series expansion [6]

$$
d(x-x_n,r_n) \simeq r_n + \frac{(x-x_n)^2}{2r_n}. \qquad (2.13)
$$

By means of the parabolic approximation the total response of a single scatterer at position (x_n,r_n) results in

$$
s_r^n(x,x_n,r_n) = \rho_n \exp\left(-\frac{2j\omega r_n}{c}\right) \exp\left(\frac{j\omega(x-x_n)^2}{cr_n}\right) \mathrm{rect}\left(\frac{x-x_n}{L_{sa}}\right) \qquad (2.14)
$$

The first exponential component has a constant phase associated with the minimum sensor-scatterer distance that is essential for SAR interferometry. The variation of the received signal phase in along-track is determined by the quadratic phase term of the second exponential contribution. The focusing in azimuth relies on evaluating this specific phase term. The rect-function

$$
\mathrm{rect}(x) = \begin{cases} 1 & \text{if } |x| \le \frac{1}{2} \\ 0 & \text{otherwise} \end{cases} \qquad (2.15)
$$

accounts for the finite illumination time.

The range migration phenomenon (2.12) causes the scatterer representation to be two-dimensional in the raw data domain. Thus, the inverse process of focusing SAR raw data is in general a two-dimensional operation. Only under some simplifying assumptions it is possible to decouple the along- and across-track variables.

2.1.3 Basic SAR Raw Data Processing

SAR raw data processing for computing an approximation of the original complex reflectivity $\rho(x, r)$ relies generally on matched filtering methods. At the pixel (x_n, r_n), the image $v(x_n, r_n)$ is calculated by

$$v(x_n, r_n) = \iint s_r^{tot}(x, t) h_{ref}(x, t, x_n, r_n) \mathrm{d}x\mathrm{d}t \tag{2.16}$$

where the received signal $s_r^{tot}(x, t) \in \mathbb{C}$ is correlated with the two-dimensional reference functions $h_{ref}(x, t, x_n, r_n)$ that corrects the phase history at (x_n, r_n).

To provide a basic understanding of SAR raw signal processing a method that is based on simplifying assumptions is outlined in the following. In practice more advanced techniques have to be employed [5, 9]. Under the condition

$$L_{sa} < 4\sqrt{r_0 \rho_{sr}} \tag{2.17}$$

the range variation of the echoes is so small during the illumination time that range time and range distance are interchangeable through $r = \frac{ct}{2}$. Then the correlation in (2.16) becomes a one-dimensional operation and an azimuth line of the image results in [85]

$$\begin{aligned} v(x, r_n) &= s_r^{tot}\left(x, t = \frac{2r_n}{c}\right) \odot_x h_{ref}(x, r_n) \\ &= s_r^{tot}\left(x, t = \frac{2r_n}{c}\right) \odot_x \exp\left(\frac{j\omega x^2}{cr_n}\right) \end{aligned} \tag{2.18}$$

where $\odot_x$ denotes the correlation in x-direction and $h_{ref}(x, r_n)$ is the matched reference function to focus a point scatterer positioned at range r_n.

The correlation for the echo of a single scatterer at (x_n, r_n) is obtained as [85]

$$\begin{aligned} & v(x, r_n) = s_r^n(x, x_n, r_n) \odot_x h_{ref}(x, r_n) \qquad (2.19) \\ = & \int_{r_n - \frac{L_{sa}}{2}}^{r_n + \frac{L_{sa}}{2}} \rho_n \exp\left(\frac{j2\omega r_n}{c}\right) \exp\left(\frac{j\omega(\xi - x_n)^2}{cr_n}\right) \exp\left(-\frac{j\omega(\xi - x)^2}{cr_n}\right) \mathrm{d}\xi \\ = & L_{sa}\rho_n \exp\left(\frac{j2\omega r_n}{c}\right) \exp\left(\frac{j\omega}{cr_n}(x - x_n)^2\right) \mathrm{sinc}\left(\frac{\omega L_{sa}}{cr_n}(x - x_n)^2\right). \end{aligned}$$

It follows that the achievable resolution in azimuth is given by

$$\rho_{az} = \frac{\pi c r_n}{\omega L_{sa}}. \tag{2.20}$$

The linear phase term in equation (2.19) is related to the minimum antenna-reflector distance.

Since this two-dimensional time domain correlation is very slow and inefficient it is performed in the frequency domain by

$$\tilde{V}(k_x, r_n) = \tilde{S}_r^{tot}\left(k_x, \frac{2r_n}{c}\right)\tilde{H}_{ref}(k_x, r_n) \tag{2.21}$$

where $\tilde{V}(k_x, r_n), \tilde{S}_r^{tot}\left(k_x, \frac{2r_n}{c}\right)$, and $\tilde{H}_{ref}(k_x, r_n)$ are the Fourier transformations of $v(x, r_n), s_r^{tot}\left(x, \frac{2r_n}{c}\right)$, and $h_{ref}(x, r_n)$, respectively, and k_x represents the spatial frequency in the x-dimension. Finally, the Fourier transform of $h_{ref}(x, r_n)$ can be written as [85]

$$\begin{aligned}\tilde{H}_{ref}(k_x, r_n) &= \frac{1}{2\pi}\int h_{ref}(x, r_n)\exp(-jk_x x)\mathrm{d}x \\ &= \frac{1}{2\pi}\int \exp\left(-\frac{j\omega x^2}{cr_n}\right)\exp(-jk_x x)\mathrm{d}x \\ &\approx \frac{1}{2\pi}\exp\left(\frac{jcr_n k_x^2}{4\omega}\right)\end{aligned} \tag{2.22}$$

where the last approximation follows from the principle of stationary phase [21]. The final image is obtained by the inverse Fourier transform of $\tilde{V}(k_x, r_n)$ in (2.21). For high resolution imaging and advanced SAR applications sophisticated SAR raw data processing techniques exist [9, 70, 71, 83].

2.1.4 SAR Image Properties

Geometric Distortions

The SAR range imaging mode causes geometric distortion phenomena. A constant resolution in slant range direction δ_{sr} is associated with the ground range resolution [31]

$$\delta_{gr} = \frac{\delta_{sr}}{\sin\vartheta}. \tag{2.23}$$

Thus, the from near to far range increasing incidence angle ϑ results in an improved ground range resolution δ_{gr}.

Examining the impact of a surface slope β, three scenarios can be distinguished [6]:

For $-\vartheta < \beta < \vartheta$, terrain slopes tilted towards the SAR sensor get compressed (foreshortening) in the image, whereas those tilted away from the SAR appear stretched.

A slope angle with $\beta \geq \vartheta$ leads to an inversion of the positions in the SAR image as illustrated in figure 2.1. For instance, in slant range a peak of a mountain with a steep slope might be projected into the same azimuth-range resolution cell as some point in the valley since the former is closer to the antenna location than the latter. This phenomenon is called layover.

Figure 2.1 shows that shadow can be noticed in radar images for $\beta \leq \vartheta - \frac{\pi}{2}$ where no backscattering energy reaches the sensor.

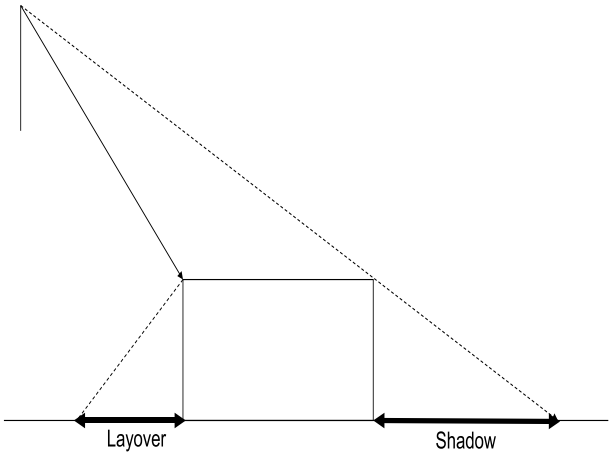

Figure 2.1: Layover and shadow phenomena.

These geometric distortion phenomena play a crucial role in SAR remote sensing of urban areas as buildings cause layover and shadow.

Speckle Effect

The generated SAR image, i.e., the backscattering reflectivity estimate, is affected by the so called speckle effect. As SAR is a coherent sensor, the speckle phenomenon is induced by interferences of waves scattered from many randomly distributed elementary reflectors inside each resolution cell leading to constructive and destructive interference.

Although speckle is a scattering phenomenon and not a noise, for extended sources it can be modeled as a multiplicative noise from the SAR data processing point of view [54,55]. Over homogeneous media, the complex speckled backscattering reflectivity is the product of the original unspeckled reflection coefficient and the multiplicative speckle contribution that is generally assumed to be a complex Gaussian distributed random variable.

Due to speckle, SAR images have a certain granularity that complicates image analysis. Before examining SAR data, it is necessary to apply filtering techniques to reduce the speckle effect [56, 57, 79].

2.2 SAR Polarimetry

Polarimetry studies how the polarization of an electromagnetic wave is modified by interacting with a target or natural media. These modifications are significantly associated with geometric characteristics and physical properties of the examined object. Thus, polarimetric information coupled with the knowledge of electromagnetic reflection behavior offers an additional dimension to describe targets using SAR data. In the SAR context, wave

polarimetry comprising two polarization states has to be extended to scattering polarimetry with four polarizations.

This section presents the basic concepts of SAR polarimetry including the mathematical formalisms. Finally, a physical interpretation of scattering processes is explained.

2.2.1 Electromagnetic Wave Polarization

The radar signal is an electromagnetic wave and its propagation can be described by the Maxwell equations. Under the assumptions that the medium where the radar waves propagate is a vacuum and non-conducting, lossless, and isotropic, the electric field $\mathbf{E}(\mathbf{r},t) \in \mathbb{R}^3$, and magnetic field $\mathbf{B}(\mathbf{r},t) \in \mathbb{R}^3$ observe the following laws:

$$\operatorname{div} \mathbf{E} = 0 \tag{2.24}$$

$$\operatorname{curl} \mathbf{E} + \frac{\partial \mathbf{B}}{\partial t} = \mathbf{0} \tag{2.25}$$

$$\operatorname{div} \mathbf{B} = 0 \tag{2.26}$$

and

$$\operatorname{curl} \mathbf{B} = \frac{1}{c^2} \frac{\partial \mathbf{E}}{\partial t} \tag{2.27}$$

where c is the wave velocity in a vacuum.

The propagation equation of the electric field can be written in vector notation as:

$$\nabla^2 \mathbf{E} + \frac{1}{c} \frac{\partial^2 \mathbf{E}}{\partial t^2} = \mathbf{0}. \tag{2.28}$$

For planar waves the solution of the propagation equation is given in complex form as

$$\mathbf{E}(\mathbf{r},t) = \Re\left(\underline{\mathbf{E}} \exp(j(\mathbf{k}\cdot\mathbf{r} - \omega t))\right) \tag{2.29}$$

where the wavevector $\mathbf{k}$ indicates the propagation direction and depends on the wavenumber

$$k = \frac{2\pi}{\lambda} = \frac{\omega}{c} \tag{2.30}$$

with the wavelength λ and the angular frequency $\omega = 2\pi f$.

In the Cartesian coordinate system and for a wave propagating in $\hat{z}$ direction the electric field can be decomposed along the axes $\hat{x}$ and $\hat{y}$ as:

$$E_x = E_{0x} \cos(\omega t - kz + \delta_x) \tag{2.31}$$

and

$$E_y = E_{0y} \cos(\omega t - kz + \delta_y) \tag{2.32}$$

where δ_x and δ_y are the absolute phases in $\hat{x}$ and $\hat{y}$, respectively.

Within a plane orthogonal to the propagation direction, chosen so that $z = 0$, the electric field $\mathbf{E}$ describes a parametric curve with

$$E_x = E_{0x} \cos(\omega t + \delta_x) \tag{2.33}$$

and

$$E_y = E_{0y} \cos(\omega t + \delta_y). \tag{2.34}$$

These are the equations of an ellipse and depend on the parameters E_{0x}, E_{0y}, and $\delta_x - \delta_y$. It can be rewritten as

$$\left(\frac{E_x}{E_{0x}}\right)^2 - 2\frac{E_x E_y}{E_{0x} E_{0y}} \cos(\delta_x - \delta_y) + \left(\frac{E_y}{E_{0y}}\right)^2 = \sin^2(\delta_x - \delta_y). \tag{2.35}$$

For $E_{0x} = E_{0y}$, and $\delta_x - \delta_y = \pm\frac{\pi}{2}$, it describes a circle, whereas for $\delta_x = \delta_y[\pi]$ it describes a line.

The electric field can be represented in complex form using the Jones vector [68], i.e., $\underline{\mathbf{E}}$ introduced in (2.29). The Jones vector is defined in the plane perpendicular to the propagation direction by

$$\underline{\mathbf{E}} = \begin{bmatrix} \underline{E}_x \\ \underline{E}_y \end{bmatrix} = \begin{bmatrix} E_{0x} \exp(j\delta_x) \\ E_{0y} \exp(j\delta_y) \end{bmatrix}. \tag{2.36}$$

The Jones vector is defined in (2.36) employing the polarization basis $(\hat{x}, \hat{y})$ that is directly linked to the geometric basis. Since the Jones vectors are elements of a complex vector space, other bases generated by orthogonal Jones vectors are possible, e.g., a circular basis including left and right hand circular vectors. For linear polarizations, the notation (h, v) instead of $(\hat{x}, \hat{y})$ is common.

2.2.2 Polarimetric Representation of Radar Targets

The interaction of an electromagnetic wave with a medium or a target generally modifies its polarization state. The Jones vector representing the reflected wave can be expressed by the incident wave and a linear transformation matrix, called scattering matrix $\mathbf{S} \in \mathbf{Mat}_2(\mathbb{C})$, or Sinclair matrix as well. It couples the illuminating field $\underline{\mathbf{E}}_i$ with the scattered field $\underline{\mathbf{E}}_s$ using the polarization basis $(\hat{h}, \hat{v})$ by [8, 78]

$$\underline{\mathbf{E}}_s = \mathbf{S}\underline{\mathbf{E}}_i = \begin{bmatrix} S_{hh} & S_{hv} \\ S_{vh} & S_{vv} \end{bmatrix} \underline{\mathbf{E}}_i. \tag{2.37}$$

The elements of $\mathbf{S}$ are distinguished by the index, where the letter on the right is associated with the incident wave polarization and the one on the left with the scattered wave polarization. The diagonal elements of the Sinclair matrix are called co-polarized since they represent the multiplicative complex coefficients relating the projections of the illuminating and reflected

Jones vectors onto the same axis of the polarization basis. The off-diagonal entries of $\mathbf{S}$ are referred to as cross-polarized. The Sinclair matrix describes completely how the polarization of a monochromatic incident wave is modified by the interaction with a radar target. The power corresponding to a radar target is denoted as SPAN and defined by

$$\text{SPAN} = |S_{hh}|^2 + |S_{hv}|^2 + |S_{vh}|^2 + |S_{vv}|^2. \tag{2.38}$$

In a monostatic configuration, i.e., when the emitter of the incident wave and the receiver of the scattered wave are located at the same position, the reciprocity theorem [12] implies that the Sinclair matrix $\mathbf{S}$ is symmetric: $S_{hv} = S_{vh}$.

Vectorizing the scattering matrix by projecting it onto a matrix group allows to obtain a target vector that contains the whole coherent polarimetric information

$$\mathbf{k} = \frac{1}{2}\text{tr}(\mathbf{S}\boldsymbol{\Psi}) = \begin{bmatrix} k_0 \\ k_1 \\ k_2 \\ k_3 \end{bmatrix} \tag{2.39}$$

where $\boldsymbol{\Psi}$ represents a set of matrices which define a projection basis. The best known bases are the one corresponding to the lexicographic ordering [12]

$$\{\boldsymbol{\Psi}_L\} = \left\{ \begin{bmatrix} 2 & 0 \\ 0 & 0 \end{bmatrix}, \begin{bmatrix} 0 & 2 \\ 0 & 0 \end{bmatrix}, \begin{bmatrix} 0 & 0 \\ 2 & 0 \end{bmatrix}, \begin{bmatrix} 0 & 0 \\ 0 & 2 \end{bmatrix} \right\} \tag{2.40}$$

and the other one based on the modified Pauli matrices

$$\{\boldsymbol{\Psi}_P\} = \left\{ \sqrt{2}\begin{bmatrix} 1 & 0 \\ 0 & 1 \end{bmatrix}, \sqrt{2}\begin{bmatrix} 1 & 0 \\ 0 & -1 \end{bmatrix}, \sqrt{2}\begin{bmatrix} 0 & 1 \\ 1 & 0 \end{bmatrix}, \sqrt{2}\begin{bmatrix} 0 & -j \\ j & 0 \end{bmatrix} \right\}. \tag{2.41}$$

The target vector associated with the lexicographic basis $\mathbf{k}_{L4} \in \mathbb{C}^4$ is given by

$$\mathbf{k}_{L4} = \begin{bmatrix} S_{hh} \\ S_{hv} \\ S_{vh} \\ S_{vv} \end{bmatrix} \tag{2.42}$$

and that related to the Pauli basis $\mathbf{k}_{P4} \in \mathbb{C}^4$ is given by

$$\mathbf{k}_{P4} = \frac{1}{\sqrt{2}} \begin{bmatrix} S_{hh} + S_{vv} \\ S_{hh} - S_{vv} \\ S_{hv} + S_{vh} \\ j(S_{hv} - S_{vh}) \end{bmatrix}. \tag{2.43}$$

For the monostatic scenario the target vectors $\mathbf{k}_{L3} \in \mathbb{C}^3$, and $\mathbf{k}_{P3} \in \mathbb{C}^3$ reduce to

$$\mathbf{k}_{L3} = \begin{bmatrix} S_{hh} \\ \sqrt{2}S_{hv} \\ S_{vv} \end{bmatrix} \qquad \text{and} \qquad \mathbf{k}_{P3} = \frac{1}{\sqrt{2}} \begin{bmatrix} S_{hh} + S_{vv} \\ S_{hh} - S_{vv} \\ 2S_{hv} \end{bmatrix}, \tag{2.44}$$

respectively.

These vectors are coherent representations of the scattering matrix and their norm equals the SPAN of the target, i.e., $\|\mathbf{k}_{L3}\|_2^2 = \|\mathbf{k}_{P3}\|_2^2 = \text{SPAN}$. The two representations are related by the unitary transformation matrix $\mathbf{A}_4 \in \mathbf{U}_4(\mathbb{C})$

$$\mathbf{k}_{L4} = \mathbf{A}_4 \mathbf{k}_{P4} = \frac{1}{\sqrt{2}} \begin{bmatrix} 1 & 1 & 0 & 0 \\ 0 & 0 & 1 & -j \\ 0 & 0 & 1 & j \\ 1 & -1 & 0 & 0 \end{bmatrix} \mathbf{k}_{P4} \tag{2.45}$$

and $\mathbf{A}_3 \in \mathbf{SO}_3(\mathbb{R})$

$$\mathbf{k}_{L3} = \mathbf{A}_3 \mathbf{k}_{P3} = \frac{1}{\sqrt{2}} \begin{bmatrix} 1 & 1 & 0 \\ 0 & 0 & \sqrt{2} \\ 1 & -1 & 0 \end{bmatrix} \mathbf{k}_{P3}, \tag{2.46}$$

respectively.

The coherent scattering matrices are measured by the radar antenna apart from a phase term. This phase contribution is generated by the sensor-reflector-sensor path and cannot be compensated. Employing quadratic forms permits to overcome this problem and to study the second order polarimetric statistics, i.e., the variance of the signals in different polarization channels and their mutual correlations.

Utilizing the lexicographic target vector $\mathbf{k}_{L4}$, the polarimetric covariance matrix $\mathbf{C}_4 \in \mathbf{Mat}_4(\mathbb{C})$ is defined as [12]

$$\mathbf{C}_4 = E\{\mathbf{k}_{L4}\mathbf{k}_{L4}^H\} = \begin{bmatrix} E\{S_{hh}S_{hh}^*\} & E\{S_{hh}S_{hv}^*\} & E\{S_{hh}S_{vh}^*\} & E\{S_{hh}S_{vv}^*\} \\ E\{S_{hv}S_{hh}^*\} & E\{S_{hv}S_{hv}^*\} & E\{S_{hv}S_{vh}^*\} & E\{S_{hv}S_{vv}^*\} \\ E\{S_{vh}S_{hh}^*\} & E\{S_{vh}S_{hv}^*\} & E\{S_{vh}S_{vh}^*\} & E\{S_{vh}S_{vv}^*\} \\ E\{S_{vv}S_{hh}^*\} & E\{S_{vv}S_{hv}^*\} & E\{S_{vv}S_{vh}^*\} & E\{S_{vv}S_{vv}^*\} \end{bmatrix}. \tag{2.47}$$

For the monostatic case, the polarimetric covariance matrix $\mathbf{C}_3 \in \mathbf{Mat}_3(\mathbb{C})$ is given by [12]

$$\mathbf{C}_3 = E\{\mathbf{k}_{L3}\mathbf{k}_{L3}^H\} = \begin{bmatrix} E\{S_{hh}S_{hh}^*\} & \sqrt{2}E\{S_{hh}S_{hv}^*\} & E\{S_{hh}S_{vv}^*\} \\ \sqrt{2}E\{S_{hv}S_{hh}^*\} & 2E\{S_{hv}S_{hv}^*\} & \sqrt{2}E\{S_{hv}S_{vv}^*\} \\ E\{S_{vv}S_{hh}^*\} & \sqrt{2}E\{S_{vv}S_{hv}^*\} & E\{S_{vv}S_{vv}^*\} \end{bmatrix}. \tag{2.48}$$

Similarly, the polarimetric coherency matrices $\mathbf{C}_4 \in \mathbf{Mat}_4(\mathbb{C})$, and $\mathbf{C}_3 \in \mathbf{Mat}_3(\mathbb{C})$ are obtained as [12]

$$\mathbf{T}_4 = E\{\mathbf{k}_{P4}\mathbf{k}_{P4}^H\} \qquad \text{and} \qquad \mathbf{T}_3 = E\{\mathbf{k}_{P3}\mathbf{k}_{P3}^H\}, \tag{2.49}$$

respectively. Since these matrices are Hermitian positive-semidefinite, their eigenvalues are real-valued nonnegative. From equations (2.45) and (2.46), it follows

$$\mathbf{C}_4 = \mathbf{A}_4\mathbf{T}_4\mathbf{A}_4^H \qquad \text{and} \qquad \mathbf{C}_3 = \mathbf{A}_3\mathbf{T}_3\mathbf{A}_3^H. \tag{2.50}$$

Thus, the covariance matrix $\mathbf{C}_4$ and the coherency matrix $\mathbf{T}_4$ (and $\mathbf{C}_3$ and $\mathbf{T}_3$, respectively) are similar and have the same eigenvalues.

2.2.3 Physical Interpretation

SAR polarimetry allows to exploit multidimensional data. By transmitting waves in diverse polarizations it is possible to characterize more accurately the electromagnetic behavior of illuminated objects. This behavior is closely related to certain physical properties of the target, such as its shape, its dielectric constant, and its electric conductivity. Hence, SAR polarimetry provides additional physical information of the examined scene.

Coherent Decompositions

Analyzing the Sinclair matrix or the associated target vectors is notably efficient for deterministic targets. In particular, the Pauli basis constitutes a starting point to model objects in a physical way. The different components of the Pauli basis can be linked to canonical scattering behaviors. For instance, a dominant contribution in the $hh + vv$ channel corresponds to a reflection on a surface or a trihedral, while a dominant component in $hh - vv$ indicates a horizontally or vertically oriented dihedral. A strong constituent in hv is associated with a dipole or a dihedral object oriented at $\frac{\pi}{4}$ according to the power in the $hh + vv$ channel. The targets have been characterized by means of the coherent scattering matrix in [10, 49, 50, 108].

Incoherent Decompositions

Various approaches have been proposed for providing a physical interpretation of the incoherent polarimetric matrices [32, 46]. A decomposition that does not assume any a priori knowledge about the reflection pattern has been suggested in [12]:

The projection of an incoherent polarimetric representation onto the basis of its eigenvectors allows to decompose in a unique manner a distributed target into a sum of three pure targets whose target vectors are orthogonal. Thus, the eigenvectors are associated with the physical characteristics and correspond to scattering mechanisms. The coherency matrix $\mathbf{T}$ can be decomposed into its eigenvectors

$$\mathbf{T}_3 = \mathbf{V}\mathbf{\Lambda}\mathbf{V}^H = \sum_{k=1}^{3} \lambda_k \mathbf{v}_k \mathbf{v}_k^H \tag{2.51}$$

where $\mathbf{V} \in \mathbf{SU}_3(\mathbb{C})$ denotes the matrix of orthonormal eigenvectors $\mathbf{v}_k$, and $\mathbf{\Lambda} \in \mathbf{Mat}_3(\mathbb{R})$ the diagonal matrix including the real-valued eigenvalues λ_k with $\lambda_k \geq 0$. The coherency matrix $\mathbf{T}$ is decomposed into a noncoherent sum

of three coherency matrices $\mathbf{T}_k = \mathbf{v}_k \mathbf{v}_k^H$, each weighted by the associated eigenvalue [12, 13]

$$\mathbf{T}_3 = \sum_{k=1}^{3} \lambda_k \mathbf{T}_k. \tag{2.52}$$

As the matrices $\mathbf{T}_k$ have unit trace, the eigenvalues represent the power associated with each contribution and are sorted: $\lambda_1 \geq \lambda_2 \geq \lambda_3 \geq 0$.

The eigenvalue set indicates the distribution of the total power on the different decomposition components. This distribution describes the proportion of power related to the mechanism and is defined by

$$p_k = \frac{\lambda_k}{\sum_{k=1}^{3} \lambda_k} \tag{2.53}$$

These normalized eigenvalues can be interpreted as pseudo-probabilities connected with the statistical properties of the reflection processes in natural media with $p_1 \geq p_2 \geq p_3 \geq 0$. The eigenvalue spectrum can be specified by two real-valued parameters, the entropy and the anisotropy [12, 13].

The entropy indicates the degree of statistical disorder of the reflection pattern and is given by

$$H = -\sum_{k=1}^{3} p_k \log_3 p_k. \tag{2.54}$$

If the entropy is zero, the first pseudo-probability equals one. In this case the coherency matrix represents a pure target and the scattering is deterministic. Entropy close to one corresponds to a uniform distribution of the probability set where the scattering process is a random noise.

The anisotropy is defined by

$$A = \frac{p_2 - p_3}{p_2 + p_3} \tag{2.55}$$

and characterizes the relative importance of the secondary reflection mechanisms.

A unitary vector $\mathbf{v} \in \mathbb{C}^3$ has five degrees of freedom and can be written as

$$\mathbf{v} = \exp(j\phi) \begin{bmatrix} \cos\alpha \\ \sin\alpha\cos\beta\exp(j\delta) \\ \sin\alpha\sin\beta\exp(j\gamma) \end{bmatrix}. \tag{2.56}$$

where $\phi, \alpha, \beta, \delta, \gamma \in \mathbb{R}$. The phase term ϕ depends on the way eigenvectors are calculated and does not contribute to the scattering type [27]. The angle α indicates the nature of the scattering mechanism. A value close to zero relates to surface reflection, α equals $\frac{\pi}{4}$ for scattering from a dipole, and reaches $\frac{\pi}{2}$ when the target consists of a dihedral object. The three remaining

parameters are related to the orientation of the examined target around the radar line-of-sight.

Using the angles $\{\alpha_1, \alpha_2, \alpha_3\}$ from the three eigenvectors of the coherency matrix the average $\bar{\alpha}$ value is computed by

$$\bar{\alpha} = \sum_{k=1}^{3} p_k \alpha_k. \tag{2.57}$$

2.3 SAR Interferometry

SAR interferometry is an established technique to measure terrain topography. The application of this technique is based on the generation of an interferogram using two complex SAR images of the same area acquired from two slightly different look angles. The phase difference contains information related to the scene topography.

The fundamental properties of SAR interferometry are outlined and the decorrelation sources of the interferometric coherence are detailed.

2.3.1 SAR Interferometry Basics

Cross-track SAR interferometry is a technique to determine the height location of a scatterer. Two complex SAR images of the same scene are aquired from slightly different sensor positions (see [6, 69, 91] and the references therein). This is realized either in a single-pass mode employing two antennas simultaneously or in a repeat-pass mode where the same region is imaged repeatedly from different parallel trajectories.

Figure 2.2 displays the basic cross-track InSAR acquisition geometry. The area is imaged by two sensors S_1 and S_2, that are separated by the baseline B with the slope angle ϵ. A scatterer ρ is positioned at the topographic height z. The range distances from the reflector ρ to S_1 and S_2 are r_1 and r_2, respectively. As the range distances r_1 and r_2 are different the incidence angle ϑ and finally the object height can be estimated. Applying the cosine law to the triangle in figure 2.2, the distance r_2 can be written as

$$r_2^2 = r_1^2 + B^2 + 2r_1 B \underbrace{\cos(\frac{\pi}{2} - \vartheta + \epsilon)}_{\sin(\vartheta - \epsilon)}. \tag{2.58}$$

This can be reformulated as

$$\sin(\vartheta - \epsilon) = \frac{r_2^2 - r_1^2 - B^2}{2r_1 B}. \tag{2.59}$$

If the baseline parameters B and ϵ are known, the look angle ϑ can be extracted by equation (2.59). Then the reflector height can be computed by

$$h = h_0 - r_1 \cos\vartheta. \tag{2.60}$$

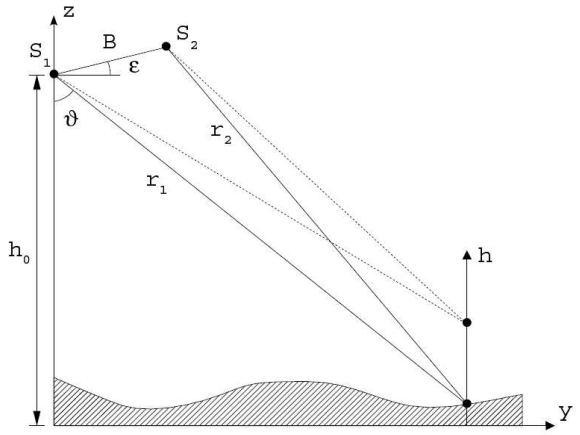

Figure 2.2: Interferometric SAR acquisition geometry.

This approach is called radar stereogrammetry [52, 53].

The precision with which the target location is determined is in the order of the range distance estimation accuracy and therefore limited by the range resolution (2.2). SAR interferometry yields a considerably finer resolution in the vertical direction since the SAR interferogram allows to measure the difference between r_1 and r_2 much more precisely than each range distance. After coregistrating the SAR images s_1 and s_2 [29], the interferogram is calculated by

$$s_1 s_2^* = |s_1||s_2|\rho_1\rho_2^* \exp\left(j\frac{4\pi}{\lambda}(r_1 - r_2)\right). \tag{2.61}$$

Under the assumption that the complex reflectivity ρ remains constant for small changes of the incidence angle, the phases of ρ_1 and ρ_2 are equal and the interferometric phase only includes the path difference between the sensors. Ignoring the fact that the phase of the interferogram is ambiguous within integer multiples of 2π, the absolute phase difference is a very precise measure of the range difference between the antennas. In comparison with radar stereogrammetry this rationale leads to noticeably enhanced angular resolution.

Utilizing $\Delta r_{12} = r_2 - r_1$, the relation (2.59) can be rewritten as

$$B\sin(\vartheta - \epsilon) = \Delta r_{12} + \frac{\Delta r_{12}^2}{2r_1} - \frac{B^2}{2r_1}. \tag{2.62}$$

If the baseline B is chosen to be small relative to the range distance r_1, the most significant contribution in equation (2.62) is the path difference Δr_{12}. Neglecting the last two terms it follows

$$\phi = \frac{4\pi}{\lambda}\Delta r_{12} \approx \frac{4\pi}{\lambda} B\sin(\vartheta - \epsilon) \tag{2.63}$$

Let $\tilde{\rho}$ be another reflector positioned at the same range distance but with a topographic height difference Δz to the first scatterer. Because of the slightly changing look angle its interferometric phase is

$$\tilde{\phi}(\Delta z) = \frac{4\pi}{\lambda} B \sin(\vartheta + \Delta\vartheta(\Delta z) - \epsilon). \tag{2.64}$$

The relation between the phase and height differences is derived by [85]

$$\begin{aligned} \Delta\phi &= \frac{4\pi}{\lambda} B(\sin(\vartheta + \Delta\vartheta(\Delta z) - \epsilon) - \sin(\vartheta - \epsilon)) \\ &\approx \frac{4\pi}{\lambda} B \cos(\vartheta - \epsilon)\Delta\vartheta(\Delta z) \\ &\approx \frac{4\pi}{\lambda} \frac{B\cos(\vartheta - \epsilon)}{r_1 \sin\vartheta} \Delta z \end{aligned} \tag{2.65}$$

where the difference quotient of the sin function is used in the first approximation and the second stems from

$$\Delta\vartheta(\Delta z) \approx \frac{\Delta z}{r_1 \sin\vartheta}. \tag{2.66}$$

Defining the orthogonal or normal baseline

$$B_\perp = B\cos(\vartheta - \epsilon) \tag{2.67}$$

the height sensitivity is

$$\frac{\Delta\phi}{\Delta z} = \frac{4\pi}{\lambda} \frac{B_\perp}{r_1 \sin\vartheta}. \tag{2.68}$$

The vertical wavenumber k_z is introduced by

$$k_z = \frac{4\pi}{\lambda} \frac{B_\perp}{r \sin\vartheta}. \tag{2.69}$$

The height of ambiguity

$$z_{2\pi} = \frac{\lambda}{2} \frac{r \sin\vartheta}{B_\perp} \tag{2.70}$$

describes the height leading to a phase change of 2π. Before calculating the topographic height from the measured wrapped phase $-\pi \leq \phi < \pi$ via equation (2.68), the absolute phase has to be reconstructed using phase unwrapping methods [20,30,35,40,82]. The ability to resolve the 2π ambiguity depends on the local terrain slope and the phase noise level caused by signal decorrelation between the two acquired images [47, 115].

2.3.2 Interferometric SAR Coherence and Decorrelation Sources

Due to the random aspect of SAR data, the correlation between the two SAR images s_1 and s_2 is defined by [115]

$$\gamma = \frac{E\{s_1 s_2^*\}}{\sqrt{E\{s_1 s_1^*\} E\{s_2 s_2^*\}}}. \tag{2.71}$$

Its absolute value $|\gamma|$ is called interferometric coherence and measures the interferogram quality: For a coherence close to one the interferometric phase distribution resembles a delta function. The phase difference appears noisy for low coherences. When the coherence is zero, the distribution is uniform and the interferogram does not contain useful information.

To analyze in detail the decorrelation sources the signal intensities of the complex SAR images s_1 and s_2 are given by

$$I_1 = E\{s_1 s_1^*\} = \int_V \sigma_{v1} |h_1(x,r)|^2 \mathrm{d}V \tag{2.72}$$

and

$$I_2 = E\{s_2 s_2^*\} = \int_V \sigma_{v2} |h_2(x,r)|^2 \mathrm{d}V \tag{2.73}$$

where σ_{v1} and σ_{v2} are the volume scattering coefficients, and h_1 and h_2 are the coherent SAR impulse response functions of s_1 and s_2, respectively. If it is assumed that $h = h_1 = h_2$, and $\sigma_v = \sigma_{v1} = \sigma_{v2}$, the interferometric correlation can be expressed by

$$\gamma = \frac{\int_V \sigma_{ve}(\mathbf{r}) \exp(-j2(\mathbf{k}_1 - \mathbf{k}_2) \cdot \mathbf{r}) |h(x,r)|^2 \mathrm{d}V}{\int_V \sigma_v |h(x,r)|^2 \mathrm{d}V + n} \tag{2.74}$$

where σ_{ve} is the product of the complex scattering amplitudes of both images. It can be interpreted as the scattering contributions that are stable in time. The location vector $\mathbf{r}$ is given by $\mathbf{r} = [x, y, z]^T$, and the wavevectors $\mathbf{k}_1$ and $\mathbf{k}_2$ by $\mathbf{k}_i = k[0, \sin\vartheta_i, \cos\vartheta_i]^T$, with the wavenumber $k = \frac{2\pi}{\lambda}$. The additive noise is denoted by n. The interferometric correlation γ can be split up into the following decorrelation sources [115]:

The thermal additive noise leads to the factor

$$\gamma_{SNR} = \frac{\int_V \sigma_v(\mathbf{r}) |h(x,r)|^2 \mathrm{d}V}{\int_V \sigma_v(\mathbf{r}) |h(x,r)|^2 \mathrm{d}V + n} = \frac{1}{1 + \frac{1}{SNR}}. \tag{2.75}$$

The lower the signal-to-noise ratio (SNR), the higher the decorrelation due to thermal noise.

In the repeat-pass scenario temporal decorrelation occurs since the scatterers' properties may change between the acquisitions:

$$\gamma_{temporal} = \frac{\int_V \sigma_{ve}(\mathbf{r}) |h(x,r)|^2 \mathrm{d}V}{\int_V \sigma_v(\mathbf{r}) |h(x,r)|^2 \mathrm{d}V}. \tag{2.76}$$

If the scattering behavior does not vary during the two passes, i.e., $\sigma_v = \sigma_{ve}$, then $\gamma_{temporal} = 1$.

As the complex reflectivity is angle-dependent the decorrelation due to the slightly different look angles is

$$\gamma_{spatial} = \frac{\int_V \sigma_{ve}(\mathbf{r}) \exp(-j2(\mathbf{k}_1 - \mathbf{k}_2) \cdot \mathbf{r}) |h(x,r)|^2 \mathrm{d}V}{\int_V \sigma_{ve} |h(x,r)|^2 \mathrm{d}V}. \tag{2.77}$$

If the incidence angles $\vartheta_1 = \vartheta_2$ and wavenumbers $k_1 = k_2$, then $\mathbf{k}_1 = \mathbf{k}_2$ and $\gamma_{spatial} = 1$. In this situation it is not possible to retrieve the reflector's topographic height. The term $\gamma_{spatial}$ can be decomposed into two constituents by means of the relation

$$\begin{aligned} & \exp(-j2(\mathbf{k}_1 - \mathbf{k}_2) \cdot \mathbf{r}) \qquad (2.78) \\ = \; & \exp\left(-j2\left(\left(\frac{k\cos\vartheta B_\perp}{r} + \Delta k \sin\vartheta\right) y + \left(\frac{k\sin\vartheta B_\perp}{r} + \Delta k \cos\vartheta\right) z\right)\right) \end{aligned}$$

where $\Delta k = k_1 - k_2$, $k = \frac{k_1 + k_2}{2}$, and the approximation $\Delta\vartheta \simeq \sin(\Delta\vartheta) = \frac{B_\perp}{r}$ are used. The first component is [33]

$$\gamma_{surface} = \frac{\int \sigma_{ve}(\mathbf{r}) \exp\left(-j2\left(\frac{k\cos\vartheta B_\perp}{r} + \Delta k \sin\vartheta\right) y\right) |h(x,r)|^2 \mathrm{d}x\mathrm{d}y}{\int |h(x,r)|^2 \mathrm{d}x\mathrm{d}y}. \tag{2.79}$$

Setting $\Delta k = -\frac{kB_\perp}{r\tan\vartheta}$ increases $\gamma_{surface}$. This decorrelation generated by different incidence angles can be reduced by wavenumber shift filtering [33, 80].

The second contribution can be expressed as [33]

$$\gamma_{volume} = \frac{\int_z \sigma_{ve}(z) \exp\left(-j2\left(\frac{k\sin\vartheta B_\perp}{r} + \Delta k \cos\vartheta\right) z\right) \mathrm{d}z}{\int_z \sigma_{ve}(z) \mathrm{d}z} \tag{2.80}$$

which describes the decorrelation caused by scatterers distributed inside a volume.

Summarizing, the coherence can be split up as

$$\begin{aligned} \gamma &= \gamma_{SNR} \cdot \gamma_{temporal} \cdot \gamma_{spatial} \\ &= \gamma_{SNR} \cdot \gamma_{temporal} \cdot \gamma_{surface} \cdot \gamma_{volume}. \end{aligned} \tag{2.81}$$

Processing artefacts such as coregistration errors that decrease as well the coherence $|\gamma|$ are not considered.

2.4 Advanced Multi-channel SAR

In this section two advanced multi-channel SAR approaches, namely polarimetric SAR interferometry and multibaseline InSAR are outlined. For

single-baseline polarimetric SAR interferometry the mathematical formalism is presented. Finally, SAR tomography using multibaseline InSAR observations is shortly introduced.

2.4.1 Single-baseline Polarimetric SAR Interferometry

While SAR interferometry permits to retrieve the topographic height of reflectors, the physics of scattering processes is investigated via SAR polarimetry. In polarimetric SAR interferometry both techniques are coherently combined to estimate the vertical location of scattering mechanisms. The notion of polarimetric SAR interferometry is introduced by extending the interferometric coherence to the polarization diversity scenario.

The scattering vectors $\mathbf{k}_1, \mathbf{k}_2$ acquired from spatially separated positions at either end of a baseline are given in the Pauli polarization basis as

$$\mathbf{k}_i = \frac{1}{\sqrt{2}} \left[S^i_{hh} + S^i_{vv}, S^i_{hh} - S^i_{vv}, 2S^i_{hv} \right]^T . \tag{2.82}$$

The covariance matrix $\mathbf{T}_6 = E\{\mathbf{k}_6 \mathbf{k}_6^H\} \in \mathbf{Mat}_6(\mathbb{C})$ is defined by [14]

$$\mathbf{T}_6 = E\left\{ \begin{bmatrix} \mathbf{k}_1 \\ \mathbf{k}_2 \end{bmatrix} \left[\mathbf{k}_1^H, \mathbf{k}_2^H \right] \right\} = \begin{bmatrix} \mathbf{T}_{11} & \mathbf{\Omega}_{12} \\ \mathbf{\Omega}_{12}^H & \mathbf{T}_{22} \end{bmatrix} \tag{2.83}$$

and is Hermitian, positive semidefinite. The matrices $\mathbf{T}_{ii} \in \mathbf{Mat}_3(\mathbb{C})$ for $i = 1, 2$ and $\mathbf{\Omega}_{12} \in \mathbf{Mat}_3(\mathbb{C})$ are obtained as

$$\mathbf{T}_{11} = E\{\mathbf{k}_1 \mathbf{k}_1^H\}, \tag{2.84}$$

$$\mathbf{T}_{22} = E\{\mathbf{k}_2 \mathbf{k}_2^H\}, \tag{2.85}$$

and

$$\mathbf{\Omega}_{12} = E\{\mathbf{k}_1 \mathbf{k}_2^H\}. \tag{2.86}$$

where $\mathbf{T}_{ii}$, are the conventional Hermitian coherency matrices containing the fully polarimetric information for each separate image. The non-Hermitian matrix $\mathbf{\Omega}_{12}$ includes the interferometric phase relations of the different polarimetric channels between both images [14].

To extend the definition of interferometric coherence to diverse polarizations the normalized vectors $\mathbf{w}_1, \mathbf{w}_2 \in \mathbb{C}^3$ with $\|\mathbf{w}_i\|_2 = 1$ for $i = 1, 2$ are introduced. They can be interpreted as two scattering mechanisms. Then the scattering coefficients $\mu_i \in \mathbb{C}$ are defined by

$$\mu_1 = \mathbf{w}_1^H \mathbf{k}_1 \qquad \text{and} \qquad \mu_2 = \mathbf{w}_2^H \mathbf{k}_2. \tag{2.87}$$

The vector interferogram is formed by

$$E\{\mu_1 \mu_2^*\} = E\{(\mathbf{w}_1^H \mathbf{k}_1)(\mathbf{w}_2^H \mathbf{k}_2)^H\} = \mathbf{w}_1^H \mathbf{\Omega}_{12} \mathbf{w}_2 \tag{2.88}$$

and the polarimetric interferometric phase by

$$\phi = \arg(E\{\mu_1 \mu_2^*\}) = \arg(\mathbf{w}_1^H \mathbf{\Omega}_{12} \mathbf{w}_2) \tag{2.89}$$

with

$$\arg(\mathbf{w}_1^H \mathbf{w}_2) = 0. \tag{2.90}$$

This leads to the generalized polarimetric interferometric coherence $\gamma \in \mathbb{C}$ with

$$\gamma = \frac{E\{\mathbf{w}_1^H \mathbf{\Omega}_{12} \mathbf{w}_2\}}{\sqrt{E\{\mathbf{w}_1^H \mathbf{T}_{11} \mathbf{w}_1\} E\{\mathbf{w}_2^H \mathbf{T}_{22} \mathbf{w}_2\}}}. \tag{2.91}$$

If $\mathbf{w}_1 \neq \mathbf{w}_2$, the contribution of the polarimetric correlation γ_{pol} between $\mathbf{w}_1$ and $\mathbf{w}_2$ is generally less than one and

$$\gamma = \gamma_{int} \cdot \gamma_{pol} \tag{2.92}$$

where γ_{int} includes the different interferometric components as explained in subsection 2.3.2. If the scattering mechanisms are identical, i.e., $\mathbf{w}_1 = \mathbf{w}_2$, then $\gamma_{pol} = 1$ and $\gamma = \gamma_{int}$. Using the formalism of the generalized coherence the interferometric coherence can be computed for any polarization combination. For instance, to determine the correlation where the first image has hh and the second $hh - vv$ polarization, the scattering mechanisms $\mathbf{w}_1 = [\frac{1}{\sqrt{2}}, \frac{1}{\sqrt{2}}, 0]^T$ and $\mathbf{w}_2 = [0, 1, 0]^T$ have to be selected, respectively. The interferometric coherence value depends strongly on the polarization channels since the backscattering processes differ with respect to the polarization state [14].

As the interferometric coherence changes noticeably with polarization an approach has been conceived to calculate the polarization combination yielding the highest correlation [14]. Other methods to optimize the interferometric coherence have been developed in [19] where both one single and two scattering mechanisms are considered. These techniques have been extended to the multibaseline POL-InSAR scenario in [72–74].

To extract physical parameters from polarimetric interferometric SAR observations a coherent model describing the scattering processes has been designed (see [75] and the references therein). It relates the SAR measurables to the forest parameters like tree height. The random volume over ground model takes a vegetation layer and ground interactions into account. Schemes to inverse the electromagnetic model for extracting forest parameters such as tree height and underlying ground topography have been introduced in [15, 75].

Besides forest parameter inversion, POL-InSAR has been applied to retrieve biophysical parameters of agricultural crops [4, 92] and mine detection and surface clutter rejection [93].

Processing polarimetric single-baseline InSAR signals by means of the ESPRIT algorithm was proposed in [114] to investigate forested areas and used in [42] to analyze urban scenes.

2.4.2 Multibaseline SAR Interferometry

An extension of conventional two-dimensional SAR imaging is SAR tomography that allows the reconstruction of a three-dimensional scatterer distribution [84,85]. An airborne multibaseline interferometric SAR configuration including fourteen parallel tracks has been used to form a synthetic aperture in elevation. This set-up permits to achieve focusing in height direction and to generate a three-dimensional SAR image.

The tomographic SAR imaging approach has been applied to forested areas where both the ground level and the forest canopy have been distinguished resulting in an estimation of tree height and ground topography [84, 85]. Since the tomographic processing preserves the phase information the scattering pattern inside the studied volume has been examined using polarization diversity [84, 85].

Spectral analysis techniques have been utilized for tomographic imaging from polarimetric multibaseline InSAR measurements in [43, 44, 64].

A three-dimensional radar imaging technique of vegetation using single and dual-baseline polarimetric interferometric SAR observations called polarization coherence tomography has been developed in [16, 17].

Another application of multibaseline InSAR is differential interferometry to produce high-quality digital elevation models (DEMs) [24] and high accuracy differential measurements for subsidence and surface deformation detection and monitoring [18, 25, 26, 76] based on a selection of stable reflectors known as permanent scatterers from spaceborne data. Airborne differential SAR interferometry has been presented in [81, 86] to retrieve the error in a DEM and to investigate the temporal evolution of deformations, for instance in agricultural fields.

Chapter 3

Single Polarization Multibaseline InSAR Spectral Analysis Techniques

Spectral analysis methods to process single polarization multibaseline (MB) interferometric SAR data are presented in this chapter. In the first section, an established signal model for sensor array processing and models of multibaseline InSAR point-like targets and extended sources are described. The next section explains model order selection algorithms relying on information theoretic criteria to estimate the number of sources. Spectral estimation techniques to retrieve the signal parameters such as the scatterer height and their reflectivity from single polarization MB InSAR observations are elaborated in the third section. Finally, a maximum likelihood estimator is introduced that solves the combined detection-estimation problem.

3.1 Single Polarization MB InSAR Signal Models

First a common signal model for sensor array processing is presented that is a starting point for conceiving some spectral analysis techniques such as the MUSIC method. Subsequently a model for deterministic multibaseline InSAR data is introduced which describes the response from point-like targets. The stochastic model for extended sources comprises the speckle effect as multiplicative noise. Finally, the two preceding approaches are joined to form a hybrid model.

3.1.1 Sensor Array Signal Model

A signal model widely used in sensor array processing (see [100,107,110,113] and the references therein) is the following: For p sensors the received signal vector $\mathbf{y}(l) \in \mathbb{C}^p$ is a superposition of a finite number of signals buried in

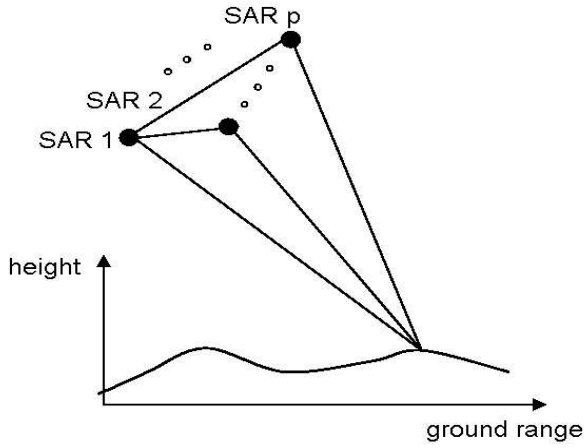

Figure 3.1: General MB InSAR imaging geometry.

additive noise

$$\mathbf{y}(l) = \sum_{i=1}^{N_s} s_i(l)\mathbf{a}(\boldsymbol{\theta}_i) + \mathbf{n}(l) \tag{3.1}$$

with the number of samples L, and $l = 1, \ldots, L$. The terminology is as follows: $s_i(l)$ is the scalar complex amplitude of the ith signal, $\mathbf{a}(\boldsymbol{\theta}_i)$ a vector dependent on the unknown parameter vector $\boldsymbol{\theta}_i$ of the ith source, and $\mathbf{n}(l)$ the additive noise. The number of sources is denoted by N_s.

In the context of single polarization multibaseline interferometric SAR data, the vector $\mathbf{a}(\boldsymbol{\theta}_i)$ has the following structure: For a uniform linear array (ULA) the steering vector $\mathbf{a}(\varphi) \in \mathbb{C}^p$ is a function of the interferometric phase at the overall baseline φ, i.e., the phase difference between the two furthest phase centers. It has the form

$$\mathbf{a}(\varphi) = [1, \exp\{j\varphi/(p-1)\}, \ldots, \exp\{j\varphi\}]^T. \tag{3.2}$$

The phase φ is related to the spatial frequency $\omega, \omega \in [-\pi, \pi)$, by [37,89,107]

$$\varphi = (p-1)\omega. \tag{3.3}$$

For a general acquisition geometry, i.e., a nonuniform and nonlinear array, the steering vector $\mathbf{a}(z)$ is dependent on the reflector height z, and is represented as

$$\mathbf{a}(z) = [1, \exp\{j\kappa_{z_2} z\}, \ldots, \exp\{j\kappa_{z_p} z\}]^T \tag{3.4}$$

where the vertical wavenumber is defined by $\kappa_{z_i} = \frac{4\pi}{\lambda} \frac{B_\perp^{(i)}}{r^{(i)} \sin\theta^{(i)}}$ (cf. equation (2.69)). In figure 3.1 an MB InSAR system with an irregular track distribution is depicted.

The noise $\mathbf{n}(l)$ is assumed to be a stationary and ergodic Gaussian random vector, independent of the signals, with zero mean and covariance matrix $\sigma_n^2\mathbf{I} \in \mathbf{Mat}_p(\mathbb{C})$ where σ_n^2 is the unknown noise power, i.e., $\mathbf{n}(l) \sim \mathcal{N}_{\mathbb{C}}^p(\mathbf{0}, \sigma_n^2\mathbf{I})$.

For a finite set of observations $\{\mathbf{y}(1), \ldots, \mathbf{y}(L)\}$, the matrix form of this model is

$$\mathbf{y}(l) = \mathbf{A}(\boldsymbol{\theta})\mathbf{s}(l) + \mathbf{n}(l) \tag{3.5}$$

with the matrix $\mathbf{A}(\boldsymbol{\theta}) = [\mathbf{a}(\boldsymbol{\theta}_1), \ldots, \mathbf{a}(\boldsymbol{\theta}_{N_s})] \in \mathbf{Mat}_{p,N_s}(\mathbb{C})$ and the parameter vector $\boldsymbol{\theta} = [\boldsymbol{\theta}_1^T, \ldots, \boldsymbol{\theta}_{N_s}^T]^T$. The signal vector is defined by $\mathbf{s}(l) = [s_1(l), \ldots, s_{N_s}(l)]^T$. The data covariance matrix $\mathbf{R} = E\{\mathbf{y}(l)\mathbf{y}^H(l)\} \in \mathbf{Mat}_p(\mathbb{C})$ is given by

$$\mathbf{R} = \mathbf{A}\mathbf{S}\mathbf{A}^H + \sigma_n^2\mathbf{I}. \tag{3.6}$$

If the signal covariance matrix $\mathbf{S} = E\{\mathbf{s}(l)\mathbf{s}^H(l)\}$ is nonsingular and diagonal, the signals are uncorrelated. When the matrix is not diagonal, they are partially correlated. If the signals are fully correlated and hence $\mathbf{S}$ is singular, the signals are called coherent.

Since the data covariance matrix is not known a priori, it has to be estimated. Under the assumption of a Gaussian distribution, the maximum likelehood estimate of the sample covariance matrix $\hat{\mathbf{R}} \in \mathbf{Mat}_p(\mathbb{C})$ is computed by

$$\hat{\mathbf{R}} = \frac{1}{L}\sum_{l=1}^{L} \mathbf{y}(l)\mathbf{y}^H(l). \tag{3.7}$$

This signal model plays an essential role in the spatial problem of source location using an array of sensors where it is common to postulate the following simplifying assumptions [107]: The sources are considered to be located in the far field of the array and to be point emitters. The sources and the sensors are supposed to be in the same plane. Moreover, the propagation medium is assumed to be homogeneous, i.e., not dispersive, and the waves arriving at the array are supposed to be planar. The signals are assumed to be narrowband and centered around a known frequency. Under these conditions, the so-called direction of arrival (DOA) determines the source location. The DOA can be also viewed as a spatial frequency.

This signal model is the basis for conceiving the model order selection techniques in section 3.2, the MUSIC algorithm in subsection 3.3.3, and the maximum likelihood estimator for solving the combined detection-estimation problem in section 3.4.

3.1.2 Deterministic MB InSAR Signal Model

For point-like scatterers, a realization of the single polarization multibaseline InSAR measurement vector $\mathbf{y}(l)$ with p antennas can be modeled as

$$\begin{aligned}\mathbf{y}(l) &= \mathbf{t} + \mathbf{n}(l) \\ &= \sum_{i=1}^{N_{s_t}} \sqrt{\tau_{t_i}} \exp(j\psi_i)\mathbf{a}(\theta_{t_i}) + \mathbf{n}(l). \end{aligned} \tag{3.8}$$

The first term, $\mathbf{t}$, is highly coherent and can be associated with deterministic targets [28]. N_{s_t} represents the number of backscattering sources, $\sqrt{\tau_{t_i}}$ the amplitude of their response, and ψ_i their phase. The steering vector $\mathbf{a}(\theta_{t_i})$ is introduced in subsection 3.1.1.

Hence, the MB InSAR received data vector $\mathbf{y}(l)$ is a Gaussian random process with nonzero mean

$$\boldsymbol{\mu} = \sum_{i=1}^{N_{s_t}} \sqrt{\tau_{t_i}} \exp(j\psi_i)\mathbf{a}(\theta_{t_i}) = \mathbf{t} \neq \mathbf{0} \tag{3.9}$$

and covariance matrix $\mathbf{R} \in \mathbf{Mat}_p(\mathbb{C})$, i.e., $\mathbf{y}(l) \sim \mathcal{N}_{\mathbb{C}}^p(\boldsymbol{\mu}, \mathbf{R})$. The returned signal (3.8) can be expressed in matrix notation as (cf. equation (3.5))

$$\mathbf{y}(l) = \mathbf{A}(\boldsymbol{\theta})\mathbf{s} + \mathbf{n}(l) \tag{3.10}$$

with the signal vector $\mathbf{s} = \left[s_1, \ldots, s_{N_{s_t}}\right]^T$, $s_i = \sqrt{\tau_{t_i}} \exp(j\psi_i)$.

The structure of the non-central covariance matrix $\mathbf{R} = E\{\mathbf{y}(l)\mathbf{y}^H(l)\}$ of the received data (3.8) is

$$\mathbf{R} = \mathbf{A}(\boldsymbol{\theta})\mathbf{S}\mathbf{A}^H(\boldsymbol{\theta}) + \sigma_n^2\mathbf{I} \tag{3.11}$$

with the signal covariance matrix $\mathbf{S} = \mathbf{s}\mathbf{s}^H$. This model takes coherent multipath scattering effects into account that might occur in urban environments.

3.1.3 Stochastic MB InSAR Signal Model

Recently, a signal model for the single polarization multibaseline InSAR configuration with p sensors has been conceived [37, 39, 63] incorporating the SAR speckle effect as multiplicative noise. For extended sources the observation vector $\mathbf{y}(l)$ is written as

$$\begin{aligned}\mathbf{y}(l) &= \mathbf{c}(l) + \mathbf{n}(l) \\ &= \sum_{j=1}^{N_{s_c}} \sqrt{\tau_{c_j}}\mathbf{x}_j(l) \odot \mathbf{a}(\theta_{c_j}) + \mathbf{n}(l) \end{aligned} \tag{3.12}$$

with the number of looks L, and $l = 1, \ldots, L$, and the Schur-Hadamard product $\odot$ (elementwise multiplication). The contribution $\mathbf{c}(l)$ represents

the response of distributed environments including the SAR speckle phenomenon as multiplicative noise [37, 39, 63]. N_{s_c} is the number of extended backscattering sources. The unknown reflectivity τ_{c_j}, the steering vector $\mathbf{a}(\theta_{c_j})$ with the unknown parameter θ_{c_j}, and the additive noise $\mathbf{n}(l)$ are defined as in subsections 3.1.1 and 3.1.2.

The multiplicative noise $\mathbf{x}_j(l) \in \mathbb{C}^p$ related to the jth source is modeled as a stationary, circular Gaussian distributed random variable with zero mean, unit variance, and covariance matrix $\mathbf{C}_j = E\{\mathbf{x}_j(l)\mathbf{x}_j^H(l)\}$. For different looks $l_1 \neq l_2$, the random processes $\mathbf{x}_j(l_1)$ and $\mathbf{x}_j(l_2)$ are assumed to be independent and identically distributed (locally stationary in a homogeneous scene). This can be written in shorthand notation $\mathbf{x}_j(l) \sim \mathcal{N}_{\mathbb{C}}^p(\mathbf{0}, \mathbf{C}_j)$. Neglecting possible multipath effects the sources can be considered as independent. If the speckle is completely correlated for each component, i.e., the speckle is constant over the array, $\mathbf{x}_j(l) = x_j(l)\mathbf{1}$ with $\mathbf{1} = [1, \ldots, 1] \in \mathbb{C}^p$, the signal is spatially fully correlated and has constant amplitude.

Thus, the stochastic MB InSAR received data vector $\mathbf{y}(l)$ is a Gaussian random process with zero mean and covariance matrix $\mathbf{R}$, which can be written as

$$\mathbf{R} = E\{\mathbf{y}(l)\mathbf{y}^H(l)\} = \sum_{j=1}^{N_{s_c}} \tau_{c_j}\mathbf{C}_j \odot \mathbf{a}(\theta_{c_j})\mathbf{a}^H(\theta_{c_j}) + \sigma_n^2\mathbf{I}. \tag{3.13}$$

An alternative form is given by

$$\mathbf{R} = \sum_{j=1}^{N_{s_c}} \tau_{c_j}\mathbf{A}_j\mathbf{C}_j\mathbf{A}_j^H + \sigma_n^2\mathbf{I} \tag{3.14}$$

with the diagonal matrix $\mathbf{A}_j = \operatorname{diag}\left(1, \exp\{j\kappa_{z_2}z_{c_j}\}, \ldots, \exp\{j\kappa_{z_p}z_{c_j}\}\right) \in \mathbf{Mat}_p(\mathbb{C})$.

Under the condition of fully correlated speckle the data covariance matrix reduces to

$$\mathbf{R} = \sum_{j=1}^{N_{s_c}} \tau_{c_j}\mathbf{a}(\theta_{c_j})\mathbf{a}^H(\theta_{c_j}) + \sigma_n^2\mathbf{I} = \mathbf{A}(\boldsymbol{\theta})\mathbf{S}\mathbf{A}^H(\boldsymbol{\theta}) + \sigma_n^2\mathbf{I} \tag{3.15}$$

where the steering matrix is defined by $\mathbf{A}(\boldsymbol{\theta}) = [\mathbf{a}(\theta_{c_1}), \ldots, \mathbf{a}(\theta_{c_{N_{s_c}}})] \in \mathbf{Mat}_{p,N_{s_c}}(\mathbb{C})$ and the diagonal signal covariance matrix by $\mathbf{S} = \operatorname{diag}\left(\tau_{c_j}\right)_{j=1}^{N_{s_c}} \in \mathbf{Mat}_{N_{s_c}}(\mathbb{R})$. In this case the covariance matrix resembles that of the sensor array signal model (3.6) introduced in subsection 3.1.1.

3.1.4 Hybrid MB InSAR Signal Model

Combining the signal models introduced in the previous two subsections a hybrid model consisting of deterministic and stochastic constituents is

presented now. The single polarization multibaseline InSAR returned signal with p sensing elements is expressed by

$$\begin{aligned}\mathbf{y}(l) &= \mathbf{t} + \mathbf{c}(l) + \mathbf{n}(l) \\ &= \sum_{i=1}^{N_{s_t}} \sqrt{\tau_{t_i}} \exp(j\psi_i)\mathbf{a}(\theta_{t_i}) \\ &+ \sum_{j=1}^{N_{s_c}} \sqrt{\tau_{c_j}}\mathbf{x}_j(l) \odot \mathbf{a}(\theta_{c_j}) + \mathbf{n}(l) \end{aligned} \tag{3.16}$$

with the number of looks L and $l = 1, \ldots, L$. The first term, $\mathbf{t}$, is a highly coherent part and can be associated with deterministic targets [28]. The second contribution, $\mathbf{c}(l)$, represents the response of distributed environments incorporating the SAR speckle effect as multiplicative noise [37,39,63]. The total number of backscattering sources N_s is the sum of the number of deterministic and stochastic reflectors, $N_s = N_{s_t} + N_{s_c}$. The characteristics of the additive noise $\mathbf{n}(l)$, and the steering vector $\mathbf{a}(\theta)$ with the unknown parameter θ are explained in subsection 3.1.1. The unknown reflectivity τ, and the complex argument ψ are defined as in subsection 3.1.2. The properties of the multiplicative noise $\mathbf{x}_j(l)$ are described in subsection 3.1.3.

The MB InSAR data vector $\mathbf{y}(l)$ is a circular Gaussian distributed random process. Since the deterministic and stochastic signal components are assumed to be independent, the structure of the non-central data covariance matrix $\mathbf{R} = E\{\mathbf{y}(l)\mathbf{y}^H(l)\}$ for the hybrid model is

$$\mathbf{R} = \mathbf{A}\mathbf{S}\mathbf{A}^H + \sum_{j=1}^{N_{s_c}} \tau_{c_j}\mathbf{C}_j \odot \mathbf{a}(\theta_{c_j})\mathbf{a}^H(\theta_{c_j}) + \sigma_n^2\mathbf{I} \tag{3.17}$$

where the steering matrix $\mathbf{A}$ and the signal covariance matrix $\mathbf{S}$ are defined in subsection 3.1.2 and the speckle covariance matrix $\mathbf{C}_j$ in subsection 3.1.3. This model accounts for multipath reflections processes that arise in urban sceneries.

The hybrid model for MB InSAR data and the sensor array signal model outlined in section 3.1.1 exhibit the following discrepancies: The deterministic part causes the returned signal to have nonzero mean and the stochastic constituent includes the speckle effect as multiplicative noise.

The task is to estimate the following unknown quantities: The number of backscattering sources N_s and the signal parameters such as the reflectivity τ and the height z (or interferometric phase φ). For single polarization multibaseline InSAR received data, the techniques to solve the detection problem are described in section 3.2 and the algorithms to estimate the properties of the signals are presented in sections 3.3 and 3.4.

3.2 Model Order Selection Techniques

Estimating the number of signals is a key issue in sensor array processing. For instance the MUSIC algorithm explained in section 3.3 requires the knowledge of the model order. In this section an approach for solving the detection problem based on the application of information theoretic criteria using the eigenvalues of the covariance matrix is presented.

To solve the detection problem, i.e., to estimate the number of sources, Wax et Kailath [110] have used a model similar to the one described in subsection 3.1.1, where the received signal vector $\mathbf{y}(l)$ is given by

$$\mathbf{y}(l) = \sum_{i=1}^{N_s} s_i(l)\mathbf{a}(\boldsymbol{\theta}_i) + \mathbf{n}(l). \tag{3.18}$$

The N_s sources with $N_s < p$, are assumed to have linearly independent steering vectors $\mathbf{a}(\boldsymbol{\theta}_i)$. The objective is to estimate the number of sources N_s. This can be done by analyzing the structure of the covariance matrix as detailed in appendix A, section A.1.

For a set of L independent observations, $\mathbf{Y} = \{\mathbf{y}(1), \ldots, \mathbf{y}(L)\}$, and a family of models, i.e., a parameterized family of probability densities $f(\mathbf{Y} \,|\, \boldsymbol{\theta}(k))$, the task is to select the best fitting model. The general information theoretic criterion (ITC) can be expressed as

$$\mathrm{ITC}(k) = -\log f(\mathbf{Y} \,|\, \hat{\boldsymbol{\theta}}(k)) + g(\eta(k)) \tag{3.19}$$

with the maximum likelihood estimate $\hat{\boldsymbol{\theta}}$ of the parameter vector $\boldsymbol{\theta}$ and the assumed number of sources k. The first term is the log-likelihood of the maximum likelihood estimator of the model parameters. The bias correction $g(\eta(k))$ accounts for the difference (with respect to the mean Kulback-Liebler distance) between the estimated density $f(\mathbf{Y} \,|\, \hat{\boldsymbol{\theta}}(k))$ and the modeled density $f(\mathbf{Y} \,|\, \boldsymbol{\theta}(k))$. It is a function of the number of free real-valued parameters $\eta(k)$ in the vector $\boldsymbol{\theta}$. Then the number of sources $\hat{N}_s$ can be estimated via

$$\hat{N}_s = \arg\min_k \mathrm{ITC}(k). \tag{3.20}$$

Different choices of the penalty function lead to various approaches such as the Akaike information criterion [1, 2]

$$\mathrm{AIC}(k) = -\log f(\mathbf{Y} \,|\, \hat{\boldsymbol{\theta}}(k)) + \eta(k) \tag{3.21}$$

and the minimum description length [87, 101]

$$\mathrm{MDL}(k) = -\log f(\mathbf{Y} \,|\, \hat{\boldsymbol{\theta}}(k)) + \frac{1}{2}\eta(k)\log L. \tag{3.22}$$

MDL is a special case of an efficient detection criterion (EDC). EDC [3,116] is a family of criteria

$$\mathrm{EDC}(k) = -\log f(\mathbf{Y} \,|\, \hat{\boldsymbol{\theta}}(k)) + \eta(k)C_L \tag{3.23}$$

where the function C_L satisfies the following conditions

$$\lim_{L\to\infty} \frac{C_L}{L} = 0 \tag{3.24}$$

and

$$\lim_{L\to\infty} \frac{C_L}{\log(\log L)} = \infty. \tag{3.25}$$

For the applications in chapter 5 two detection criteria have been utilized [38, 65]: $C_L^1 = \log L$ referred to as EDC_1 and $C_L^2 = \sqrt{L \log L}$ called EDC_2.

Let $k \in \{0, 1, \ldots, p-1\}$ be the assumed number of sources and let $\lambda_1 \geq \cdots \geq \lambda_p$ and $\mathbf{v}_1, \ldots, \mathbf{v}_p$ be the eigenvalues and eigenvectors, respectively, of the covariance matrix $\mathbf{R}$. As explained in appendix A, section A.2, the model is described by the parameter vector

$$\boldsymbol{\theta}(k) = (\lambda_1, \ldots, \lambda_k, \sigma_n^2, \mathbf{v}_1^T, \ldots, \mathbf{v}_k^T)^T. \tag{3.26}$$

Using the eigenvalues $\hat{\lambda}_1 > \cdots > \hat{\lambda}_p$ of the sample covariance matrix $\hat{\mathbf{R}}$ the log-likelihood of the maximum likelihood estimator of the model parameters (see appendix A, section A.2) can be formulated as [110]

$$\log f(\mathbf{Y} \mid \hat{\boldsymbol{\theta}}(k)) = (p-k)L \log \left(\frac{\prod_{i=k+1}^{p} \hat{\lambda}_i^{1/(p-k)}}{\frac{1}{p-k}\sum_{i=k+1}^{p} \hat{\lambda}_i} \right). \tag{3.27}$$

As derived in appendix A, section A.2, the degrees of freedom (DoF) for the single polarization multibaseline interferometric configuration are [110]

$$\eta(k) = k + 1 + k(2p - 1 - k) = k(2p-k) + 1. \tag{3.28}$$

For the single polarization scenario the DoF depend on the number of sensors p that equals the dimension of the observation space.

The final information theoretic criteria are obtained by inserting (3.27) and (3.28) into (3.21), (3.22), and (3.23), respectively. For the Akaike information criterion this yields

$$\text{AIC}(k) = -(p-k)L \log \left(\frac{\prod_{i=k+1}^{p} \hat{\lambda}_i^{1/(p-k)}}{\frac{1}{p-k}\sum_{i=k+1}^{p} \hat{\lambda}_i} \right) + k(2p-k). \tag{3.29}$$

The minimum description length is given by

$$\text{MDL}(k) = -(p-k)L \log \left(\frac{\prod_{i=k+1}^{p} \hat{\lambda}_i^{1/(p-k)}}{\frac{1}{p-k}\sum_{i=k+1}^{p} \hat{\lambda}_i} \right) + \frac{1}{2}k(2p-k)\log L \tag{3.30}$$

and the efficient detection criteria can be written as

$$\text{EDC}(k) = -(p-k)L \log \left(\frac{\prod_{i=k+1}^{p} \hat{\lambda}_i^{1/(p-k)}}{\frac{1}{p-k}\sum_{i=k+1}^{p} \hat{\lambda}_i} \right) + k(2p-k)C_L. \tag{3.31}$$

It has been proved [110] that the MDL estimator is consistent, i.e., the estimator attains the true number of signals with probability one if the number of independent samples converges to infinity, $L \to \infty$. The EDC are consistent [3, 116] as well, whereas the AIC estimator is inconsistent. Asymptotically AIC overestimates the number of signals [110].

A preprocessing technique to stabilize the variations of the small eigenvalues is diagonal loading [38, 65]

$$\tilde{\mathbf{R}} = \hat{\mathbf{R}} + \delta\sigma_n^2\mathbf{I} \tag{3.32}$$

where δ is the loading factor and σ_n^2 the additive noise power.

The data model from which the order selection methods are derived and the properties of the MB InSAR signals as modeled in subsection 3.1.4 differ. This means the eigenvalues-based information theoretic criteria techniques operate under model mismatch. The performance of the various ITC methods for analyzing single polarization multibaseline InSAR data has been investigated by numerical simulations [38, 65] by taking into account the speckle effect as multiplicative noise. EDC methods were found to be most robust to model mismatching.

Estimating the number of signals is typically a part of the joint detection-estimation problem. In general this problem is solved in two steps: First the number of sources is determined, subsequently the signal parameters are retrieved using the estimate of the first step. For example the model order estimate may be fed into the MUSIC algorithm to extract the properties of the signals. An alternative approach that is computationally much more complex is the combined detection-estimation. Such a technique based on the maximum likelihood estimator is presented in section 3.4. This method is particularly beneficial in the threshold regime [110], i.e., in the situation of low signal-to-noise ratio, small sample size, or closely "spaced" signals.

3.3 Spectral Estimation Algorithms

Spectral estimation algorithms to analyze single polarization multibaseline InSAR observations are presented in this section. They allow to determine the parameters of multicomponent MB InSAR signals that are affected by the speckle effect. The parameters are the spatial frequency to retrieve the scatterer height and solve the layover problem and the reflectivity for 3D imaging. The techniques can be classified in nonparametric and model-based methods. Beamforming and Capon are nonparametric approaches to estimate the spatial frequency and reflectivity which make no assumption about the statistical properties of the received signals. If a data model exists parametric or model-based techniques might have better performance even in the case of model mismatch. The superresolution MUSIC algorithm

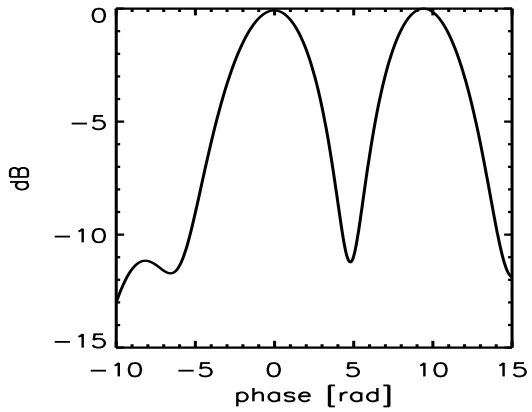

Figure 3.2: Beamforming spectrum including two sources.

extracts the spatial frequency, the linear least-squares method the reflectivity, and the superresolution M-RELAX both the spatial frequency and the reflectivity. The number of sources is assumed to be known.

3.3.1 Conventional Beamforming

Beamforming was the first algorithm that was suggested for solving the layover problem using multibaseline InSAR data [45]. The beamforming method for spatial frequency estimation can be derived as a Finite Impulse Response (FIR) filter [107]. The basic principle for the filter design is that it lets the signals associated with a particular spatial frequency pass undistorted while attenuating the signals at all other frequencies. The derivation of the classical beamforming algorithm is explained in detail in appendix B, section B.1.

Using the relation (3.3) between the phase and the spatial frequency, the spectrum of the beamforming method is obtained as

$$\hat{P}_{BF}(\omega) = \frac{1}{p^2 L} \sum_{l=1}^{L} |\mathbf{a}^H(\omega)\mathbf{y}(l)|^2 = \frac{\mathbf{a}^H(\omega)\hat{\mathbf{R}}\mathbf{a}(\omega)}{p^2}. \tag{3.33}$$

The frequency estimates $\hat{\boldsymbol{\omega}} = [\hat{\omega}_1, \ldots, \hat{\omega}_{N_s}]^T$ correspond to the locations of the N_s maxima of the spectrum. The reflectivity estimate at frequency $\hat{\omega}_i$ is determined by $\hat{\tau}_i = \hat{P}_{BF}(\hat{\omega}_i)$.

In figure 3.2 the beamforming spectrum is displayed for received data including two sources, one at $\varphi_1 = 0$ rad and the second at $\varphi = 3\pi$ rad.

It can be shown [107] that the beamforming method is not consistent for the frequency estimation problem with multiple sources, $N_s > 1$. In the beamforming filter design the signals are assumed to be uncorrelated, i.e.,

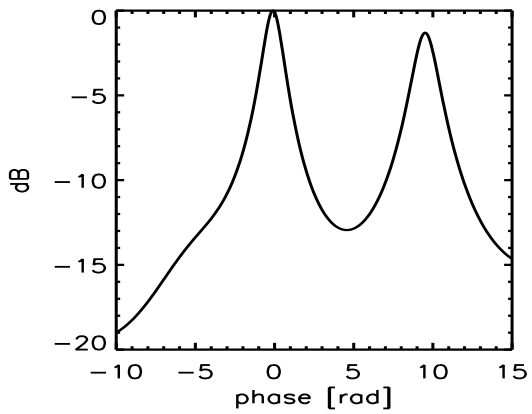

Figure 3.3: Capon spectrum with two sources.

$\mathbf{R} = \mathbf{I}$. As the data is generally correlated, $\mathbf{R} \neq \mathbf{I}$, the Capon method is developed next.

3.3.2 Capon Method

In the derivation of the beamforming technique it was assumed that the received signal is spatially white with unit variance, i.e., $\mathbf{R} = \mathbf{I}$. For designing the Capon method the identity matrix $\mathbf{I}$ is replaced by the covariance matrix $\mathbf{R}$ as outlined in appendix B, section B.2.

The Capon spectrum is given by [11]

$$\hat{P}_C(\omega) = \frac{1}{\mathbf{a}^H(\omega)\hat{\mathbf{R}}^{-1}\mathbf{a}(\omega)}. \tag{3.34}$$

The inverse matrix $\hat{\mathbf{R}}^{-1}$ exists under the condition that the noise term has a positive definite covariance matrix and $L \geq p$. The frequency estimates $\hat{\boldsymbol{\omega}} = [\hat{\omega}_1, \ldots, \hat{\omega}_{N_s}]^T$ are associated with the frequencies of the N_s highest peaks of the spectrum $\hat{P}_C$. The reflectivity at frequency $\hat{\omega}_i$ is estimated by $\hat{\tau}_i = \hat{P}_C(\hat{\omega}_i)$.

It has been shown empirically [37, 107] that the Capon method exhibits better performance compared to beamforming with regard to spatial resolution and sidelobe suppression.

Figure 3.3 illustrates the Capon spectrum employing the same simulation parameters as in the computation of the beamforming spectrum (figure 3.2). In comparison to beamforming the spectral peaks are narrower and the leakage is noticeably reduced.

These nonparametric techniques do not require any assumptions about the statistical characteristics of the received signals. In cases where an ap-

propriate data model exists model-based or parametric approaches yield generally superior estimation accuracy [37, 107].

3.3.3 MUSIC Algorithm

The MUltiple SIgnal Classification (or MUltiple SIgnal Characterization) method [7,100] is a parametric spatial frequency estimator for signals buried in white noise. Since MUSIC decomposes the covariance matrix in its eigenvalues and eigenvectors and analyzes their properties, it is a subspace-based technique. Compared to nonparametric approaches such as beamforming and Capon, the MUSIC method exhibits a better performance if the data satisfy the postulated covariance matrix model. The derivation of the conventional MUSIC technique is elaborated in appendix B, section B.4.

The spectral MUSIC algorithm can be formulated as follows: First the sample covariance matrix $\hat{\mathbf{R}}$ has to be calculated like in equation (3.7), subsection 3.1.1. The eigendecomposition of $\hat{\mathbf{R}}$ provides the eigenvalues $\hat{\lambda}_1 \geq \cdots \geq \hat{\lambda}_p$ and the respective eigenvectors $(\hat{\mathbf{f}}_1, \ldots, \hat{\mathbf{f}}_{N_s})$ and $(\hat{\mathbf{g}}_1, \ldots, \hat{\mathbf{g}}_{p-N_s})$. The matrix $\hat{\mathbf{F}} = [\hat{\mathbf{f}}_1, \ldots, \hat{\mathbf{f}}_{N_s}] \in \mathbf{Mat}_{p,N_s}(\mathbb{C})$ corresponds to the signal subspace and $\hat{\mathbf{G}} = [\hat{\mathbf{g}}_1, \ldots, \hat{\mathbf{g}}_{p-N_s}] \in \mathbf{Mat}_{p,p-N_s}(\mathbb{C})$ is associated with the noise subspace. The spatial frequency estimates are determined as the N_s maxima of the pseudo-spectrum

$$\hat{P}_{MU}(\omega) = \frac{1}{\mathbf{a}^H(\omega)\hat{\mathbf{G}}\hat{\mathbf{G}}^H\mathbf{a}(\omega)}. \tag{3.35}$$

The subspace spanned by the noise eigenvectors must be at least of dimension one

$$p \geq N_s + 1. \tag{3.36}$$

It has been demonstrated by numerical analysis that the MUSIC method produces generally better estimation results than beamforming and Capon, even if multiplicative noise is present [37, 39].

It can be observed in figure 3.4 that the MUSIC pseudo-spectrum has finer resolution and lower sidelobes than beamforming (figure 3.2) and Capon (figure 3.3).

It has been shown by numerical simulation and proven theoretically [104, 106] that the MUSIC algorithm possesses good performance for uncorrelated signals, whereas the estimation precision deteriorates significantly when the signals are highly correlated. As the maximum likelihood estimators are expected to have superior estimation accuracy, the M-RELAX method and an MLE based on the stochastic signals model are described in subsection 3.3.5 and section 3.4, respectively.

3.3.4 Least-Squares Method

The least-squares method for amplitude estimation is based on a model of multiple complex sinusoids of known frequency embedded in additive

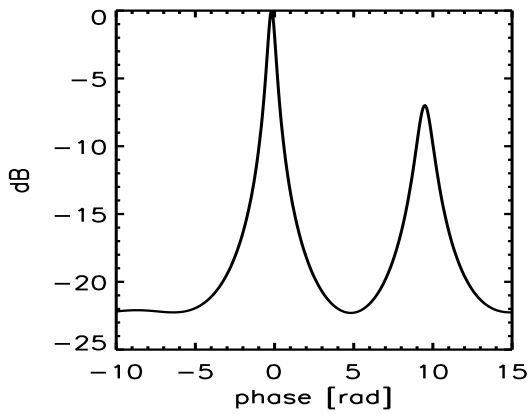

Figure 3.4: MUSIC pseudo-spectrum comprising two sources.

noise [39,63,107]. The N_s complex amplitudes are simultaneously estimated to reduce interference from close frequencies. The spatial frequencies have to be determined first by nonparametric methods such as beamforming and Capon or by model-based techniques like MUSIC [63].

The unknown reflectivities $\{\tau_i\}_{i=1}^{N_s}$ are retrieved by minimizing the linear least-squares error function [63, 107]

$$Q_L(\boldsymbol{\alpha}(1), \boldsymbol{\alpha}(2), \ldots, \boldsymbol{\alpha}(L)) = \frac{1}{L} \sum_{l=1}^{L} \left\| \mathbf{y}(l) - \sum_{i=1}^{N_s} \alpha_i(l) \mathbf{a}(\omega_i) \right\|_2^2 \tag{3.37}$$

where $\boldsymbol{\alpha}(l) = [\alpha_1(l), \ldots, \alpha_{N_s}(l)]^T \in \mathbb{C}^{N_s}$ are the amplitudes of the cisoids of the lth look, $l = 1, \ldots, L$, and $\|\cdot\|_2$ signifies the Euclidian norm. Optimizing this equation with respect to $\boldsymbol{\alpha}(l)$ results in the least-squares solution [34]

$$\hat{\boldsymbol{\alpha}}(l) = \left(\mathbf{A}^H \mathbf{A}\right)^{-1} \mathbf{A}^H \mathbf{y}(l) \tag{3.38}$$

with the steering matrix $\mathbf{A} = [\mathbf{a}(\omega_1), \ldots, \mathbf{a}(\omega_{N_s})] \in \mathbf{Mat}_{p,N_s}(\mathbb{C})$. As the frequencies $\omega_i, i = 1, \ldots, N_s$, are unknown, the steering matrix $\mathbf{A}$ has to be replaced by

$$\hat{\mathbf{A}} = [\mathbf{a}(\hat{\omega}_1), \ldots, \mathbf{a}(\hat{\omega}_{N_s})] \in \mathbf{Mat}_{p,N_s}(\mathbb{C}) \tag{3.39}$$

employing the frequency estimates $\{\hat{\omega}_i\}_{i=1}^{N_s}$. The complex amplitudes are determined as [39, 63]

$$\hat{\boldsymbol{\alpha}}(l) = \left(\hat{\mathbf{A}}^H \hat{\mathbf{A}}\right)^{-1} \hat{\mathbf{A}}^H \mathbf{y}(l). \tag{3.40}$$

Finally, the reflectivities are extracted by

$$\hat{\tau}_i = \frac{1}{L} \sum_{l=1}^{L} |\hat{\alpha}_i(l)|^2, \qquad i = 1, \ldots, N_s. \tag{3.41}$$

It has been proved [63] that this estimator is unbiased in the absence of additive noise and asymptotically (with respect to $p \to \infty$) unbiased in the presence of additive noise if the frequencies are known and the multiplicative noise terms are fully correlated.

The LS algorithm can be used to improve the reflectivity estimates of the nonparametric estimation methods like beamforming and Capon and to retrieve the reflectivities after determining the spatial frequencies by means of the MUSIC technique.

3.3.5 M-RELAX

The RELAX algorithm [58] is a superresolution technique to determine iteratively the parameters of multicomponent complex exponential signals corrupted by autoregressive noise. The frequencies and complex amplitudes are simultaneously estimated by minimizing a nonlinear least-squares (NLLS) criterion. For additive white Gaussian noise, the ML estimator coincides with the NLLS joint frequency and amplitude estimator [63, 107]. The nonlinear least-squares function involves a multidimensional nonconvex optimization problem. The RELAX method searches for the global minimum of the NLLS criterion by solving a sequence of one-dimensional problems.

In the single look case ($L = 1$), the RELAX algorithm [58] minimizes the nonlinear least-squares error function

$$Q_1(\boldsymbol{\alpha}, \boldsymbol{\omega}) = \left\| \mathbf{y} - \sum_{i=1}^{N_s} \alpha_i \mathbf{a}(\omega_i) \right\|_2^2 \tag{3.42}$$

where the frequencies $\boldsymbol{\omega} = [\omega_1, \ldots, \omega_{N_s}]^T$ and complex amplitudes $\boldsymbol{\alpha} = [\alpha_1, \ldots, \alpha_{N_s}]^T$ are estimated from the data vector $\mathbf{y}$.

The basic idea of the RELAX algorithm is as follows: In the first step, it determines the parameters of the dominant component. In the second step, a corrected data vector is calculated by subtracting the first component from the received data employing the preliminarily estimated parameters. Subsequently, the frequency and complex amplitude of the second component are extracted using this new data vector. The parameters of the first component are redetermined by constructing a corrected data vector with the information about the second component's parameters. The procedure of the second step is iterated until a convergence criterion is fulfilled. This scheme is repeated until the assumed number of sources N_s is reached resulting in frequency $\{\hat{\omega}_i\}_{i=1}^{N_s}$ and complex amplitude $\{\hat{\alpha}_i\}_{i=1}^{N_s}$ estimates. They are asymptotically ($p \gg 1$) Gaussian distributed, unbiased, and statistically efficient [58], i.e., the estimates achieve asymptotically the Cramér-Rao bound.

To apply this method for retrieving the signals' parameters from MB InSAR measurements, it was generalized to the multilook scenario [37, 63]

by defining the multilook nonlinear least-squares cost function

$$Q_L(\boldsymbol{\alpha}(1), \boldsymbol{\alpha}(2), \ldots, \boldsymbol{\alpha}(L), \boldsymbol{\omega}) = \frac{1}{L} \sum_{l=1}^{L} \left\| \mathbf{y}(l) - \sum_{i=1}^{N_s} \alpha_i(l) \mathbf{a}(\omega_i) \right\|_2^2 \tag{3.43}$$

where the data $\mathbf{y}(l)$ and the amplitudes $\boldsymbol{\alpha}(l) = [\alpha_1(l), \ldots, \alpha_{N_s}(l)]^T$ depend on the look number l. It can be observed that the formula on the right side is the same as for the least-squares approach (3.37) in subsection 3.3.4, where the error function is independent of the spatial frequencies.

To formulate the M-RELAX algorithm in a rigorous way, the following definitions are introduced: The corrected data vector is

$$\mathbf{y}_m(l) = \mathbf{y}(l) - \sum_{i=1, i \neq m}^{N_s} \hat{\alpha}_i(l) \mathbf{a}(\hat{\omega}_i), \qquad l = 1, \ldots, L \tag{3.44}$$

where the parameters $\{\hat{\omega}_i, \hat{\alpha}_i(l)\}_{i=1, i \neq m}^{N_s}$ have been already determined in the previous steps. After replacing $\mathbf{y}(l)$ with $\mathbf{y}_m(l)$, the minimization of the cost function (3.43) with respect to ω_m leads to the frequency estimate

$$\hat{\omega}_m = \arg \max_{\omega} \{\mathbf{a}^H(\omega) \hat{\mathbf{R}}_m \mathbf{a}(\omega)\} \tag{3.45}$$

where the the sample covariance matrix $\hat{\mathbf{R}}_m$ of $\{\mathbf{y}_m(l)\}_{l=1}^{L}$ is utilized. By optimizing (3.43) with respect to $\alpha_m(l)$, the amplitude estimate is obtained as

$$\hat{\alpha}_m(l) = \frac{\mathbf{a}^H(\hat{\omega}_m) \mathbf{y}_m(l)}{p}. \tag{3.46}$$

It can be noted that equation (3.45) for the frequency estimate corresponds to the beamforming spectrum (3.33) of the data $\{\mathbf{y}_m(l)\}_{l=1}^{L}$ apart from normalization.

The algorithmic scheme of M-RELAX [37,63] is summarized in appendix C.

M-RELAX estimates the frequencies $\{\hat{\omega}_i\}_{i=1}^{N_s}$ and complex amplitudes $\{\hat{\alpha}_i(l)\}_{i=1}^{N_s}, l = 1, \ldots, L$. Finally, the reflectivity can be extracted as

$$\hat{\tau}_i = \frac{1}{L} \sum_{l=1}^{L} |\hat{\alpha}_i(l)|^2, \qquad i = 1, \ldots, N_s. \tag{3.47}$$

The RELAX method is robust to mismodeling errors [58] and for MB InSAR observations M-RELAX can provide higher estimation precision than MUSIC [39, 63], especially in the threshold regime, i.e., when the signal-to-noise ratio is low and the number of looks is small.

3.4 Maximum Likelihood Joint Detection and Estimation

A maximum likelihood estimator based on the stochastic signals model for solving the combined detection-estimation problem is presented in this section. Unlike MUSIC, it remains optimal even for fully correlated signals. After describing the data model and stating the problem, the simultaneous detection-estimation method is derived.

3.4.1 Data Model and Problem Formulation

Like in subsection 3.1.1, the signal $\mathbf{y}(l)$ received by the p sensors can be expressed as [113]

$$\mathbf{y}(l) = \sum_{i=1}^{N_s} s_i(l)\mathbf{a}(\omega_i) + \mathbf{n}(l). \tag{3.48}$$

In contrast to the MUSIC algorithm explained in subsection 3.3.3, there is no assumption made about the structure of the signal covariance matrix. $\mathbf{S}$ might be even singular, i.e., the signals can be fully correlated. Thus, this signal model includes multipath propagation effects [113]. The steering vectors $\mathbf{a}(\omega_i)$ are assumed to be linearly independent and $N_s < p$ [111].

The matrix notation of the signal model is given by

$$\mathbf{y}(l) = \mathbf{A}(\boldsymbol{\omega})\mathbf{s}(l) + \mathbf{n}(l) \tag{3.49}$$

with the steering vector matrix $\mathbf{A}(\boldsymbol{\omega}) \in \mathbf{Mat}_{p,N_s}(\mathbb{C})$ and the vector of unknown spatial frequencies $\boldsymbol{\omega} = [\omega_1, \ldots, \omega_{N_s}]$.

The objective is to determine the number of sources N_s and the spatial frequencies $\omega_1, \ldots, \omega_{N_s}$. The former problem is called the detection problem and the latter the estimation problem.

3.4.2 Combined Detection-Estimation Method

Let k be the presumed number of sources, $k \in \{0, \ldots, p-1\}$. In this situation the data model is

$$\mathbf{y}(l) = \mathbf{A}(\boldsymbol{\omega}(k))\mathbf{s}(l) + \mathbf{n}(l) \tag{3.50}$$

with the steering vector matrix $\mathbf{A}(\boldsymbol{\omega}(k)) \in \mathbf{Mat}_{p,k}(\mathbb{C})$

$$\mathbf{A}(\boldsymbol{\omega}(k)) = [\mathbf{a}(\omega_1), \ldots, \mathbf{a}(\omega_k)]. \tag{3.51}$$

As shown in the derivation of the MUSIC method in subsection 3.3.3, $\mathbf{y}(l)$ can be split up into two components, scilicet $\mathbf{y_s}(l) \in \mathbb{C}^k$ and $\mathbf{y_n}(l) \in \mathbb{C}^{p-k}$ belonging to the signal and noise subspace, respectively. It exists a unitary coordinate transformation $\mathbf{G}(\boldsymbol{\omega}(k)) \in \mathbf{Mat}_p(\mathbb{C})$ with

$$\mathbf{y}(l) = \mathbf{G}(\boldsymbol{\omega}(k)) \begin{bmatrix} \mathbf{y_s}(l) \\ \mathbf{y_n}(l) \end{bmatrix}. \tag{3.52}$$

The orthogonal projection on the signal subspace $\mathbf{P}_{\mathbf{A}(\boldsymbol{\omega}(k))} \in \mathbf{Mat}_p(\mathbb{C})$ is defined by [113]

$$\mathbf{P}_{\mathbf{A}(\boldsymbol{\omega}(k))} = \mathbf{A}(\boldsymbol{\omega}(k)) \left[\mathbf{A}^H(\boldsymbol{\omega}(k))\mathbf{A}(\boldsymbol{\omega}(k))\right]^{-1} \mathbf{A}^H(\boldsymbol{\omega}(k)) \tag{3.53}$$

and the orthogonal projection on the noise subspace $\mathbf{P}^{\perp}_{\mathbf{A}(\boldsymbol{\omega}(k))} \in \mathbf{Mat}_p(\mathbb{C})$ by

$$\mathbf{P}^{\perp}_{\mathbf{A}(\boldsymbol{\omega}(k))} = \mathbf{I} - \mathbf{P}_{\mathbf{A}(\boldsymbol{\omega}(k))}. \tag{3.54}$$

Then

$$\mathbf{P}_{\mathbf{A}(\boldsymbol{\omega}(k))}\mathbf{y}(l) = \mathbf{G}(\boldsymbol{\omega}(k)) \begin{bmatrix} \mathbf{y_s}(l) \\ \mathbf{0} \end{bmatrix} \tag{3.55}$$

and

$$\mathbf{P}^{\perp}_{\mathbf{A}(\boldsymbol{\omega}(k))}\mathbf{y}(l) = \mathbf{G}(\boldsymbol{\omega}(k)) \begin{bmatrix} \mathbf{0} \\ \mathbf{y_n}(l) \end{bmatrix}. \tag{3.56}$$

Each $\boldsymbol{\omega}(k)$ results in a different partitioning of the space $\mathbb{C}^p$ into signal and noise subspaces and thus a different model for the data. The model that best fits the sampled data is determined by the minimum description length principle [87, 88]: The shortest code length for encoding the data set $\mathbf{Y} = \{\mathbf{y}(1), \ldots, \mathbf{y}(L)\}$ is asymptotically given by (cf. section 3.2)

$$\mathscr{L}\{\mathbf{y}(l)\} = -\log f(\mathbf{Y} \,|\, \hat{\boldsymbol{\theta}}) + g(\eta) \tag{3.57}$$

where $f(\mathbf{Y} \,|\, \hat{\boldsymbol{\theta}})$ is the probabilistic model with the maximum likelihood estimate $\hat{\boldsymbol{\theta}}$ of the unknown parameter vector $\boldsymbol{\theta}$

$$\hat{\boldsymbol{\theta}} = \arg\max_{\boldsymbol{\theta}} \log f(\mathbf{Y} \,|\, \boldsymbol{\theta}). \tag{3.58}$$

The penalty function $g(\eta)$ balances for the difference between the estimated density $f(\mathbf{Y} \,|\, \hat{\boldsymbol{\theta}})$ and the modeled density $f(\mathbf{Y} \,|\, \boldsymbol{\theta})$, and depends on the number of free real-valued parameters η in the vector $\boldsymbol{\theta}$.

The computation of the code length required to encode the data $\{\mathbf{y}(l)\}_{l=1}^{L}$ is performed in three steps: Firstly, the noise subspace component $\{\mathbf{y_n}(l)\}_{l=1}^{L}$ is encoded assuming that $\boldsymbol{\omega}(k)$ is given (see appendix D). Omitting constant quantities that are independent of k, the code length required to encode the noise subspace components is obtained as [113]

$$\mathscr{L}\{\mathbf{y_n}(l) \,|\, \boldsymbol{\omega}(k)\} = L \log\det[\hat{\sigma}^2(\boldsymbol{\omega}(k))\mathbf{I}] + L(p-k) + g(1). \tag{3.59}$$

Secondly, the signal subspace components $\{\mathbf{y_s}(l)\}_{l=1}^{L}$ are encoded as explained in appendix D. The number of free real-valued parameters in the signal data covariance matrix $\mathbf{R_s}(\boldsymbol{\omega}(k)) \in \mathbf{Mat}_k(\mathbb{C})$ is

$$k + 2\sum_{i=1}^{k-1} i = k^2. \tag{3.60}$$

Disregarding constant terms the code length of the signal subspace components is obtained as [113]

$$\mathscr{L}\{\mathbf{y_s}(l)\,|\,\boldsymbol{\omega}(k)\} = L\log\det[\hat{\mathbf{R}}_\mathbf{s}(\boldsymbol{\omega}(k))] + Lk + g(k^2) \tag{3.61}$$

where $\hat{\mathbf{R}}_\mathbf{s}(\boldsymbol{\omega}(k)) \in \mathbf{Mat}_k(\mathbb{C})$ is the maximum likelihood estimate of $\mathbf{R}_\mathbf{s}(\boldsymbol{\omega}(k))$. The sum of (3.59) and (3.61) yields the total code length necessary to encode the noise and signal subspace components

$$\mathscr{L}\{\mathbf{y_n}(l), \mathbf{y_s}(l)\,|\,\boldsymbol{\omega}(k)\} = L\log\left[\det[\hat{\mathbf{R}}_\mathbf{s}(\boldsymbol{\omega}(k))]\det[\hat{\sigma}^2(\boldsymbol{\omega}(k))\mathbf{I}]\right] + g(k^2). \tag{3.62}$$

Finally, for encoding the unknown parameter vector $\boldsymbol{\omega}(k) \in \mathbb{R}^k$, it has to be estimated according to equation (3.62) by

$$\hat{\boldsymbol{\omega}}(k) = \arg\min_{\boldsymbol{\omega}(k)} \det[\hat{\mathbf{R}}_\mathbf{s}(\boldsymbol{\omega}(k))]\det[\hat{\sigma}^2(\boldsymbol{\omega}(k))\mathbf{I}]. \tag{3.63}$$

It can be shown that this estimator is consistent [113].

Two expressions of the relation (3.63) are derived in appendix D. For the sake of conciseness the abbreviation $\mathbf{A} = \mathbf{A}(\boldsymbol{\omega}(k))$ is used in the following. The first formulation of the estimate (3.63) is given by [113]

$$\hat{\boldsymbol{\omega}}(k) = \arg\min_{\boldsymbol{\omega}(k)} \det[\mathbf{P_A}\hat{\mathbf{R}}\mathbf{P_A} + \frac{1}{p-k}\mathrm{tr}[\mathbf{P}_\mathbf{A}^\perp\hat{\mathbf{R}}]\mathbf{P}_\mathbf{A}^\perp] \tag{3.64}$$

where $\hat{\mathbf{R}} \in \mathbf{Mat}_p(\mathbb{C})$ is the sample covariance matrix of $\mathbf{y}(l)$. The second form of the estimate (3.63) utilizes the eigendecompositions of the matrices $\mathbf{P_A}\hat{\mathbf{R}}\mathbf{P_A}$ and $\mathbf{P}_\mathbf{A}^\perp\hat{\mathbf{R}}\mathbf{P}_\mathbf{A}^\perp$:

Let $l_1^\mathbf{s}(\boldsymbol{\omega}(k)) \geq \cdots \geq l_k^\mathbf{s}(\boldsymbol{\omega}(k))$ be the nonzero eigenvalues of the matrix $\mathbf{P_A}\hat{\mathbf{R}}\mathbf{P_A}$ and $l_1^\mathbf{n}(\boldsymbol{\omega}(k)) \geq \cdots \geq l_{p-k}^\mathbf{n}(\boldsymbol{\omega}(k))$ be the nonzero eigenvalues of the matrix $\mathbf{P}_\mathbf{A}^\perp\hat{\mathbf{R}}\mathbf{P}_\mathbf{A}^\perp$. As detailed in appendix D, the second expression of the estimator is [113]

$$\hat{\boldsymbol{\omega}}(k) = \arg\min_{\boldsymbol{\omega}(k)} \left(\prod_{i=1}^{k} l_i^\mathbf{s}(\boldsymbol{\omega}(k))\right)\left(\frac{1}{p-k}\sum_{i=1}^{p-k} l_i^\mathbf{n}(\boldsymbol{\omega}(k))\right)^{p-k}. \tag{3.65}$$

The calculation of the ML estimate (3.63) is a nonlinear and nonconvex optimization problem of dimension k. It can be solved via (3.65) by alternating maximization [117].

The code length in $\boldsymbol{\omega}(k)$ is k. Therefore, the total number of free real-valued parameters results in

$$\eta(k) = k(k+1). \tag{3.66}$$

The information theoretic criterion (ITC) estimator is given by

$$\mathrm{ITC}_{ML}(k) = L\log\left[\left(\prod_{i=1}^{k} l_i^\mathbf{s}(\hat{\boldsymbol{\omega}}(k))\right)\left(\frac{1}{p-k}\sum_{i=1}^{p-k} l_i^\mathbf{n}(\hat{\boldsymbol{\omega}}(k))\right)^{p-k}\right] + g(k(k+1)). \tag{3.67}$$

The ITC estimate of the number of sources is the minimum value

$$\hat{N}_s = \arg \min_{k \in \{0,\ldots,p-1\}} \mathrm{ITC}_{ML}(k). \tag{3.68}$$

Choosing the Akaike penalty function $g(\eta(k)) = \eta(k)$ provides the AIC estimator [1, 2]

$$\mathrm{AIC}_{ML}(k) = L \log \left[\left(\prod_{i=1}^{k} l_i^{\mathbf{s}}(\hat{\boldsymbol{\omega}}(k)) \right) \left(\frac{1}{p-k} \sum_{i=1}^{p-k} l_i^{\mathbf{n}}(\hat{\boldsymbol{\omega}}(k)) \right)^{p-k} \right] + k(k+1) \tag{3.69}$$

that is inconsistent and overestimates asymptotically the number of signals. With the bias correction term $g(\eta(k)) = \frac{1}{2}\eta(k) \log L$ the minimum description length [87, 101]

$$\mathrm{MDL}_{ML}(k) = L \log \left[\left(\prod_{i=1}^{k} l_i^{\mathbf{s}}(\hat{\boldsymbol{\omega}}(k)) \right) \left(\frac{1}{p-k} \sum_{i=1}^{p-k} l_i^{\mathbf{n}}(\hat{\boldsymbol{\omega}}(k)) \right)^{p-k} \right] + \frac{1}{2} k(k+1) \log L \tag{3.70}$$

is stronlgy consistent [112, 116], i.e, $\hat{k}$ converges to N_s for $L \to \infty$. Furthermore, if $g(\eta(k)) = \eta(k) C_L$ is selected with

$$\lim_{L \to \infty} \frac{C_L}{L} = 0 \tag{3.71}$$

and

$$\lim_{L \to \infty} \frac{C_L}{\log(\log L)} = \infty, \tag{3.72}$$

then the efficient detection criterion [3, 116]

$$\mathrm{EDC}_{ML}(k) = L \log \left[\left(\prod_{i=1}^{k} l_i^{\mathbf{s}}(\hat{\boldsymbol{\omega}}(k)) \right) \left(\frac{1}{p-k} \sum_{i=1}^{p-k} l_i^{\mathbf{n}}(\hat{\boldsymbol{\omega}}(k)) \right)^{p-k} \right] + k(k+1) C_L \tag{3.73}$$

is stronly consistent as well [3, 116].

Since the steering matrix $\mathbf{A}(\boldsymbol{\omega}(k)) \in \mathbf{Mat}_{p,k}(\mathbb{C})$ has by definition rank k, $\mathrm{rank}(\mathbf{A}) = k$, the rank of the orthogonal projection on the signal subspace $\mathbf{P}_{\mathbf{A}} \in \mathbf{Mat}_p(\mathbb{C})$ is k, $\mathrm{rank}(\mathbf{P}_{\mathbf{A}}) = k$, and the rank of the orthogonal projection on the noise subspace $\mathbf{P}_{\mathbf{A}}^{\perp} \in \mathbf{Mat}_p(\mathbb{C})$ is $p-k$, $\mathrm{rank}(\mathbf{P}_{\mathbf{A}}^{\perp}) = p-k$. This implies that their minimum eigenvalues $\lambda_{\min}(\mathbf{P}_{\mathbf{A}}) = 0$ and $\lambda_{\min}(\mathbf{P}_{\mathbf{A}}^{\perp}) = 0$, and the Hermitian projection matrices are ill-conditioned [41, 102]:

$$\kappa_2(\mathbf{P}_{\mathbf{A}}) = \frac{\lambda_{\max}(\mathbf{P}_{\mathbf{A}})}{\lambda_{\min}(\mathbf{P}_{\mathbf{A}})} = \infty \tag{3.74}$$

and

$$\kappa_2(\mathbf{P}_{\mathbf{A}}^{\perp}) = \frac{\lambda_{\max}(\mathbf{P}_{\mathbf{A}}^{\perp})}{\lambda_{\min}(\mathbf{P}_{\mathbf{A}}^{\perp})} = \infty. \tag{3.75}$$

As the covariance matrix $\hat{\mathbf{R}}$ is assumed to be nonsingular, it follows that the Hermitian matrices $\mathbf{P_A}\hat{\mathbf{R}}\mathbf{P_A} \in \mathbf{Mat}_p(\mathbb{C})$ and $\mathbf{P_A^\perp}\hat{\mathbf{R}}\mathbf{P_A^\perp} \in \mathbf{Mat}_p(\mathbb{C})$ have $\text{rank}(\mathbf{P_A}\hat{\mathbf{R}}\mathbf{P_A}) = k$, and $\text{rank}(\mathbf{P_A^\perp}\hat{\mathbf{R}}\mathbf{P_A^\perp}) = p - k$, respectively. Thus

$$\kappa_2(\mathbf{P_A}\hat{\mathbf{R}}\mathbf{P_A}) = \frac{\lambda_{\max}(\mathbf{P_A}\hat{\mathbf{R}}\mathbf{P_A})}{\lambda_{\min}(\mathbf{P_A}\hat{\mathbf{R}}\mathbf{P_A})} = \infty \tag{3.76}$$

and

$$\kappa_2(\mathbf{P_A^\perp}\hat{\mathbf{R}}\mathbf{P_A^\perp}) = \frac{\lambda_{\max}(\mathbf{P_A^\perp}\hat{\mathbf{R}}\mathbf{P_A^\perp})}{\lambda_{\min}(\mathbf{P_A^\perp}\hat{\mathbf{R}}\mathbf{P_A^\perp})} = \infty. \tag{3.77}$$

Hence, these matrices are ill-conditioned by construction and their eigenvalues have to be computed carefully in the estimator (3.65).

There exist some striking differences between the model order selection techniques based on the eigenvalues of the covariance matrix (CM MOS) described in section 3.2 and the MOS approach using the MLE (MLE MOS) explained in this section: The degrees of freedom of the former (3.28) are a function of the number of sensors, i.e., the dimension of the observation space, whereas the DoF of the latter (3.66) depend on the number of parameters that have to be estimated, i.e., the dimension of the space of unknown parameters. Moreover, the CM MOS method does not consider the available information about the steering vectors that provides a measure for the achievable resolution in height direction. The ML estimator takes this knowledge into account leading to a sensitivity to the vertical distribution of the reflectors.

For instance, for a sample inside the building layover that is closest to the antenna positions, there are two main contributions: one corresponds to the building roof, the other one to the ground topography. In a single polarization dual-baseline interferometric SAR configuration, at most two components can be separated within one azimuth-range resolution cell, even if there might be several elements on the roof that generate backscattering such as a balcony, windows, and eaves gutter. Thus, the MLE MOS algorithm is not only - like the covariance matrix based MOS technique - sensitive to azimuth-range resolution[1], but also - in contrast to CM MOS - sensitive to the achievable resolution in vertical direction.

The fundamental distinction between the MUSIC algorithm (see subsection 3.3.3) and the ML estimator is the fact that the MLE analyzes the structure of both the noise and the signal subspaces, while the MUSIC pseudo-spectrum computation relies solely on the noise subspace matrix.

[1]Spatial filtering has a significant impact on MOS results as will be shown in chapter 5

3.5 Conclusions

The spectral analysis techniques to process single polarization multibaseline interferometric SAR images have been described in this chapter. In addition to the well-known stochastic model for distributed sources that includes the speckle effect as multiplicative noise, a model for deterministic multibaseline InSAR data has been introduced which characterizes the response from point-like targets. The hybrid model combines both approaches. Model order selection methods that rely on information theoretic criteria using the eigenvalues of the covariance matrix to estimate the number of sources have been explained. Subsequently, spectral estimation techniques have been detailed. They determine the spatial frequency to retrieve the scatterer height and solve the layover problem and the reflectivity for 3D imaging from single polarization MB InSAR observations. Beamforming and Capon are nonparametric methods to extract the spatial frequency and reflectivity without making any assumption about the statistical features of the returned signals. Whereas the model-based superresolution MUSIC algorithm and the linear least-squares technique estimate the spatial frequency and the reflectivity, respectively, the superresolution M-RELAX determines both the spatial frequency and the reflectivity. Finally, a maximum likelihood estimator based on the stochastic signals model for solving simultaneously the detection-estimation problem has been introduced. Unlike MUSIC, it remains optimal even for fully correlated signals.

Chapter 4

Polarimetric Multibaseline InSAR Spectral Analysis Techniques

Spectral analysis techniques are adapted to the polarimetric multibaseline interferometric SAR scenario in this chapter according to the following idea: In passive sensor systems, the antennas only receive the signals in diverse polarizations resulting in two polarization channels. In SAR applications, sensors are active and both transmit the electromagnetic waves and receive the echo in polarimetric mode leading to up to four polarization states. This marks the transition from wave polarimetry with two polarization channels to scattering polarimetry including four polarizations.

First, the signal models are extended to include polarization diversity yielding the multibaseline polarimetric interferometric steering vector. Model order selection techniques to estimate the number of sources from MB POL-InSAR observations are elaborated in the second section. Subsequently, the spectral estimation algorithms are adapted to process polarimetric MB InSAR data. They permit to retrieve the spatial frequencies, the associated optimal scattering vectors, and the polarimetric reflectivities. Finally, the polarimetric maximum likelihood estimator is developed for solving simultaneously the detection-estimation problem.

4.1 Polarimetric MB InSAR Signal Models

The signal models for single polarization multibaseline InSAR observations described in section 3.1 are generalized to take polarization diversity into account. This leads to the notion of the multibaseline polarimetric interferometric steering vector. First, the deterministic and stochastic signal models are extended to the MB POL-InSAR scenario. Finally, they are fused into the polarimetric hybrid model.

Polarization state	N_{pol}
single polarization	1
dual-polarized	2
fully polarimetric	3
quad-polarized	4

Table 4.1: The polarization number N_{pol}.

4.1.1 Deterministic MB POL-InSAR Signal Model

For point-like reflectors the polarimetric multibaseline InSAR received signal with p sensors can be modeled as

$$\begin{aligned} \mathbf{y}(l) &= \mathbf{t} + \mathbf{n}(l) \\ &= \sum_{i=1}^{N_{s_t}} \sqrt{\tau_{t_i}} \exp(j\psi_i)\mathbf{b}(\boldsymbol{\theta}_{t_i}) + \mathbf{n}(l) \end{aligned} \tag{4.1}$$

with the number of independent realizations L and $l = 1, \ldots, L$. The polarimetric observation vector $\mathbf{y}(l)$ has the dimension $\tilde{p}$, where $\tilde{p}$ is the product of the number of antennas p and the polarization number N_{pol}, $\tilde{p} = pN_{pol}$. The coefficient N_{pol} attains values ranging from $N_{pol} = 1$ for conventional single polarization data to $N_{pol} = 4$ for quad-polarized measurements. For dual-polarized configurations the polarimetric number adopts $N_{pol} = 2$ and $N_{pol} = 3$ for fully polarimetric set-ups with equal cross-polarization channels. The values of N_{pol} are summarized in table 4.1.

The main modification compared to the single polarization MB InSAR signal model (3.8) is the structure of the multibaseline polarimetric interferometric (MBPI) steering vector $\mathbf{b}(\boldsymbol{\theta}_t), \mathbf{b}(\boldsymbol{\theta}_t) \in \mathbb{C}^{\tilde{p}}$. It depends on the vector of unknown parameters $\boldsymbol{\theta}_t$, that are modeled as deterministic quantities. In the following, the characteristics of the MBPI steering vector are explained by using the notation of the interferometric phase φ for a uniform linear array. The description for the case of a general acquisition geometry employing the height parameter z is evident. The features of the polarimetric steering vector are developed in the framework of quad-polarized observations, the changes with respect to other polarimetric modes being mentioned whenever necessary. The MBPI steering vector is a linear combination of four vectors $\mathbf{a}_{\gamma_i}(\varphi) \in \mathbb{C}^{\tilde{p}}$, each of them associated with one particular polarization

$$\begin{aligned} \mathbf{b}(\varphi, \mathbf{k}) &= k_1\mathbf{a}_{\gamma_1}(\varphi) + k_2\mathbf{a}_{\gamma_2}(\varphi) + k_3\mathbf{a}_{\gamma_3}(\varphi) + k_4\mathbf{a}_{\gamma_4}(\varphi) \\ &= \begin{bmatrix} k_1\mathbf{a}(\varphi) \\ k_2\mathbf{a}(\varphi) \\ k_3\mathbf{a}(\varphi) \\ k_4\mathbf{a}(\varphi) \end{bmatrix}. \end{aligned} \tag{4.2}$$

The vector $\mathbf{a}(\varphi)$ is the familiar single polarization MB interferometric SAR steering vector introduced in subsection 3.1.1. For a ULA it is represented as (cf. equation (3.2))

$$\mathbf{a}(\varphi) = [1, \exp(j\varphi/(p-1)), \ldots, \exp(j\varphi)]^T. \tag{4.3}$$

For an irregular array the vector $\mathbf{a}(z)$ depending on height z is expressed by (compare equation (3.4))

$$\mathbf{a}(z) = [1, \exp(j\kappa_{z_2} z), \ldots, \exp(j\kappa_{z_p} z)]^T. \tag{4.4}$$

The weighting coefficients $k_i \in \mathbb{C}$ form a vector

$$\mathbf{k} = [k_1, k_2, k_3, k_4]^T \tag{4.5}$$

that may be interpreted as a unitary scattering mechanism, $\mathbf{k}^H\mathbf{k} = 1$. This complex vector is uniquely defined apart from an exponential term $\exp(j\xi)$ with $\xi \in \mathbb{R}$, that cancels out when forming $\mathbf{b}(\boldsymbol{\theta}_t)\mathbf{b}^H(\boldsymbol{\theta}_t)$. The scattering mechanism introduces into the MB POL-InSAR model additional unknown parameters. Hence, for the deterministic model the parameter vector $\boldsymbol{\theta}_t$ consists of one phase φ (respectively height z) of the reflector and the parameters that describe its related scattering type $\mathbf{k}$, i.e.,

$$\boldsymbol{\theta}_t = [\varphi, \Re(k_2), \Im(k_2), \Re(k_3), \Im(k_3), \Re(k_4), \Im(k_4)] \in \mathbb{R}^{N_{par}}. \tag{4.6}$$

Without loss of generality $\Re(k_1)$ and $\Im(k_1)$ are considered to be fixed due to the normalization of $\mathbf{k}$, and the exponential term, respectively. The number of real-valued free parameters[1] N_{par} is given by

$$N_{par} = 1 + 2(N_{pol} - 1) = 2N_{pol} - 1 \tag{4.7}$$

for $1 \leq N_{pol} \leq 4$. The values of N_{par} are recapitulated in table 4.2.

The MBPI steering vector can be written in matrix notation as

$$\mathbf{b}(\varphi, \mathbf{k}) = \mathbf{B}(\varphi)\mathbf{k} \tag{4.8}$$

with the MBPI steering vector matrix $\mathbf{B}(\varphi) \in \mathbf{Mat}_{\tilde{p}, N_{pol}}(\mathbb{C})$

$$\mathbf{B}(\varphi) = \begin{bmatrix} \mathbf{a}(\varphi) & \mathbf{0} & \mathbf{0} & \mathbf{0} \\ \mathbf{0} & \mathbf{a}(\varphi) & \mathbf{0} & \mathbf{0} \\ \mathbf{0} & \mathbf{0} & \mathbf{a}(\varphi) & \mathbf{0} \\ \mathbf{0} & \mathbf{0} & \mathbf{0} & \mathbf{a}(\varphi) \end{bmatrix}. \tag{4.9}$$

[1] The other unknown parameters of the signal model such as the number of backscattering sources N_{s_t}, the reflectivity τ_t, and the complex argument ψ_i are not included in the vector of free parameters. The reason will be clarified in section 4.4 about the polarimetric joint detection-estimation ML estimator.

Polarization state	N_{par}
single polarization	1
dual-polarized	3
fully polarimetric	5
quad-polarized	7

Table 4.2: The number of free parameters N_{par} in the deterministic signal model.

The number of backscattering sources is denoted by N_{s_t}. The unknown parameter τ_{t_i} is called the polarimetric reflectivity of the ith source: While the absolute value of the scattering mechanism coefficients $|k_j|$ in equation (4.5) indicates the relative intensity between the polarizations, the reflectivity τ specifies the SPAN defined in (2.38).

The additive white Gaussian noise $\mathbf{n}(l) \in \mathbb{C}^{\tilde{p}}$ is assumed to have zero mean and power σ_n^2, i.e., $\mathbf{n}(l) \sim \mathcal{N}_{\mathbb{C}}^{\tilde{p}}(\mathbf{0}, \sigma_n^2 \mathbf{I})$. Thus, the polarimetric MB InSAR observation vector $\mathbf{y}(l)$ is a Gaussian random process with nonzero mean $\boldsymbol{\mu} \in \mathbb{C}^{\tilde{p}}$, and covariance matrix $\mathbf{R} \in \mathbf{Mat}_{\tilde{p}}(\mathbb{C})$.

The returned signal (4.1) can be written in matrix notation as

$$\mathbf{y}(l) = \mathbf{D}(\boldsymbol{\theta}_t)\mathbf{s} + \mathbf{n}(l) \tag{4.10}$$

with the matrix $\mathbf{D}(\boldsymbol{\theta}_t) \in \mathbf{Mat}_{\tilde{p},N_{s_t}}(\mathbb{C})$ of steering vectors

$$\mathbf{D}(\boldsymbol{\theta}_t) = \left[\mathbf{b}(\boldsymbol{\theta}_{t_1}), \ldots, \mathbf{b}(\boldsymbol{\theta}_{t_{N_{s_t}}})\right], \tag{4.11}$$

the signal vector $\mathbf{s} = \left[s_1, \ldots, s_{N_{s_t}}\right]^T$, $s_i = \sqrt{\tau_{t_i}} \exp(j\psi_i)$, and the parameter vector $\boldsymbol{\theta}_t = \left[\boldsymbol{\theta}_{t_1}^T, \ldots, \boldsymbol{\theta}_{t_{N_{s_t}}}^T\right]^T \in \mathbb{R}^{N_{s_t} N_{par}}$.

Since signals and noise are assumed to be independent, the shape of the non-central covariance matrix $\mathbf{R} = E\{\mathbf{y}(l)\mathbf{y}^H(l)\}$ of the observation (4.1) is

$$\mathbf{R} = \mathbf{D}(\boldsymbol{\theta}_t)\mathbf{S}\mathbf{D}^H(\boldsymbol{\theta}_t) + \sigma_n^2 \mathbf{I} \tag{4.12}$$

with the signal covariance matrix $\mathbf{S} = \mathbf{s}\mathbf{s}^H$. This model incorporates multipath reflection phenomena that might appear in urban scenes.

The sample covariance matrix $\hat{\mathbf{R}} \in \mathbf{Mat}_{\tilde{p}}(\mathbb{C})$ is calculated by

$$\hat{\mathbf{R}} = \frac{1}{L} \sum_{l=1}^{L} \mathbf{y}(l)\mathbf{y}^H(l). \tag{4.13}$$

The model can be generalized to hybrid systems where the antennas acquire different polarimetric channels. If N_{sp}, N_{dp}, N_{fp}, and N_{qp} denote

the number of sensors in single polarization, dual-polarized and fully polarimetric with equal and diverse cross-polarization mode, respectively, $\tilde{p} = N_{sp} + 2N_{dp} + 3N_{fp} + 4N_{qp}$. The construction of the MBPI steering vector is evident. For instance a triple baseline interferometric configuration including one sensor that is fully polarimetric with hh, vv, and hv polarizations and two dual-polarized antennas that operate in hh and vv and hh and hv polarizations respectively results in $\tilde{p} = 7$.

4.1.2 Stochastic MB POL-InSAR Signal Model

In the case of deterministic signals it was assumed that the steering vector depends only on one single interferometric phase φ. Consequently this phase is related to all polarimetric channels and the corresponding scattering mechanism $\mathbf{k}$ describes a polarization combination. This reasoning is valid for deterministic or almost determinstic targets where the interferometric phase variations are small with respect to polarization. For distributed environments such as forests that can be modeled as a volume over ground [14, 75], the location of the effective phase center varies considerably in regard of polarization [14, 75, 85]. Hence, in the stochastic model characterizing the response of natural objects it is supposed that each polarization channel is associated with one particular phase. Therefore, the MBPI steering vector is a function of these phases. The polarimetric multibaseline InSAR measurements $\mathbf{y}(l)$ with p antennas and $\tilde{p} = pN_{pol}$ elements is modeled as

$$\begin{aligned} \mathbf{y}(l) &= \mathbf{c}(l) + \mathbf{n}(l) \\ &= \sum_{j=1}^{N_{sc}} \sqrt{\tau_{c_j}} \mathbf{x}_j(l) \odot \mathbf{b}(\boldsymbol{\theta}_{c_j}) + \mathbf{n}(l). \end{aligned} \tag{4.14}$$

The multibaseline polarimetric interferometric steering vector $\mathbf{b}(\boldsymbol{\theta}_c)$ is dependent on the unknown parameter vector $\boldsymbol{\theta}_c$. The MBPI steering vector is linearly combined by N_{pol} vectors $\mathbf{a}(\varphi_i) \in \mathbb{C}^p$, each related to one single polarization

$$\mathbf{b}(\boldsymbol{\varphi}, \mathbf{k}) = [k_1 \mathbf{a}^T(\varphi_1), \ldots, k_{N_{pol}} \mathbf{a}^T(\varphi_{N_{pol}})]^T \tag{4.15}$$

where $\boldsymbol{\varphi} = \left[\varphi_1, \ldots, \varphi_{N_{pol}}\right]^T$. The weighting coefficients $k_i \in \mathbb{C}$ generate the vector

$$\mathbf{k} = \left[k_1, \ldots, k_{N_{pol}}\right]^T. \tag{4.16}$$

For the special case of equal phase centers in all polarization channels, it may be viewed as a unitary scattering mechanism, $\mathbf{k}^H \mathbf{k} = 1$. This complex vector is uniquely determined except for an exponential contribution $\exp(j\xi)$ with $\xi \in \mathbb{R}$, that neutralizes when calculating $\mathbf{b}(\boldsymbol{\theta}_c)\mathbf{b}^H(\boldsymbol{\theta}_c)$. Thus, for the stochastic model the parameter vector $\boldsymbol{\theta}_c$ contains N_{pol} phases φ_i and the parameters characterizing the vector $\mathbf{k}$, i.e.,

$$\boldsymbol{\theta}_c = \left[\varphi_1, \ldots, \varphi_{N_{pol}}, \Re(k_2), \Im(k_2), \ldots, \Re(k_{N_{pol}}), \Im(k_{N_{pol}})\right] \in \mathbb{R}^{N_{par}^{pd}}. \tag{4.17}$$

Polarization state	N_{par}^{pd}
single polarization	1
dual-polarized	4
fully polarimetric	7
quad-polarized	10

Table 4.3: The number of free parameters N_{par}^{pd} in the stochastic signal model.

Without loss of generality $\Re(k_1)$ and $\Im(k_1)$ are supposed to be fixed on account of the normalization $\|\mathbf{k}\|_2 = 1$ and the exponential component, respectively. The number of real-valued free parameters[2] N_{par}^{pd} is given by

$$N_{par}^{pd} = N_{pol} + 2(N_{pol} - 1) = 3N_{pol} - 2 \tag{4.18}$$

for $1 \leq N_{pol} \leq 4$, as summarized in table 4.3. The matrix notation of the MBPI steering vector is

$$\mathbf{b}(\boldsymbol{\varphi}, \mathbf{k}) = \mathbf{B}(\boldsymbol{\varphi})\mathbf{k} \tag{4.19}$$

with the MBPI steering vector matrix $\mathbf{B}(\boldsymbol{\varphi}) \in \mathbf{Mat}_{\tilde{p},N_{pol}}(\mathbb{C})$

$$\mathbf{B}(\boldsymbol{\varphi}) = \begin{bmatrix} \mathbf{a}(\varphi_1) & & \\ & \ddots & \\ & & \mathbf{a}(\varphi_{N_{pol}}) \end{bmatrix}. \tag{4.20}$$

The total number of backscattering sources is given by $N_{s_c}^{tot} = N_{s_c} N_{pol}$. The absolute value of the scattering type coefficients $|k_i|$ in equation (4.16) designates the relative intensity between the polarization channels, whereas the product $\tau|k_i|^2$ specifies the absolute backscattered power of the associated polarization.

The multiplicative noise $\mathbf{x}_j(l) \in \mathbb{C}^{\tilde{p}}$ corresponding to the jth source is modeled as a stationary, circular Gaussian random vector with zero mean, unit variance, and covariance matrix $\mathbf{C}_j$. The random processes $\mathbf{x}_j(l_1)$ and $\mathbf{x}_j(l_2)$ are supposed to be independent and identically distributed for different looks $l_1 \neq l_2$. In the particular scenario of fully correlated speckle the variations of the phases related to one single steering vector are expected to be small. Hence, the polarimetric MB InSAR measurement $\mathbf{y}(l)$ is a Gaussian random vector with zero mean and covariance matrix $\mathbf{R}$, which can be expressed by

$$\mathbf{R} = E\{\mathbf{y}(l)\mathbf{y}^H(l)\} = \sum_{j=1}^{N_{s_c}} \tau_{c_j} \mathbf{C}_j \odot \mathbf{b}(\boldsymbol{\theta}_{c_j})\mathbf{b}^H(\boldsymbol{\theta}_{c_j}) + \sigma_n^2 \mathbf{I}. \tag{4.21}$$

[2]The free parameter vector does not comprise the other unknown quantities like the quantity τ_c, the cause of this being elucidated in section 4.4 about the polarimetric joint detection-estimation ML estimator.

4.1.3 Hybrid MB POL-InSAR Signal Model

The hybrid model contains both the deterministic and stochastic contributions defined in the two preceding subsections. For p sensors the multibaseline InSAR received signal including polarization diversity can be written as

$$\begin{aligned}\mathbf{y}(l) &= \mathbf{t} + \mathbf{c}(l) + \mathbf{n}(l) \\ &= \sum_{i=1}^{N_{s_t}} \sqrt{\tau_{t_i}} \exp(j\psi_i)\mathbf{b}(\boldsymbol{\theta}_{t_i}) \\ &+ \sum_{j=1}^{N_{s_c}} \sqrt{\tau_{c_j}}\mathbf{x}_j(l) \odot \mathbf{b}(\boldsymbol{\theta}_{c_j}) + \mathbf{n}(l) \end{aligned} \tag{4.22}$$

with the number of looks L and $l = 1, \ldots, L$. The first contribution, $\mathbf{t}$, is a highly coherent component and corresponds to deterministic targets [28]. The second constituent, $\mathbf{c}(l)$, represents the response of natural environments comprising the SAR speckle effect as multiplicative noise [37, 39, 63]. The total number of backscattering sources is calculated by $N_s = N_{s_t} + N_{s_c}^{tot}$ where N_{s_t} and $N_{s_c}^{tot} = N_{s_c} N_{pol}$ are the number of sources associated to the deterministic and stochastic part, respectively. The unknown reflectivity τ_t, the complex argument ψ, and the deterministic MBPI steering vector $\mathbf{b}(\boldsymbol{\theta}_t)$ with the unknown parameter vector $\boldsymbol{\theta}_t$ are introduced in subsection 4.1.1. The properties of the additive noise $\mathbf{n}(l)$ are outlined in subsection 4.1.1.

The unknown quantity τ_c, the stochastic MBPI steering vector $\mathbf{b}(\boldsymbol{\theta}_c)$ being a function of the unknown parameters $\boldsymbol{\theta}_c$, and the multiplicative noise $\mathbf{x}(l)$ are characterized in subsection 4.1.2.

The polarimetric MB InSAR observations $\mathbf{y}(l) \in \mathbb{C}^{\tilde{p}}$ are circular Gaussian distributed random vectors with nonzero mean and covariance matrix $\mathbf{R}$. The non-central data covariance matrix $\mathbf{R} = E\{\mathbf{y}(l)\mathbf{y}^H(l)\}$ for the hybrid model is given by

$$\mathbf{R} = \mathbf{D}(\boldsymbol{\theta}_t)\mathbf{S}\mathbf{D}^H(\boldsymbol{\theta}_t) + \sum_{j=1}^{N_{s_c}} \tau_{c_j}\mathbf{C}_j \odot \mathbf{b}(\boldsymbol{\theta}_{c_j})\mathbf{b}^H(\boldsymbol{\theta}_{c_j}) + \sigma_n^2\mathbf{I} \tag{4.23}$$

where the MBPI steering matrix $\mathbf{D}(\boldsymbol{\theta}_t)$ and the signal covariance matrix $\mathbf{S}$ are defined in subsection 4.1.1 and the speckle covariance matrices $\mathbf{C}_j$ in subsection 4.1.2. Multipath propagation phenomena are included in this model.

In the following the relation of the polarimetric MB InSAR covariance matrix to two special cases is studied, firstly to the single polarization scenario from chapter 3, and secondly to the single-baseline POL-InSAR set-up developed in [14]. For p antennas the MB polarimetric InSAR observation

vector $\mathbf{y}(l) \in \mathbb{C}^{3p}$ with equal cross-polarizations is given in the Pauli basis by

$$\mathbf{y}(l) = \frac{1}{\sqrt{2}}[S^1_{hh}(l) + S^1_{vv}(l), \ldots, S^p_{hh}(l) + S^p_{vv}(l), S^1_{hh}(l) - S^1_{vv}(l), \ldots \\ \ldots, S^p_{hh}(l) - S^p_{vv}(l), 2S^1_{hv}(l), \ldots, 2S^p_{hv}(l)]^T. \quad (4.24)$$

The data covariance matrix $\mathbf{R} = E\{\mathbf{y}(l)\mathbf{y}^H(l)\} \in \mathbf{Mat}_{3p}(\mathbb{C})$ is the block matrix

$$\mathbf{R} = \begin{bmatrix} \mathbf{R}_{11} & \mathbf{R}_{12} & \mathbf{R}_{13} \\ \mathbf{R}^H_{12} & \mathbf{R}_{22} & \mathbf{R}_{23} \\ \mathbf{R}^H_{13} & \mathbf{R}^H_{23} & \mathbf{R}_{33} \end{bmatrix}. \quad (4.25)$$

$\mathbf{R}_{ii} \in \mathbf{Mat}_p(\mathbb{C})$ are the standard Hermitian matrices of the single polarization multibaseline InSAR configuration described in chapter 3, where $\mathbf{R}_{11}, \mathbf{R}_{22}$, and $\mathbf{R}_{33}$ are linked to $hh + vv, hh - vv$, and hv polarization, respectively. The matrices $\mathbf{R}_{ij} \in \mathbf{Mat}_p(\mathbb{C})$, that are in general not Hermitian comprehend both polarimetric and interferometric information. More precisely, they inclose the interferometric phase correlations between two different polarizations in each case.

The single-baseline POL-InSAR returned signal can be expressed as [14]

$$\mathbf{k}_6(l) = \frac{1}{\sqrt{2}}[S^1_{hh}(l) + S^1_{vv}(l), S^1_{hh}(l) - S^1_{vv}(l), 2S^1_{hv}(l), \\ S^2_{hh}(l) + S^2_{vv}(l), S^2_{hh}(l) - S^2_{vv}(l), 2S^2_{hv}(l)]^T. \quad (4.26)$$

The covariance matrix $\mathbf{T}_6 = E\{\mathbf{k}_6(l)\mathbf{k}^H_6(l)\} \in \mathbf{Mat}_6(\mathbb{C})$ is the block matrix

$$\mathbf{T}_6 = \begin{bmatrix} \mathbf{T}_{11} & \mathbf{\Omega}_{12} \\ \mathbf{\Omega}^H_{12} & \mathbf{T}_{22} \end{bmatrix}. \quad (4.27)$$

$\mathbf{T}_{ii} \in \mathbf{Mat}_3(\mathbb{C})$ are the conventional Hermitian coherency matrices containing the fully polarimetric information for each separate image. The non-Hermitian matrix $\mathbf{\Omega}_{12} \in \mathbf{Mat}_3(\mathbb{C})$ comprises the interferometric phase relations of the different polarimetric channels between both images [14]. For $p = 2$, the measurement $\mathbf{y}(l) \in \mathbb{C}^6$ from equation (4.24) is a permutation of $\mathbf{k}_6(l)$, i.e., $\mathbf{y}(l) = \mathbf{P}\mathbf{k}_6(l)$, where the permutation matrix $\mathbf{P} \in \mathbf{Mat}_6(\mathbb{Z}_2)$ has the shape

$$\mathbf{P} = \begin{bmatrix} 1 & & & & & \\ & 0 & 0 & 1 & & \\ & 1 & 0 & & & \\ & & & 0 & 1 & \\ & & 1 & 0 & 0 & \\ & & & & & 1 \end{bmatrix}. \quad (4.28)$$

For the covariance matrix $\mathbf{R} \in \mathbf{Mat}_6(\mathbb{C})$ of equation (4.25) it follows that $\mathbf{R} = \mathbf{P}\mathbf{T}_6\mathbf{P}^T$. Therefore $\mathbf{R}$ and $\mathbf{T}_6$ are permutation-similar.

The objective is to determine the following unknown quantities: The number of backscattering sources N_s and the signal features as the reflectivity τ, the interferometric phase φ (or the height z), and the scattering mechanism $\mathbf{k}$. For multibaseline polarimetric InSAR measurements the algorithms to solve the detection problem are detailed in section 4.2 and the methods to extract the characteristics of the signals are elaborated in sections 4.3 and 4.4.

4.2 Polarimetric Model Order Selection Algorithms

The generalization of the model order selection techniques for estimating the number of sources from polarimetric MB InSAR data is developed in this section. Since the rationale to derive these methods is the same as for the case of single polarization MB InSAR signals described in section 3.2, the polarimetric MOS algorithms are stated by highlighting the differences between both set-ups.

Like in section 3.2, the received signal $\mathbf{y}(l) \in \mathbb{C}^{\tilde{p}}$ with $\tilde{p} = pN_{pol}$ is modeled as

$$\mathbf{y}(l) = \sum_{i=1}^{N_s} s_i(l)\mathbf{b}(\boldsymbol{\theta}_i) + \mathbf{n}(l). \tag{4.29}$$

The steering vectors $\mathbf{b}(\boldsymbol{\theta}_i)$ are assumed to be linearly independent, and $N_s < \tilde{p}$. The task is to estimate the number of sources N_s.

Let $k \in \{0, 1, \ldots, \tilde{p}-1\}$ be the assumed number of sources and let $\lambda_1 \geq \cdots \geq \lambda_{\tilde{p}}$ and $\mathbf{v}_1, \ldots, \mathbf{v}_{\tilde{p}}$ be the eigenvalues and eigenvectors, respectively, of the data covariance matrix $\mathbf{R} \in \mathbf{Mat}_{\tilde{p}}(\mathbb{C})$. Thus the parameter vector of the model is given by

$$\boldsymbol{\theta}(k) = (\lambda_1, \ldots, \lambda_k, \sigma_n^2, \mathbf{v}_1^T, \ldots, \mathbf{v}_k^T)^T. \tag{4.30}$$

Employing the eigenvalues $\hat{\lambda}_1 > \cdots > \hat{\lambda}_{\tilde{p}}$ of the sample covariance matrix $\hat{\mathbf{R}} \in \mathbf{Mat}_{\tilde{p}}(\mathbb{C})$ defined by

$$\hat{\mathbf{R}} = \frac{1}{L}\sum_{l=1}^{L} \mathbf{y}(l)\mathbf{y}^H(l) \tag{4.31}$$

the log-likelihood of the maximum likelihood estimator of the model parameters can be written as [110]

$$\log f(\mathbf{Y}|\hat{\boldsymbol{\theta}}(k)) = (\tilde{p}-k)L \log \left(\frac{\prod_{i=k+1}^{\tilde{p}} \hat{\lambda}_i^{1/(\tilde{p}-k)}}{\frac{1}{\tilde{p}-k}\sum_{i=k+1}^{\tilde{p}} \hat{\lambda}_i} \right). \tag{4.32}$$

The dimension of the space spanned by $\boldsymbol{\theta}(k)$ provides the number of free real-valued parameters $\eta(k)$: The k eigenvectors constitute a basis of the

matrix space $\mathbf{Mat}_{\tilde{p},k}(\mathbb{C})$ with $\dim(\mathbf{Mat}_{\tilde{p},k}(\mathbb{C})) = 2\tilde{p}k$. Since they are elements of the special orthogonal group over the complex number field $\mathbf{SO}_{\tilde{p}}(\mathbb{C})$ the degrees of freedom (DoF) are reduced by the value $2k$ due to the normalization, and by $k(k-1)$ in consequence of the mutual orthogonalization. Hence the orthonormal eigenvectors span a space of dimension $2\tilde{p}k - 2k - k(k-1) = k(2\tilde{p} - 1 - k)$. The real-valued eigenvalues add k DoF. Therefore the degrees of freedom for the polarimetric multibaseline InSAR signals result in

$$\eta(k) = k + 1 + k(2\tilde{p} - 1 - k) = k(2\tilde{p} - k) + 1. \tag{4.33}$$

For the scenario of polarization diversity, the number of free parameters depends on $\tilde{p} = pN_{pol}$, i.e., on both the number of antennas p and the polarization number N_{pol}. Compared to the single polarization MB InSAR configuration the major modification is the augmentation of the observation space dimension.

Plugging equations (4.32) and (4.33) into (3.21) leads to the polarimetric Akaike information criterion

$$\mathrm{AIC}(k) = -(\tilde{p} - k)L \log \left(\frac{\prod_{i=k+1}^{\tilde{p}} \hat{\lambda}_i^{1/(\tilde{p}-k)}}{\frac{1}{\tilde{p}-k} \sum_{i=k+1}^{\tilde{p}} \hat{\lambda}_i} \right) + k(2\tilde{p} - k). \tag{4.34}$$

The polarimetric minimum description length is

$$\mathrm{MDL}(k) = -(\tilde{p} - k)L \log \left(\frac{\prod_{i=k+1}^{\tilde{p}} \hat{\lambda}_i^{1/(\tilde{p}-k)}}{\frac{1}{\tilde{p}-k} \sum_{i=k+1}^{\tilde{p}} \hat{\lambda}_i} \right) + \frac{1}{2} k(2\tilde{p} - k) \log L \tag{4.35}$$

and the efficient detection criteria is given by

$$\mathrm{EDC}(k) = -(\tilde{p} - k)L \log \left(\frac{\prod_{i=k+1}^{\tilde{p}} \hat{\lambda}_i^{1/(\tilde{p}-k)}}{\frac{1}{\tilde{p}-k} \sum_{i=k+1}^{\tilde{p}} \hat{\lambda}_i} \right) + k(2\tilde{p} - k) C_L. \tag{4.36}$$

Finally the number of sources $\hat{N}_s$ is estimated by

$$\hat{N}_s = \arg\min_k \mathrm{ITC}(k). \tag{4.37}$$

In the following the most significant special cases are examined: For $N_{pol} = 1$ the detection techniques reduce to the methods for multibaseline InSAR data with one single polarization derived in section 3.2. By introducing polarization diversity the polarization number attains values $2 \leq N_{pol} \leq 4$. The polarimetric MOS algorithms may also be applied to a polarimetric image without interferometric baseline diversity for $p = 1$ and $N_{pol} = 2, 3, 4$. This provides an alternative approach compared to the reasoning in [27] where the number of scattering mechanisms is estimated by means of the polarimetric entropy H and anisotropy A. The model order

selection techniques can also be adapted to the setting of hybrid antenna configurations with $\tilde{p} = N_{sp}+2N_{dp}+3N_{fp}+4N_{qp}$. N_{sp}, N_{dp}, N_{fp}, and N_{qp} signify the number of sensors that operate under single polarization, dual-polarized and fully polarimetric with equal and diverse cross-polarization mode, respectively. For example a triple baseline interferometric system comprising two antennas that are fully polarimetric with equal cross-polarizations and one single polarization sensor leads to $\tilde{p} = 8$.

A polarimetric joint detection-estimation algorithm based on the maximum likelihood estimator is presented in section 4.4.

4.3 Polarimetric Spectral Estimation Methods

The spectral estimation algorithms are extended to the polarimetric multibaseline InSAR configuration in this section. The adaptation to the polarimetric case not merely increases the number of observables, but particularly determines the polarization combination for spatial frequency estimation that is optimal with respect to the specific method. These optimal scattering mechanisms allow the examination of the reflector physical properties by analyzing their polarimetric behavior. First, the nonparametric beamforming and Capon methods are generalized to the MB POL-InSAR scenario that permit to extract the spatial frequencies, the associated optimal scattering vectors, and the polarimetric reflectivities. Subsequently, the model-based polarimetric techniques are developed: The MUSIC and M-RELAX algorithms extract the spatial frequency and the corresponding scattering mechanism. The linear least-squares approach and M-RELAX estimate the polarimetric reflectivity.

4.3.1 Polarimetric Beamforming

The beamforming method has been extended to the particular scenario of polarization diversity in the receive channel in [23]. In this section, the polarimetric beamforming method to process polarimetric MB InSAR observations is developed using the filter design approach of subsection 3.3.1. The single polarization MB InSAR steering vector $\mathbf{a}(\omega) \in \mathbb{C}^p$ has to be substituted by the MB polarimetric InSAR steering vector $\mathbf{b}(\omega, \mathbf{k}) \in \mathbb{C}^{\tilde{p}}$. The minimization problem of polarimetric beamforming can be expressed by

$$\min_{\mathbf{h}} \mathbf{h}^H \mathbf{h} \qquad \text{subject to} \qquad \mathbf{h}^H \mathbf{b}(\omega, \mathbf{k}) = 1. \tag{4.38}$$

The derivation of the polarimetric beamforming filter employing the quadratic minimization theorem (see appendix B, section B.3 for details) results in

$$\mathbf{h}_{BF}^{P} = \frac{\mathbf{b}(\omega, \mathbf{k})}{\mathbf{b}^H(\omega, \mathbf{k})\mathbf{b}(\omega, \mathbf{k})} = \frac{\mathbf{b}(\omega, \mathbf{k})}{p}. \tag{4.39}$$

In the last equation the relation of the MBPI steering vector

$$\mathbf{b}^H(\omega,\mathbf{k})\mathbf{b}(\omega,\mathbf{k}) = \mathbf{a}^H(\omega)\mathbf{a}(\omega)\sum_{i=1}^{N_{pol}} k_i^* k_i = p\|\mathbf{k}\|_2^2 = p \tag{4.40}$$

was used that follows from (4.2). The power of the filtered signal is given by

$$E\{|y_F(l)|^2\} = E\{|(\mathbf{h}_{BF}^P)^H\mathbf{y}(l)|^2\} = \frac{\mathbf{b}^H(\omega,\mathbf{k})\mathbf{R}\mathbf{b}(\omega,\mathbf{k})}{p^2}. \tag{4.41}$$

It can be maximized with respect to the polarization state $\mathbf{k}$ by

$$\max_{\|\mathbf{k}\|_2=1} \frac{\mathbf{b}^H(\omega,\mathbf{k})\mathbf{R}\mathbf{b}(\omega,\mathbf{k})}{p^2}. \tag{4.42}$$

This maximization problem can be solved via (4.8) by calculating the maximum eigenvalue of the Hermitian matrix $\mathbf{B}^H(\omega)\mathbf{R}\mathbf{B}(\omega) \in \mathbf{Mat}_{N_{pol}}(\mathbb{C})$

$$\mathbf{B}^H(\omega)\mathbf{R}\mathbf{B}(\omega)\mathbf{k}_{\max} = \lambda_{\max}\mathbf{k}_{\max}. \tag{4.43}$$

Replacing the data covariance matrix $\mathbf{R}$ by the sample covariance matrix $\hat{\mathbf{R}}$ the spectrum of the polarimetric beamforming is

$$\hat{P}_{BF}^P(\omega) = \frac{\lambda_{\max}(\mathbf{B}^H(\omega)\hat{\mathbf{R}}\mathbf{B}(\omega))}{p^2} \tag{4.44}$$

where $\lambda_{\max}(\cdot)$ is the maximum eigenvalue operator. This means that for each frequency ω the maximal eigenvalue and its corresponding eigenvector of the linear system

$$\mathbf{B}^H(\omega)\hat{\mathbf{R}}\mathbf{B}(\omega)\mathbf{k}_{\max} = \lambda_{\max}\mathbf{k}_{\max} \tag{4.45}$$

has to be computed. In particular the dimension of the Hermitian matrix $\mathbf{B}^H(\omega)\hat{\mathbf{R}}\mathbf{B}(\omega) \in \mathbf{Mat}_{N_{pol}}(\mathbb{C})$ is independent of the number of sensors p. The unitary eigenvector $\mathbf{k}_{\max}$ can be interpreted as a polarimetric scattering mechanism allowing a polarimetric analysis to retrieve the physical properties of the reflector. It encodes the polarization combination that is optimal in the sense of beamforming.

The frequency estimates $\hat{\boldsymbol{\omega}} = [\hat{\omega}_1,\ldots,\hat{\omega}_{N_s}]^T$ are related to the positions of the N_s largest peaks of the spectrum. The polarimetric reflectivity at frequency $\hat{\omega}_i$ is estimated by $\hat{\tau}_i = \hat{P}_{BF}^P(\hat{\omega}_i)$.

Figure 4.1 demonstrates the polarimetric beamforming spectrum for simulated signals containing two sources, the first at $\varphi_1 = 0$ rad and the second at $\varphi = 3\pi$ rad.

To adapt the polarimetric beamforming method to the scenario of different phase centers, the steering vector $\mathbf{b}(\boldsymbol{\omega},\mathbf{k}) \in \mathbb{C}^{\tilde{p}}$ with $\boldsymbol{\omega} = [\omega_1,\ldots,\omega_{N_{pol}}]^T$

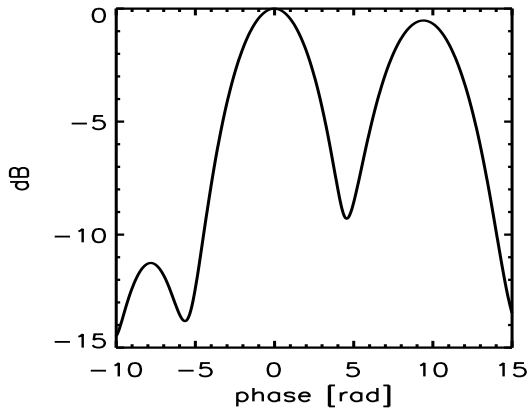

Figure 4.1: Polarimetric beamforming spectrum containing two sources.

has to be considered. The development conforms fundamentally with the deterministic case by noticing that

$$\mathbf{b}^H(\boldsymbol{\omega},\mathbf{k})\mathbf{b}(\boldsymbol{\omega},\mathbf{k}) = \sum_{i=1}^{N_{pol}} k_i^* k_i \mathbf{a}^H(\omega_i)\mathbf{a}(\omega_i) = p\|\mathbf{k}\|_2^2 = p. \tag{4.46}$$

For instance, in the fully polarimetric configuration with equal cross-polarizations the structure of the Hermitian matrix $\mathbf{B}^H(\boldsymbol{\omega})\mathbf{R}\mathbf{B}(\boldsymbol{\omega}) \in \mathbf{Mat}_3(\mathbb{C})$ is

$$\mathbf{B}^H(\boldsymbol{\omega})\mathbf{R}\mathbf{B}(\boldsymbol{\omega}) = \begin{bmatrix} \mathbf{a}^H(\omega_1)\mathbf{R}_{11}\mathbf{a}(\omega_1) & \mathbf{a}^H(\omega_1)\mathbf{R}_{12}\mathbf{a}(\omega_2) & \mathbf{a}^H(\omega_1)\mathbf{R}_{13}\mathbf{a}(\omega_3) \\ \mathbf{a}^H(\omega_2)\mathbf{R}_{12}^H\mathbf{a}(\omega_1) & \mathbf{a}^H(\omega_2)\mathbf{R}_{22}\mathbf{a}(\omega_2) & \mathbf{a}^H(\omega_2)\mathbf{R}_{23}\mathbf{a}(\omega_3) \\ \mathbf{a}^H(\omega_3)\mathbf{R}_{13}^H\mathbf{a}(\omega_1) & \mathbf{a}^H(\omega_3)\mathbf{R}_{23}^H\mathbf{a}(\omega_2) & \mathbf{a}^H(\omega_3)\mathbf{R}_{33}\mathbf{a}(\omega_3) \end{bmatrix}. \tag{4.47}$$

The polarimetric beamforming spectrum is given by

$$\hat{P}_{BF}^{P2}(\boldsymbol{\omega}) = \frac{\lambda_{\max}(\mathbf{B}^H(\boldsymbol{\omega})\hat{\mathbf{R}}\mathbf{B}(\boldsymbol{\omega}))}{p^2}. \tag{4.48}$$

The spectrum is a function of N_{pol} parameters. The frequency estimates $\hat{\boldsymbol{\omega}}_{\boldsymbol{i}}, i = 1,\ldots,N_s$, are obtained as the locations of the N_s maxima of $\hat{P}_{BF}^{P2}(\boldsymbol{\omega})$.

4.3.2 Polarimetric Capon Method

The Capon approach has been adapted to the special configuration of polarization diversity in the receive antennas in [23]. In this subsection, the polarimetric Capon method for analyzing MB POL-InSAR measurements is conceived paralleling the filter design procedure of subsection 3.3.2. The MB polarimetric InSAR steering vector $\mathbf{b}(\omega,\mathbf{k})$ is employed in lieu of the single

polarization MB InSAR steering vector $\mathbf{a}(\omega)$. The optimization problem of the polarimetric Capon method can be stated as

$$\min_{\mathbf{h}} \mathbf{h}^H \mathbf{R} \mathbf{h} \qquad \text{subject to} \qquad \mathbf{h}^H \mathbf{b}(\omega, \mathbf{k}) = 1. \tag{4.49}$$

The derivation of the polarimetric Capon filter utilizing the quadratic minimization theorem (explained in appendix B, section B.3) leads to

$$\mathbf{h}_C^P = \frac{\mathbf{R}^{-1}\mathbf{b}(\omega, \mathbf{k})}{\mathbf{b}^H(\omega, \mathbf{k})\mathbf{R}^{-1}\mathbf{b}(\omega, \mathbf{k})}. \tag{4.50}$$

The power of the filtered signal can be expressed by

$$E\{|y_F(l)|^2\} = E\{|(\mathbf{h}_C^P)^H \mathbf{y}(l)|^2\} = \frac{1}{\mathbf{b}^H(\omega, \mathbf{k})\mathbf{R}^{-1}\mathbf{b}(\omega, \mathbf{k})}. \tag{4.51}$$

Maximizing it with respect to the polarization state $\mathbf{k}$ yields

$$\max_{\|\mathbf{k}\|_2=1} \frac{1}{\mathbf{b}^H(\omega, \mathbf{k})\mathbf{R}^{-1}\mathbf{b}(\omega, \mathbf{k})}. \tag{4.52}$$

The solution of this maximization problem is the minimum eigenvalue of the Hermitian matrix $\mathbf{B}^H(\omega)\mathbf{R}^{-1}\mathbf{B}(\omega) \in \mathbf{Mat}_{N_{pol}}(\mathbb{C})$

$$\mathbf{B}^H(\omega)\mathbf{R}^{-1}\mathbf{B}(\omega)\mathbf{k}_{\min} = \lambda_{\min}\mathbf{k}_{\min}. \tag{4.53}$$

With the sample covariance matrix $\hat{\mathbf{R}}$ the spectrum of the polarimetric Capon method is given by

$$\hat{P}_C^P(\omega) = \frac{1}{\lambda_{\min}(\mathbf{B}^H(\omega)\hat{\mathbf{R}}^{-1}\mathbf{B}(\omega))} \tag{4.54}$$

where $\lambda_{\min}(\cdot)$ is the minimum eigenvalue operator. For each frequency ω the minimal eigenvalue and associated eigenvector of the linear system

$$\mathbf{B}^H(\omega)\hat{\mathbf{R}}^{-1}\mathbf{B}(\omega)\mathbf{k}_{\min} = \lambda_{\min}\mathbf{k}_{\min} \tag{4.55}$$

has to be calculated. The dimension of the Hermitian matrix $\mathbf{B}^H(\omega)\hat{\mathbf{R}}^{-1}\mathbf{B}(\omega) \in \mathbf{Mat}_{N_{pol}}(\mathbb{C})$ does not depend on the number of antennas p. The inverse matrix $\hat{\mathbf{R}}^{-1}$ exists if the noise term has a positive definite covariance matrix and $L \geq pN_{pol}$.

The unitary polarimetric scattering type $\mathbf{k}_{\min}$ permits to extract the physical behavior of the scatterer. The polarization combination represented by $\mathbf{k}_{\min}$ is optimal with respect to the Capon criterion. The frequency estimates $\hat{\boldsymbol{\omega}} = [\hat{\omega}_1, \ldots, \hat{\omega}_{N_s}]^T$ are given by the locations of the N_s maxima of the spectrum $\hat{P}_C^P$. The polarimetric reflectivity at frequency $\hat{\omega}_i$ is extracted by $\hat{\tau}_i = \hat{P}_C^P(\hat{\omega}_i)$.

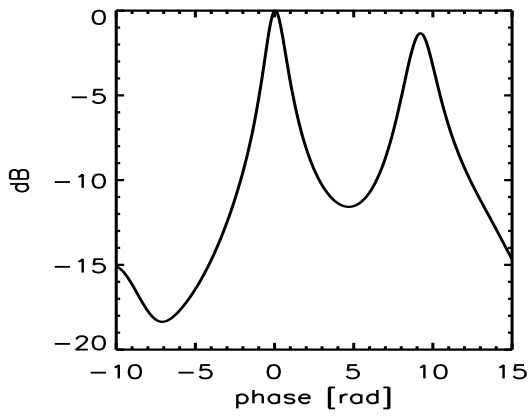

Figure 4.2: Polarimetric Capon spectrum comprising two sources.

The polarimetric Capon spectrum in figure 4.2 exhibits finer resolution and considerably suppressed sidelobes compared to the polarimetric beamforming spectrum in figure 4.1.

In the case of different phase centers, the polarimetric Capon spectrum is obtained as

$$\hat{P}_C^{P2}(\boldsymbol{\omega}) = \frac{1}{\lambda_{\min}(\mathbf{B}^H(\boldsymbol{\omega})\hat{\mathbf{R}}^{-1}\mathbf{B}(\boldsymbol{\omega}))} \tag{4.56}$$

The frequency estimates $\hat{\boldsymbol{\omega}}_{\boldsymbol{i}}$ are computed as the positions of the N_s highest peaks of the spectrum $\hat{P}_C^{P2}(\boldsymbol{\omega})$ that depends on N_{pol} parameters.

4.3.3 Polarimetric MUSIC Algorithm

The MUSIC technique has been proposed for sensors having polarization diversity on receive in [23, 100]. The adaptation of the MUSIC method to process polarimetric MB InSAR data is elaborated by following the argumentation in subsection 3.3.3 for deriving the standard MUSIC algorithm.

Like in subsection 3.3.3, the returned signal $\mathbf{y}(l) \in \mathbb{C}^{\tilde{p}}$ with $\tilde{p} = pN_{pol}$ is modeled as

$$\mathbf{y}(l) = \sum_{i=1}^{N_s} s_i(l)\mathbf{b}(\omega_i, \mathbf{k}_i) + \mathbf{n}(l). \tag{4.57}$$

The MBPI steering vectors $\mathbf{b}(\omega_i, \mathbf{k}_i)$ are supposed to be linearly independent with $N_s < \tilde{p}$.

Let $\lambda_1 \geq \cdots \geq \lambda_{\tilde{p}}$ be the eigenvalues of the covariance matrix $\mathbf{R}$ in nonincreasing order. Let $(\mathbf{f}_1, \ldots, \mathbf{f}_{N_s})$ denote the orthonormal eigenvectors related to $(\lambda_1, \ldots, \lambda_{N_s})$ and $(\mathbf{g}_1, \ldots, \mathbf{g}_{\tilde{p}-N_s})$ the orthonormal eigenvectors associated with $(\lambda_{N_s+1}, \ldots, \lambda_{\tilde{p}})$. Define the matrices $\mathbf{F} = [\mathbf{f}_1, \ldots, \mathbf{f}_{N_s}] \in$

$\mathbf{Mat}_{\tilde{p},N_s}(\mathbb{C})$ and $\mathbf{G} = [\mathbf{g}_1, \ldots, \mathbf{g}_{\tilde{p}-N_s}] \in \mathbf{Mat}_{\tilde{p},\tilde{p}-N_s}(\mathbb{C})$ of eigenvectors that span the signal and the noise subspace, respectively.

The main result in developing the polarimetric MUSIC algorithm can be formulated as follows:

The true frequency values $\{\omega_i\}_{i=1}^{N_s}$ with the associated scattering mechanisms $\{\mathbf{k}_i\}_{i=1}^{N_s}$ are the only solutions of the equation

$$\mathbf{b}^H(\omega, \mathbf{k})\mathbf{G}\mathbf{G}^H\mathbf{b}(\omega, \mathbf{k}) = 0. \tag{4.58}$$

Employing the fundamental conclusion (4.58), the polarimetric spectral MUSIC method is stated in the following way: First, the sample covariance matrix $\hat{\mathbf{R}}$ is computed according to equation (4.13), subsection 4.1.1. The eigendecomposition of $\hat{\mathbf{R}}$ produces the eigenvalues $\hat{\lambda}_1 \geq \cdots \geq \hat{\lambda}_{\tilde{p}}$ and the eigenvectors $(\hat{\mathbf{f}}_1, \ldots, \hat{\mathbf{f}}_{N_s})$ and $(\hat{\mathbf{g}}_1, \ldots, \hat{\mathbf{g}}_{\tilde{p}-N_s})$ that generate the signal and noise subspace, respectively. By means of the matrices $\hat{\mathbf{F}} = [\hat{\mathbf{f}}_1, \ldots, \hat{\mathbf{f}}_{N_s}] \in \mathbf{Mat}_{\tilde{p},N_s}(\mathbb{C})$ and $\hat{\mathbf{G}} = [\hat{\mathbf{g}}_1, \ldots, \hat{\mathbf{g}}_{\tilde{p}-N_s}] \in \mathbf{Mat}_{\tilde{p},\tilde{p}-N_s}(\mathbb{C})$, the pseudo-spectrum of the polarimetric MUSIC method is

$$\hat{P}_{MU}^P(\omega) = \frac{1}{\lambda_{\min}(\mathbf{B}^H(\omega)\hat{\mathbf{G}}\hat{\mathbf{G}}^H\mathbf{B}(\omega))}. \tag{4.59}$$

For each frequency ω the minimum eigenvalue and its eigenvector of the linear system

$$\mathbf{B}^H(\omega)\hat{\mathbf{G}}\hat{\mathbf{G}}^H\mathbf{B}(\omega)\mathbf{k}_{\min} = \lambda_{\min}\mathbf{k}_{\min} \tag{4.60}$$

is calculated. The dimension of the Hermitian matrix $\mathbf{B}^H(\omega)\hat{\mathbf{G}}\hat{\mathbf{G}}^H\mathbf{B}(\omega) \in \mathbf{Mat}_{N_{pol}}(\mathbb{C})$ only depends on the polarization number N_{pol} and is not a function of the number of sensors p. The minimum eigenvector $\mathbf{k}_{\min}, \|\mathbf{k}_{\min}\|_2 = 1$, can be regarded as a polarimetric scattering mechanism permitting to determine the physical features of the target. It specifies the optimum polarization combination in terms of the polarimetric MUSIC algorithm.

The frequency estimates $\hat{\boldsymbol{\omega}} = [\hat{\omega}_1, \ldots, \hat{\omega}_{N_s}]^T$ correspond to the locations of the N_s maxima of the pseudo-spectrum $\hat{P}_{MU}^P(\omega)$. The matrix in (4.60) must be nonsingular, otherwise $\lambda_{\min} = 0$, the spectrum (4.59) is infinite, and the spatial frequencies cannot be determined. A necessary criterion for the linear system having full rank is

$$\tilde{p} \geq N_s + N_{pol}, \tag{4.61}$$

i.e., the dimension of the noise subspace must be at least N_{pol}, $\text{rank}(\hat{\mathbf{G}}) \geq N_{pol}$. For $\tilde{p} - N_s > N_s$ the computation cost of the polarimetric MUSIC method can be reduced by using the matrix $\mathbf{I} - \hat{\mathbf{F}}\hat{\mathbf{F}}^H \in \mathbf{Mat}_{\tilde{p},N_s}(\mathbb{C})$ in place of $\hat{\mathbf{G}}\hat{\mathbf{G}}^H \in \mathbf{Mat}_{\tilde{p},\tilde{p}-N_s}(\mathbb{C})$ in equation (4.59).

It is apparent in figure 4.3 that the polarimetric MUSIC algorithm produces narrower spectral peaks and reduced leakage than polarimetric beamforming (figure 4.1) and polarimetric Capon (figure 4.2).

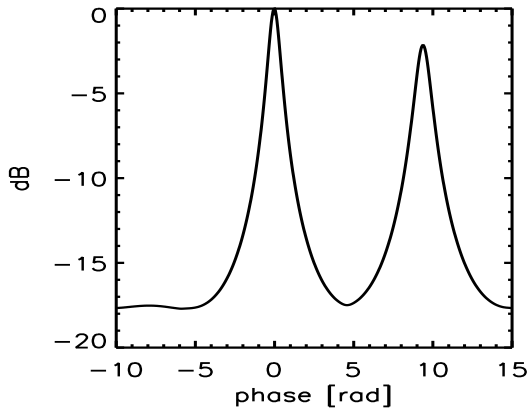

Figure 4.3: Polarimetric MUSIC pseudo-spectrum including two sources.

To generalize the polarimetric MUSIC method to the case of stochastic data the MBPI steering vector $\mathbf{b}(\boldsymbol{\omega}, \mathbf{k}) \in \mathbb{C}^{\tilde{p}}$ with $\boldsymbol{\omega} = [\omega_1, \ldots, \omega_{N_{pol}}]^T$ replaces the deterministic steering vector $\mathbf{b}(\omega, \mathbf{k}) \in \mathbb{C}^{\tilde{p}}$. The reasoning is the same as in the deterministic scenario and leads to the stochastic polarimetric MUSIC pseudo-spectrum

$$\hat{P}_{MU}^{P2}(\boldsymbol{\omega}) = \frac{1}{\lambda_{\min}(\mathbf{B}^H(\boldsymbol{\omega})\hat{\mathbf{G}}\hat{\mathbf{G}}^H\mathbf{B}(\boldsymbol{\omega}))}. \tag{4.62}$$

The frequency estimates $\hat{\boldsymbol{\omega}}_{\boldsymbol{i}}$ are calculated as the locations of the N_s largest peaks of the pseudo-spectrum $\hat{P}_{MU}^{P2}(\boldsymbol{\omega})$ that depends on N_{pol} parameters.

4.3.4 Polarimetric Least-Squares Method

To extend the least-squares method introduced in subsection 3.3.4 to the polarimetric MB InSAR scenario, the single polarization MB InSAR steering vector $\mathbf{a}(\omega)$ is substituted by the MBPI steering vector $\mathbf{b}(\omega, \mathbf{k})$. This implies that the spatial frequencies $\{\omega_i\}_{i=1}^{N_s}$ and the scattering mechanisms $\{\mathbf{k}_i\}_{i=1}^{N_s}$ have to be retrieved beforehand using nonparametric algorithms such as polarimetric beamforming and Capon or model-based approaches like polarimetric MUSIC.

The unknown polarimetric reflectivities $\{\tau_i\}_{i=1}^{N_s}$ are extracted by minimizing the linear least-squares cost function

$$Q_L^P(\boldsymbol{\beta}(1), \ldots, \boldsymbol{\beta}(L)) = \frac{1}{L}\sum_{l=1}^{L}\left\|\mathbf{y}(l) - \sum_{i=1}^{N_s}\beta_i(l)\mathbf{b}(\omega_i, \mathbf{k}_i)\right\|_2^2 \tag{4.63}$$

where $\boldsymbol{\beta}(l) = [\beta_1(l), \ldots, \beta_{N_s}(l)]^T \in \mathbb{C}^{N_s}$ are the amplitudes of the complex sinusoids of the lth look, $l = 1, \ldots, L$. Minimizing this relation with respect

to $\boldsymbol{\beta}(l)$ leads to the least-squares solution

$$\hat{\boldsymbol{\beta}}(l) = \left(\mathbf{D}^H\mathbf{D}\right)^{-1}\mathbf{D}^H\mathbf{y}(l) \tag{4.64}$$

with the MBPI steering matrix $\mathbf{D} = [\mathbf{b}(\omega_1, \mathbf{k}_1), \ldots, \mathbf{b}(\omega_{N_s}, \mathbf{k}_{N_s})] \in \mathbf{Mat}_{\tilde{p},N_s}(\mathbb{C})$. Since the frequencies ω_i and the scattering vectors $\mathbf{k}_i$ are unknown, the steering matrix $\mathbf{D}$ is replaced by

$$\hat{\mathbf{D}} = [\mathbf{b}(\hat{\omega}_1, \hat{\mathbf{k}}_1), \ldots, \mathbf{b}(\hat{\omega}_{N_s}, \hat{\mathbf{k}}_{N_s})] \in \mathbf{Mat}_{\tilde{p},N_s}(\mathbb{C}), \tag{4.65}$$

utilizing the estimates of the frequencies $\{\hat{\omega}_i\}_{i=1}^{N_s}$ and the reflection mechanisms $\hat{\mathbf{k}}_i$. Now, the complex amplitudes are estimated by

$$\hat{\boldsymbol{\beta}}(l) = \left(\hat{\mathbf{D}}^H\hat{\mathbf{D}}\right)^{-1}\hat{\mathbf{D}}^H\mathbf{y}(l). \tag{4.66}$$

Finally, the polarimetric reflectivities are determined by

$$\hat{\tau}_i = \frac{1}{L}\sum_{l=1}^{L}|\hat{\beta}_i(l)|^2, \qquad i = 1, \ldots, N_s. \tag{4.67}$$

The polarimetric LS method can be employed to enhance the polarimetric reflectivity estimation accuracy of the nonparametric techniques such as polarimetric beamforming and Capon. Furthermore, the frequencies and scattering mechanisms can be first estimated by the polarimetric MUSIC algorithm to subsequently retrieve the polarimetric reflectivities by the LS approach.

It is straightforward to adapt the least-squares method to the case of polarimetric stochastic signals.

4.3.5 Polarimetric M-RELAX

The M-RELAX algorithm presented in subsection 3.3.5 is adapted to the polarimetric MB InSAR configuration by replacing the single polarization MB InSAR steering vector $\mathbf{a}(\omega)$ with the MBPI steering vector $\mathbf{b}(\omega, \mathbf{k})$.

The polarimetric multilook nonlinear least-squares (NLLS) cost function is defined as

$$Q_L^P(\boldsymbol{\beta}(1), \ldots, \boldsymbol{\beta}(L), \boldsymbol{\omega}, \mathbf{k}_{vec}) = \frac{1}{L}\sum_{l=1}^{L}\left\|\mathbf{y}(l) - \sum_{i=1}^{N_s}\beta_i(l)\mathbf{b}(\omega_i, \mathbf{k}^i)\right\|_2^2 \tag{4.68}$$

where L is the number of looks and $l = 1, \ldots, L$. The polarimetric MB InSAR observations are $\mathbf{y}(l) \in \mathbb{C}^{\tilde{p}}$, the spatial frequencies $\boldsymbol{\omega} = [\omega_1, \ldots, \omega_{N_s}] \in \mathbb{R}^{N_s}$, the scattering mechanisms $\mathbf{k}_{vec} = [(\mathbf{k}^1)^T, \ldots, (\mathbf{k}^{N_s})^T]^T \in \mathbb{C}^{N_s N_{pol}}$, and the amplitudes $\boldsymbol{\beta}(l) = [\beta_1(l), \ldots, \beta_{N_s}(l)]^T \in \mathbb{C}^{N_s}$.

The polarimetric NLLS function depends on the amplitudes, frequencies, and scattering mechanisms, whereas the linear least-squares cost function (4.63) in subsection 4.3.4 only depends on the complex amplitudes.

The following definitions are necessary to state the polarimetric M-RELAX algorithm: The corrected data vector is

$$\mathbf{y}_m(l) = \mathbf{y}(l) - \sum_{i=1, i\neq m}^{N_s} \hat{\beta}_i(l)\mathbf{b}(\hat{\omega}_i, \hat{\mathbf{k}}^i), \qquad l = 1, \ldots, L \tag{4.69}$$

where the parameters $\{\hat{\omega}_i, \hat{\beta}_i, \hat{\mathbf{k}}^i\}_{i=1, i\neq m}^{N_s}$ are supposed to be known. Substituting $\mathbf{y}_m(l)$ for $\mathbf{y}(l)$, the error function (4.68) is minimized with respect to $\omega_m, \mathbf{k}^m$, and β_m. Employing the sample covariance matrix $\hat{\mathbf{R}}_m \in \mathbf{Mat}_{\tilde{p}}(\mathbb{C})$ of $\{\mathbf{y}_m(l)\}_{l=1}^L$, the frequency and polarimetric scattering vector estimates are obtained as

$$(\hat{\omega}_m, \hat{\mathbf{k}}^m) = \arg\max_{(\omega, \mathbf{k})} \{\mathbf{b}^H(\omega, \mathbf{k})\hat{\mathbf{R}}_m\mathbf{b}(\omega, \mathbf{k})\}. \tag{4.70}$$

This maximization problem is solved by using relation (4.8): The frequency $\hat{\omega}_m$ is determined through computing the maximum eigenvalues of the Hermitian matrix $\mathbf{B}^H(\omega)\hat{\mathbf{R}}_m\mathbf{B}(\omega) \in \mathbf{Mat}_{N_{pol}}(\mathbb{C})$

$$\hat{\omega}_m = \arg\max_{\omega} \lambda_{\max}(\mathbf{B}^H(\omega)\hat{\mathbf{R}}_m\mathbf{B}(\omega)). \tag{4.71}$$

The associated maximum eigenvector of the linear system

$$\mathbf{B}^H(\omega)\hat{\mathbf{R}}_m\mathbf{B}(\omega)\mathbf{k}_{\max} = \lambda_{\max}\mathbf{k}_{\max}. \tag{4.72}$$

provides the scattering mechanism estimate $\hat{\mathbf{k}}^m = \mathbf{k}_{\max}$. It represents the polarization combination that is optimal with regard to M-RELAX and permits a polarimetric analysis to extract the physical characteristics of the reflector. Equation (4.71) for the frequency estimate is similar to the beamforming spectrum (4.44) of the data $\{\mathbf{y}_m(l)\}_{l=1}^L$ except for normalization. The amplitude estimate $\beta_m(l)$ is extracted as

$$\hat{\beta}_m(l) = \frac{\mathbf{b}^H(\hat{\omega}_m, \hat{\mathbf{k}}^m)\mathbf{y}_m(l)}{p}. \tag{4.73}$$

The polarimetric M-RELAX algorithm can be sketched as follows:

Step (1)
Assume $N_s = 1$. Estimate the frequency $\hat{\omega}_1$, the scattering vector $\hat{\mathbf{k}}_1$, and the amplitudes $\{\hat{\beta}_1(l)\}_{l=1}^L$ by means of formulas (4.70) and (4.73), respectively, using the samples $\{\mathbf{y}(l)\}_{l=1}^L$.

Step (2)

Assume $N_s = 2$. Calculate the corrected data vector $\{\mathbf{y}_2(l)\}_{l=1}^{L}$ by inserting $\hat{\omega}_1$, $\hat{\mathbf{k}}_1$, and $\{\hat{\beta}_1(l)\}_{l=1}^{L}$ of step (1) in (4.69). Determine the frequency $\hat{\omega}_2$, the scattering vector $\hat{\mathbf{k}}_2$, and the amplitude $\{\hat{\beta}_2(l)\}_{l=1}^{L}$ estimates via (4.70) and (4.73), respectively, from $\{\mathbf{y}_2(l)\}_{l=1}^{L}$.
Calculate the corrected data $\{\mathbf{y}_1(l)\}_{l=1}^{L}$ from (4.69) where $\hat{\omega}_2$, $\hat{\mathbf{k}}_2$, and $\{\hat{\beta}_2(l)\}_{l=1}^{L}$ of substep 1 are employed. Redetermine $\hat{\omega}_1$, $\hat{\mathbf{k}}_1$, and $\{\hat{\beta}_1(l)\}_{l=1}^{L}$ from $\{\mathbf{y}_1(l)\}_{l=1}^{L}$ through equations (4.70) and (4.73).
Iterate these two substeps until the convergence condition explained below is satisfied.

Step (3)
Assume $N_s = 3$. Calculate $\{\mathbf{y}_3(l)\}_{l=1}^{L}$ by inserting $\hat{\omega}_i$, $\hat{\mathbf{k}}_i$, and $\{\hat{\beta}_i(l)\}_{l=1}^{L}$ for $i = 1, 2$ of step (2) in (4.69). Determine $\hat{\omega}_3$, $\hat{\mathbf{k}}_3$ and $\{\hat{\beta}_3(l)\}_{l=1}^{L}$ via (4.70) and (4.73), respectively, utilizing $\{\mathbf{y}_3(l)\}_{l=1}^{L}$.
Calculate $\{\mathbf{y}_1(l)\}_{l=1}^{L}$ by inserting $\hat{\omega}_i$, $\hat{\mathbf{k}}_i$, and $\{\hat{\beta}_i(l)\}_{l=1}^{L}$ for $i = 2, 3$ into (4.69). Redetermine $\hat{\omega}_1$, $\hat{\mathbf{k}}_1$, and $\{\hat{\beta}_1(l)\}_{l=1}^{L}$.
Calculate $\{\mathbf{y}_2(l)\}_{l=1}^{L}$ by inserting $\hat{\omega}_i$, $\hat{\mathbf{k}}_i$, and $\{\hat{\beta}_i(l)\}_{l=1}^{L}$ for $i = 1, 3$ into (4.69). Redetermine $\hat{\omega}_2$, $\hat{\mathbf{k}}_2$, and $\{\hat{\beta}_2(l)\}_{l=1}^{L}$.
Iterate these three substeps until the termination criterion is met.

Remaining steps.
Repeat this procedure until the assumed or estimated number of sources N_s is reached.

The relative change of the cost function (4.68) is chosen as the termination criterion for the iterative process: If it is less than a user given threshold ε, the iteration is stopped.

The polarimetric M-RELAX method estimates the frequencies $\{\hat{\omega}_i\}_{i=1}^{N_s}$, the optimal scattering mechanisms $\{\hat{\mathbf{k}}_i\}_{i=1}^{N_s}$, and the complex amplitudes $\{\hat{\beta}_i(l)\}_{i=1}^{N_s}, l = 1, \ldots, L$. Finally, the polarimetric reflectivity is retrieved by

$$\hat{\tau}_i = \frac{1}{L}\sum_{l=1}^{L} |\hat{\beta}_i(l)|^2, \qquad i = 1, \ldots, N_s. \tag{4.74}$$

The extension of the M-RELAX algorithm to process stochastic MB POL-InSAR observations is evident.

4.4 Polarimetric ML Joint Detection and Estimation

The extension of the maximum likelihood estimator for solving the joint detection-estimation problem to MB polarimetric interferometric SAR ob-

servations is introduced in this section. These techniques have been developed for the special case of polarization diversity in the receive channel in [118]. As the reasoning for deriving these algorithms is similar to the scenario of MB InSAR measurements with one single polarization presented in section 3.4, the polarimetric ML estimator is formulated while emphasizing the differences between the two modes.

The received signal $\mathbf{y}(l) \in \mathbb{C}^{\tilde{p}}$ with $\tilde{p} = pN_{pol}$ is modeled as

$$\mathbf{y}(l) = \sum_{i=1}^{N_s} s_i(l)\mathbf{b}(\omega_i, \mathbf{k}^i) + \mathbf{n}(l). \tag{4.75}$$

The statistical properties of the signals $\{\mathbf{s}(l)\}_{l=1}^{L}$ where $\mathbf{s}(l) = [s_1(l), \ldots, s_{N_s}(l)]^T$, the additive noise $\{\mathbf{n}(l)\}_{l=1}^{L}$, and the returned signal $\{\mathbf{y}(l)\}_{l=1}^{L}$ are specified in subsection 3.4.1. The MB polarimetric interferometric steering vectors $\mathbf{b}(\omega_i, \mathbf{k}^i)$ with the spatial frequency ω_i and the scattering mechanism $\mathbf{k}^i = [k_1^i, \ldots, k_{N_{pol}}^i]^T$ of the ith source are assumed to be linearly independent and $N_s < \tilde{p}$.

The closed-form matrix expression of the polarimetric MB InSAR signal with N_s sources is

$$\mathbf{y}(l) = \mathbf{D}(\boldsymbol{\omega}, \mathbf{k}_{vec})\mathbf{s}(l) + \mathbf{n}(l) \tag{4.76}$$

where the the matrix $\mathbf{D}(\boldsymbol{\omega}, \mathbf{k}_{vec}) \in \mathbf{Mat}_{\tilde{p},N_s}(\mathbb{C})$ contains the MBPI steering vectors $\mathbf{b}(\omega_i, \mathbf{k}^i)$

$$\mathbf{D}(\boldsymbol{\omega}, \mathbf{k}_{vec}) = [\mathbf{b}(\omega_1, \mathbf{k}^1), \ldots, \mathbf{b}(\omega_{N_s}, \mathbf{k}^{N_s})] \tag{4.77}$$

with the unknown spatial frequencies $\boldsymbol{\omega} = [\omega_1, \ldots, \omega_{N_s}] \in [-\pi, \pi)^{N_s}$, and the unknown scattering mechanisms

$$\mathbf{k}_{vec} = [(\mathbf{k}^1)^T, \ldots, (\mathbf{k}^{N_s})^T]^T \in \mathbb{C}^{N_s N_{pol}}. \tag{4.78}$$

This matrix can be rewritten as

$$\mathbf{D}(\boldsymbol{\omega}, \mathbf{k}_{vec}) = \mathbf{C}(\boldsymbol{\omega})\mathbf{K} \tag{4.79}$$

where the matrix $\mathbf{C}(\boldsymbol{\omega}) \in \mathbf{Mat}_{\tilde{p},N_s N_{pol}}(\mathbb{C})$ is given by

$$\mathbf{C}(\boldsymbol{\omega}) = [\mathbf{B}(\omega_1), \ldots, \mathbf{B}(\omega_{N_s})] \tag{4.80}$$

with $\mathbf{B}(\omega_i) \in \mathbf{Mat}_{\tilde{p},N_{pol}}(\mathbb{C})$ defined in equation (4.9). The matrix $\mathbf{K} \in \mathbf{Mat}_{N_s N_{pol},N_s}(\mathbb{C})$ comprises the scattering mechanisms

$$\mathbf{K} = \begin{bmatrix} \mathbf{k}^1 & \mathbf{0} & & \\ \mathbf{0} & \mathbf{k}^2 & & \\ & \mathbf{0} & \ddots & \\ & & & \mathbf{k}^{N_s} \end{bmatrix}. \tag{4.81}$$

The task is to estimate the number of sources N_s, the spatial frequencies $\omega_1, \ldots, \omega_{N_s}$, and the polarimetric scattering types $\mathbf{k}^1, \ldots, \mathbf{k}^{N_s}$.

Let $k \in \{0, 1, \ldots, \tilde{p} - 1\}$ be the assumed number of sources. Using the abbreviation $\boldsymbol{\theta} = (\boldsymbol{\omega}, \mathbf{k}_{vec})$, the data model is

$$\mathbf{y}(l) = \mathbf{D}(\boldsymbol{\theta}(k))\mathbf{s}(l) + \mathbf{n}(l) \tag{4.82}$$

with the MBPI steering vector matrix $\mathbf{D}(\boldsymbol{\theta}(k)) \in \mathbf{Mat}_{\tilde{p},k}(\mathbb{C})$

$$\mathbf{D}(\boldsymbol{\theta}(k)) = [\mathbf{b}(\omega_1, \mathbf{k}^1), \ldots, \mathbf{b}(\omega_k, \mathbf{k}^k)]. \tag{4.83}$$

The received signal $\mathbf{y}(l)$ can be partitioned into $\mathbf{y_s}(l) \in \mathbb{C}^k$ and $\mathbf{y_n}(l) \in \mathbb{C}^{\tilde{p}-k}$ associated with the signal and noise subspace, respectively. The orthogonal projection on the signal subspace $\mathbf{P}_{\mathbf{D}(\boldsymbol{\theta}(k))} \in \mathbf{Mat}_{\tilde{p}}(\mathbb{C})$ is given by

$$\mathbf{P}_{\mathbf{D}(\boldsymbol{\theta}(k))} = \mathbf{D}(\boldsymbol{\theta}(k)) \left[\mathbf{D}^H(\boldsymbol{\theta}(k))\mathbf{D}(\boldsymbol{\theta}(k))\right]^{-1} \mathbf{D}^H(\boldsymbol{\theta}(k)) \tag{4.84}$$

and the orthogonal projection on the noise subspace $\mathbf{P}^{\perp}_{\mathbf{D}(\boldsymbol{\theta}(k))} \in \mathbf{Mat}_{\tilde{p}}(\mathbb{C})$ by

$$\mathbf{P}^{\perp}_{\mathbf{D}(\boldsymbol{\theta}(k))} = \mathbf{I} - \mathbf{P}_{\mathbf{D}(\boldsymbol{\theta}(k))}. \tag{4.85}$$

Similarly to the derivation of the single polarization MB InSAR combined detection-estimation in subsection 3.4.2, the code length necessary to encode the noise subspace components $\{\mathbf{y_n}(l)\}_{l=1}^{L}$ assuming that $\boldsymbol{\theta}(k)$ is given results in

$$\mathscr{L}\{\mathbf{y_n}(l) \,|\, \boldsymbol{\theta}(k)\} = L \log \det[\hat{\sigma}^2(\boldsymbol{\theta}(k))\mathbf{I}] + L(\tilde{p} - k) + g(1) \tag{4.86}$$

where constant terms independent of k are neglected.

Since the number of free parameters in the signal data covariance matrix $\mathbf{R_s}(\boldsymbol{\theta}(k)) \in \mathbf{Mat}_k(\mathbb{C})$ is k^2, the code length of the signal subspace components is obtained as

$$\mathscr{L}\{\mathbf{y_s}(l) \,|\, \boldsymbol{\theta}(k)\} = L \log \det[\hat{\mathbf{R}}_{\mathbf{s}}(\boldsymbol{\theta}(k))] + Lk + g(k^2) \tag{4.87}$$

where constant quantities are omitted and $\hat{\mathbf{R}}_{\mathbf{s}}(\boldsymbol{\theta}(k)) \in \mathbf{Mat}_k(\mathbb{C})$ is the ML estimate of $\mathbf{R_s}(\boldsymbol{\theta}(k))$.

The total code length required to encode the noise and signal subspace components is the sum of (4.86) and (4.87):

$$\mathscr{L}\{\mathbf{y_n}(l), \mathbf{y_s}(l) \,|\, \boldsymbol{\theta}(k)\} = L \log \left[\det[\hat{\mathbf{R}}_{\mathbf{s}}(\boldsymbol{\theta}(k))] \det[\hat{\sigma}^2(\boldsymbol{\theta}(k))\mathbf{I}]\right] + g(k^2). \tag{4.88}$$

Using equation (4.88), the unknown parameter vector $\boldsymbol{\theta}(k)$ is estimated as

$$\hat{\boldsymbol{\theta}}(k) = \arg \min_{\boldsymbol{\theta}(k)} \det[\hat{\mathbf{R}}_{\mathbf{s}}(\boldsymbol{\theta}(k))] \det[\hat{\sigma}^2(\boldsymbol{\theta}(k))\mathbf{I}]. \tag{4.89}$$

To evaluate the equation (4.89) and calculate the estimate $\hat{\boldsymbol{\theta}}(k)$, it is reformulated by means of the abbreviation $\mathbf{D} = \mathbf{D}(\boldsymbol{\theta}(k))$, keeping in mind that the matrix $\mathbf{D}$ includes both spatial frequency and polarization information, in the following ways:

The first formulation of the estimate (4.89) can be stated as

$$\hat{\boldsymbol{\theta}}(k) = \arg\min_{\boldsymbol{\theta}(k)} \det[\mathbf{P_D}\hat{\mathbf{R}}\mathbf{P_D} + \frac{1}{p-k}\mathrm{tr}[\mathbf{P}_\mathbf{D}^\perp\hat{\mathbf{R}}]\mathbf{P}_\mathbf{D}^\perp]. \tag{4.90}$$

with the sample covariance matrix $\hat{\mathbf{R}}$.

Let $l_1^{\mathbf{s}}(\boldsymbol{\theta}(k)) \geq \cdots \geq l_k^{\mathbf{s}}(\boldsymbol{\theta}(k))$ be the nonzero eigenvalues of the Hermitian matrix $\mathbf{P_D}\hat{\mathbf{R}}\mathbf{P_D}$ and $l_1^{\mathbf{n}}(\boldsymbol{\theta}(k)) \geq \cdots \geq l_{\tilde{p}-k}^{\mathbf{n}}(\boldsymbol{\theta}(k))$ be the nonzero eigenvalues of the Hermitian matrix $\mathbf{P}_\mathbf{D}^\perp\hat{\mathbf{R}}\mathbf{P}_\mathbf{D}^\perp$. Then the second expression of the estimate (4.89) can be written as

$$\hat{\boldsymbol{\theta}}(k) = \arg\min_{\boldsymbol{\theta}(k)} \left(\prod_{i=1}^{k} l_i^{\mathbf{s}}(\boldsymbol{\theta}(k))\right)\left(\frac{1}{\tilde{p}-k}\sum_{i=1}^{\tilde{p}-k} l_i^{\mathbf{n}}(\boldsymbol{\theta}(k))\right)^{\tilde{p}-k}. \tag{4.91}$$

The nonlinear, nonconvex, and high-dimensional optimization problem of calculating the ML estimate (4.89) can be solved by alternating maximization [117] using (4.91).

The degrees of freedom of $\boldsymbol{\theta}(k)$ are obtained as kN_{par}, where $N_{par} = 2N_{pol} - 1$ for $1 \leq N_{pol} \leq 4$. The values of N_{par} are summarized in table 4.2. Hence, for polarimetric MB InSAR measurements the total number of unknown free parameters is:

$$\eta(k) = k(k + N_{par}). \tag{4.92}$$

Finally, the number of sources is estimated by

$$\hat{N}_s = \arg\min_{k\in\{0,\ldots,\tilde{p}-1\}} \mathrm{ITC}_{ML}(k) \tag{4.93}$$

where the information theoretic criterion estimator is:

$$\mathrm{ITC}_{ML}(k) = L\log\left[\left(\prod_{i=1}^{k} l_i^{\mathbf{s}}(\hat{\boldsymbol{\theta}}_k)\right)\left(\frac{1}{\tilde{p}-k}\sum_{i=1}^{\tilde{p}-k} l_i^{\mathbf{n}}(\hat{\boldsymbol{\theta}}_k)\right)^{\tilde{p}-k}\right] + g(k(k+N_{par})). \tag{4.94}$$

Selecting the Akaike bias correction term $g(\eta(k)) = \eta(k)$ yields the AIC estimator [1, 2]

$$\mathrm{AIC}_{ML}(k) = L\log\left[\left(\prod_{i=1}^{k} l_i^{\mathbf{s}}(\hat{\boldsymbol{\theta}}_k)\right)\left(\frac{1}{\tilde{p}-k}\sum_{i=1}^{\tilde{p}-k} l_i^{\mathbf{n}}(\hat{\boldsymbol{\theta}}_k)\right)^{\tilde{p}-k}\right] + k(k+N_{par}) \tag{4.95}$$

that is inconsistent and overestimates asymptotically the number of signals. Using the penalty function $g(\eta(k)) = \frac{1}{2}\eta(k)\log L$, the minimum description length [87, 101]

$$\mathrm{MDL}_{ML}(k) = L\log\left[\left(\prod_{i=1}^{k} l_i^{\mathbf{s}}(\hat{\boldsymbol{\theta}}_k)\right)\left(\frac{1}{\tilde{p}-k}\sum_{i=1}^{\tilde{p}-k} l_i^{\mathbf{n}}(\hat{\boldsymbol{\theta}}_k)\right)^{\tilde{p}-k}\right] + \frac{1}{2}k(k+N_{par})\log L \tag{4.96}$$

is stronlgy consistent [112, 116]. By choosing $g(\eta(k)) = \eta(k)C_L$ with

$$\lim_{L\to\infty}\frac{C_L}{L} = 0 \tag{4.97}$$

and

$$\lim_{L\to\infty}\frac{C_L}{\log(\log L)} = \infty, \tag{4.98}$$

the efficient detection criterion [3, 116]

$$\mathrm{EDC}_{ML}(k) = L\log\left[\left(\prod_{i=1}^{k} l_i^{\mathbf{s}}(\hat{\boldsymbol{\theta}}_k)\right)\left(\frac{1}{\tilde{p}-k}\sum_{i=1}^{\tilde{p}-k} l_i^{\mathbf{n}}(\hat{\boldsymbol{\theta}}_k)\right)^{\tilde{p}-k}\right] + k(k+N_{par})C_L \tag{4.99}$$

is stronly consistent as well [3, 116].

The Hermitian matrices $\mathbf{P_D}\hat{\mathbf{R}}\mathbf{P_D} \in \mathbf{Mat}_{\tilde{p}}(\mathbb{C})$ and $\mathbf{P_D^{\perp}}\hat{\mathbf{R}}\mathbf{P_D^{\perp}} \in \mathbf{Mat}_{\tilde{p}}(\mathbb{C})$ are by construction ill-conditioned with [41, 102]

$$\kappa_2(\mathbf{P_D}\hat{\mathbf{R}}\mathbf{P_D}) = \frac{\lambda_{\max}(\mathbf{P_D}\hat{\mathbf{R}}\mathbf{P_D})}{\lambda_{\min}(\mathbf{P_D}\hat{\mathbf{R}}\mathbf{P_D})} = \infty \tag{4.100}$$

and

$$\kappa_2(\mathbf{P_D^{\perp}}\hat{\mathbf{R}}\mathbf{P_D^{\perp}}) = \frac{\lambda_{\max}(\mathbf{P_D^{\perp}}\hat{\mathbf{R}}\mathbf{P_D^{\perp}})}{\lambda_{\min}(\mathbf{P_D^{\perp}}\hat{\mathbf{R}}\mathbf{P_D^{\perp}})} = \infty. \tag{4.101}$$

Thus, in the estimator (4.91) the eigenvalues have to be calculated with care.

For $N_{pol} = 1$, the estimation-detection algorithm reduces to the technique for processing multibaseline InSAR observations with one single polarization detailed in section 3.4. The generalization to data with polarization diversity leads to $2 \leq N_{pol} \leq 4$. The adaptation to hybrid antenna constellations is straightforward. The extension of the ML estimator to analyze stochastic polarimetric MB InSAR measurements is obvious.

A difference between the polarimetric model order selection algorithm based on the covariance matrix (CM MOS) presented in section 4.2 and the MOS approach relying on the ML estimator (MLE MOS) developed in this section can be observed: The degrees of freedom of the MLE MOS (4.92) are a function of the number of parameters to be determined, i.e., the

dimension of the space of unknown parameters: In particular, it depends on the variable N_{par}, but does not depend on the number of sensors p. In contrast, the DoF of the CM MOS (4.33) depend both on the number of antennas and the polarization number N_{pol}, i.e., the dimension of the observation space $\tilde{p} = pN_{pol}$.

A fundamental discrepancy between the polarimetric ML estimator and the polarimetric methods to estimate the spatial frequencies like beamforming, Capon, MUSIC, and M-RELAX introduced in section 4.3 is as follows: The dimension of the linear system that has to be solved in the MLE (4.91) is $\tilde{p} = pN_{pol}$, i.e., it depends on both the number of antennas p and the polarization number N_{pol}. On the other hand, the dimension of the matrices that have to be computed for the polarimetric beamforming, Capon, MUSIC, and M-RELAX is invariably N_{pol} and independent of the number of sensors p.

4.5 Conclusions

In this chapter, array signal processing techniques have been generalized to the polarimetric multibaseline interferometric SAR scenario based on the following principle: In passive sensor systems, the antennas only receive the signals in diverse polarizations leading to two polarization channels. In contrast, in the context of SAR the sensors are active and both transmit the electromagnetic waves and receive the echo of the backscattered signals in polarimetric mode resulting in up to four polarization states. First, the signal models have been extended to take polarization diversity into account yielding the notion of the multibaseline polarimetric interferometric steering vector. It is a linear combination of four vectors each of them associated with one particular polarization.

The model order selection techniques have been adapted to estimate the number of sources from MB POL-InSAR measurements. Subsequently, the spectral estimation algorithms have been extended to the polarimetric multibaseline InSAR configuration. The adaptation to the polarimetric case not merely increases the number of observables, but particularly determines the optimal polarization combination for spatial frequency estimation. These polarimetric methods permit to retrieve the spatial frequencies, the associated optimal scattering vectors, and the polarimetric reflectivities. The optimal scattering mechanisms allow the examination of the reflector physical properties by analysis of their polarimetric behavior. The nonparametric beamforming and Capon algorithms have been generalized to the MB POL-InSAR scenario to extract the spatial frequencies, the corresponding optimal reflection mechanisms, and the polarimetric reflectivities. Model-based techniques possess generally better performance than nonparametric methods concerning resolution and sidelobe suppression. The superresolu-

tion polarimetric MUSIC and M-RELAX approaches have been conceived to determine the spatial frequency and the related scattering mechanism. The linear least-squares method and M-RELAX estimate the polarimetric reflectivity. Finally, the polarimetric maximum likelihood estimator has been introduced for solving the joint detection-estimation problem from MB POL-InSAR observations. These polarimetric spectral analysis techniques have been developed in their most general form: They can be employed in polarimetric MB InSAR configurations in all possible combinations. Their mathematical features have been explained in detail.

Chapter 5

Applications of Polarimetric Multibaseline InSAR Spectral Analysis Techniques

To demonstrate the performance of the spectral analysis techniques introduced in the two previous chapters, they are applied to fully polarimetric dual-baseline InSAR observations of an urban environment. After presenting the dataset, the number of backscattering sources is estimated by model order selection algorithms. Using single-baseline POL-InSAR measurements the scatterer height and reflection mechanisms are determined to produce a three-dimensional model of an urban scene. Subsequently, the building layover is analyzed by means of polarimetric dual-baseline interferometric SAR data. Finally, three-dimensional images are generated that include polarimetric information about the reflection processes.

5.1 Presentation of the Dataset

The proposed array signal processing methods are applied to fully polarimetric and repeat pass dual-baseline interferometric SAR images at L-band acquired on August 1st, 2000, over the city of Dresden in Germany by DLR's experimental SAR (E-SAR) system.

Figure 5.1 shows a Pauli color-coded POLSAR image of a large scene that includes buildings, vegetation, and surfaces as illustrated in the corresponding optical image in figure 5.2. The resolution of the SAR images is 2.2 m in range and 3.0 m in azimuth. The sensor flight direction is on the left hand side, i.e., far range is located on the right and near range on the left side. For the studied area, the incidence angle varies from $43\,^\circ$ to $48\,^\circ$. Polarimetric dual-baseline interferometric SAR measurements are available with a small baseline of about 10 m and a large baseline of around 40 m. The height of ambiguity ranges from 55 m to 73 m for the small baseline,

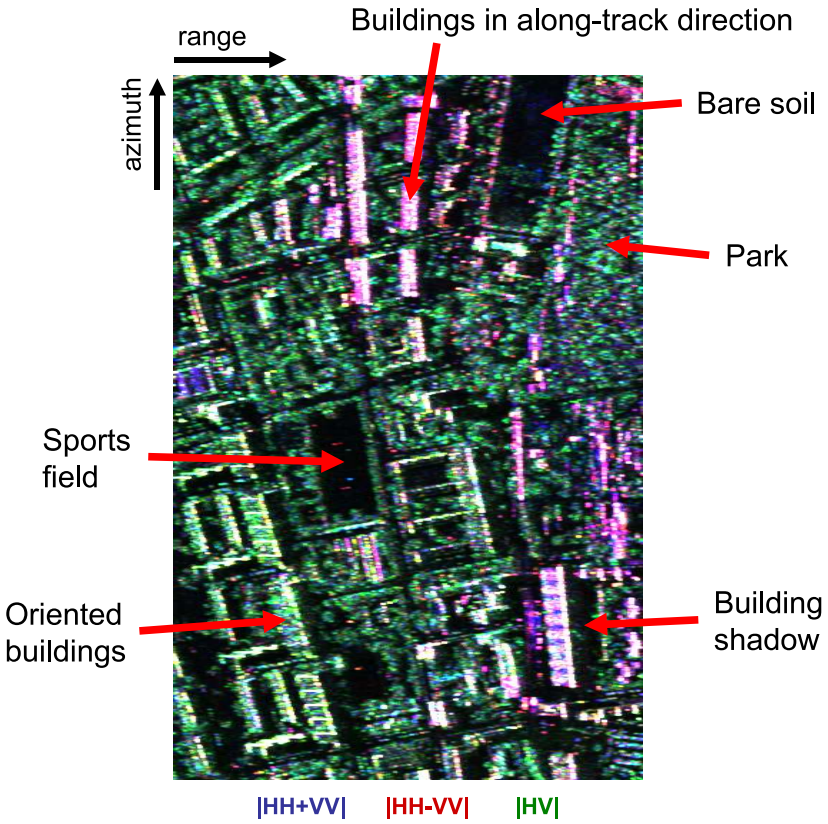

Figure 5.1: Pauli color-coded POLSAR image of the large urban scene.

and attains values between 14 m and 18 m for the large baseline.

The scene contains small edifices such as barracks shown in figure 5.3. As illustrated in figure 5.4, the large buildings consist of a maximum of a dozen floors resulting in building heights of more than 30 meters. The vegetation comprises trees, parks, and grassland (see figure 5.5). Figure 5.6 depicts surfaces like sports fields and bare soils.

5.2 Dual-baseline POL-InSAR Model Order Selection

The model order selection (MOS) methods are evaluated using fully polarimetric dual-baseline InSAR data [99] of the scene depicted in figure 5.1. First, the number of sources is determined by means of single polarization dual-baseline interferometric observations employing the MOS technique and EDC without diagonal loading (figure 5.7). The maximum number of detectable components is two. Bare soils and shadows that are generated

Figure 5.2: Optical image of the large urban scene (copyright Google Earth).

Figure 5.3: Optical image: Small buildings such as barracks (copyright G.S.).

Figure 5.4: Optical image: Large buildings (copyright G.S.).

Figure 5.5: Optical image: Vegetation including trees, parks, and grassland (copyright G.S.).

Figure 5.6: Optical image: Surfaces such as sport fields (copyright G.S.).

by buildings are partially assigned to the class of zero sources. Vegetated areas include one or two backscattering contributions, whereas the building layover is associated with the class containing two or more signal components.

Figure 5.8 depicts the estimation result with diagonal loading and loading factor $\delta = 10$. Diagonal loading reduces considerably the model order. The building shadow is now clearly identified as an area without a detected signal, just like some surfaces such as the smooth sports field. The building layover that comprises two or more backscattering sources is noticeably surrounded by resolution cells where only one component is present.

To compare single polarization and fully polarimetric InSAR MOS, the number of detected signal components is first restricted to two utilizing the polarimetric dual-baseline interferometric data (figure 5.9). Globally, the results of the single polarization and fully polarimetric estimation resemble quite strongly. Especially over man made objects the polarimetric MOS tends to estimate slighlty more reflecting sources than the single polarization approach and less over some vegetated areas.

To investigate the building layover in more detail a sub-area including edifices that are oriented in the sensor flight direction is selected. For display purposes, the maximum number of estimated sources is set to five. At the layover edges (figure 5.10), the model order is low with one or two signal

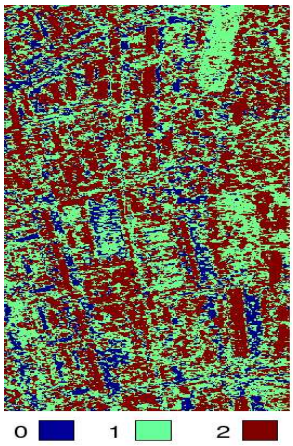

Figure 5.7: Single polarization dual-baseline InSAR MOS without diagonal loading.

components, reaching its maximum of five in the middle of the layover. Two-dimensional filtering causes a mixture of scattering mechanisms comprising single-bounce reflections from the ground, the wall, and the roof, double bounce from the ground-wall interaction and possible multipath phenomena. To limit the influence of two-dimensional 5×5 boxcar averaging, an adaptive filtering with a filter size of ten pixels is applied. It is evident (figure 5.11) that this preprocessing reduces the model order, in particular inside the layover.

5.3 Multibaseline POL-InSAR Height and Scattering Mechanism Estimation

In this section, array signal processing techniques are used to generate a 3D model comprising scattering mechanisms estimated from single-baseline POL-InSAR data of an urban area. The building layover is analyzed using polarimetric dual-baseline interferometric SAR measurements.

5.3.1 Single-baseline POL-InSAR Height and Scattering Mechanism Estimation for 3D Modeling

The height and physical characteristics of the dominant scatterers are determined by the single-baseline fully polarimetric MUSIC algorithm with a baseline of approximately 10 m [94, 95].

The fully polarimetric MUSIC method not only allows height estimation, but also a polarimetric analysis by means of the optimal scattering vector $\mathbf{k}_{\min}$. Three canonical reflection mechanisms are identified and assigned

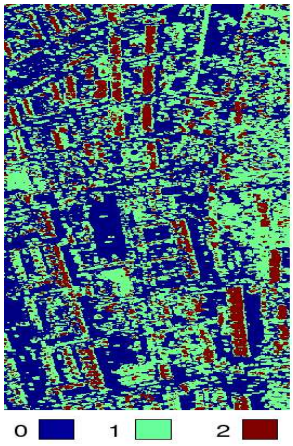

Figure 5.8: Single polarization dual-baseline InSAR MOS with diagonal loading.

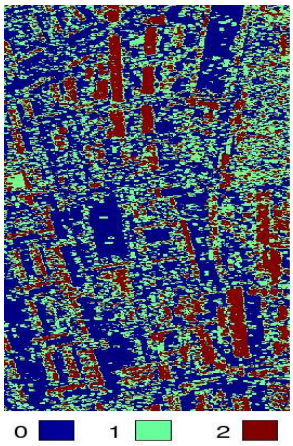

Figure 5.9: Polarimetric dual-baseline InSAR MOS with diagonal loading.

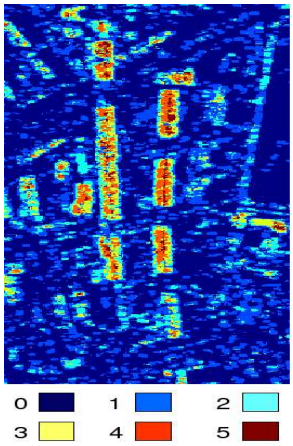

Figure 5.10: Polarimetric dual-baseline InSAR MOS with 5×5 boxcar filtering.

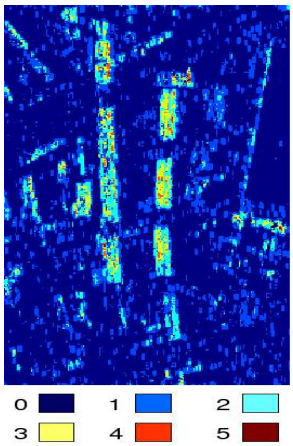

Figure 5.11: Polarimetric dual-baseline InSAR MOS with adaptive filtering.

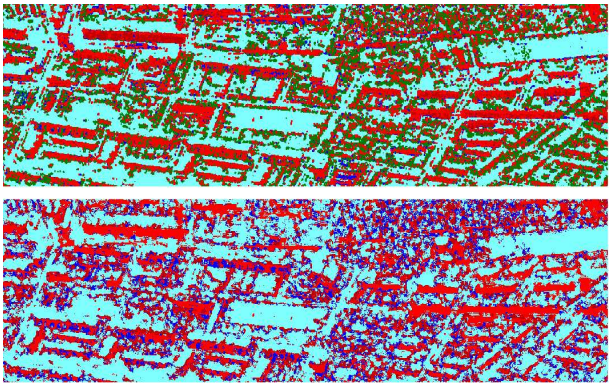

Figure 5.12: Identification of three basic scattering mechanisms (DB red, SR blue, VD green). Top: Original data, bottom: Polarimetric scattering mechanism generated by MUSIC analysis.

to the double bounce (DB), surface reflection (SR), and volume diffusion (VD) class [27]. While all these backscattering phenomena are present in the classification of the original data (figure 5.12, top), the MUSIC method is able to eliminate the volume diffusion class (figure 5.12, bottom): This suggests that the algorithm reduces the phase offset in a complex scene including vegetation and man-made objects.

The building height is estimated by the small baseline (≈ 10 m) fully polarimetric MUSIC method. The 3D image (figure 5.13) shows a large scene of the Dresden dataset. It is color-coded by the magnitude $|hh|$. Samples belonging to weakly correlated or shadowed areas are masked out by a criterion based on a threshold of the amplitudes and coherences: Pixels whose coherence is lower than 0.8 and whose modulus in the vv channel is less than the average modulus in the whole area are eliminated. Whereas height estimation of edifices aligned in azimuth direction is feasible, buildings with another orientation are partially masked out due to low backscattered power. It has to be borne in mind that layover effects are still visible.

Figure 5.14 illustrates in a 3D view the physical characteristics of the dominant scatterer by means of the angle α_1, defined in equation (2.56): Blue represents surface reflection ($\alpha_1 \approx 0$), red double bounce ($\alpha_1 \approx \pi/2$). On the top of buildings, double bounce scattering prevails. This can be explained by particular roof structures or multipath reflection processes generated by surrounding buildings. This argument is confirmed by average α_1 values for the isolated building in the rear part of the scene.

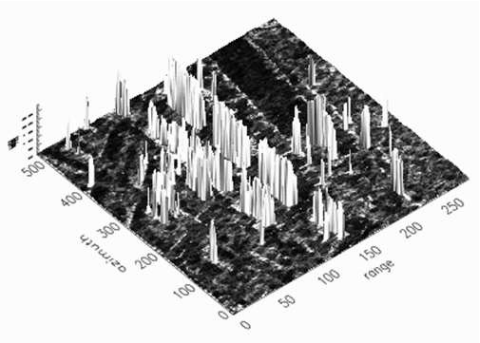

Figure 5.13: 3D building height estimation using the small baseline fully polarimetric MUSIC method.

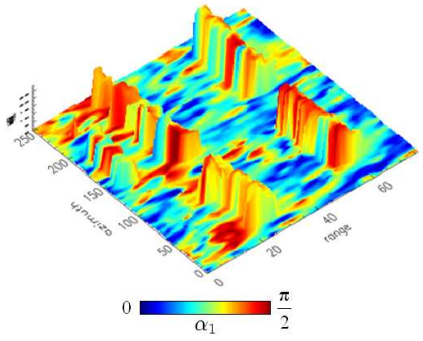

Figure 5.14: 3D building height estimation and scattering mechanism extraction using the small baseline fully polarimetric MUSIC method.

5.3.2 Dual-baseline POL-InSAR Height Estimation for Layover Analysis

In this subsection, the building layover is examined in detail using the dual-baseline POL-InSAR configuration [96,97]. To analyze the layover, a building that is oriented in sensor flight direction is selected (see figure 5.15). The edifice consists of five floors and a pitched roof leading to a height of approximately 17 m. As depicted in figure 5.16, the along-track direction is on the left side, i.e., far range is situated on the right and near range on the left side. The diagram 5.17 displays the scattering pattern inside the building layover: Going from right to left, i.e., from far range towards the SAR sensor position, there is first the wall-ground interaction point indicated by the number one. It is located at the ground topographic height. In the middle, there is a mixture of various reflection processes from the ground, the wall, and the roof. On the left hand side at number two, i.e., at the samples of the building layover that are closest to the antennas, there are contributions from the ground and the roof inside one azimuth-range resolution cell.

In the following, the spectra of beamforming and Capon and the pseudo-spectra of MUSIC and the maximum likelihood estimator are investigated for the scenario of one single polarization (vv) and for the case of fully polarimetric observations with equal cross-polarizations. The pseudo-spectra of the single polarization (SP) and polarimetric (FP) MLEs are evaluated by assuming $N_s = 1$, and are defined as

$$\hat{P}_{ML} = \frac{1}{\hat{\boldsymbol{\omega}}(1)} \tag{5.1}$$

using equation (3.65), and

$$\hat{P}^{P}_{ML} = \frac{1}{\hat{\boldsymbol{\theta}}(1)} \tag{5.2}$$

employing equation (4.91), respectively.

The height of ambiguity of the acquisition system with the small and large baseline is given by $H^{sb}_{amb} \approx 67.5$ m and $H^{lb}_{amb} \approx 15$ m, respectively. To illustrate the behavior of the (pseudo-)spectra, they are computed in a very wide range of $[-30\text{ m}, \frac{3}{4}H^{sb}_{amb}\text{ m}]$. If not otherwise stated, a 5×5 boxcar filter is employed to average spatially the data.

The (pseudo-)spectra are determined for the samples along the line inside the building layover shown in figure 5.16 on the right hand side. In the following figures, their order is from left to right and top to bottom. That means, the (pseudo-)spectra at the top correspond to far range, i.e., to the ground-wall interaction points, and those at the bottom are related to near range, i.e., to the samples inside the layover that are closest to the antenna location.

Figure 5.15: Optical image of building number one. Left: View from the side, right: View from the front (copyright G.S.).

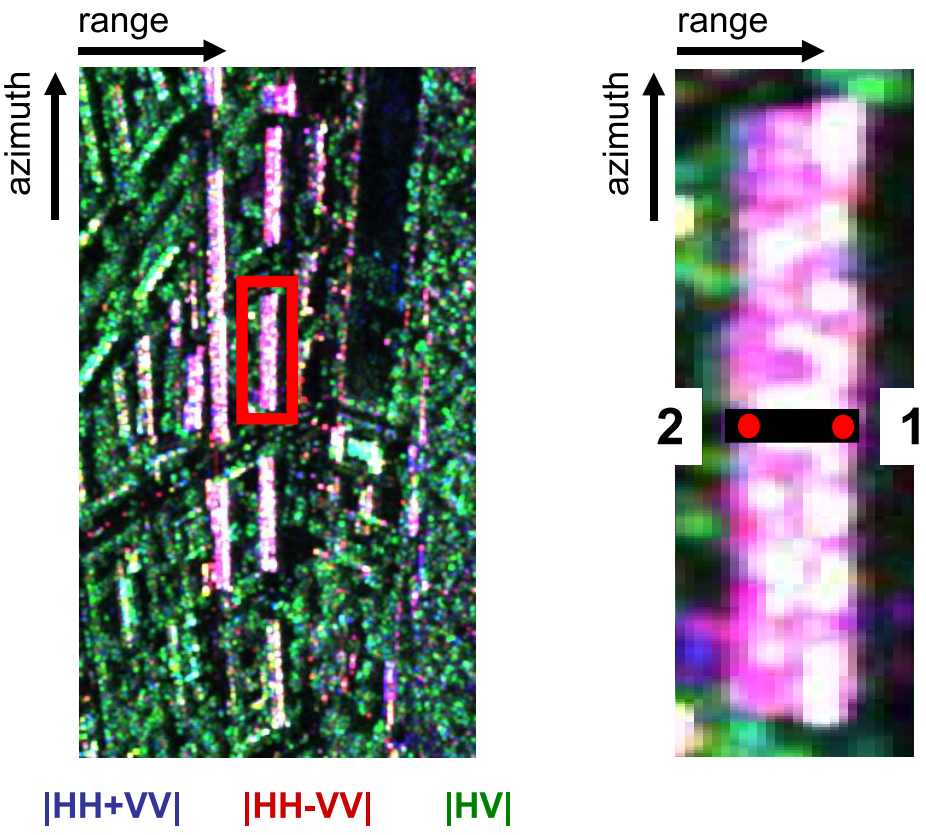

Figure 5.16: Pauli color-coded urban scene (left). The along-track direction is on the left side, i.e., far range on the right side. Close-up view of the building layover inside the red box with indicated sample line (right).

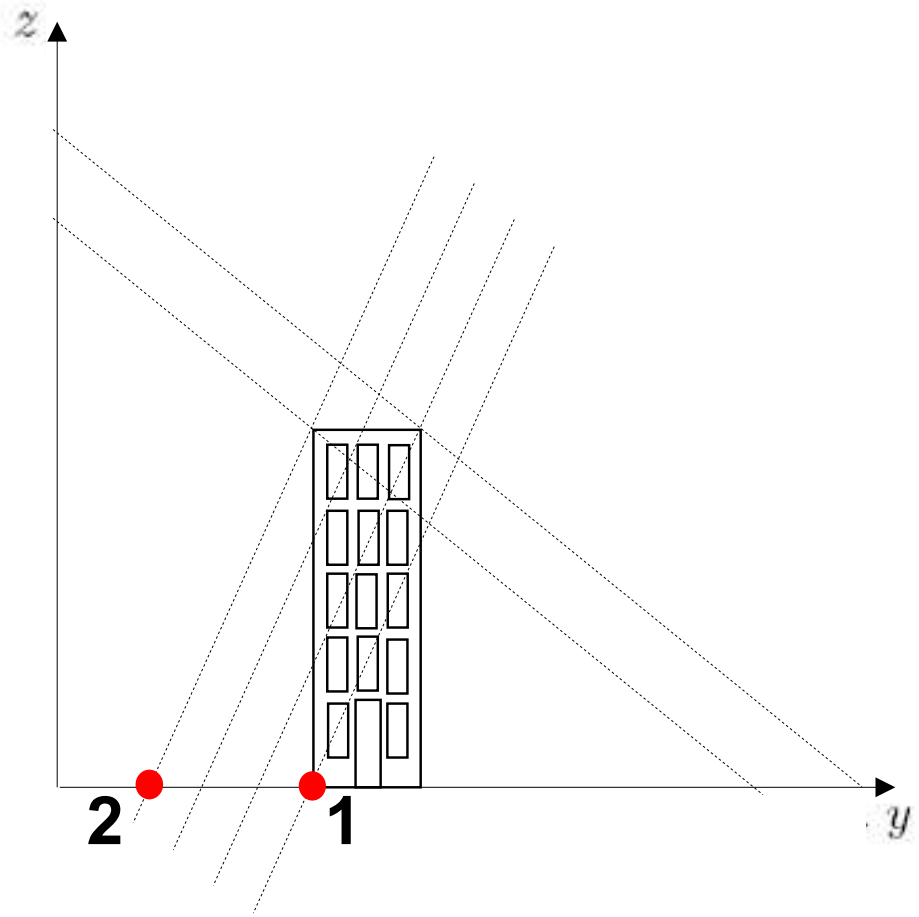

Figure 5.17: Schematic view of building layover with sensor on the left side. The wall-ground interaction point in far range is indicated by the number one, the azimuth-range resolution cell inside the layover that is closest to the sensor position by the number two.

The spectra of the single polarization and fully polarimetric beamforming methods in the first row of figures 5.18 and 5.19, respectively, show a broad mainlobe at approximately 0 m corresponding to the height of the ground and significant sidelobes at around -1 dB or below. The locations of the mainlobes in the spectra depicted in the second row jump from around 0 m to about 13 m. In the third and fourth row of figure 5.18, the single polarization beamforming spectra have mainlobes whose positions increase from 12 m to 17 m associated with the building wall and roof. The secondary peaks between -4 m and 0 m are most probably sidelobes caused by the nonuniform array geometry. The other sidelobes are suppressed below -2 dB. In the last two rows of figure 5.19, the polarimetric beamforming exhibits a mainlobe at about 17 m related to the building roof. The secondary maxima at around 1 m might correspond to a backscattering source at the ground or might be an ambiguity generated by the uneven sampling. The sidelobes are reduced below -3 dB.

Figures 5.20 and 5.21 illustrate the Capon spectra in single polarization and fully polarimetric mode, respectively. In the first row, the mainlobes of the Capon spectra are located at around -1 m and correspond to the ground height. The sidelobes of the polarimetric Capon method are at around -7 dB or less, whereas the sidelobes of the single polarization Capon algorithm are below -11 dB. This may be explained by a finer resolution capability of the polarimetric Capon. Compared to the beamforming technique, the spectral peaks are much narrower and the sidelobes are noticeably decreased. In the second row, the mainlobes are positioned between 0 m and 5 m. In the third and fourth row, the height location of the mainlobe rises from 7 m to 17 m for the single polarization Capon algorithm and lies in the range of 11 m to 17 m for the polarimetric Capon method. These maxima are caused by reflectors at the building wall and roof. Particularly in the last two spectra of the fourth row, there are second peaks situated at about 4 m. They might be induced by targets near the ground or represent spurious sidelobes. The other sidelobes are at around -6 dB or below.

Since the Capon algorithm requires the computation of the inverse of the covariance matrix, it is very sensitive to the number of samples employed to calculate the covariance matrix. Thus, the single polarization and fully polarimetric Capon spectra are evaluated after 7×7 boxcar filtering as shown in figures 5.22 and 5.23, respectively. They resemble largely the Capon spectra using 5×5 boxcar averaging. The most conspicuous difference can be found in the first two polarimetric Capon spectra of the last row: The mainlobes are located at approximately 12 m and related to the building wall. Spikes close to the mainlobe at around 18 m possess strong magnitude and may be associated with the building roof.

Next, the single polarization (figure 5.24) and fully polarimetric (figure 5.25) MUSIC pseudo-spectra are calculated with model order fixed to one. In the first row of the MUSIC pseudo-spectra, one mainlobe is visible at

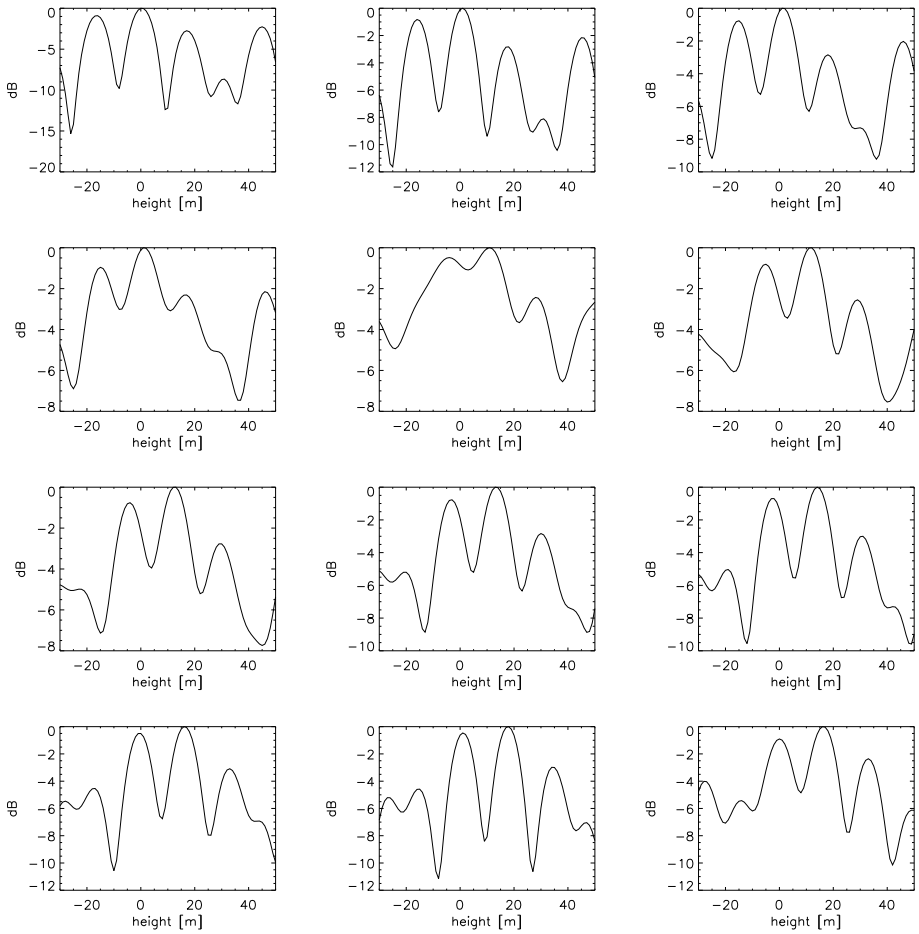

Figure 5.18: Single polarization beamforming spectra. The spectra are evaluated for the samples along the line inside the building layover illustrated in figure 5.16 on the right hand side. Their order is from left to right and top to bottom. The spectra at the top correspond to far range, i.e., to the ground-wall interaction points, and those at the bottom are related to near range, i.e., to the samples inside the layover that are closest to the antenna location.

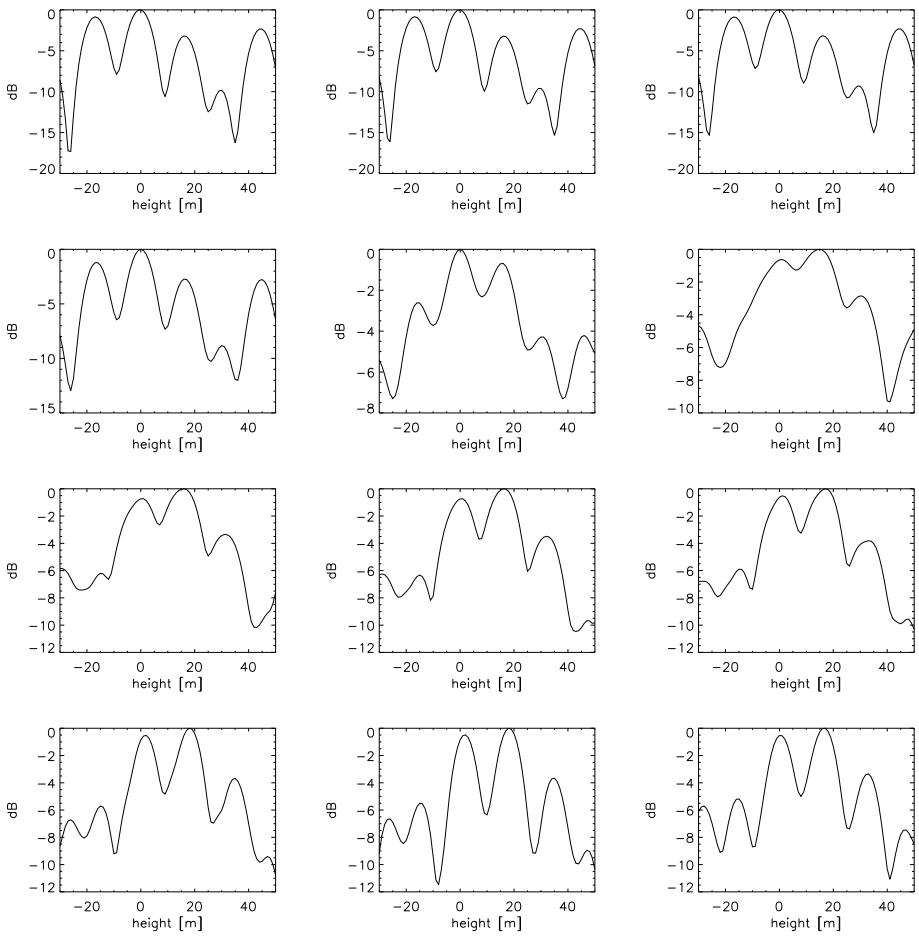

Figure 5.19: Fully polarimetric beamforming spectra.

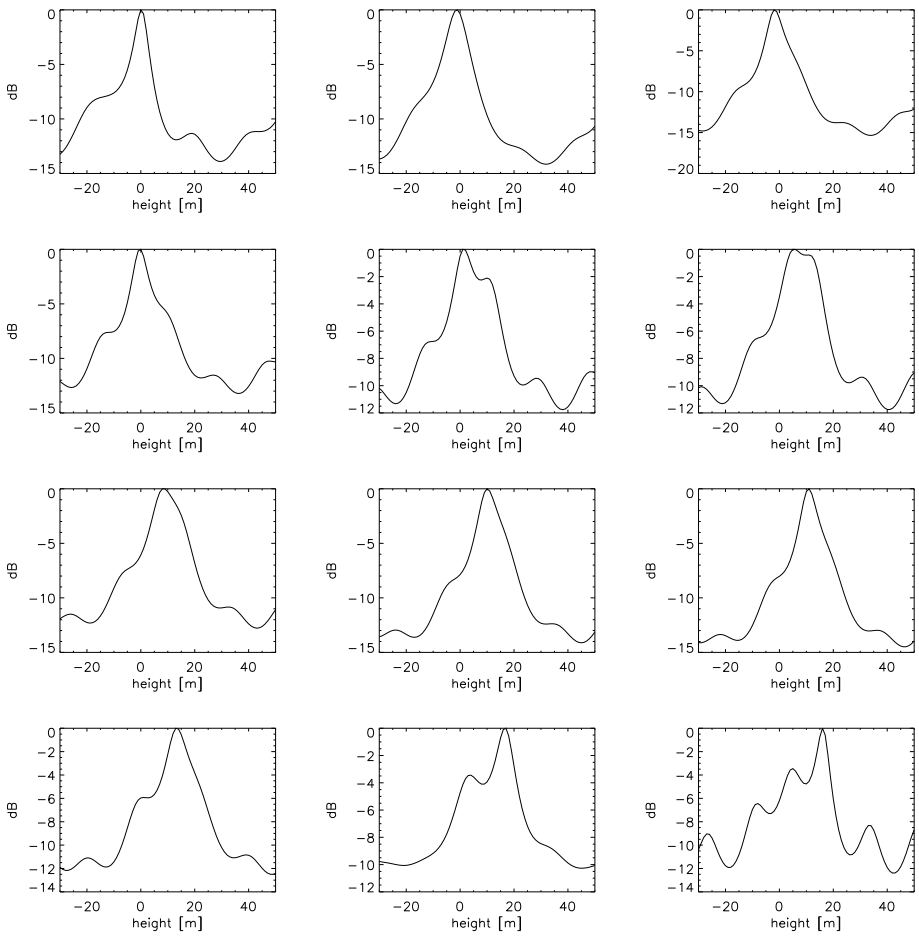

Figure 5.20: Single polarization Capon spectra.

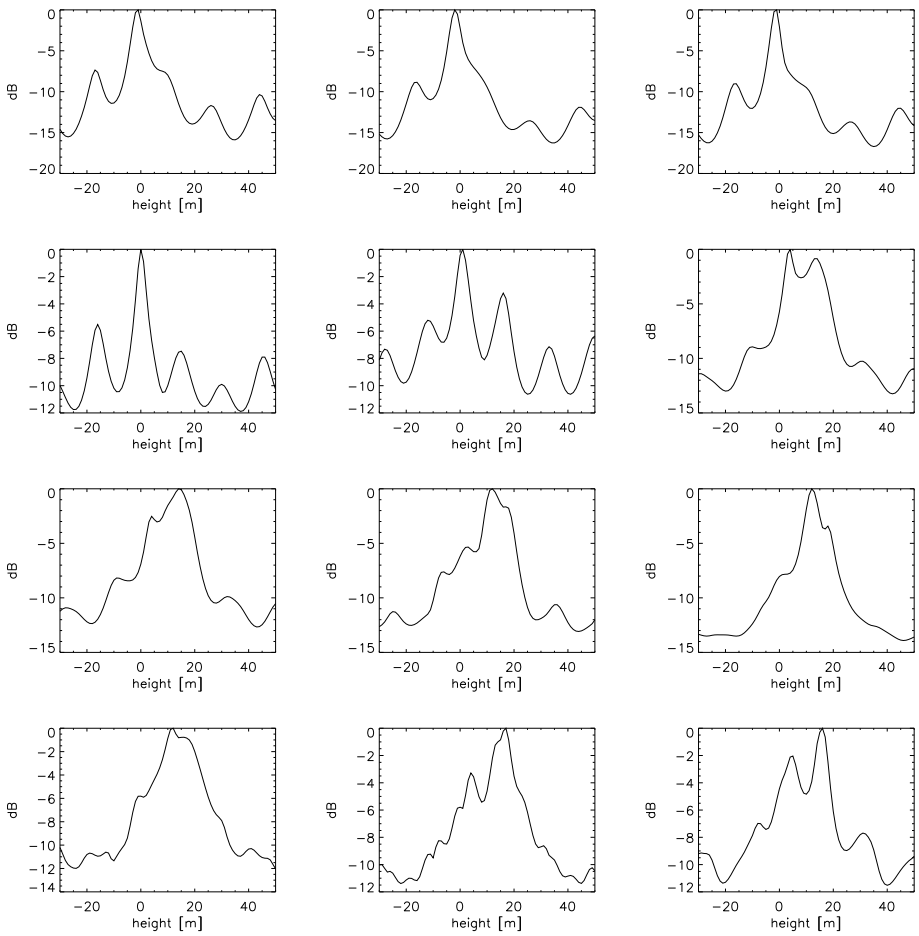

Figure 5.21: Fully polarimetric Capon spectra.

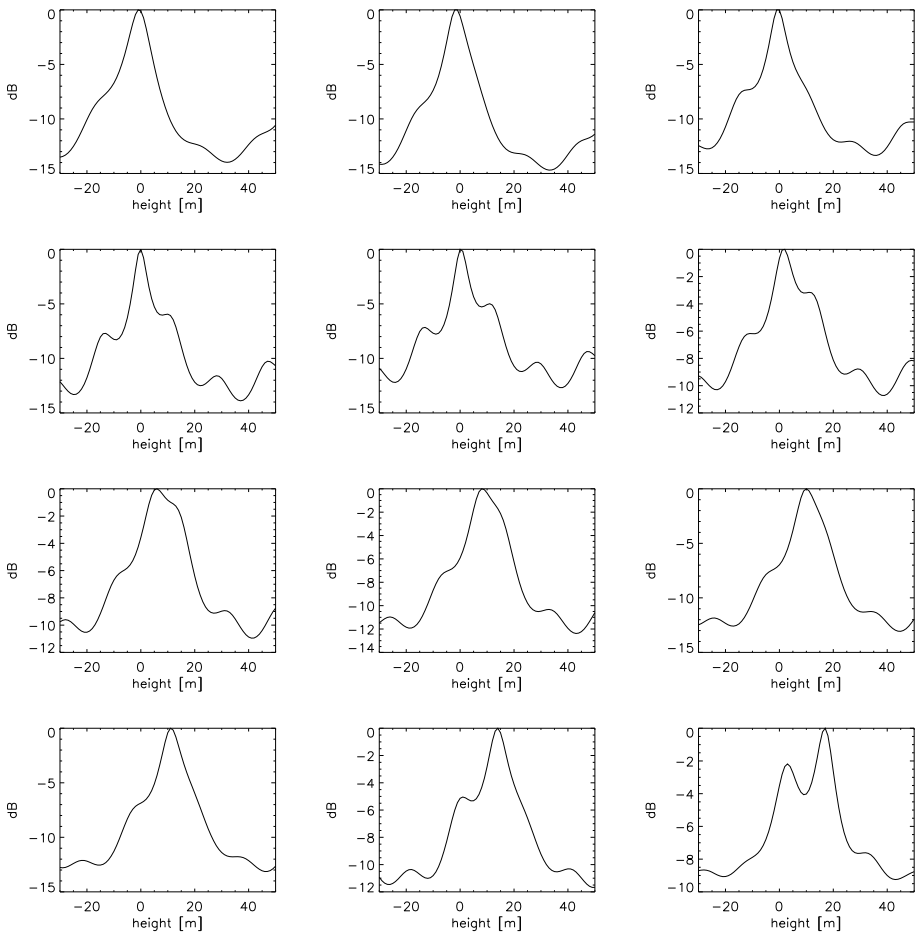

Figure 5.22: Single polarization Capon spectra with 7×7 boxcar filter.

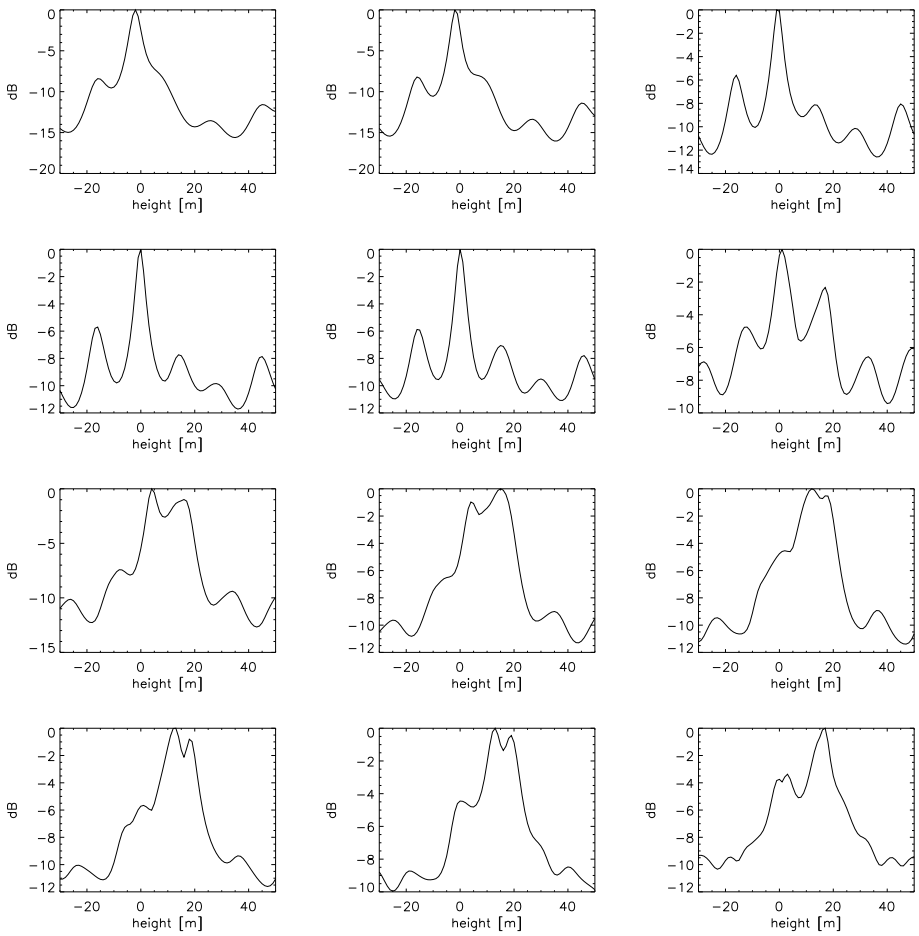

Figure 5.23: Fully polarimetric Capon spectra with 7×7 boxcar filter.

approximately 0 m and associated with the ground. The spurious sidelobes are at -7 dB or less. Starting from the image in the middle of the second row in figure 5.24, the mainlobe of the single polarization MUSIC pseudo-spectra ranges from 11 m to 18 m, and the second peak from -5 m to 0 m. The sidelobes are lowered to a value smaller than -8 dB. For the fully polarimetric MUSIC algorithm (figure 5.25), the highest peak is located at about 17 m, and the second spike at approximately 1 m (except for the pseudo-spectrum in the middle of row two where the order of spectral peaks is inverted). In the last row, the sidelobes are diminished to < -7 dB. The maxima are linked to backscattering sources on the building wall and roof. The second spikes might be generated by objects on the ground or they represent anomalous sidelobes induced by the uneven track distribution. While the single polarization and polarimetric MUSIC methods possess very similar ratios between the second peak and the maximum sidelobe of about two to three, the positions of the two spikes are more stable for the polarimetric than the single polarization MUSIC technique. In comparison to beamforming and Capon, both the single polarization and the fully polarimetric MUSIC methods lead to finer resolution and reduce considerably the leakage problem.

Subsequently, the MUSIC pseudo-spectra are computed under the assumption of model order two. They are depicted in figure 5.26 for the SP MUSIC and in figure 5.27 for the polarimetric MUSIC method. Interestingly, the single polarization MUSIC algorithm (figure 5.26) merely detects one source located at around -5 m to 12 m apart from the pseudo-spectrum in the last row at the right side: Two peaks of almost equal power are positioned at about 6 m and 16 m. Sidelobes are apparently decreased. It has to be kept in mind that the single polarization MUSIC algorithm of model order two constitutes an extreme case: The model order of the conventional MUSIC method is limited by two in a single polarization dual-baseline InSAR scenario (see equation (3.36)). In this situation the MUSIC approach seems to estimate an average interferometric phase.

In the first row of the polarimetric MUSIC pseudo-spectra in figure 5.27, a spectral maximum at around 0 m is visible with sidelobes at less than -7 dB (except for the secondary maximum at the right hand side). In the third row and the two first images of the last row, two pairs of spikes are identified, namely centered at around 16 m and 0 m with a noise level below -10 dB. Whereas the mainlobes are positioned at approximately 13 m and correspond to the building wall, the second peaks are very close at around 18 m and related to the building top. The order of the first and second lobe is inverted in the pseudo-spectrum in the center of the last row. This implies that inside the building layover the polarimetric MUSIC algorithm of model order two is capable of separating two components within one azimuth-range resolution cell that is near to the sensor location. The height of two very close sources is estimated: The first at around 13 m is associated

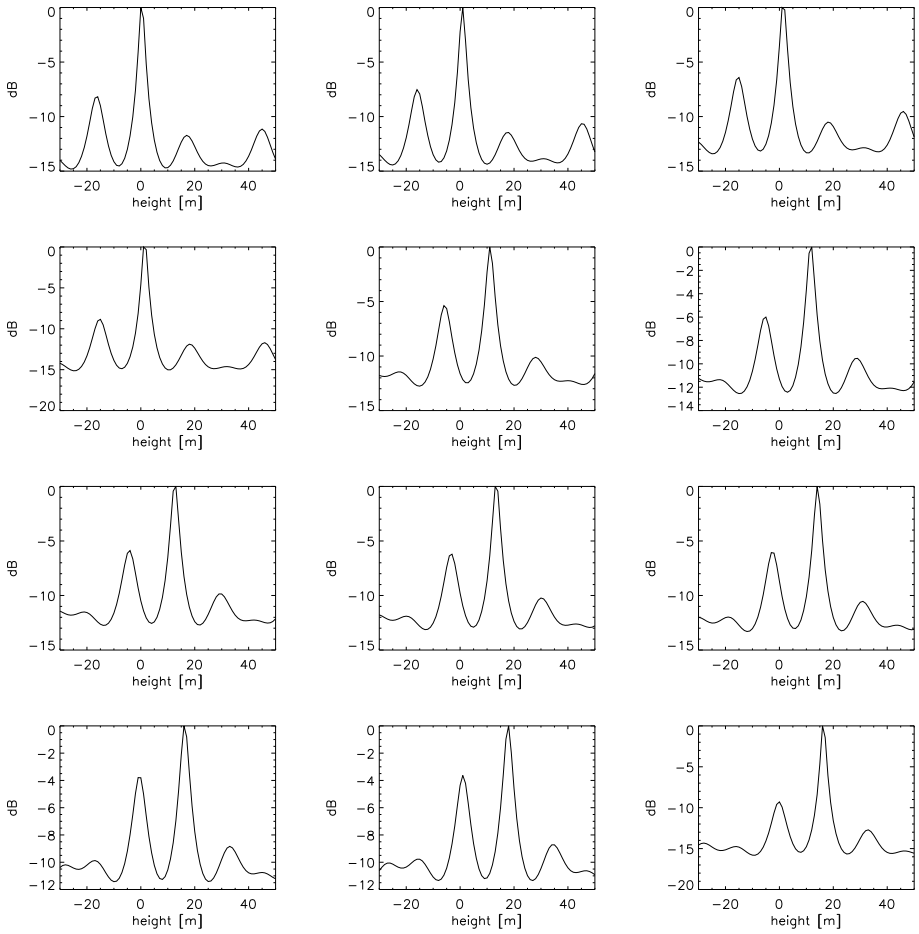

Figure 5.24: Single polarization MUSIC pseudo-spectra, model order set to one.

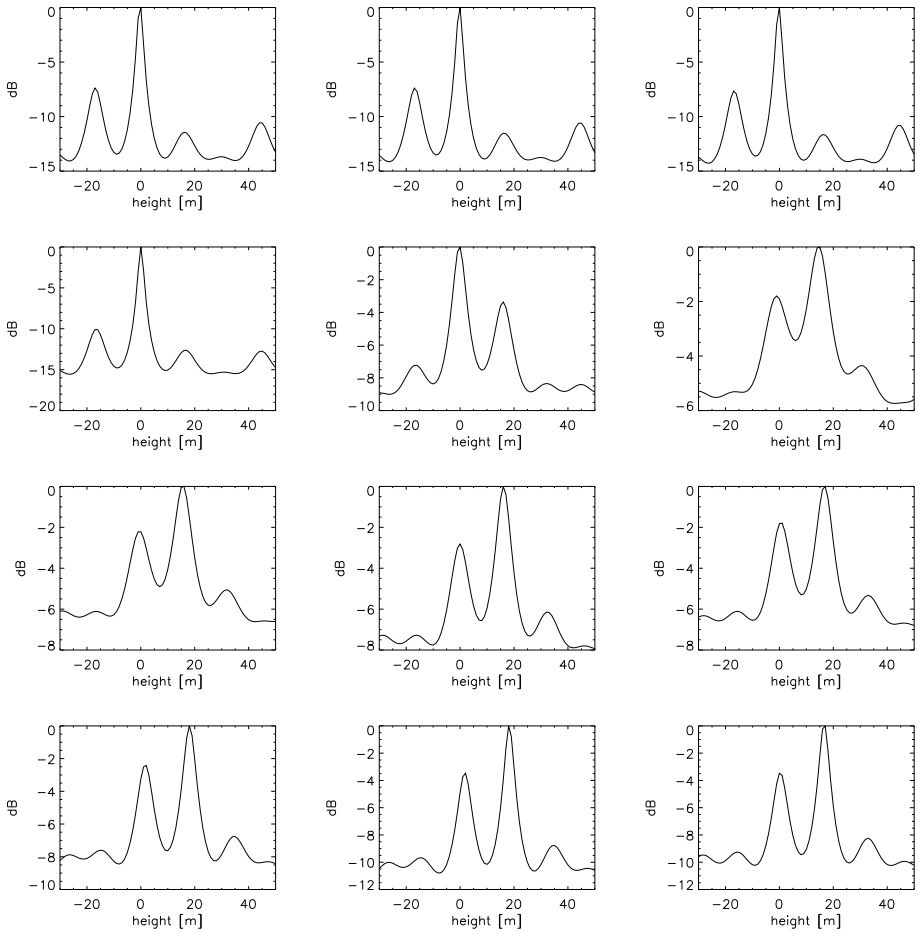

Figure 5.25: Fully polarimetric MUSIC pseudo-spectra, model order set to one.

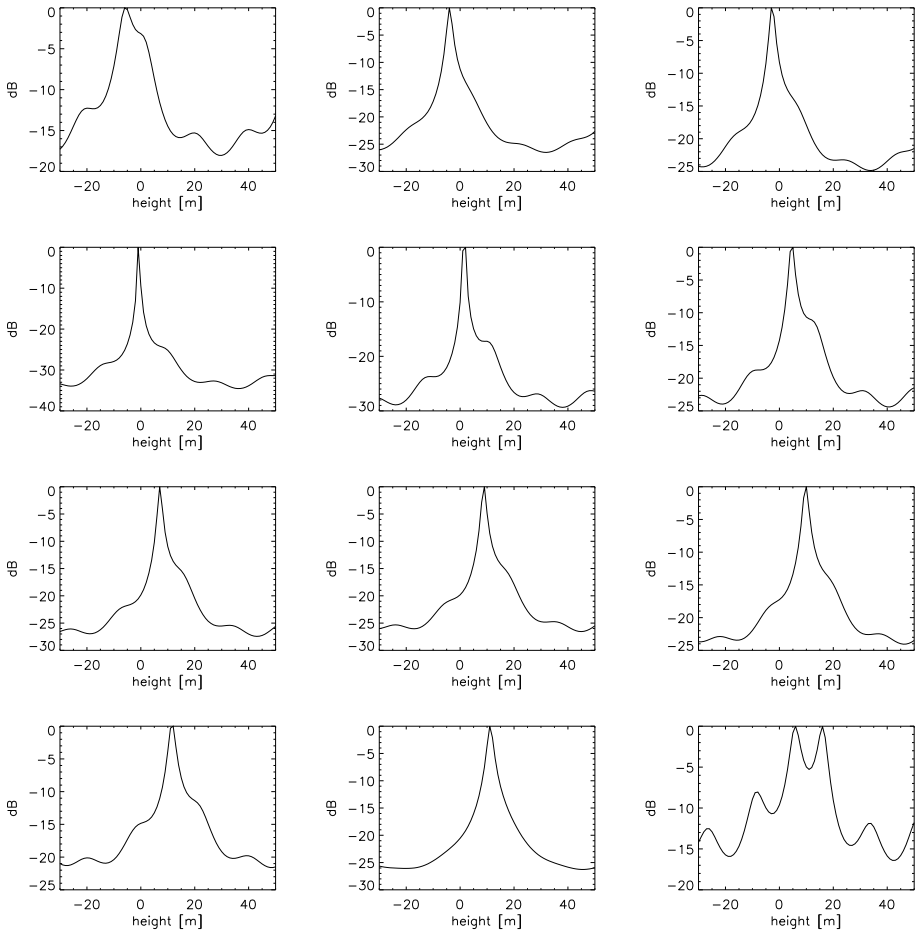

Figure 5.26: Single polarization MUSIC pseudo-spectra, model order set to two.

with an object along the building wall, the second at about 18 m with the building roof. This phenomenon will be investigated in more detail in the next section by analyzing the polarimetric signatures.

In contrast to the single polarization dual-baseline InSAR MUSIC method, the fully polarimetric MUSIC pseudo-spectra can be computed for model orders greater than two (cf. equation (4.61)). The behavior of the pseudo-spectra of the polarimetric MUSIC algorithm with model order fixed at three is represented in figure 5.28: In the first row, the main peak is located at around -3 m. Subsequently, the position of the mainlobe increases from -1 m to 15 m. The spectral patterns shown in the last two images of the third row and the first two images of the fourth row are quite similar to those of the FP MUSIC method of model order two: The mainlobes are located in a range from 9 m to 14 m and the second spikes are at around 19 m.

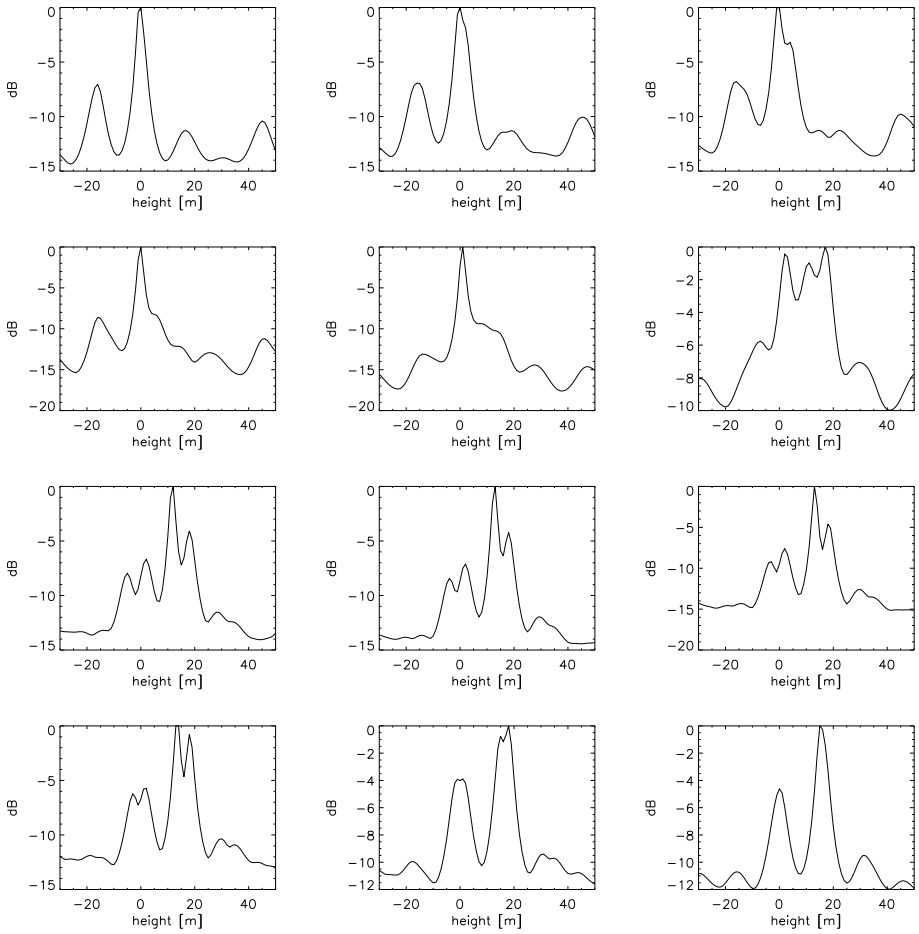

Figure 5.27: Fully polarimetric MUSIC pseudo-spectra, model order set to two.

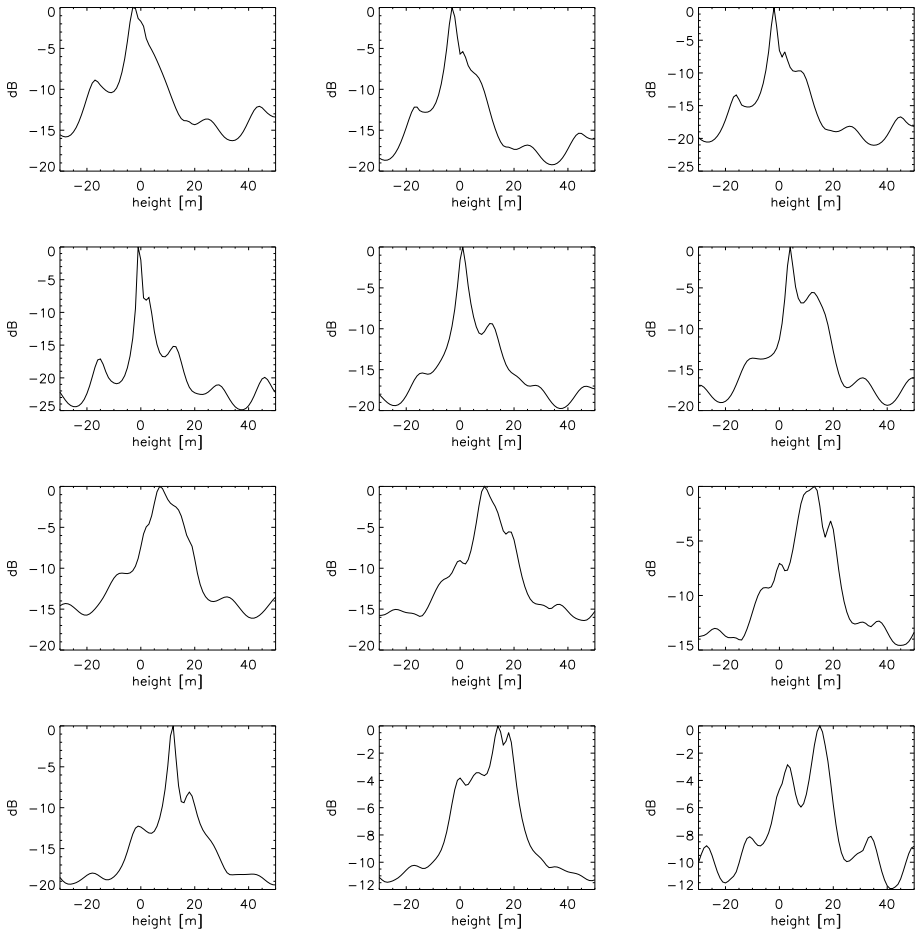

Figure 5.28: Fully polarimetric MUSIC pseudo-spectra, model order set to three.

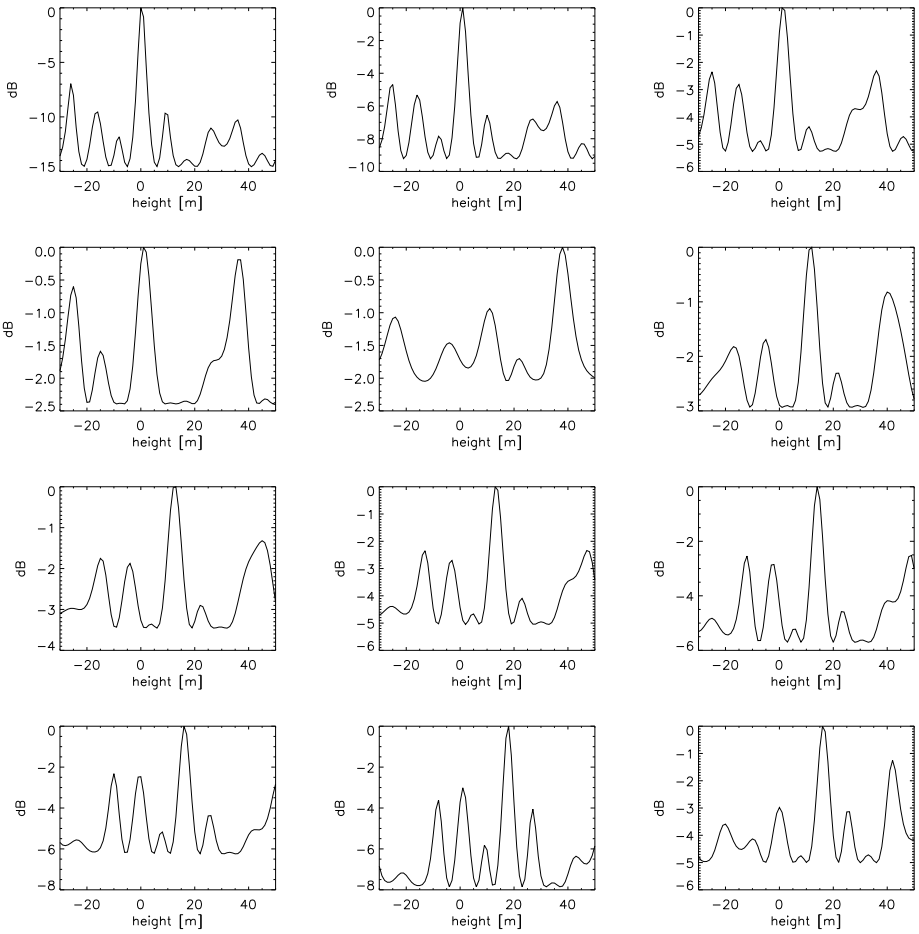

Figure 5.29: Single polarization MLE pseudo-spectra.

Finally, the single polarization and fully polarimetric MLE pseudo-spectra are illustrated in figures 5.29 and 5.30, respectively. Going from top left to bottom right, the mainlobe of the SP MLE is located from 0 m to 18 m (except for the pseudo-spectrum in the middle of the second row that exhibits a peak at 37 m). The sidelobe reduction is rather weak. In the first row of the fully polarimetric MLE displayed in figure 5.30, the mainlobe is situated at 0 m and the sidelobes are diminished below −25 dB. Starting from the image at the end of the second row, the maxima at around 17 m correspond to targets at the building top. Again, the second peaks at approximately 0 m might originate from a weak scatterer at the ground or they might be quasi-grating lobes caused by the irregular sampling. It can be observed that the sidelobes are considerably reduced, in the last row to less than −30 dB. Ratios between the second peak and the maximum sidelobe attain values around three.

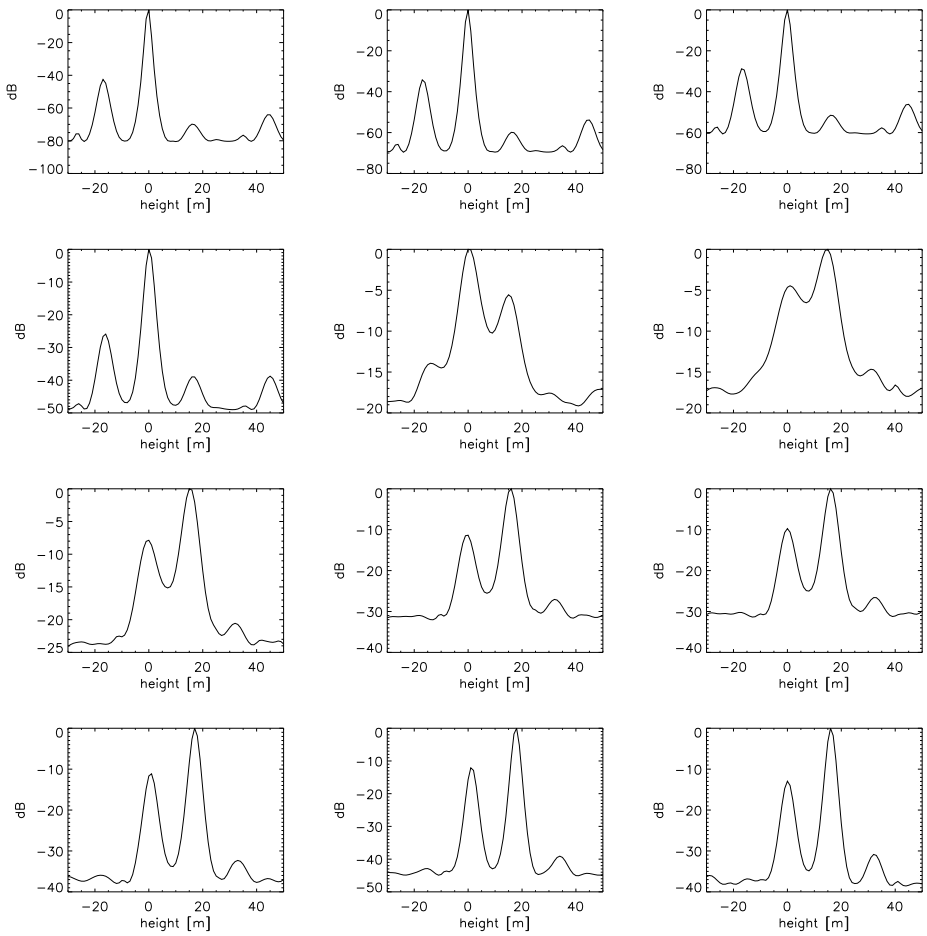

Figure 5.30: Fully polarimetric MLE pseudo-spectra.

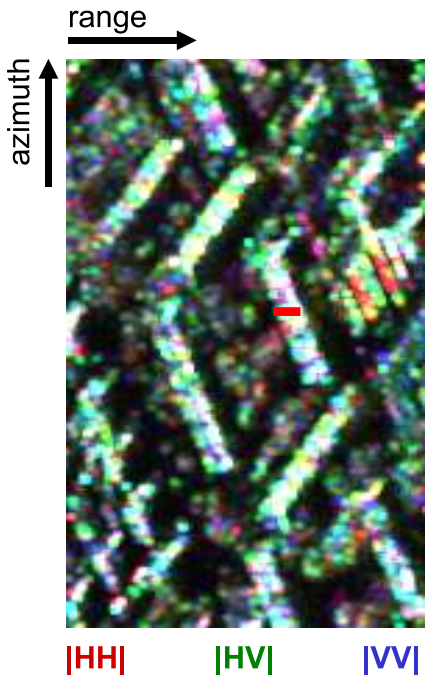

Figure 5.31: Pauli color-coded urban scene including oriented buildings. The flight trajectory is on the left hand side. The sample line is marked by red color.

So far, the layover of a building aligned in sensor flight direction has been studied. This analysis is possible as well for edifices that have a different orientation like the one depicted in figure 5.31. The pseudo-spectra of the single polarization and fully polarimetric MUSIC method with model order fixed at one, and of the polarimetric maximum likelihood estimator are evaluated for the samples along the red line. Again, going from right to left on the sample line, i.e., from far to near range, corresponds to the order of the pseudo-spectra from top to bottom and from left to right.

In the first row of figure 5.32 illustrating the single polarization MUSIC pseudo-spectra with model order fixed to one, the mainlobes are located at around 2 m and associated with the ground height. Sidelobes lie at < -9 dB. In the second and third row, the position of the mainlobe increases from 3 m to 12 m. The spectral behavior of the polarimetric MUSIC algorithm of model order one (figure 5.33) and the polarimetric MLE (figure 5.34) is rather similar: In the first row, a peak at 0 m is detected and the sidelobes are diminished below -9 dB and -30 dB, respectively. In the second and third row, the location of the mainlobe rises from 1 m to 13 m. In the middle of the last row, the SP MUSIC and FP MLE pseudo-spectra exhibit a dominant target located at 15 m and a second peak at 0 m, whereas the

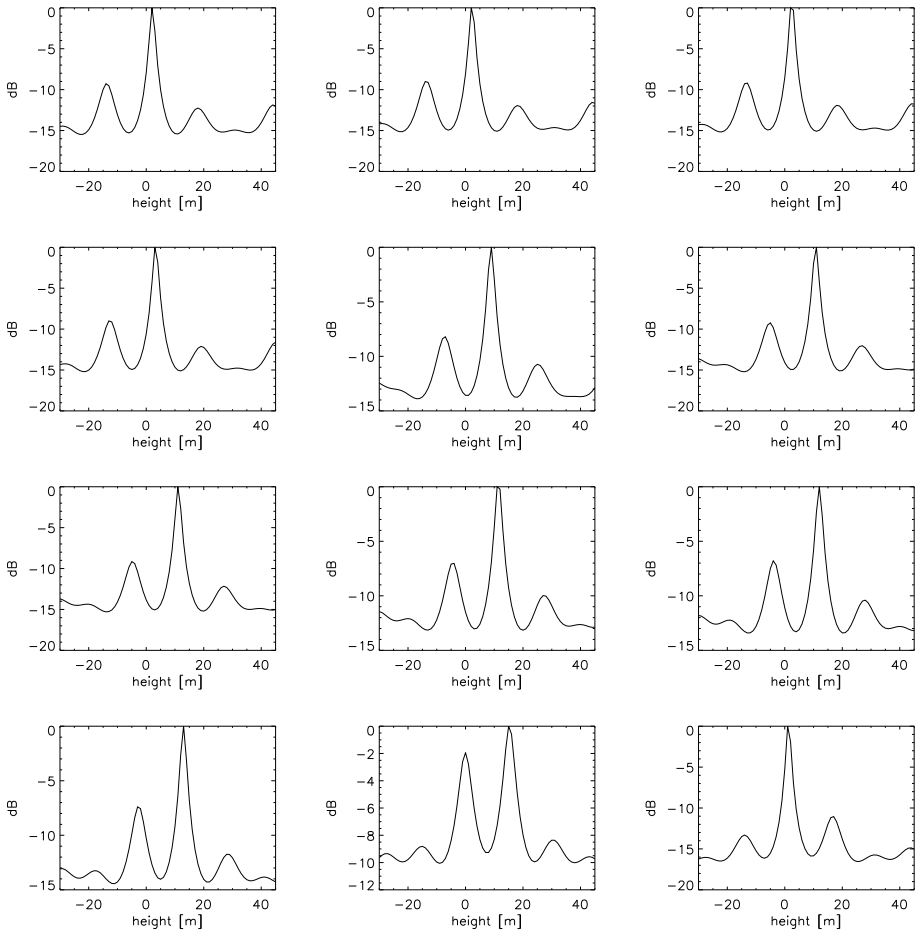

Figure 5.32: Oriented building: Single polarization MUSIC pseudo-spectra, model order set to one.

FP MUSIC pseudo-spectrum possesses the dominant scatterer at 0 m and a second spike at 15 m. This observation is an indication that the SP and FP MUSIC methods and the polarimetric MLE are adequate to identify two components within one azimuth-range resolution cell: The first reflector is related to the ground topography, the second to the building top. It is apparent that the sidelobes are significantly suppressed.

Analyzing the building layover by means of dual-baseline polarimetric InSAR measurements, the following conclusions can be drawn: The single polarization (SP) and fully polarimetric (FP) beamforming algorithms result in spectra that are characterized by broad peaks and high sidelobes. The SP and FP Capon methods are capable of narrowing the peaks and diminishing the leakage problem noticeably compared to beamforming. This facilitates the topographic height detection using the samples that belong to

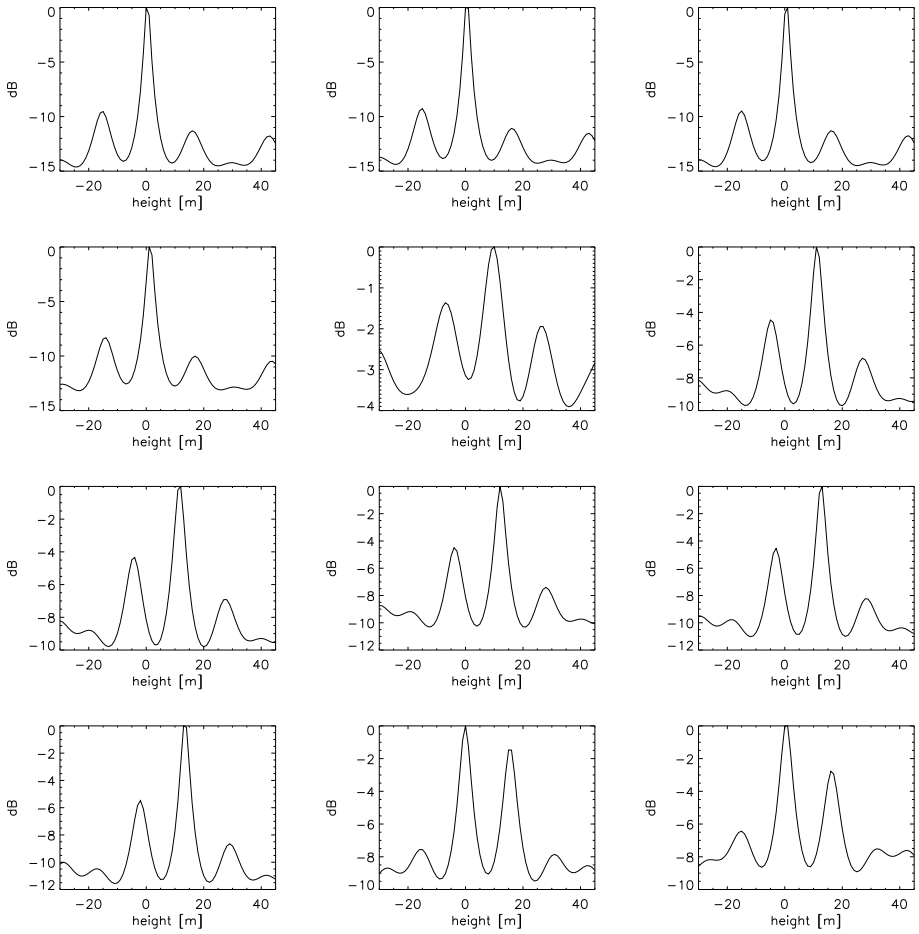

Figure 5.33: Oriented building: Fully polarimetric MUSIC pseudo-spectra, model order set to one.

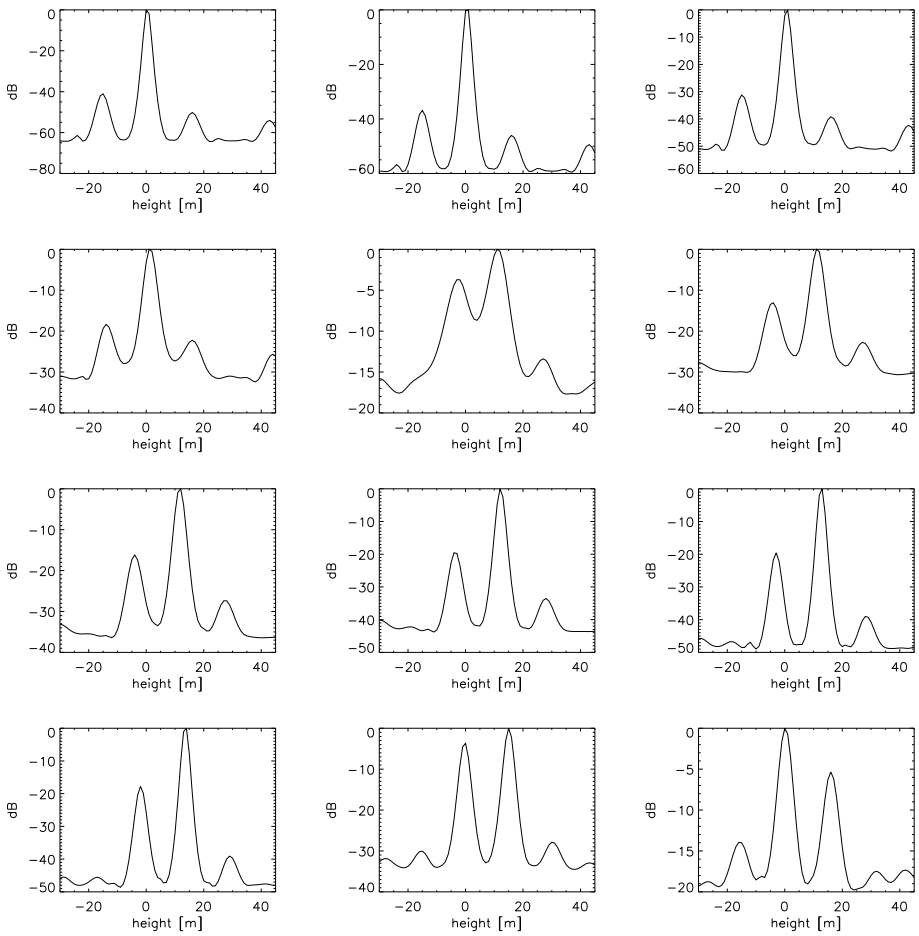

Figure 5.34: Oriented building: Fully polarimetric MLE pseudo-spectra.

the wall-ground interaction points, but it is not sufficient to identify clearly more than one contribution in the building layover samples that are nearest to the antenna position. The SP MUSIC with model order set to two and the SP ML estimator discern merely the height of one single signal showing rather good and very weak secondary lobe reduction, respectively. The MUSIC algorithms both with and without polarization diversity whose model order are fixed to one, and the polarimetric MLE refine the resolution and reduce sidelobes in a visible way. For the wall-ground interaction samples in the far range of the building layover, one peak located at the ground height is perceived conspicuously. For the samples that are closest to the sensor location, two sources can be separated and their heights estimated, associated with the ground topography and the building roof. In the spectral patterns of the polarimetric MUSIC method with model order set to two, one source at the ground is clearly spotted in far range. In near range two very close constituents are detected within one azimuth-range resolution cell, one positioned along the building wall, the other at the building top. The behavior of the polarimetric MUSIC approach with model order fixed to three is quite similar. The MUSIC algorithms, particularly the polarimetric MUSIC, and the polarimetric ML estimator possess the best performance among the spectral estimation techniques: They are most robust to process data from the nonuniform nonlinear sensor array. These techniques are adequate to solve the building layover problem, i.e., to recover two components within one azimuth-range resolution cell.

5.4 Dual-baseline POL-InSAR Reflectivity and Scattering Mechanism Estimation for 3D Imaging

In this section, the urban scene is analyzed by producing three-dimensional images from the dual-baseline POL-InSAR measurements. First, the layover of the building illustrated in figures 5.16 and 5.15, subsection 5.3.2, is investigated. Tomographic slices are calculated by the beamforming and Capon methods using observations in vv channel and with polarization diversity. The single polarization and fully polarimetric MUSIC and maximum likelihood estimator generate pseudo-tomograms. The three-dimensional images are computed in the range $[-10\text{ m}, 25\text{ m}]$ in the vertical direction. The (pseudo-)tomograms are extracted for the samples along the line inside the building layover depicted in figure 5.16 on the right hand side.

The tomographic slices shown in figures 5.35 and 5.36 are calculated by the single polarization (SP) and fully polarimetric (FP) beamforming algorithms, respectively. On the right hand side, the backscattering from the wall-ground interaction at the topographic height of approximately 0 m is visible. The mainlobe is broad and the sidelobes are rather strong,

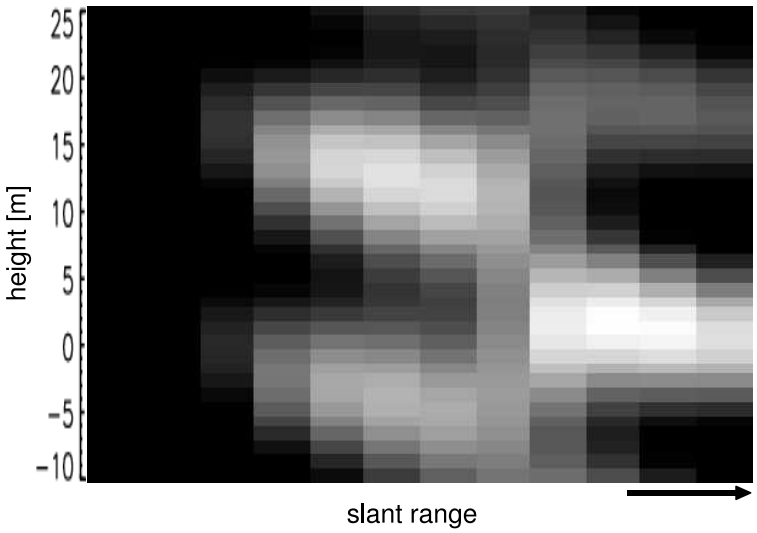

Figure 5.35: Three-dimensional imaging of building layover. The x-axis corresponds to slant range with far range on the right hand side. The y-axis is related to the estimated height going from -10 m to 25 m. Single polarization beamforming tomographic slice.

especially for the polarimetric beamforming. In the middle of the 3D image, the SP beamformer shows reflectors between 10 and 15 m associated with the building wall. The high sidelobes below 0 m are caused by the irregular sampling. Compared to the very bright backscattering from the wall-ground interaction, the reflectivity is weak at the left hand side for the SP and FP and in the middle for the FP beamforming method.

The three-dimensional imaging results of the single polarization and fully polarimetric Capon techniques are illustrated in figures 5.37 and 5.38, respectively. On the right side, both algorithms detect a signal at around 0 m originating from the building base. In comparison with the beamforming method, the Capon algorithms lead to finer resolution and better leakage reduction. Going to the left, the elevation of the scatterer increases to about 10 m for the SP Capon, whereas the FP Capon separates two contributions, the first slightly above 0 m, and the second at approximately 15 m related to the building height. To a limited extent, the fully polarimetric Capon technique possesses sufficiently narrow peaks to identify two components at different height locations. Again, on the left side, the backscattering is very weak.

The pseudo-tomograms of the single polarization and fully polarimetric MUSIC methods with fixed model order one are shown in figures 5.39 and 5.40, respectively. Both algorithms are appropriate to recognize one reflector at around 0 m corresponding to the wall-ground interaction points at the

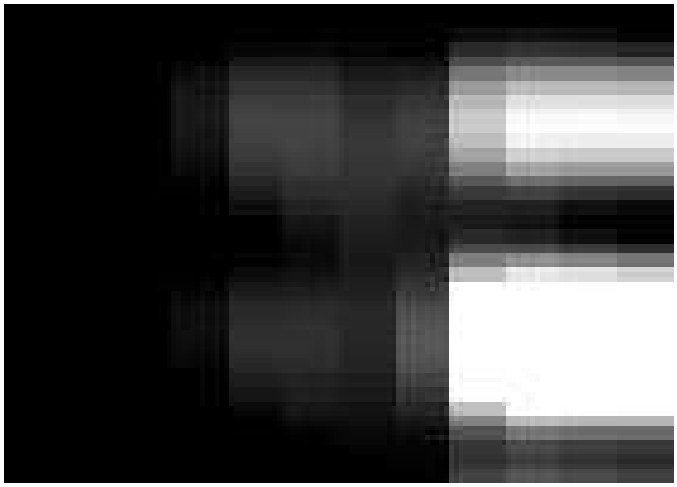

Figure 5.36: Fully polarimetric beamforming tomographic slice.

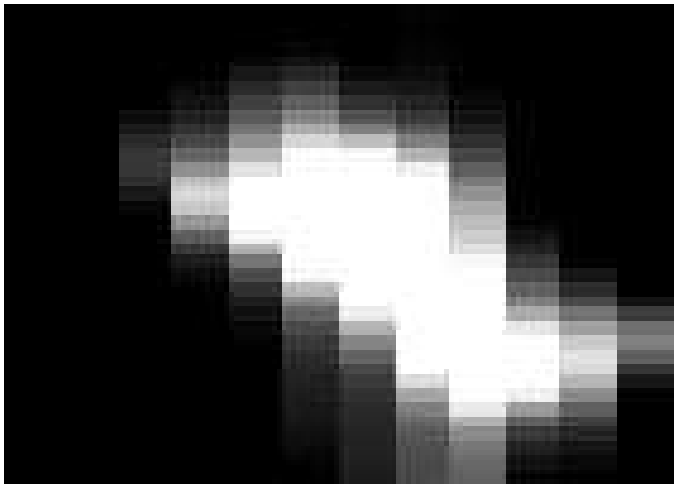

Figure 5.37: Single polarization Capon tomographic slice.

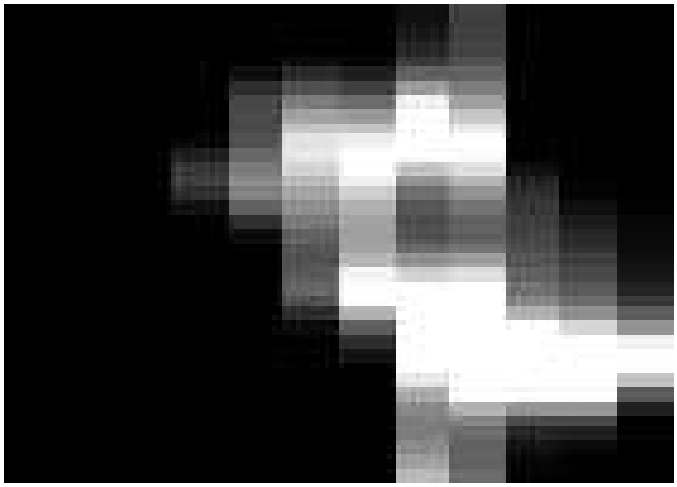

Figure 5.38: Fully polarimetric Capon tomographic slice.

right hand side. Compared to the beamforming and Capon techniques, the spectral peaks of MUSIC with model order one are very narrow and the sidelobes are visibly decreased. While the height of the main scatterer rises from around 11 m to 18 m in the SP MUSIC image, the elevation of the main reflector of the FP MUSIC method is very stable at approximately 17 m. They are associated with the building wall and roof. The second peaks at around -2 m (SP) and 0 m (FP) seem to be sidelobes in the height of ambiguity.

The pseudo-tomographic slices of the SP MUSIC (figure 5.41) and the FP MUSIC (figure 5.42) methods where the model order is set to two are quite different: The elevation of one single reflector grows from -5 m to more than 10 m in the single polarization MUSIC 3D image. It has to be noted that the classical MUSIC algorithm of model order two represents a limiting case if it is applied to single polarization dual-baseline InSAR measurements (see equation (3.36)). It seems to compute an average phase. On the right hand side of the fully polarimetric MUSIC pseudo-tomogram, one source at around 0 m related to the building base can be seen. Compared to the polarimetric MUSIC algorithm of model order one, the resolution is slightly deteriorated: This degradation may be explained by overmodeling or by an object near the wall-ground interaction points. In the middle and on the left side, two strong scatterers that are very close to each other are distinguished: The first at approximately 13 m is generated by targets along the building wall, the second is very stable at 18 m and caused by the building roof. Sidelobes are visible at about 0 m.

The pseudo-reflectivities of the polarimetric ML estimator on the left side of figure 5.43 are that strong that the scatterers in the other parts of the image cannot be discerned.

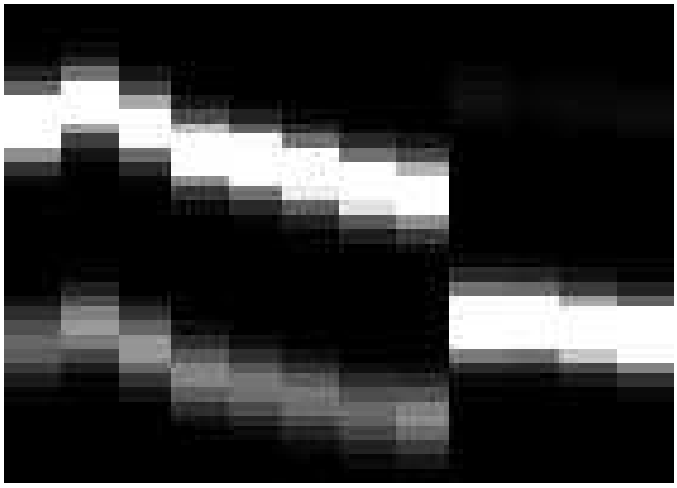

Figure 5.39: Single polarization MUSIC pseudo-tomographic slice, model order fixed to one.

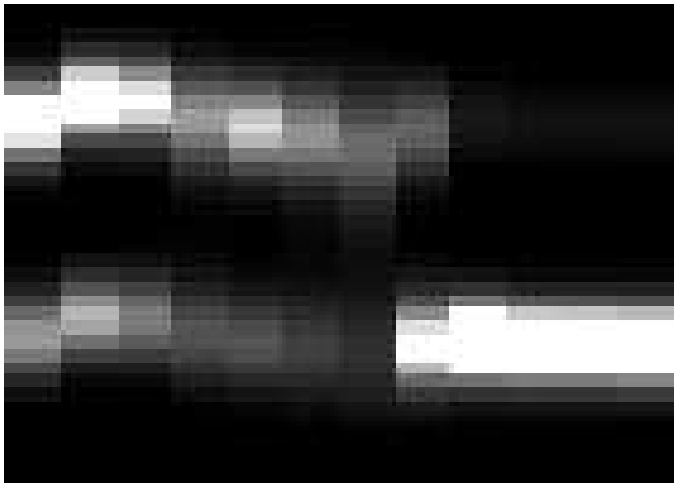

Figure 5.40: Fully polarimetric MUSIC pseudo-tomographic slice, model order fixed to one.

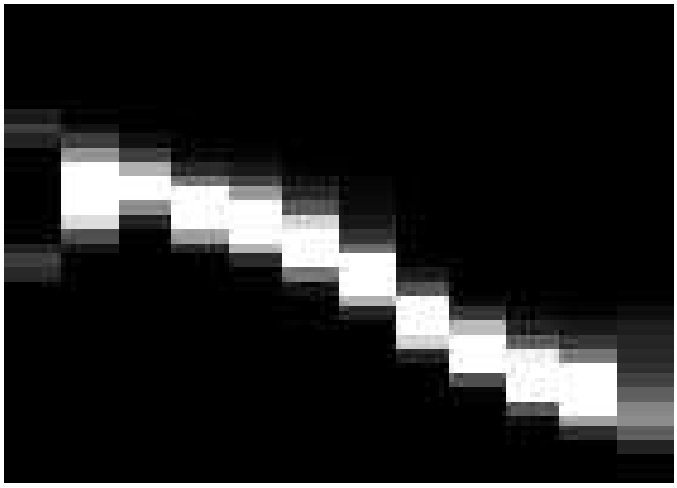

Figure 5.41: Single polarization MUSIC pseudo-tomographic slice, model order fixed to two.

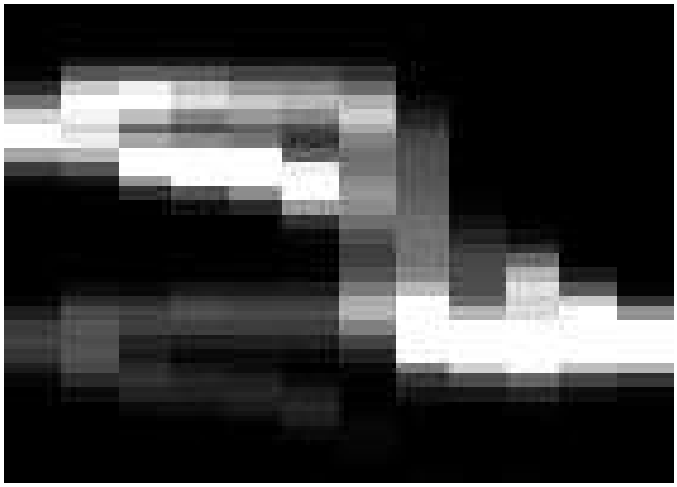

Figure 5.42: Fully polarimetric MUSIC pseudo-tomographic slice, model order fixed to two.

Figure 5.43: Fully polarimetric MLE pseudo-tomographic slice.

Next, the optimal MUSIC scattering vectors $\mathbf{k}_{\min}$ are employed to form three-dimensional images illustrating the reflection processes [98]. Figures 5.44 and 5.45 show the minimum scattering mechanisms computed by the fully polarimetric MUSIC method with model order set to one and two, respectively. On the right hand side, the relative power between the polarizations is alike. For the polarimetric MUSIC algorithm with model order fixed to one, the first component of the Pauli polarization basis associated with surface scattering prevails on the left side at the building top. The MUSIC method of model order two in figure 5.45 reveals surface reflection on the building roof, and an additional scattering phenomenon very close to the building top where the polarization channels seem to have quite equal amplitudes. It is evident that these reflection processes which are only separated by a few meters exhibit very disparate polarization signatures.

In the following, scattering patterns are examined in more detail by using the polarimetric indicator α_1 of the dominant reflector inside the optimal vectors $\mathbf{k}_{\min}$. In figures 5.46 (model order one) and 5.47 (model order two) a mask based on a threshold of the pseudo-reflectivities is applied to set the samples to black color whose backscattering power is less than the mean of the imaged area. On the right hand side at the wall-ground interaction points, the α_1 value is rather high suggesting double bounce reflection. In the middle part of the image, the polarimetric descriptor reaches values of about $\frac{\pi}{2}$, linked to the double bounce class. At the left hand side, α_1 attains average to low values at the roof that are related to surface reflection. Again, it is conspicuous that the polarimetric MUSIC algorithm of model order two is adequate to differentiate within one azimuth-range resolution cell two neighboring scatterers that possess very distinct polarimetric behavior: Whereas at the roof the α_1 value is low and corresponds to surface scattering,

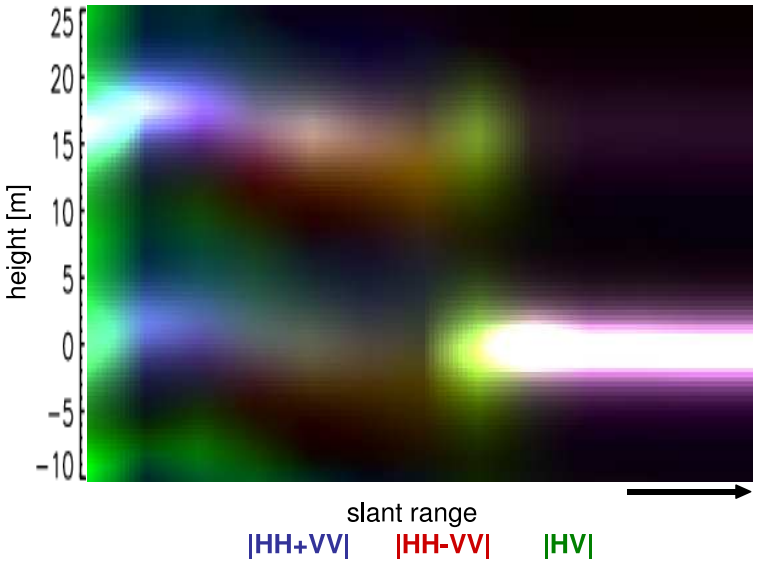

Figure 5.44: Pseudo-tomographic slice of the optimal MUSIC scattering mechanisms $\mathbf{k}_{\min}$, model order fixed to one.

Figure 5.45: Pseudo-tomographic slice of the optimal MUSIC scattering mechanisms $\mathbf{k}_{\min}$, model order fixed to two.

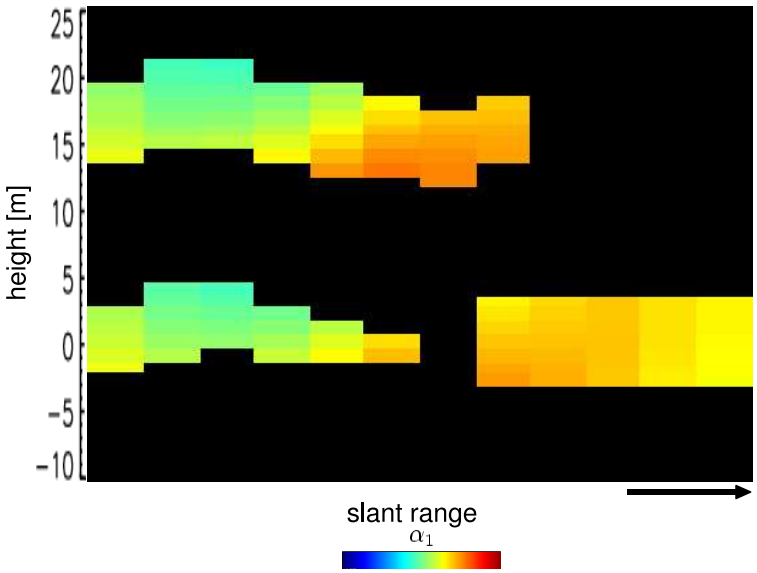

Figure 5.46: Polarimetric indicator α_1 of the optimal MUSIC scattering vector, model order fixed to one.

it is high for the sources below the building top and related to double bounce reflection.

So far, the layover of one single building has been investigated. Now, three-dimensional images of a large scene are generated along the sample line defined in figure 5.48. The area contains three tall buildings as illustrated in the diagram 5.49. Building number one and two on the right enclose a spacious courtyard shown in figures 5.15 and 5.50 consisting of several trees, small barracks, hanging bars and a playground with a slide. Building number two and three on the left are separated by a street as can be seen in figure 5.51. The sensor is located on the left hand side.

The pseudo-tomograms are computed by the SP MUSIC (model order one) and the FP MUSIC (model order one and two) algorithms depicted in figures 5.52 (SP MUSIC MO 1), 5.53 (FP MUSIC MO 1), and 5.54 (FP MUSIC MO 2), respectively. Going from right to left, i.e., from far to near range, the wall-ground interaction samples of the first building are apparent at about 0 m, followed by the strong backscattering from the roof. In the courtyard, there is one contribution at the topographic height and strong reflectors at approximately 10 m. Some spurious sidelobes lie beneath 0 m. In the center of the images is the shadow of building number two, where scattering processes occur as well. At the left end of the pseudo-tomographic slices, two buildings can be recovered: First, signals at around 0 m related to the wall-ground double bounce reflections appear, then a component located at the roof is detected. Globally, the polarimetric MUSIC MO 1 three-

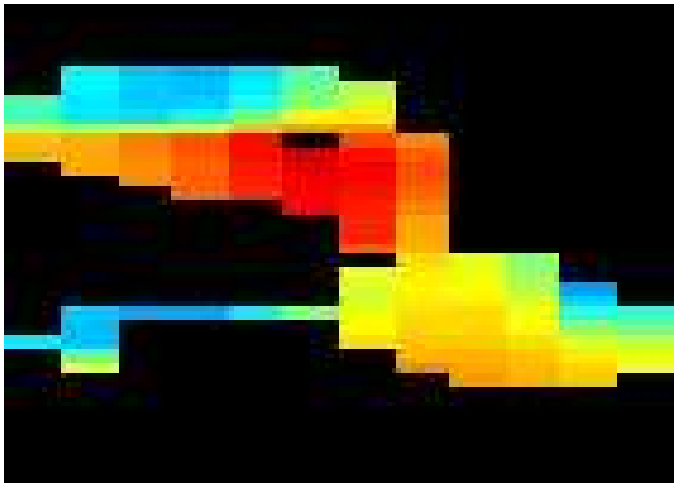

Figure 5.47: Polarimetric indicator α_1 of the optimal MUSIC scattering vector, model order fixed to two.

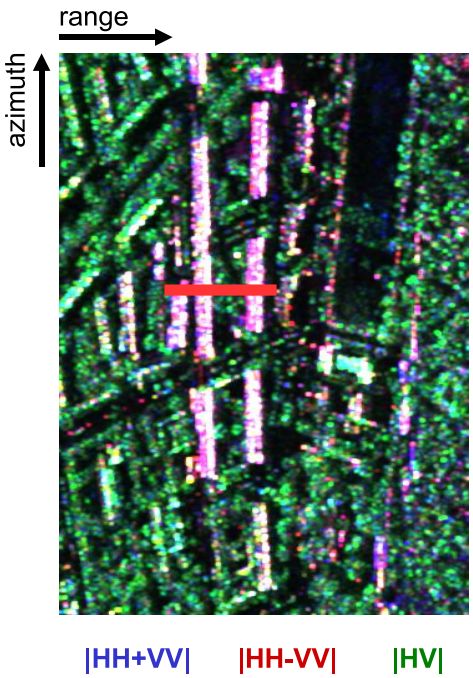

Figure 5.48: Large scene containing three tall buildings and a spacious courtyard with trees. Azimuth is on the left hand side. The sample line is marked by red color.

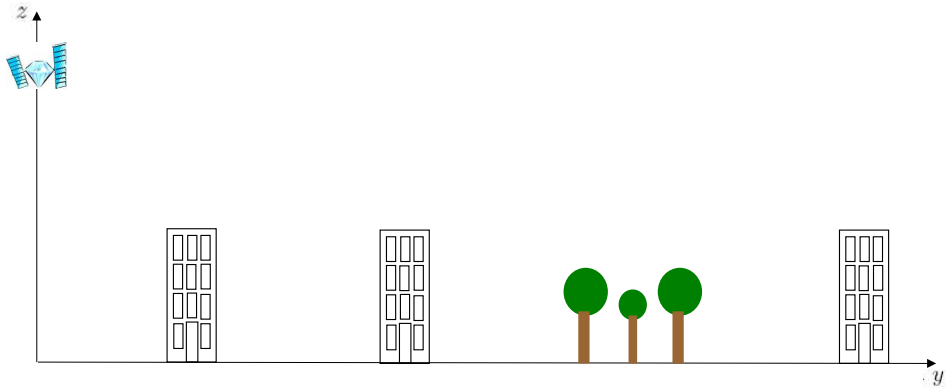

Figure 5.49: Diagram of the large scene containing three tall buildings and a spacious courtyard with trees.

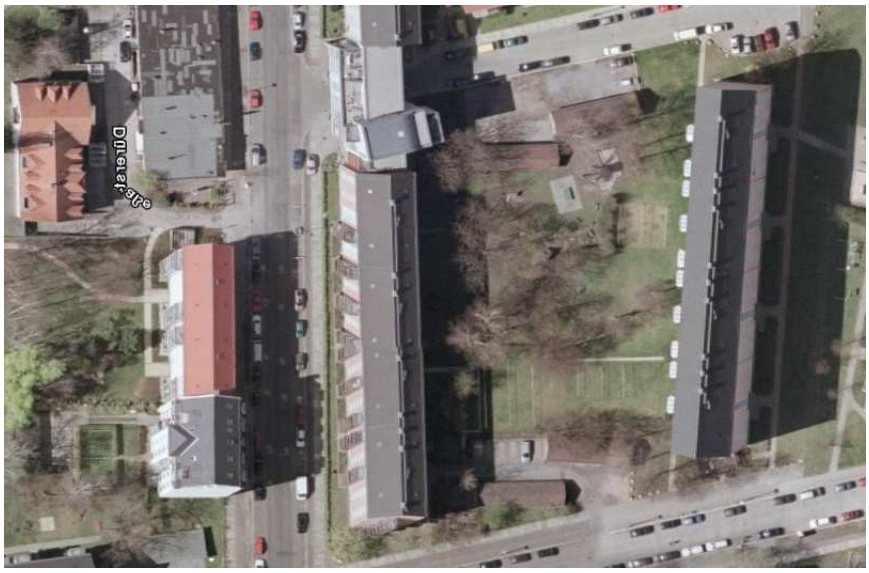

Figure 5.50: Optical image of the large scene (copyright Google Earth).

Figure 5.51: Optical image. Left: Building number two, right: Building number three (copyright G.S.).

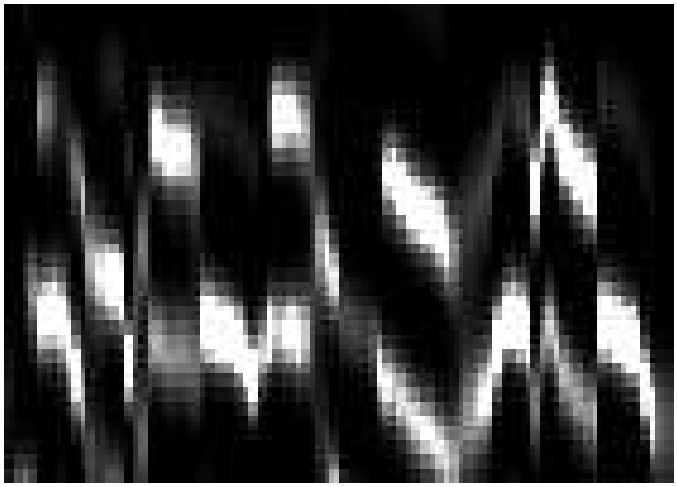

Figure 5.52: Large scene containing three buildings and a spacious courtyard: Single polarization MUSIC pseudo-tomographic slice, model order fixed to one.

dimensional image can be interpreted rather easily, whereas the scattering processes of the SP MUSIC MO 1 and FP MUSIC MO 2 methods are more difficult to analyze.

The interpretation of the reflection pattern is facilitated by the optimal MUSIC scattering vectors $\mathbf{k}_{\min}$: Figures 5.55 and 5.56 illustrate the reflection mechanisms of the fully polarimetric MUSIC technique with model order fixed to one and two, respectively. The wall-ground interaction points of the three buildings are associated with the second component of the Pauli polarization basis ($hh - vv$). At the roofs, the first ($hh + vv$) and second contributions are dominant. Inside the courtyard, the backscattering of an object at around 10 m is related to the third term of the Pauli basis (hv). The rather broad peak and the high sidelobes below 0 m suggest that it represents the response of a distributed target such as a tree canopy. The strong signal at approximately 0 m on its right side might be caused by backscattering from the tree trunk-ground.

Finally, a second large scene consisting of two oriented buildings and a courtyard is analyzed. The pseudo-tomograms are evaluated along the sample line in figure 5.57 by the single polarization and fully polarimetric MUSIC algorithms with model order one. At the left and right side of the three-dimensional images depicted in figures 5.58 and 5.59, the contributions from the wall-ground interaction samples at the topographic height and from the roof at approximately 15 m are noticeable. Inside the courtyard, there are some targets at the ground and at a height of around 8 m that may originate from a barrack. This interpretation is backed by the pseudo-tomographic slice of the optimal MUSIC scattering mechanisms illustrated

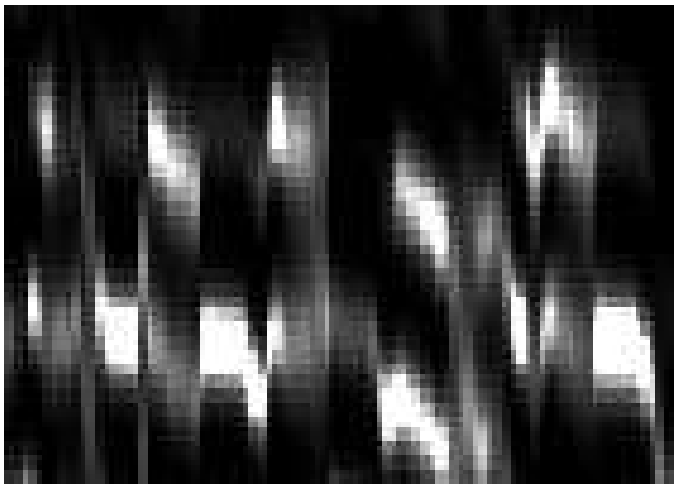

Figure 5.53: Large scene: Fully polarimetric MUSIC pseudo-tomographic slice, model order fixed to one.

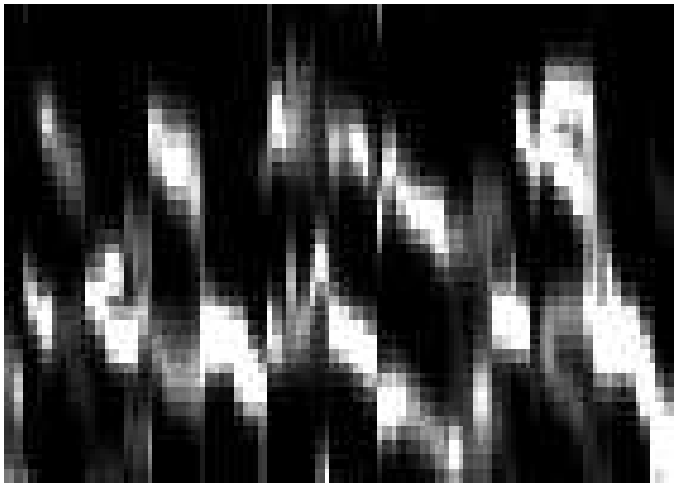

Figure 5.54: Large scene: Fully polarimetric MUSIC pseudo-tomographic slice, model order fixed to two.

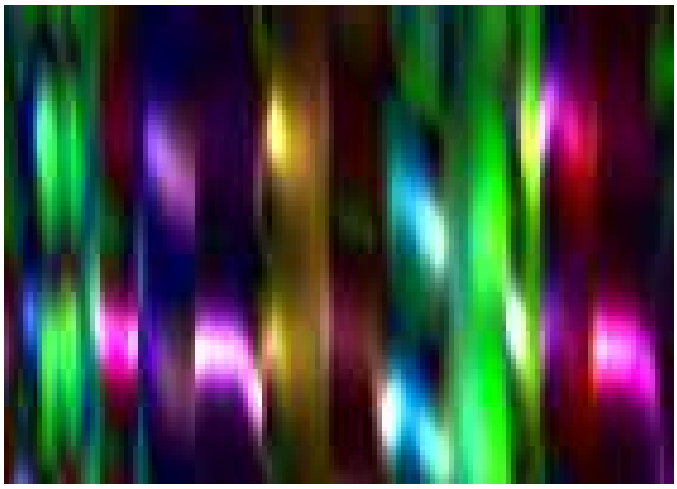

Figure 5.55: Large scene: Pseudo-tomographic slice of the optimal MUSIC scattering mechanisms $\mathbf{k}_{\min}$, model order fixed to one.

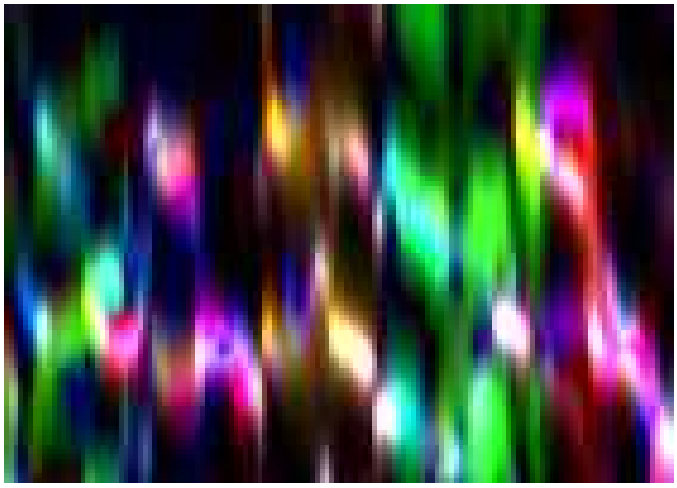

Figure 5.56: Large scene: Pseudo-tomographic slice of the optimal MUSIC scattering mechanisms $\mathbf{k}_{\min}$, model order fixed to two.

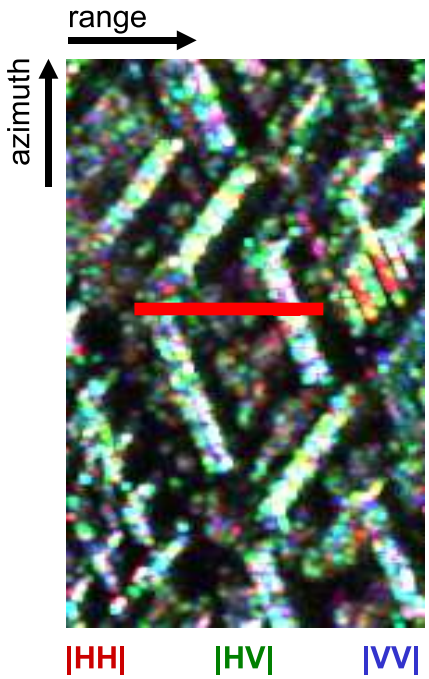

Figure 5.57: Large scene containing two oriented buildings. Azimuth is on the left hand side. The sample line is marked by red color.

in figure 5.60. In the center of the courtyard, a strong backscattering with dominant $hh-vv$ component at 0 m and a reflection related to hv at around 8 m on its left side can be discerned.

The generation of three-dimensional (3D) images from polarimetric dual-baseline interferometric SAR observations can be summarized as follows: The single polarization and fully polarimetric beamforming methods produce tomographic slices with low resolution and strong sidelobes. Even though the single polarization and fully polarimetric Capon algorithms refine the spectral peaks and reduce the leakage problem, it is still difficult to analyze the tomograms of the building layover. The single polarization MUSIC technique of model order two estimates an average phase. The pseudo-reflectivities determined by the polarimetric ML estimator are rather strong on one side so that the sources in the other parts of the sample line cannot be recognized. The 3D images computed by the single polarization and fully polarimetric MUSIC algorithms with model order set to one show very high resolution and considerably diminished leakage: In far range, contributions associated with the wall-ground interaction points are clearly detected. In near range, the reflectors are related to the building wall and top. The pseudo-tomographic slice of the polarimetric MUSIC technique whose model order is fixed to two exhibits one signal at the building base in far range.

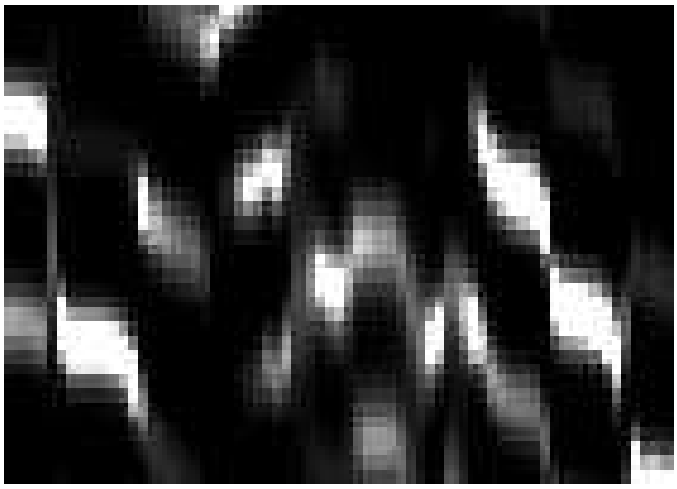

Figure 5.58: Large scene containing two oriented buildings: Single polarization MUSIC pseudo-tomographic slice, model order fixed to one.

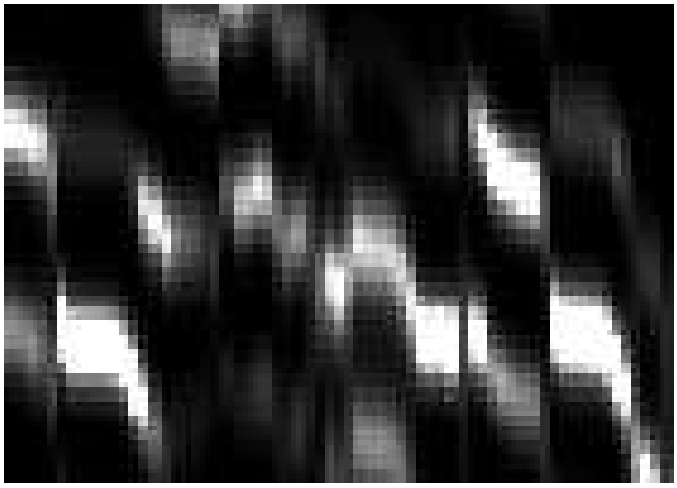

Figure 5.59: Large scene containing two oriented buildings: Fully polarimetric MUSIC pseudo-tomographic slice, model order fixed to one.

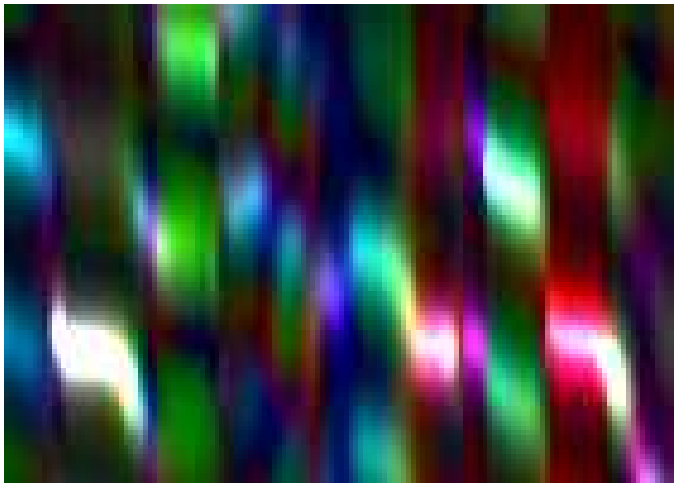

Figure 5.60: Large scene containing two oriented buildings: Pseudo-tomographic slice of the optimal MUSIC scattering mechanisms $\mathbf{k}_{\min}$, model order fixed to one.

Compared to the MUSIC methods of order one the spectral pattern is broadened due to overmodeling or a target near the ground-wall interaction points. For the samples closer to the antenna positions, the polarimetric MUSIC of model order two is capable of identifying two neighboring objects within one azimuth-range resolution cell: The first scatterer is located at the building roof, the second along the wall. The height separation is much lower than the height of ambiguity of the large baseline, i.e., far beyond the Rayleigh resolution.

The 3D image interpretation is enhanced by investigating the optimal polarimetric MUSIC scattering mechanisms: For the wall-ground interaction samples double bounce is dominant. The backscattering from the building roof corresponds to surface reflection. The polarimetric MUSIC technique of model order two is apt to distinguish two close targets that are linked to distinct polarization behavior: The reflection caused by the roof is related to surface scattering, the objects along the wall to double bounce.

Finally, large heterogeneous scenes have been examined containing several edifices, other man-made items, and diverse vegetation. The building base and roof are visibly diagnosed both for oriented and non-oriented buildings. Furthermore, electromagnetic processes generated by natural environments can be measured and their height extracted.

5.5 Conclusions

In this chapter, array signal processing techniques have been applied to fully polarimetric dual-baseline InSAR observations of an urban environment.

First, the number of backscattering sources has been determined by polarimetric model order selection methods. The maximum number of detectable components is two for single polarization dual-baseline InSAR data, whereas it is eight in a fully polarimetric dual-baseline interferometric SAR configuration with equal cross-polarizations. The estimation results of the single polarization and polarimetric detection techniques are rather similar, if the number of sources is limited to two for comparison purposes. In particular inside building layover the number of signal components retrieved by the fully polarimetric algorithm is two or more.

The scatterer height and reflection processes have been extracted from fully polarimetric single-baseline InSAR measurements. The polarimetric MUSIC technique determines both the building height and the associated scattering mechanisms generating a three-dimensional model of a large urban scene that comprises the reflection types.

Subsequently, a complex urban area has been analyzed by means of dual-baseline polarimetric InSAR data. First, the layover of a single building has been examined in detail employing the (pseudo-)spectra and three-dimensional imaging: The single polarization (SP) and fully polarimetric (FP) beamforming techniques lead to spectra characterized by low resolution and strong sidelobes. Although the SP and FP Capon methods are appropriate to narrow the spectral peaks and alleviate the leakage problem, it remains complicated to discern the various features in building layover. The single polarization MUSIC algorithm with model order set to two and the single polarization ML estimator identify only the height of one contribution having quite good and very weak sidelobe suppression, respectively.

The pseudo-spectra and three-dimensional images evaluated by the MUSIC techniques both with and without polarization diversity whose model order is fixed to one exhibit fine resolution and noticeably reduced leakage: For the wall-ground interaction samples in far range, one backscattering source at the topographic height is detected. The elevation of two components can be determined inside one azimuth-range resolution cell close to the sensor position, corresponding to the ground and the building top. Whereas the spectral patterns of the polarimetric MUSIC of model order one and the polarimetric ML estimator resemble, the pseudo-tomogram produced by the polarimetric MLE shows a dominant scatterer in one part of the slice. The three-dimensional image of the polarimetric MUSIC method with model order fixed to two (MO 2) reveals one target at the building base in far range. Overmodeling or an object near the ground-wall interaction points blur slightly the peak in comparison with the polarimetric MUSIC approach of model order one. For samples close to the antenna location, the polarimetric MUSIC MO 2 algorithm recognizes two neighboring constituents within a single azimuth-range resolution cell: One reflector is positioned at the building top, the other along the wall. The height separation is far beyond the Rayleigh resolution, i.e., much lower than the height

of ambiguity of the large baseline. The spectral behavior of the polarimetric MUSIC method of model order three is quite similar.

Investigating the optimal polarimetric MUSIC reflection types supports the three-dimensional image interpretation: Double bounce prevails at the wall-ground interaction samples. The scatterers caused by the roof are related to surface reflection. In near range, the polarimetric MUSIC technique of model order two differentiates two close sources associated with disparate polarization signatures: Besides surface scattering from the building top, the targets along the wall correspond to double bounce.

Finally, large heterogeneous urban scenes have been analyzed consisting of several buildings, other man-made objects, and diverse vegetation. The building base and roof are conspicuous both for oriented and non-oriented edifices. Additionally, the height of backscattering phenomena induced by distributed environments has been retrieved.

Among the spectral estimation techniques, the MUSIC algorithms, especially the polarimetric MUSIC, offer the best performance: They are most robust to process data acquired by an irregular array configuration. These methods are capable of resolving the building layover problem, i.e., separating two components within one azimuth-range resolution cell.

Chapter 6

Conclusions and Perspectives

In this thesis, spectral analysis techniques have been generalized to process polarimetric multibaseline interferometric SAR data. These polarimetric array signal processing algorithms have been described in a rigorous mathematical way and applied to urban areas. They permit the estimation of the reflector height, the scattering mechanism, and the polarimetric reflectivity. From single-baseline POL-InSAR observations, a digital elevation model of an urban scene has been generated including the scattering types. Using polarimetric dual-baseline InSAR data, the building layover problem has been resolved and three-dimensional SAR images have been produced that reveal the reflection mechanisms.

Basic and advanced concepts of Synthetic Aperture Radar have been presented in chapter 2: First, basic properties of SAR data have been explained. Two conventional extensions of single-channel SAR, namely SAR polarimetry and SAR interferometry have been introduced and two advanced multichannel SAR approaches have been outlined: Polarimetric SAR interferometry and multibaseline InSAR including SAR tomography.

In chapter 3, spectral analysis techniques to process multibaseline interferometric single polarization SAR images have been detailed. While the well-known stochastic signal model describes extended scatterers and comprises the speckle phenomenon as multiplicative noise, the deterministic multibaseline InSAR data model represents the response from point-like reflectors. These two approaches have been joined to form the hybrid model. To determine the number of backscattering sources model order selection algorithms have been elaborated. They are based on the application of information theoretic criteria and employ the eigenvalues of the covariance matrix. Subsequently, spectral estimation methods have been explained. They compute both the spatial frequency to extract the reflector height and resolve the layover problem and the reflectivity to generate 3D images. The spatial frequency and reflectivity are retrieved by the nonparametric beamforming and Capon algorithms that do not make any assumption about

the statistical properties of the received signals. The model-based superresolution MUSIC technique calculates the spatial frequency and the linear least-squares method the reflectivity. The superresolution M-RELAX estimates both the spatial frequency and the reflectivity. Finally, a maximum likelihood estimator which relies on the stochastic signals model has been derived: It solves the combined detection-estimation problem. In contrast to MUSIC, it is even optimal for fully correlated signals.

Array signal processing methods have been adapted to the polarimetric multibaseline interferometric SAR configuration in chapter 4 based on the following idea: In passive sensor systems, the antennas merely receive the signals in diverse polarizations resulting in two polarization states. In contrast, in the context of SAR the sensors are active and both transmit the electromagnetic waves and receive the echo of the reflected signals in polarimetric mode leading to up to four polarization channels. First, the signal models have been generalized to take polarization diversity into account yielding the notion of the multibaseline polarimetric interferometric steering vector. It is a linear combination of four vectors each related to one specific polarization.

The generalization of the model order selection algorithms to determine the number of sources from MB POL-InSAR measurements has been introduced. Subsequently, the spectral estimation techniques have been extended to the polarimetric multibaseline InSAR case. The adaptation to the polarimetric scenario not only increases the number of observables, but particularly computes the optimal polarization combination for spatial frequency estimation. These polarimetric methods allow the extraction of the spatial frequencies, the corresponding optimal scattering vectors, and the polarimetric reflectivities. The optimal reflection mechanisms permit the examination of the scatterer physical characteristics by analyzing their polarimetric behavior. The nonparametric beamforming and Capon algorithms have been adapted to the multibaseline POL-InSAR configuration to retrieve the spatial frequencies, the associated optimal reflection types, and the polarimetric reflectivities. As model-based polarimetric techniques, the superresolution MUSIC and M-RELAX approaches have been developed to estimate the spatial frequency and the related scattering mechanism. The linear least-squares method and M-RELAX extract the polarimetric reflectivity. Finally, the polarimetric maximum likelihood estimator has been conceived for solving the joint detection-estimation problem from MB POL-InSAR observations. These polarimetric spectral analysis techniques have been derived in their most general form: They can be used in polarimetric multibaseline InSAR configurations in all possible combinations. Their mathematical properties have been elaborated.

In chapter 5, array signal processing techniques have been applied to fully polarimetric dual-baseline interferometric SAR measurements of an urban scene.

First, the number of backscattering sources has been extracted by polarimetric model order selection algorithms. The maximum number of detectable signals is two for single polarization dual-baseline InSAR observations, whereas it is eight in a fully polarimetric dual-baseline interferometric SAR scenario with equal cross-polarizations. The estimation results of the single polarization and polarimetric detection methods resemble strongly, if the number of sources is restricted to two for comparison purposes. In particular inside building layover the number of components determined by the fully polarimetric algorithm is two or more.

The reflection height and scattering processes have been retrieved using fully polarimetric single-baseline InSAR data. The polarimetric MUSIC technique estimates both the building height and the related reflection mechanisms generating a three-dimensional model of a large urban area that contains the scattering types.

Subsequently, a complex urban scene has been investigated using fully polarimetric dual-baseline interferometric SAR observations. First, the layover of one building has been studied thoroughly by means of the spectra and three-dimensional imaging: The single polarization and fully polarimetric beamforming algorithms produce spectra with broad peaks and high sidelobes. Even though the single polarization and polarimetric Capon methods refine the resolution and diminish the leakage problem, it remains difficult to analyze the tomograms of the building layover. The single polarization MUSIC technique of model order two and the single polarization ML estimator detect only the height of one source showing rather good and very weak sidelobe reduction, respectively.

The pseudo-spectra and three-dimensional images computed by the single polarization and fully polarimetric MUSIC algorithms with model order set to one possess narrow spectral peaks and visibly decreased sidelobes: In far range, one backscattering component is detected at the topographic height for the wall-ground interaction samples. The elevation of two targets can be extracted inside a single azimuth-range resolution cell close to the antenna location, associated with the ground and the building top. Whereas the spectral patterns of the polarimetric MUSIC with model order one and the polarimetric ML estimator are quite similar, the pseudo-tomographic slice generated by the polarimetric MLE exhibits a dominant reflector in one part of the image. The three-dimensional image of the polarimetric MUSIC method of model order two reveals one signal at the ground-wall interaction points in far range. Compared to the MUSIC algorithms with order one the spectral peaks are broadened due to overmodeling or objects near the building base. For the samples closer to the sensor position, the polarimetric MUSIC with model order two identifies two neighboring scatterers within one azimuth-range resolution cell: The first target is located at the building top, the second along the wall. The height separation is much lower than the height of ambiguity of the large baseline, i.e., far beyond

the Rayleigh resolution. The spectral behavior of the polarimetric MUSIC methods with model order two and three is alike.

The three-dimensional image interpretation is facilitated by examining the optimal polarimetric MUSIC scattering mechanisms: Double bounce is dominant for the wall-ground interaction points. The scatterers at the roof are linked to surface reflection. The polarimetric MUSIC algorithm of model order two differentiates two close sources that are associated with distinct polarization signatures: The reflection caused by the roof is related to surface scattering, the targets along the wall to double bounce.

Finally, large heterogeneous urban scenes have been analyzed containing several buildings, other man-made items, and diverse vegetation. The building base and roof are recognized both for oriented and non-oriented edifices. Moreover, the height of reflection effects generated by natural distributed environments has been determined.

The MUSIC methods, in particular the polarimetric MUSIC, possess the best performance among the spectral estimation techniques: They are most robust to process data acquired by a nonuniform nonlinear sensor array. These techniques are capable of solving the building layover problem, i.e., recovering two components within one azimuth-range resolution cell.

Two main directions of further investigations should be pursued:

Firstly, the conceived methods should be applied to tomographic datasets consisting of more than two baselines. This will provide an enhanced insight into the reflection phenomena occuring in densely built-up scenes such as multipath propagation effects. Moreover, using the proposed algorithms on tomographic observations with a larger number of tracks the three-dimensional modeling and imaging quality shall be improved with respect to increased resolution in the vertical direction and sidelobe suppression. Furthermore, the performance of fully polarimetric and dual polarization approaches shall be compared: It is anticipated that co-polarized channels ($hh + vv$ and $hh - vv$) are most important in urban areas, whereas co- and cross-polarized measurements (e.g., vv and hv) are essential for forested scenes. With regard to current and future satellite missions, the polarimetric algorithms shall be also examined over urban environments in other frequency bands. These studies can be carried out on existing airborne datasets, e.g., from the E-SAR system of DLR. Finally, the techniques shall be applied to space-borne observations from TerraSAR-X and TanDEM-X in sceneries with stable reflectors like in mountainous and urban areas by employing the Spotlight interferometric constellation [48].

Secondly, additional spectral analysis techniques might be developed and applied in the future. For instance, the M-APES algorithm produces normally better reflectivity estimates than Capon. It has not been employed in the framework of this thesis since M-APES yields generally lower resolution than Capon [59] and is therefore not suitable for closely spaced

signals [36, 63]. Additionally, its performance degrades for irregularly sampled data. To account for array miscalibrations, robust beamforming methods such as robust Capon [51, 60, 61] might be utilized. As the MUSIC method possesses a certain degree of inherent robustness to steering vector errors [62], robust beamformers have not been investigated in the context of this work.

Appendix A

Derivation of the Standard Model Order Selection Techniques

In this appendix an approach for solving the detection problem based on the application of information theoretic criteria using the eigenvalues of the covariance matrix is elaborated. First the data model is introduced and the problem is formulated. Subsequently the the model order selection techniques are derived.

A.1 Data Model and Problem Formulation

To solve the detection problem, i.e., to estimate the number of sources, Wax et Kailath [110] have used a model similar to the one described in subsection 3.1.1, where the received signal vector $\mathbf{y}(l)$ is given by

$$\mathbf{y}(l) = \sum_{i=1}^{N_s} s_i(l)\mathbf{a}(\boldsymbol{\theta}_i) + \mathbf{n}(l). \tag{A.1}$$

The N_s sources with $N_s < p$, are assumed to have linearly independent steering vectors $\mathbf{a}(\boldsymbol{\theta}_i)$. The objective is to estimate the number of sources N_s. The returned signal can be expressed in matrix formulation as

$$\mathbf{y}(l) = \mathbf{A}\mathbf{s}(l) + \mathbf{n}(l) \tag{A.2}$$

with the matrix $\mathbf{A} = [\mathbf{a}(\boldsymbol{\theta}_1), \ldots, \mathbf{a}(\boldsymbol{\theta}_{N_s})] \in \mathbf{Mat}_{p,N_s}(\mathbb{C})$. The data covariance matrix $\mathbf{R} = E\{\mathbf{y}(l)\mathbf{y}^H(l)\} \in \mathbf{Mat}_p(\mathbb{C})$ is

$$\mathbf{R} = \mathbf{A}\mathbf{S}\mathbf{A}^H + \sigma_n^2\mathbf{I}. \tag{A.3}$$

The assumption that the vectors $\mathbf{a}(\boldsymbol{\theta}_i)$ are linearly independent is equivalent to the fact that the matrix $\mathbf{A}$ has full column rank, $\text{rank}(\mathbf{A}) = N_s$.

Furthermore, assuming that the signal covariance matrix is nonsingular, $\text{rank}(\mathbf{S}) = N_s$, it follows that $\text{rank}(\mathbf{ASA}^H) = N_s$ and the $p - N_s$ smallest eigenvalues of this matrix are all equal to zero. Let $\lambda_1 \geq \cdots \geq \lambda_p$ be the eigenvalues of the covariance matrix $\mathbf{R}$ in descending order. Then the smallest $p - N_s$ eigenvalues $\lambda_i = \sigma_n^2$ for $i = N_s + 1, \ldots, p$. Hence, the number of sources can be retrieved by the multiplicity of the smallest eigenvalues. The problem is that the covariance matrix is unknown and has to be estimated from a finite dataset. This implies unequal eigenvalues with probability one. Moreover in the application of detecting the number of signals from single polarization multibaseline InSAR data, the above described model for order selection and the MB InSAR data model from section 3.1.4 differ in several ways: The deterministic component leads to a received data vector with nonzero mean and the stochastic part comprises the speckle effect as multiplicative noise.

A.2 Model Order Selection Techniques

Let $k \in \{0, 1, \ldots, p-1\}$ be the assumed number of sources and let $\lambda_1 \geq \cdots \geq \lambda_p$ and $\mathbf{v}_1, \ldots, \mathbf{v}_p$ be the eigenvalues and eigenvectors, respectively, of the covariance matrix $\mathbf{R}$. Using the spectral theorem for Hermitian matrices [102], the covariance matrix $\mathbf{R}(\boldsymbol{\theta}(k))$ that comprises k sources can be written as

$$\mathbf{R}(\boldsymbol{\theta}(k)) = \sum_{i=1}^{p} \lambda_i \mathbf{v}_i \mathbf{v}_i^H = \sum_{i=1}^{k} (\lambda_i - \sigma_n^2) \mathbf{v}_i \mathbf{v}_i^H + \sigma_n^2 \mathbf{I}. \tag{A.4}$$

Hence, the model is described by the parameter vector

$$\boldsymbol{\theta}(k) = (\lambda_1, \ldots, \lambda_k, \sigma_n^2, \mathbf{v}_1^T, \ldots, \mathbf{v}_k^T)^T. \tag{A.5}$$

First the log-likelihood of the maximum likelihood estimator of the model parameters is derived [110]: Since the samples are assumed to be statistically independent and identically distributed with

$$\mathbf{y}(l) \,|\, \boldsymbol{\theta}(k) \sim \mathcal{N}_{\mathbb{C}}^k(\mathbf{0}, \mathbf{R}(\boldsymbol{\theta}(k))) \tag{A.6}$$

their joint probability density is

$$f(\{\mathbf{y}(l)\} \,|\, \boldsymbol{\theta}(k)) = \prod_{l=1}^{L} \frac{1}{\det[\pi \mathbf{R}(\boldsymbol{\theta}(k))]} \exp\{-\mathbf{y}^H(l) \mathbf{R}^{-1}(\boldsymbol{\theta}(k)) \mathbf{y}(l)\}. \tag{A.7}$$

Employing the sample covariance matrix defined by

$$\hat{\mathbf{R}} = \frac{1}{L} \sum_{l=1}^{L} \mathbf{y}(l) \mathbf{y}^H(l) \tag{A.8}$$

this probability density can be rewritten as

$$f(\{\mathbf{y}(l)\}\,|\,\boldsymbol{\theta}(k)) = \det[\pi\mathbf{R}(\boldsymbol{\theta}(k))]^{-L} \exp\left\{-L\mathrm{tr}\left[\mathbf{R}^{-1}(\boldsymbol{\theta}(k))\hat{\mathbf{R}}\right]\right\}. \quad \text{(A.9)}$$

Ignoring constants that are independent of $\boldsymbol{\theta}(k)$ the log-likelihood function is given by

$$\log f(\mathbf{Y}\,|\,\boldsymbol{\theta}(k)) = -L\log\det[\mathbf{R}(\boldsymbol{\theta}(k))] - L\mathrm{tr}\left[\mathbf{R}^{-1}(\boldsymbol{\theta}(k))\hat{\mathbf{R}}\right]. \quad \text{(A.10)}$$

Using the eigenvalues $\hat{\lambda}_1 > \cdots > \hat{\lambda}_p$ of the sample covariance matrix $\hat{\mathbf{R}}$ the log-likelihood of the maximum likelihood estimator of the model parameters can be formulated as [110]

$$\log f(\mathbf{Y}\,|\,\hat{\boldsymbol{\theta}}(k)) = (p-k)L\log\left(\frac{\prod_{i=k+1}^{p}\hat{\lambda}_i^{1/(p-k)}}{\frac{1}{p-k}\sum_{i=k+1}^{p}\hat{\lambda}_i}\right). \quad \text{(A.11)}$$

To calculate the number of free real-valued parameters $\eta(k)$, the dimension of the space spanned by $\boldsymbol{\theta}(k)$ has to be determined: Since the eigenvalues of the covariance matrix are real-valued, they contribute k degrees of freedom (DoF). The k complex eigenvectors form an orthonormal basis of the matrix space $\mathbf{Mat}_{p,k}(\mathbb{C})$ with $\dim(\mathbf{Mat}_{p,k}(\mathbb{C})) = 2pk$. The normalization decreases the DoF by $2k$, the mutual orthogonalization by

$$2\sum_{i=1}^{k-1} i = 2\frac{1}{2}k(k-1). \quad \text{(A.12)}$$

Hence, the orthonormal eigenvectors span a space of dimension $2pk - 2k - k(k-1) = k(2p-1-k)$. Thus, the degrees of freedom for the single polarization multibaseline interferometric configuration are

$$\eta(k) = k + 1 + k(2p-1-k) = k(2p-k) + 1. \quad \text{(A.13)}$$

Appendix B

Derivation of the Beamforming, Capon, and MUSIC Methods

In this appendix the beamforming, Capon, and MUSIC algorithms are derived.

The following result on linearly constrained quadratic minimization [107] is necessary to derive both the single polarization and polarimetric nonparametric spectral estimation techniques such as beamforming and Capon:

Theorem 1 *Let* $\mathbf{D} \in \mathbf{Mat}_n(\mathbb{C})$ *be a Hermitian positive definite matrix, and let* $\mathbf{X} \in \mathbf{Mat}_{n,m}(\mathbb{C})$, $\mathbf{G} \in \mathbf{Mat}_{n,k}(\mathbb{C})$, *and* $\mathbf{C} \in \mathbf{Mat}_{m,k}(\mathbb{C})$. *Assume that* $\mathbf{G}$ *has full column rank equal to* k *(hence* $n \geq k$*). Then the unique solution to the minimization problem*

$$\min_{\mathbf{X}} \mathbf{X}^H \mathbf{D} \mathbf{X} \qquad \textit{subject to} \qquad \mathbf{X}^H \mathbf{G} = \mathbf{C} \tag{B.1}$$

is given by

$$\mathbf{X}_0 = \mathbf{D}^{-1}\mathbf{G}\left(\mathbf{G}^H\mathbf{D}^{-1}\mathbf{G}\right)^{-1}\mathbf{C}^H. \tag{B.2}$$

The proof can be found in [107].

If $m = k = 1$ and $\mathbf{C} = 1$, then $\mathbf{X}, \mathbf{G} \in \mathbb{C}^n$ and

$$\mathbf{X}_0 = \frac{\mathbf{D}^{-1}\mathbf{G}}{\mathbf{G}^H\mathbf{D}^{-1}\mathbf{G}}. \tag{B.3}$$

B.1 Derivation of the Classical Beamforming Method

The beamforming method for spatial frequency estimation can be derived as a Finite Impulse Response (FIR) filter [107]. The basic principle for the filter

design is that it lets the signals associated with a particular spatial frequency pass undistorted while attenuating the signals at all other frequencies. This can be formulated in the following mathematical way: The filtered signal is defined as

$$y_F(l) = \mathbf{h}^H \mathbf{y}(l) \tag{B.4}$$

with the filter $\mathbf{h} = [h_0, \ldots, h_{p-1}]^T \in \mathbb{C}^p$ and the spatial samples $\mathbf{y}(l) \in \mathbb{C}^p, l = 1, \ldots, L$. Then the power of the spatially filtered signal is

$$E\{|y_F(l)|^2\} = \mathbf{h}^H \mathbf{R} \mathbf{h} \tag{B.5}$$

with the data covariance matrix $\mathbf{R} = E\{\mathbf{y}(l)\mathbf{y}^H(l)\} \in \mathbf{Mat}_p(\mathbb{C})$. The first condition of the filter construction translates to $\mathbf{h}^H \mathbf{a}(\omega) = 1$. Under the assumption that the received data $\mathbf{y}(l)$ is spatially white with $\mathbf{R} = \mathbf{I}$, the power of the filtered signal (B.5) takes the form $E\{|y_F(l)|^2\} = \mathbf{h}^H \mathbf{h}$. Hence, the minimization problem of the beamforming method can be stated as [107]

$$\min_{\mathbf{h}} \mathbf{h}^H \mathbf{h} \qquad \text{subject to} \qquad \mathbf{h}^H \mathbf{a}(\omega) = 1. \tag{B.6}$$

The derivation of the beamforming filter employing the theorem from linearly constrained quadratic minimization leads to

$$\mathbf{h}_{BF} = \frac{\mathbf{a}(\omega)}{\mathbf{a}^H(\omega)\mathbf{a}(\omega)} = \frac{\mathbf{a}(\omega)}{p} \tag{B.7}$$

where the second equation follows from the property of the steering vector $\mathbf{a}^H(\omega)\mathbf{a}(\omega) = p$ (cf. equations (3.2) and (3.4)). Plugging the filter (B.7) into (B.5), the power of the filtered signal is

$$E\{|y_F(l)|^2\} = \frac{\mathbf{a}^H(\omega)\mathbf{R}\mathbf{a}(\omega)}{p^2}. \tag{B.8}$$

Since the data covariance matrix $\mathbf{R}$ is not available, it has to be replaced by the finite sample estimate $\hat{\mathbf{R}} \in \mathbf{Mat}_p(\mathbb{C})$

$$\hat{\mathbf{R}} = \frac{1}{L} \sum_{l=1}^{L} \mathbf{y}(l)\mathbf{y}^H(l). \tag{B.9}$$

Finally, the spectrum of the beamforming method is obtained as

$$\hat{P}_{BF}(\omega) = \frac{1}{p^2 L} \sum_{l=1}^{L} |\mathbf{a}^H(\omega)\mathbf{y}(l)|^2 = \frac{\mathbf{a}^H(\omega)\hat{\mathbf{R}}\mathbf{a}(\omega)}{p^2}. \tag{B.10}$$

The frequency estimates $\hat{\boldsymbol{\omega}} = [\hat{\omega}_1, \ldots, \hat{\omega}_{N_s}]^T$ correspond to the locations of the N_s maxima of the spectrum. Since the interferometric phase φ is related to the spatial frequency $\omega, \omega \in [-\pi, \pi)$, by $\varphi = (p-1)\omega$ (see equation (3.3)), the unambiguous estimation range for φ is $[-(p-1)\pi, (p-1)\pi)$ in the case of uniform linear arrays. The achievable resolution that is called the Rayleigh limit [107] is approximately λ/arraylength. The Rayleigh limit of the interferometric phase [37] is $\Delta\varphi_{BF} = 2\pi(p-1)/p$. The reflectivity estimate at frequency $\hat{\omega}_i$ is determined by $\hat{\tau}_i = \hat{P}_{BF}(\hat{\omega}_i)$.

B.2 Derivation of the Standard Capon Algorithm

In the derivation of the beamforming technique it was assumed that the received signal is spatially white with unit variance, i.e., $\mathbf{R} = \mathbf{I}$. For designing the Capon method the identity matrix $\mathbf{I}$ is replaced by the covariance matrix $\mathbf{R}$ so that the minimization problem reads [11]

$$\min_{\mathbf{h}} \mathbf{h}^H \mathbf{R} \mathbf{h} \qquad \text{subject to} \qquad \mathbf{h}^H \mathbf{a}(\omega) = 1. \tag{B.11}$$

The derivation of the Capon filter using the theorem from quadratic minimization yields

$$\mathbf{h}_C = \frac{\mathbf{R}^{-1}\mathbf{a}(\omega)}{\mathbf{a}^H(\omega)\mathbf{R}^{-1}\mathbf{a}(\omega)}. \tag{B.12}$$

Inserting $\mathbf{h}_C$ into equation (B.5) the filtered signal power is

$$E\{|y_F(l)|^2\} = \frac{1}{\mathbf{a}^H(\omega)\mathbf{R}^{-1}\mathbf{a}(\omega)}. \tag{B.13}$$

Utilizing the sample covariance matrix $\hat{\mathbf{R}}$, the Capon spectrum is given by [11]

$$\hat{P}_C(\omega) = \frac{1}{\mathbf{a}^H(\omega)\hat{\mathbf{R}}^{-1}\mathbf{a}(\omega)}. \tag{B.14}$$

The inverse matrix $\hat{\mathbf{R}}^{-1}$ exists under the condition that the noise term has a positive definite covariance matrix and $L \geq p$. The frequency estimates $\hat{\boldsymbol{\omega}} = [\hat{\omega}_1, \ldots, \hat{\omega}_{N_s}]^T$ are associated with the frequencies of the N_s highest peaks of the spectrum $\hat{P}_C$. The reflectivity at frequency $\hat{\omega}_i$ is estimated by $\hat{\tau}_i = \hat{P}_C(\hat{\omega}_i)$.

B.3 Derivation of the Polarimetric Beamforming and Capon Filters

As introduced in subsection 4.3.1 the polarimetric beamforming design problem reads

$$\min_{\mathbf{h}} \mathbf{h}^H \mathbf{h} \qquad \text{subject to} \qquad \mathbf{h}^H \mathbf{b}(\omega, \mathbf{k}) = 1. \tag{B.15}$$

From equation (4.2) and $\|\mathbf{k}\|_2 = 1$ it follows for the multibaseline polarimetric interferometric steering vector $\mathbf{b}(\omega, \mathbf{k}) \in \mathbb{C}^{\tilde{p}}$

$$\mathbf{b}(\omega, \mathbf{k})^H \mathbf{b}(\omega, \mathbf{k}) = \mathbf{a}^H(\omega)\mathbf{a}(\omega) \sum_{i=1}^{N_{pol}} k_i^* k_i = p\|\mathbf{k}\|_2^2 = p. \tag{B.16}$$

Utilizing the quadratic minimization theorem leads to the polarimetric beamforming filter

$$\mathbf{h}_{BF}^P = \frac{\mathbf{b}(\omega, \mathbf{k})}{\mathbf{b}^H(\omega, \mathbf{k})\mathbf{b}(\omega, \mathbf{k})} = \frac{\mathbf{b}(\omega, \mathbf{k})}{p}. \tag{B.17}$$

The property (4.15) of the stochastic MBPI steering vector $\mathbf{b}(\boldsymbol{\omega}, \mathbf{k}) \in \mathbb{C}^{\tilde{p}}$ implies

$$\mathbf{b}(\boldsymbol{\omega}, \mathbf{k})^H \mathbf{b}(\boldsymbol{\omega}, \mathbf{k}) = \sum_{i=1}^{N_{pol}} k_i^* k_i \mathbf{a}^H(\omega_i)\mathbf{a}(\omega_i) = p\|\mathbf{k}\|_2^2 = p. \tag{B.18}$$

Then the polarimetric beamforming filter is obtained as

$$\mathbf{h}_{BF}^{P2} = \frac{\mathbf{b}(\boldsymbol{\omega}, \mathbf{k})}{\mathbf{b}^H(\boldsymbol{\omega}, \mathbf{k})\mathbf{b}(\boldsymbol{\omega}, \mathbf{k})} = \frac{\mathbf{b}(\boldsymbol{\omega}, \mathbf{k})}{p}. \tag{B.19}$$

Like in subsection 4.3.2 the minimization problem of the polarimetric Capon method is expressed by

$$\min_{\mathbf{h}} \mathbf{h}^H \mathbf{R} \mathbf{h} \qquad \text{subject to} \qquad \mathbf{h}^H \mathbf{b}(\omega, \mathbf{k}) = 1. \tag{B.20}$$

Plugging the FIR filter $\mathbf{h} \in \mathbb{C}^{\tilde{p}}$ and the MBPI steering vector $\mathbf{b}(\omega, \mathbf{k}) \in \mathbb{C}^{\tilde{p}}$ into theorem 1 gives the polarimetric Capon filter

$$\mathbf{h}_C^P = \frac{\mathbf{R}^{-1}\mathbf{b}(\omega, \mathbf{k})}{\mathbf{b}^H(\omega, \mathbf{k})\mathbf{R}^{-1}\mathbf{b}(\omega, \mathbf{k})}. \tag{B.21}$$

In the same manner the stochastic Capon filter is derived

$$\mathbf{h}_C^{P2} = \frac{\mathbf{R}^{-1}\mathbf{b}(\boldsymbol{\omega}, \mathbf{k})}{\mathbf{b}^H(\boldsymbol{\omega}, \mathbf{k})\mathbf{R}^{-1}\mathbf{b}(\boldsymbol{\omega}, \mathbf{k})}. \tag{B.22}$$

B.4 Derivation of the Conventional MUSIC Technique

The starting point for deriving the MUSIC method is the signal model introduced in subsection 3.1.1:

$$\mathbf{y}(l) = \sum_{i=1}^{N_s} s_i(l)\mathbf{a}(\omega_i) + \mathbf{n}(l). \tag{B.23}$$

The received signal $\mathbf{y}(l) \in \mathbb{C}^p$ can be expressed in matrix notation as

$$\mathbf{y}(l) = \mathbf{A}\mathbf{s}(l) + \mathbf{n}(l). \tag{B.24}$$

It is assumed that the steering vector matrix $\mathbf{A} = [\mathbf{a}(\omega_1), \ldots, \mathbf{a}(\omega_{N_s})] \in \mathbf{Mat}_{p,N_s}(\mathbb{C})$ has full column rank, $\text{rank}(\mathbf{A}) = N_s$. The data covariance matrix $\mathbf{R} = E\{\mathbf{y}(l)\mathbf{y}^H(l)\} \in \mathbf{Mat}_p(\mathbb{C})$ has the form

$$\mathbf{R} = \mathbf{A}\mathbf{S}\mathbf{A}^H + \sigma_n^2 \mathbf{I}. \tag{B.25}$$

The signal covariance matrix $\mathbf{S} \in \mathbf{Mat}_{N_s}(\mathbb{C})$ is supposed to be nonsingular, $\text{rank}(\mathbf{S}) = N_s$, but it is not necessarily a diagonal matrix. This means the signals might be partially correlated.

The eigenvalues of $\mathbf{R}$ are denoted in nonincreasing order by $\lambda_1 \geq \lambda_2 \geq \cdots \geq \lambda_p$. Let $(\mathbf{f}_1, \ldots, \mathbf{f}_{N_s})$ be the orthonormal eigenvectors corresponding to $(\lambda_1, \ldots, \lambda_{N_s})$ and $(\mathbf{g}_1, \ldots, \mathbf{g}_{p-N_s})$ the orthonormal eigenvectors associated with $(\lambda_{N_s+1}, \ldots, \lambda_p)$. From the above described situation it follows that the matrix $\mathbf{ASA}^H \in \mathbf{Mat}_p(\mathbb{C})$ has $\text{rank}(\mathbf{ASA}^H) = N_s$. Thus, the first N_s eigenvalues $\tilde{\lambda}_1 \geq \cdots \geq \tilde{\lambda}_p$ of the matrix $\mathbf{ASA}^H$ are strictly positive and the $p - N_s$ smallest eigenvalues are all equal to zero. Since $\lambda_i = \tilde{\lambda}_i + \sigma_n^2, i = 1, \ldots, p$, the eigenvalues of $\mathbf{R}$ can be partitioned into the two subsets

$$(1) \quad \lambda_i > \sigma_n^2 \qquad \text{for } i = 1, \ldots, N_s, \tag{B.26}$$

$$(2) \quad \lambda_i = \sigma_n^2 \qquad \text{for } i = N_s + 1, \ldots, p. \tag{B.27}$$

The characteristics of the corresponding eigenvectors lead to the MUSIC method [107]: Define the matrices $\mathbf{F} = [\mathbf{f}_1, \ldots, \mathbf{f}_{N_s}] \in \mathbf{Mat}_{p,N_s}(\mathbb{C})$ and $\mathbf{G} = [\mathbf{g}_1, \ldots, \mathbf{g}_{p-N_s}] \in \mathbf{Mat}_{p,p-N_s}(\mathbb{C})$ of eigenvectors and the diagonal matrices $\mathbf{\Lambda}_1 = \text{diag}\,(\lambda_1, \ldots, \lambda_{N_s}) \in \mathbf{Mat}_{N_s}(\mathbb{R})$ and $\mathbf{\Lambda}_2 = \text{diag}\,(\lambda_{N_s+1}, \ldots, \lambda_p) = \sigma_n^2\mathbf{I} \in \mathbf{Mat}_{p-N_s}(\mathbb{R})$ of eigenvalues. Using the spectral theorem for Hermitian matrices [41], the covariance matrix can be written as

$$\mathbf{R} = \mathbf{F}\mathbf{\Lambda}_1\mathbf{F}^H + \mathbf{G}\mathbf{\Lambda}_2\mathbf{G}^H. \tag{B.28}$$

Multiplying the matrix $\mathbf{G}$ from the right side yields

$$\mathbf{RG} = \mathbf{F}\mathbf{\Lambda}_1 \underbrace{\mathbf{F}^H\mathbf{G}}_{=\mathbf{0}} + \mathbf{G}\mathbf{\Lambda}_2 \underbrace{\mathbf{G}^H\mathbf{G}}_{=\mathbf{I}} = \sigma_n^2\mathbf{G}. \tag{B.29}$$

Utilizing the relation (B.25), this matrix can be also represented as

$$\mathbf{RG} = \mathbf{ASA}^H\mathbf{G} + \sigma_n^2\mathbf{G}. \tag{B.30}$$

Subtracting equations (B.30) and (B.29) implies $\mathbf{ASA}^H\mathbf{G} = \mathbf{0}$. Since the matrix $\mathbf{AS} \in \mathbf{Mat}_{p,N_s}(\mathbb{C})$ has full column rank it follows the first fundamental result

$$\mathbf{A}^H\mathbf{G} = \mathbf{0}. \tag{B.31}$$

Next, the subspaces that are spanned by the matrices $\mathbf{A}$ and $\mathbf{F}$ are analyzed: First the product of $\mathbf{R}$ and $\mathbf{F}$ is calculated by employing the eigendecomposition (B.28)

$$\mathbf{RF} = \mathbf{F}\mathbf{\Lambda}_1 \underbrace{\mathbf{F}^H\mathbf{F}}_{=\mathbf{I}} + \mathbf{G}\mathbf{\Lambda}_2 \underbrace{\mathbf{G}^H\mathbf{F}}_{=\mathbf{0}} = \mathbf{F}\mathbf{\Lambda}_1. \tag{B.32}$$

Inserting the covariance data model (B.25) this product can be also represented as

$$\mathbf{RF} = \mathbf{ASA}^H\mathbf{F} + \sigma_n^2\mathbf{F}. \tag{B.33}$$

It follows $\mathbf{F} = \mathbf{A}\mathbf{S}\mathbf{A}^H\mathbf{F}\left(\mathbf{\Lambda}_1 - \sigma_n^2\mathbf{I}\right)^{-1}$. This relation implies $\mathrm{im}(\mathbf{F}) \subset \mathrm{im}(\mathbf{A})$. As the subspaces $\mathrm{im}(\mathbf{F})$ and $\mathrm{im}(\mathbf{A})$ have the same dimension, $\dim(\mathrm{im}(\mathbf{F})) = \dim(\mathrm{im}(\mathbf{A})) = N_s$, the second main result is

$$\mathrm{im}(\mathbf{F}) = \mathrm{im}(\mathbf{A}). \tag{B.34}$$

Due to the facts (B.31) and (B.34) the subspaces $\mathrm{im}(\mathbf{F})$ and $\mathrm{im}(\mathbf{G})$ are referred to as the signal subspace and the noise subspace, respectively.

The principle idea in conceiving the MUSIC algorithm can be stated as follows:

The true frequency values $\{\omega_i\}_{i=1}^{N_s}$ are the only solutions of the equation

$$\mathbf{a}^H(\omega)\mathbf{G}\mathbf{G}^H\mathbf{a}(\omega) = 0. \tag{B.35}$$

Equation (B.31) implies that a solution ω_i fulfills the above condition. It still has to be shown that $\{\omega_i\}_{i=1}^{N_s}$ are the only solutions of the frequency estimation problem. Let $\tilde{\omega}$ be another possible solution with $\tilde{\omega} \neq \omega_i, i = 1, \ldots, N_s$, i.e., the vector $\mathbf{a}(\tilde{\omega})$ satisfies equation (B.35) and is linearly independent of the vectors $\{\mathbf{a}(\omega_i)\}_{i=1}^{N_s}$. It follows that

$$0 = \mathbf{a}^H(\tilde{\omega})\mathbf{G}\mathbf{G}^H\mathbf{a}(\tilde{\omega}) = \langle \mathbf{G}^H\mathbf{a}(\tilde{\omega}), \mathbf{G}^H\mathbf{a}(\tilde{\omega})\rangle = \|\mathbf{G}^H\mathbf{a}(\tilde{\omega})\|_2^2. \tag{B.36}$$

Hence, $\mathbf{G}^H\mathbf{a}(\tilde{\omega}) = \mathbf{0}$ and the vector $\mathbf{a}(\tilde{\omega})$ is in the kernel or null space of the matrix $\mathbf{G}^H$, $\mathbf{a}(\tilde{\omega}) \in \ker(\mathbf{G}^H)$. The dimension of the kernel subspace is N_s, $\dim\left(\ker(\mathbf{G}^H)\right) = N_s$. This is a contradiction to the linear independence of the vectors $\mathbf{a}(\tilde{\omega}) \cup \{\mathbf{a}(\omega_i)\}_{i=1}^{N_s} \in \ker(\mathbf{G}^H)$. A subspace of dimension N_s cannot contain $N_s + 1$ linearly independent vectors.

Utilizing these features of the eigenvectors of the covariance matrix, the spectral MUSIC algorithm can be formulated as follows: First the sample covariance matrix $\hat{\mathbf{R}}$ has to be calculated like in equation (3.7), subsection 3.1.1. The eigendecomposition of $\hat{\mathbf{R}}$ provides the eigenvalues $\hat{\lambda}_1 \geq \cdots \geq \hat{\lambda}_p$ and the respective eigenvectors $(\hat{\mathbf{f}}_1, \ldots, \hat{\mathbf{f}}_{N_s})$ and $(\hat{\mathbf{g}}_1, \ldots, \hat{\mathbf{g}}_{p-N_s})$. The matrix $\hat{\mathbf{F}} = [\hat{\mathbf{f}}_1, \ldots, \hat{\mathbf{f}}_{N_s}] \in \mathbf{Mat}_{p,N_s}(\mathbb{C})$ corresponds to the signal subspace and $\hat{\mathbf{G}} = [\hat{\mathbf{g}}_1, \ldots, \hat{\mathbf{g}}_{p-N_s}] \in \mathbf{Mat}_{p,p-N_s}(\mathbb{C})$ is associated with the noise subspace. The spatial frequency estimates are determined as the N_s maxima of the pseudo-spectrum

$$\hat{P}_{MU}(\omega) = \frac{1}{\mathbf{a}^H(\omega)\hat{\mathbf{G}}\hat{\mathbf{G}}^H\mathbf{a}(\omega)}. \tag{B.37}$$

The subspace spanned by the noise eigenvectors must be at least of dimension one, $p \geq N_s + 1$. For the special case $p = N_s + 1$ the MUSIC algorithm conforms to the Pisarenko method [77]. For $p - N_s > N_s$ the computational complexity of the MUSIC method can be alleviated by exploiting the matrix $\mathbf{I} - \hat{\mathbf{F}}\hat{\mathbf{F}}^H \in \mathbf{Mat}_{p,N_s}(\mathbb{C})$ instead of $\hat{\mathbf{G}}\hat{\mathbf{G}}^H \in \mathbf{Mat}_{p,p-N_s}(\mathbb{C})$ in equation (B.37). The modified MUSIC algorithm [105] that can be also applied to coherent signals and the Root MUSIC estimator are not addressed in this context since they are merely suitable for uniform linear arrays.

Appendix C

Algorithmic Scheme of the Conventional M-RELAX

The algorithmic scheme of M-RELAX [37, 63] can be summarized in the following way:

Step (1)
Assume $N_s = 1$. Estimate the frequency $\hat{\omega}_1$ and amplitudes $\{\hat{\alpha}_1(l)\}_{l=1}^{L}$ by means of formulas (3.45) and (3.46), respectively, using the samples $\{\mathbf{y}(l)\}_{l=1}^{L}$.

Step (2)
Assume $N_s = 2$. Calculate the corrected data vector $\{\mathbf{y}_2(l)\}_{l=1}^{L}$ by inserting $\hat{\omega}_1$ and $\{\hat{\alpha}_1(l)\}_{l=1}^{L}$ of step (1) in (3.44). Determine the frequency $\hat{\omega}_2$ and amplitude $\{\hat{\alpha}_2(l)\}_{l=1}^{L}$ estimates via (3.45) and (3.46), respectively, from $\{\mathbf{y}_2(l)\}_{l=1}^{L}$.
Calculate the corrected data $\{\mathbf{y}_1(l)\}_{l=1}^{L}$ from (3.44) where $\hat{\omega}_2$ and $\{\hat{\alpha}_2(l)\}_{l=1}^{L}$ of substep 1 are employed. Redetermine $\hat{\omega}_1$ and $\{\hat{\alpha}_1(l)\}_{l=1}^{L}$ from $\{\mathbf{y}_1(l)\}_{l=1}^{L}$ through equations (3.45) and (3.46).
Iterate these two substeps until the convergence condition explained below is satisfied.

Step (3)
Assume $N_s = 3$. Calculate $\{\mathbf{y}_3(l)\}_{l=1}^{L}$ by inserting $\hat{\omega}_i$ and $\{\hat{\alpha}_i(l)\}_{l=1}^{L}$ for $i = 1, 2$ of step (2) in (3.44). Determine $\hat{\omega}_3$ and $\{\hat{\alpha}_3(l)\}_{l=1}^{L}$ via (3.45) and (3.46), respectively, utilizing $\{\mathbf{y}_3(l)\}_{l=1}^{L}$.
Calculate $\{\mathbf{y}_1(l)\}_{l=1}^{L}$ by inserting $\hat{\omega}_i$ and $\{\hat{\alpha}_i(l)\}_{l=1}^{L}$ for $i = 2, 3$ into (3.44). Redetermine $\hat{\omega}_1$ and $\{\hat{\alpha}_1(l)\}_{l=1}^{L}$.
Calculate $\{\mathbf{y}_2(l)\}_{l=1}^{L}$ by inserting $\hat{\omega}_i$ and $\{\hat{\alpha}_i(l)\}_{l=1}^{L}$ for $i = 1, 3$ into (3.44). Redetermine $\hat{\omega}_2$ and $\{\hat{\alpha}_2(l)\}_{l=1}^{L}$.
Iterate these three substeps until the termination criterion is met.

Remaining steps.
Repeat this procedure until the assumed or estimated number of sources N_s is reached.

The termination criterion for the iterative process consists of the relative change of the cost function (3.43): If it is less than a user given threshold ε, the iteration is stopped.

Appendix D

Derivation of the Standard MLE

The computation of the code length required to encode the data $\{\mathbf{y}(l)\}_{l=1}^{L}$ is performed in three steps: Firstly, the noise subspace component $\{\mathbf{y_n}(l)\}_{l=1}^{L}$ is encoded assuming that $\boldsymbol{\omega}(k)$ is given. From the statistical assumptions and equation (3.56) it follows

$$\mathbf{y_n}(l)\,|\,\boldsymbol{\omega}(k) \sim \mathcal{N}_{\mathbb{C}}^{p-k}(\mathbf{0}, \sigma^2\mathbf{I}). \tag{D.1}$$

Thus, the probability density for the noise subspace component yields

$$f(\{\mathbf{y_n}(l)\}_{l=1}^{L}\,|\,\boldsymbol{\omega}(k)) = \prod_{l=1}^{L} \frac{1}{\det[\pi\sigma^2\mathbf{I}]} \exp\{-\mathbf{y}_{\mathbf{n}}^{H}(l)\sigma^{-2}\mathbf{y_n}(l)\}. \tag{D.2}$$

Using the sample covariance matrix $\hat{\mathbf{R}}_{\mathbf{n}}(\boldsymbol{\omega}(k)) \in \mathbf{Mat}_{p-k}(\mathbb{C})$ of $\mathbf{y_n}(l)$

$$\hat{\mathbf{R}}_{\mathbf{n}}(\boldsymbol{\omega}(k)) = \frac{1}{L}\sum_{l=1}^{L} \mathbf{y_n}(l)\mathbf{y}_{\mathbf{n}}^{H}(l) \tag{D.3}$$

it can be transformed to

$$f(\{\mathbf{y_n}(l)\}_{l=1}^{L}\,|\,\boldsymbol{\omega}(k)) = \det[\pi\sigma^2\mathbf{I}]^{-L} \exp\left\{-\sigma^{-2}L\mathrm{tr}\left[\hat{\mathbf{R}}_{\mathbf{n}}(\boldsymbol{\omega}(k))\right]\right\}. \tag{D.4}$$

This probabilistic model depends only on the parameter σ^2, whose ML estimator is

$$\hat{\sigma}^2(\boldsymbol{\omega}(k)) = \frac{1}{p-k}\mathrm{tr}\left[\hat{\mathbf{R}}_{\mathbf{n}}(\boldsymbol{\omega}(k))\right]. \tag{D.5}$$

Omitting constant quantities that are independent of k, the code length required to encode the noise subspace components is obtained as [113]

$$\mathscr{L}\{\mathbf{y_n}(l)\,|\,\boldsymbol{\omega}(k)\} = L\log\det[\hat{\sigma}^2(\boldsymbol{\omega}(k))\mathbf{I}] + L(p-k) + g(1). \tag{D.6}$$

Secondly, the signal subspace components $\{\mathbf{y_s}(l)\}_{l=1}^{L}$ are encoded. The statistical properties and equation (3.55) imply that

$$\mathbf{y_s}(l)\,|\,\boldsymbol{\omega}(k) \sim \mathcal{N}_{\mathbb{C}}^{k}(\mathbf{0}, \mathbf{R_s}(\boldsymbol{\omega}(k))) \tag{D.7}$$

where $\mathbf{R_s}(\boldsymbol{\omega}(k)) \in \mathbf{Mat}_k(\mathbb{C})$ is the signal data covariance matrix. The probabilistic model for the signal subspace component reads

$$f(\{\mathbf{y_s}(l)\}\,|\,\boldsymbol{\omega}(k)) = \prod_{l=1}^{L} \frac{1}{\det[\pi \mathbf{R_s}(\boldsymbol{\omega}(k))]} \exp\{-\mathbf{y_s}^H(l)\mathbf{R_s}^{-1}(\boldsymbol{\omega}(k))\mathbf{y_s}(l)\}. \tag{D.8}$$

Employing the maximum likelihood estimate $\hat{\mathbf{R}}_\mathbf{s}(\boldsymbol{\omega}(k)) \in \mathbf{Mat}_k(\mathbb{C})$ of $\mathbf{R_s}(\boldsymbol{\omega}(k))$ defined by

$$\hat{\mathbf{R}}_\mathbf{s}(\boldsymbol{\omega}(k)) = \frac{1}{L}\sum_{l=1}^{L} \mathbf{y_s}(l)\mathbf{y_s}^H(l) \tag{D.9}$$

this can be rewritten as

$$\begin{aligned} f(\{\mathbf{y_s}(l)\}\,|\,\boldsymbol{\omega}(k)) = \det[\pi \mathbf{R_s}(\boldsymbol{\omega}(k))]^{-L} \cdot \\ \cdot \exp\left\{-L\mathrm{tr}\left[\mathbf{R_s}^{-1}(\boldsymbol{\omega}(k))\hat{\mathbf{R}}_\mathbf{s}(\boldsymbol{\omega}(k))\right]\right\}. \end{aligned} \tag{D.10}$$

The number of free real-valued parameters in $\mathbf{R_s}(\boldsymbol{\omega}(k))$ is

$$k + 2\sum_{i=1}^{k-1} i = k^2. \tag{D.11}$$

Disregarding constant terms the code length of the signal subspace components is obtained as [113]

$$\mathscr{L}\{\mathbf{y_s}(l)\,|\,\boldsymbol{\omega}(k)\} = L\log\det[\hat{\mathbf{R}}_\mathbf{s}(\boldsymbol{\omega}(k))] + Lk + g(k^2). \tag{D.12}$$

The sum of (D.6) and (D.12) yields the total code length necessary to encode the noise and signal subspace components

$$\mathscr{L}\{\mathbf{y_n}(l), \mathbf{y_s}(l)\,|\,\boldsymbol{\omega}(k)\} = L\log\left[\det[\hat{\mathbf{R}}_\mathbf{s}(\boldsymbol{\omega}(k))]\det[\hat{\sigma}^2(\boldsymbol{\omega}(k))\mathbf{I}]\right] + g(k^2). \tag{D.13}$$

Finally, for encoding the unknown parameter vector $\boldsymbol{\omega}(k) \in \mathbb{R}^k$, it has to be estimated according to equation (D.13) by

$$\hat{\boldsymbol{\omega}}(k) = \arg\min_{\boldsymbol{\omega}(k)} \det[\hat{\mathbf{R}}_\mathbf{s}(\boldsymbol{\omega}(k))]\det[\hat{\sigma}^2(\boldsymbol{\omega}(k))\mathbf{I}]. \tag{D.14}$$

It can be shown that this estimator is consistent [113].

Next, two expressions of the relation (D.14) are derived. For the sake of conciseness the abbreviation $\mathbf{A} = \mathbf{A}(\boldsymbol{\omega}(k))$ is used in the following. From equations (3.55) and (3.56), it follows

$$\mathbf{P_A}\hat{\mathbf{R}}\mathbf{P_A} = \mathbf{G}(\boldsymbol{\omega}(k)) \begin{bmatrix} \hat{\mathbf{R}}_{\mathbf{s}}(\boldsymbol{\omega}(k)) & \mathbf{0} \\ \mathbf{0} & \mathbf{0} \end{bmatrix} \mathbf{G}^H(\boldsymbol{\omega}(k)) \tag{D.15}$$

and

$$\mathbf{P}_{\mathbf{A}}^{\perp}\hat{\mathbf{R}}\mathbf{P}_{\mathbf{A}}^{\perp} = \mathbf{G}(\boldsymbol{\omega}(k)) \begin{bmatrix} \mathbf{0} & \mathbf{0} \\ \mathbf{0} & \hat{\mathbf{R}}_{\mathbf{n}}(\boldsymbol{\omega}(k)) \end{bmatrix} \mathbf{G}^H(\boldsymbol{\omega}(k)) \tag{D.16}$$

where the sample covariance matrix $\hat{\mathbf{R}} \in \mathbf{Mat}_p(\mathbb{C})$ of $\mathbf{y}(l)$ is defined by

$$\hat{\mathbf{R}} = \frac{1}{L}\sum_{l=1}^{L} \mathbf{y}(l)\mathbf{y}^H(l). \tag{D.17}$$

Moreover,

$$\mathbf{P}_{\mathbf{A}}^{\perp}\hat{\sigma}^2(\boldsymbol{\omega}(k))\mathbf{P}_{\mathbf{A}}^{\perp} = \mathbf{G}(\boldsymbol{\omega}(k)) \begin{bmatrix} \mathbf{0} & \mathbf{0} \\ \mathbf{0} & \hat{\sigma}^2(\boldsymbol{\omega}(k))\mathbf{I} \end{bmatrix} \mathbf{G}^H(\boldsymbol{\omega}(k)). \tag{D.18}$$

Due to the similarity invariance of the trace[1], the relation (D.16) implies

$$\mathrm{tr}[\hat{\mathbf{R}}_{\mathbf{n}}(\boldsymbol{\omega}(k))] = \mathrm{tr}[\mathbf{P}_{\mathbf{A}}^{\perp}\hat{\mathbf{R}}] \tag{D.19}$$

and inserting (D.5) gives

$$\hat{\sigma}^2(\boldsymbol{\omega}(k)) = \frac{1}{p-k}\mathrm{tr}[\mathbf{P}_{\mathbf{A}}^{\perp}\hat{\mathbf{R}}]. \tag{D.20}$$

The sum of (D.15) and (D.18) is

$$\mathbf{P_A}\hat{\mathbf{R}}\mathbf{P_A} + \mathbf{P}_{\mathbf{A}}^{\perp}\hat{\sigma}^2(\boldsymbol{\omega}(k)) = \mathbf{G}(\boldsymbol{\omega}(k)) \begin{bmatrix} \hat{\mathbf{R}}_{\mathbf{s}}(\boldsymbol{\omega}(k)) & \mathbf{0} \\ \mathbf{0} & \hat{\sigma}^2(\boldsymbol{\omega}(k))\mathbf{I} \end{bmatrix} \mathbf{G}^H(\boldsymbol{\omega}(k)). \tag{D.21}$$

Since the matrix $\mathbf{G}(\boldsymbol{\omega}(k))$ is unitary, the determinant of (D.21) is

$$\det[\mathbf{P_A}\hat{\mathbf{R}}\mathbf{P_A} + \mathbf{P}_{\mathbf{A}}^{\perp}\hat{\sigma}^2(\boldsymbol{\omega}(k))] = \det[\hat{\mathbf{R}}_{\mathbf{s}}(\boldsymbol{\omega}(k))]\det[\hat{\sigma}^2(\boldsymbol{\omega}(k))\mathbf{I}]. \tag{D.22}$$

The first formulation of the estimate (D.14) is finally given by [113]

$$\hat{\boldsymbol{\omega}}(k) = \arg\min_{\boldsymbol{\omega}(k)} \det[\mathbf{P_A}\hat{\mathbf{R}}\mathbf{P_A} + \frac{1}{p-k}\mathrm{tr}[\mathbf{P}_{\mathbf{A}}^{\perp}\hat{\mathbf{R}}]\mathbf{P}_{\mathbf{A}}^{\perp}]. \tag{D.23}$$

The second form of the estimate (D.14) utilizes the eigendecompositions of the matrices $\mathbf{P_A}\hat{\mathbf{R}}\mathbf{P_A}$ and $\mathbf{P}_{\mathbf{A}}^{\perp}\hat{\mathbf{R}}\mathbf{P}_{\mathbf{A}}^{\perp}$:

[1] $\mathrm{tr}[\mathbf{B}^{-1}\mathbf{AB}] = \mathrm{tr}[\mathbf{A}]$ for $\mathbf{A} \in \mathbf{Mat}_n(\mathbb{C})$ and $\mathbf{B} \in \mathbf{GL}_n(\mathbb{C})$

Let $l_1^{\mathbf{s}}(\boldsymbol{\omega}(k)) \geq \cdots \geq l_k^{\mathbf{s}}(\boldsymbol{\omega}(k))$ be the nonzero eigenvalues of the matrix $\mathbf{P_A}\hat{\mathbf{R}}\mathbf{P_A}$ and $l_1^{\mathbf{n}}(\boldsymbol{\omega}(k)) \geq \cdots \geq l_{p-k}^{\mathbf{n}}(\boldsymbol{\omega}(k))$ be the nonzero eigenvalues of the matrix $\mathbf{P}_{\mathbf{A}}^{\perp}\hat{\mathbf{R}}\mathbf{P}_{\mathbf{A}}^{\perp}$. Then the determinant of equation (D.15) is

$$\det[\hat{\mathbf{R}}_{\mathbf{s}}(\boldsymbol{\omega}(k))] = \prod_{i=1}^{k} l_i^{\mathbf{s}}(\boldsymbol{\omega}(k)) \tag{D.24}$$

and the trace of (D.16) is

$$\mathrm{tr}[\hat{\mathbf{R}}_{\mathbf{n}}(\boldsymbol{\omega}(k))] = \sum_{i=1}^{p-k} l_i^{\mathbf{n}}(\boldsymbol{\omega}(k)). \tag{D.25}$$

Together with (D.5), this yields

$$\hat{\sigma}^2(\boldsymbol{\omega}(k)) = \frac{1}{p-k} \sum_{i=1}^{p-k} l_i^{\mathbf{n}}(\boldsymbol{\omega}(k)). \tag{D.26}$$

Plugging equations (D.24) and (D.26) into (D.14) leads to the second expression of the estimator [113]

$$\hat{\boldsymbol{\omega}}(k) = \arg\min_{\boldsymbol{\omega}(k)} \left(\prod_{i=1}^{k} l_i^{\mathbf{s}}(\boldsymbol{\omega}(k)) \right) \left(\frac{1}{p-k} \sum_{i=1}^{p-k} l_i^{\mathbf{n}}(\boldsymbol{\omega}(k)) \right)^{p-k}. \tag{D.27}$$

Bibliography

[1] H. Akaike: *Information theory and an extension of the maximum likelihood principle*, Proceedings 2nd Int. Symp. Inform. Theory, suppl. Problems of Control and Inform. Theory, pp. 267-281, 1973.

[2] H. Akaike: *A new look at the statistical model identification*, IEEE Trans. Automat. Contr., vol. AC-19, pp. 716-723, 1974.

[3] Z. D. Bai, P. R. Krishnaiah, L. C. Zhao: *On rates of convergence of fast detection criteria in signal processing with white noise*, Tech. Rep. 84-85, Centre for Multivariate Analysis, University of Pittsburgh, Pittsburgh, PA, USA, 1985.

[4] J. D. Ballester-Berman, J. M. Lopez-Sanchez, and J. Fortuny-Guasch: *Retrieval of Biophysical Parameters of Agricultural Crops Using Polarimetric SAR Interferometry*, IEEE Trans. Geoscience Remote Sensing, vol. 43, no. 4, pp. 683-694, April 2005.

[5] R. Bamler: *A comparison of range-doppler and wavenumber domain SAR focusing algorithms*, IEEE Trans. on Geoscience and Remote Sensing, vol. 30, pp. 706-713, July 1992.

[6] R. Bamler, P. Hartl: *Synthetic aperture radar interferometry*, Inverse Problems, vol. 14, no. 4, pp 1-54, August 1998.

[7] G. Bienvenu: *Influence of the spatial coherence of the background noise on high resolution passive methods*, Proceedings of the International Conference on Acoustics, Speech, and Signal Processing, pp. 306-309, 1979.

[8] W. M. Boerner, E. Lueneburg, H. Mott, Z. H. Czyz, J. J. Van Zyl, P. Dubois, S. R. Cloude, M. Tanaka, Y. Yamaguchi, A. I. Kozlov: *Formulation of unique sets of polarimetric radar scattering matrices for the forward propagation (similarity) versus backward scattering (con-similarity) arrangements and the development of associated optimal polarimetric contrast enhancement coefficients*, Proc. JIPR3, Nantes, France, 1995.

[9] C. Cafforio, C. Prati, F. Rocca: *SAR Data Focusing Using Seismic Migration Techniques*, IEEE Transactions on Aerospace and Electronic Systems, vol. 27, no. 2, pp. 194-207, 1991.

[10] W. L. Cameron, N. N. Youssef, L. K. Leung: *Simulated polarimetric signatures of primitive geometrical shapes*, IEEE Trans. Geosci. Remote Sensing, vol. 34, no. 3, pp. 793-803, May 1996.

[11] J. Capon: *High-resolution frequency-wavenumber spectrum analysis*, Proceedings of the IEEE, vol. 57(8), pp. 1408-1418, 1969.

[12] S. R. Cloude, E. Pottier: *A Review of Target Decomposition Theorems in Radar Polarimetry*, IEEE Trans. Geoscience Remote Sensing, vol. 34, no. 2, pp. 498-518, Feb. 1996.

[13] S. R. Cloude, E. Pottier: *An Entropy Based Classification Scheme for Land Applications of Polarimetric SAR*, IEEE Trans. Geoscience Remote Sensing, vol. 35, pp. 68-78, Jan. 1997.

[14] S. R. Cloude, K. P. Papathanassiou: *Polarimetric SAR interferometry*, IEEE Trans. Geoscience Remote Sensing, vol. 36, pp. 1551-1565, Sept. 1998.

[15] S. R. Cloude, K. P. Papathanassiou: *Three stage inversion process for polarimetric SAR interferometry*, IEEE Proc.-Radar Sonar Navig., vol. 150, pp. 125-134, June 2003.

[16] S. R. Cloude: *Polarization coherence tomography*, Radio Science, vol. 41, Aug. 2006.

[17] S. R. Cloude: *Dual-baseline coherence tomography*, IEEE Geoscience and Remote Sensing Letters, vol. 4, no. 1, pp. 127-131, Jan. 2007.

[18] C. Colesanti, A. Ferretti, F. Novali, C. Prati, F. Rocca: *SAR Monitoring of Progressive and Seasonal Ground Deformation Using the Permanent Scatterers Technique*, IEEE Trans. Geosci. Remote Sensing, vol. 41, no. 7, pp. 1685-1701, July 2003.

[19] E. Colin, C. Titin-Schnaider, W. Tabbara: *An interferometric coherence optimization method in radar polarimetry for high-resolutionimagery*, IEEE Trans. Geosci. Remote Sens., vol. 44, no. 1, pp. 167-175, Jan. 2006.

[20] M. Constantini: *A novel phase unwraping method based on network programming*, IEEE Transactions on Geoscience and Remote Sensing, vol. 36, vo. 3, pp. 813-821, 1999.

[21] I. G. Cumming, F. H. Wong: *Digital Processing of Synthetic Apterure Radar Data*, 2006.

[22] J. C. Curlander, R. N. McDonough: *Synthetic Aperture Radar: Systems and Processing*, JohnWiley and Sons, New York, 1991.

[23] E. R. Ferrara, T. M. Parks: *Direction Finding with an Array of Antennas Having Diverse Polarizations*, IEEE Trans. on Antennas and Propagation, vol. 31, pp. 231-236, March 1983.

[24] A. Ferretti, C. Prati, F. Rocca: *Multibaseline InSAR DEM Reconstruction: The Wavelet Approach*, IEEE Trans. Geosci. Remote Sensing, vol. 37, no. 2, pp. 705-715, March 1999.

[25] A. Ferretti, C. Prati, F. Rocca: *Nonlinear Subsidence Rate Estimation Using Permanent Scatterers in Differential SAR Interferometry*, IEEE Trans. Geosci. Remote Sensing, vol. 38, no. 5, pp. 705-715, Sept. 2000.

[26] A. Ferretti, C. Prati, F. Rocca: *Permanent Scatterers in SAR Interferometry*, IEEE Trans. Geosci. Remote Sensing, vol. 39, no. 1, pp. 8-20, Jan. 2001.

[27] L. Ferro-Famil, E. Pottier, and J. S. Lee: *Unsupervised Classification of Natural Scenes from Polarimetric Interferometric SAR Data*, Ser. Frontiers of Remote Sensing Information Processing, C. H. Chen, Ed. Dartmouth, Univ. Massachusetts, 2003.

[28] L. Ferro-Famil, A. Reigber, E. Pottier: *Study and Applications of POLSAR Data Time-Frequency Correlation Properties*, Proceedings of POLINSAR'07, Jan. 2007.

[29] G. Fornaro, G. Franceschetti: *Image Registration in Interferometric SAR Processing*, IEE Proceedings on Radar, Sonar and Navigation, vol. 142, no. 6, pp. 313-320, 1995.

[30] G. Fornaro, G. Franceschetti, R. Lanari: *Interferometric SAR Phase Unwrapping Using Green's Formulation*, IEEE Transactions on Geoscience and Remote Sensing, vol. 34, no. 3, pp. 720-727, 1996.

[31] G. Franceschetti, R. Lanari: *Synthetic Aperture Radar Processing*, CRC Press, Boca Ratón, Florida, 1999.

[32] A. Freeman, S. L. Durden: *A three-component scattering model for polarimetric SAR Data*, IEEE Trans. Geosci. Remote Sensing, vol. 36, no. 3, pp. 963-973, May 1998.

[33] F. Gatelli, A. M. Guarneri, F. Parizzi, P. Pasquali, C. Prati, F. Rocca: *The wavenumber shift in SAR interferometry*, IEEE Trans. Geosci. Remote Sensing, vol. 32, no. 4, pp. 855-865, July 1994.

[34] C. F. Gauß: *Theoria motus corporum coelestium*, Perthes et Besser, Hamburgi (1809), Werke vol. 7, 1-288.

[35] D. C. Ghiglia, L. A. Romero: *Robust two-dimensional weighted and unweighted phase unwrapping that uses fast transforms and iterative methods*, Journal Optical Society America, vol. 11, no. 1, pp. 107-117, 1994.

[36] F. Gini, F. Lombardini: *Multilook APES for Multibaseline SAR Interferometry*, IEEE Trans. on Signal Processing, vol. 50, pp. 1800-1803, July 2002.

[37] F. Gini, F. Lombardini, M. Montanari: *Layover Solution in Multibaseline SAR Interferometry*, IEEE Trans. Aerospace Electronic Systems, vol. 38, no. 4, pp. 1344-1356, Oct. 2002.

[38] F. Gini, F. Bordoni: *On the behavior of information theoretic criteria for model order selection of InSAR signals corrupted by multiplicative noise*, Signal Processing, vol. 83, pp. 1047-1063, 2003.

[39] F. Gini, F. Lombardini: *Multibaseline Cross-Track SAR Interferometry: A Signal Processing Perspective*, IEEE A E Systems Magazine, vol. 20, pp. 71-93, August 2005.

[40] R. M. Goldstein, H. A. Zebker, C. L. Werner: *Satellite radar interferometry: Two-dimensional phase unwrapping*, Radio Science, vol. 23, pp. 713-720, 1988.

[41] G. H. Golub, C. F. Van Loan: *Matrix Computations*, 2nd ed., Baltimore, MD, Johns Hopkins Univ. Press, 1983.

[42] S. Guillaso, L. Ferro-Famil, A. Reigber, E. Pottier: *Building Characterisation Using L-Band Polarimetric Interferometric SAR Data*, IEEE Geoscience and Remote Sensing Letters, vol. 2, no. 3, pp. 347-351, July 2005.

[43] S. Guillaso, A. Reigber: *Scatterer Characterisation Using Polarimetric SAR Tomography*, Proceedings of IGARSS'05, July 2005.

[44] S. Guillaso, M. Jäger, A. Reigber: *Information Extraction from Tomographic SAR Data*, Proceedings of EUSAR'06, May 2006.

[45] J. Homer, I. D. Longstaff, G. Callaghan: *High resolution 3-D SAR via multi-baseline interferometry*, Proceedings of IGARSS'96, 1996.

[46] J. R. Huynen: *Phenomenological theory of radar targets*, PhD thesis, Rotterdam, 1970.

[47] D. Just, R. Bamler: *Phase Statistics of Interferograms with Applications to Synthetic Aperture Radar*, Applied Optics, vol. 33, no. 20, pp. 4361-4368, 1994.

[48] G. Krieger, A. Moreira, H. Fiedler, I. Hajnsek, M. Werner, M. Younis, M. Zink: *TanDEM-X: A Satellite Formation for High-Resolution SAR Interferometry*, IEEE Trans. Geosci. Remote Sensing, vol. 45, no. 11, pp. 3317-3341, Nov. 2007.

[49] E. Krogager: *Decomposition of the Sinclair Matrix into Fundamental Components with Application to High Resolution Radar Target Imaging*, Direct and Inverse Methods in Radar Polarimetry, Part 2, ed. W. M. Boerner, Kluwer Academic Publishers, Dordrecht, The Netherlands, pp. 1459-1478, 1992.

[50] E. Krogager: *Aspects of Polarimetric Radar Imaging*, Ph.D. thesis, Technical University of Denmark (TUD), Electromagnetics Institute, Lyngby, DK, March 1993.

[51] A. Jakobsson, F. Gini, F. Lombardini: *Robust Estimation of Radar Reflectivities in Multibaseline InSAR*, IEEE Trans. Aerospace Electronic Systems, vol. 41, no. 2, pp. 751-758, April 2005.

[52] F. Leberl: *Mapping of Lunar Surface from Side-Looking Orbital Radar Imagery*, The Moon, vol. 15, pp. 329-342, 1976.

[53] F. Leberl, K. E. Maurice, J. K. Thomas: *Radargrammetric Analysis with Magellan Data of Planet Venus*, Proceedings of ISPRS92, pp. 253-263, Albuquerque, USA, 1992.

[54] J. S. Lee: *Digital image enhancement and noise filtering by use of local statistics*, IEEE Trans. Pattern Anal. Machine Intell., PAMI-2, no.2, pp. 165-168, 1980.

[55] J. S. Lee: *Refined filtering of image noise using local statistics*, Comput. Vision, Graphics, Image Process, 15(2), pp.380-389, 1981.

[56] J. S. Lee, M. R. Grunes, R. Kwok: *Classification of Multi-look Polarimetric SAR Imagery Based on Complex Wishart Distribution*, International Journal of Remote Sensing, vol. 15, no. 11, pp. 2299-2311, 1994.

[57] J. S. Lee, M. R. Grunes, G. De Grandi: *Polarimetric SAR speckle filtering and its implication for classification*, IEEE Trans. Geosci. Remote Sensing, vol. 37, no. 5, pp. 2363-2373, Sept. 1999.

[58] J. Li, P. Stoica: *Efficient Mixed-Spectrum Estimation with Applications to Target Feature Extraction*, IEEE Trans. on Signal Processing, vol. 44, pp. 281-295, Feb. 1996.

[59] J. Li, P. Stoica: *An Adaptive Filtering Approach to Spectral Estimation and SAR Imaging*, IEEE Trans. on Signal Processing, vol. 44, pp. 1469-1484, June 1996.

[60] J. Li, P. Stoica, Z. Wang: *On Robust Capon Beamforming and Diagonal Loading*, IEEE Trans. on Signal Processing, vol. 51, no 7, pp. 1702-1715, July 2003.

[61] J. Li, P. Stoica, Z. Wang: *Doubly Constrained Robust Capon Beamformer*, IEEE Trans. on Signal Processing, vol. 52, no 9, pp. 2407-2423, Sept. 2004.

[62] P. Stoica, Z. Wang, J. Li: *Extended Derivations of MUSIC in the Presence of Steering Vector Errors*, IEEE Trans. on Signal Processing, vol. 53, no 3, pp. 1209-1211, March 2005.

[63] F. Lombardini, M. Montanari, F. Gini: *Reflectivity Estimation for Multibaseline Interferometric Radar Imaging of Layover Extended Sources*, IEEE Trans. on Signal Processing, vol. 51, pp. 1508-1519, June 2003.

[64] F. Lombardini, A. Reigber: *Adaptive Spectral Estimation for Multibaseline SAR Tomography with Airborne L-band Data*, Proceedings of IGARSS'03, July 2003.

[65] F. Lombardini, F. Gini: *Model Order Selection in Multi-baseline Interferometric Radar Systems*, EURASIP Journal on Applied Signal Processing 2005, vol. 20, pp. 3206-3219, 2005.

[66] F. Lombardini, L. Rössing, J. Ender, F. Cai: *Interferometric Model Order Selection: Validation of ITC Methods with Airborne Three-antenna SAR Data*, Proceedings of IGARSS'06, August 2006.

[67] F. Lombardini, L. Rössing, J. Ender, F. Viviani: *Towards a Complete Processing Chain of Multibaseline Airborne InSAR Data for Layover Scatterers Separation*, Proceedings of URBAN'07, April 2007.

[68] E. Lueneburg: *Principles of radar polarimetry*, IEI-CE Trans. on Electronics, Special Issue on Electromagnetics, no. 10, pp. 1339-1345, 1995.

[69] D. Massonnet, K. L. Feigl: *Radar Interferometry and its Application to Changes in the Earth's Surface*, 1998.

[70] J. Mittermayer, A. Moreira, O. Loffeld: *The Frequency Scaling Algorithm for Spotlight SAR Data Processing*, IEEE Transactions on Geoscience and Remote Sensing, vol. 37, no. 5, September 1999.

[71] A. Moreira, J. Mittermayer, R. Scheiber: *Extended Chirp Scaling Algorithm for Air- and Spaceborne SAR Data Processing in Stripmap and ScanSAR Imaging Modes*, IEEE Transactions on Geoscience and Remote Sensing, vol. 34, no. 5, pp. 1123-1136, Sep. 1996.

[72] M. Neumann, A. Reigber, L. Ferro-Famil: *POLInSAR Coherence Set Theory and Application*, Proceedings of EUSAR'06, May 2006.

[73] M. Neumann, L. Ferro-Famil, A. Reigber: *Multibaseline POLInSAR Coherence Modelling and Optimization*, Proceedings of IGARSS'07, July 2007.

[74] M. Neumann, L. Ferro-Famil, A. Reigber: *Multibaseline Polarimetric SAR Interferometry Coherence Optimization*, IEEE Geoscience and Remote Sensing Letters, vol. 5, no. 1, pp. 93-97, Jan. 2008.

[75] K. P. Papathanassiou, S. R. Cloude: *Single-Baseline Polarimetric SAR Interferometry*, IEEE Trans. Geoscience Remote Sensing, vol. 39, pp. 2352-2363, Nov. 2001.

[76] D. Perissin, F. Rocca: *High-Accuracy Urban DEM Using Permanent Scatterers*, IEEE Trans. Geoscience Remote Sensing, vol. 44, no. 11 pp. 3338-3347, Nov. 2006.

[77] V. F. Pisarenko: *The retrieval of harmonics from a covariance function*, Geophys. J. Royal Astron. Soc., vol. 33, pp. 347-366, 1973.

[78] E. Pottier, J. Saillard: *Fondement mathématique de la polarimétrie et son application au domaine radar*, Annales des Télécommunications, vol. 47, no. 7-8, pp. 314-336, 1992.

[79] E. Pottier, J. S. Lee: *Unsupervised Classification Scheme of POLSAR Images Based on the Complex Wishart Distribution and the $H/A/\alpha$ Polarimetric Decomposition Theorem*, , Proceedings EUSAR2000, pp. 265-268, Munich, Germany, 2000.

[80] C. Prati, F. Rocca: *Improving slant range resolution of stationary objects with multiple SAR surveys*, IEEE Trans. Aerospace Electron. Systems, vol. 29, pp. 135-144, Jan. 1993.

[81] P. Prats, A. Reigber, P. Blanco, J. J. Mallorqui, A. Moreira: *Advanced Differential SAR Interferometric Techniques Applied to Airborne Data*, Proceedings of EUSAR'06, May 2006.

[82] M. Pritt: *Phase unwrapping by Means of Multigrid Techniques for Interferometric SAR*, IEEE Transactions on Geoscience and Remote Sensing, vol. 34, no. 3, pp. 728-738, 1996.

[83] R. K. Raney, H. Runge, R. Bamler, I. Cumming, F. Wong: *Precision SAR Processing without interpolation for range cell migration correction*, IEEE Transactions on Geoscience and Remote Sensing, vol. 32, pp. 786-799, July 1994.

[84] A. Reigber, A. Moreira: *First Demonstration of Airborne SAR Tomography Using Multibaseline L-Band Data*, IEEE Trans. Geoscience Remote Sensing, vol. 38, no. 5, pp. 2142-2152, Sept. 2000.

[85] A. Reigber: *Airborne Polarimetric SAR Tomography*, PhD thesis, University of Stuttgart, Oct. 2001.

[86] A. Reigber, R. Scheiber: *Airborne Differential SAR Interferometry: First Results at L-Band*, IEEE Trans. Geoscience Remote Sensing, vol. 41, no.6, pp. 1516-1520, June 2003.

[87] J. Rissanen: *Modeling by shortest data description*, Automatica, vol. 14, pp. 465-471, 1978.

[88] J. Rissanen: *A universal prior for the integers and estimation by minimum description length*, Ann. Stat., vol. 11, pp. 416-431, 1983.

[89] E. Rodriguez, J. M. Martin: *Theory and design of interferometric synthetic aperture radars*, Proc. Inst. Elect. Eng. F, vol. 139, no. 2, pp. 147-159, April 1992.

[90] L. Roessing, J. H. G. Ender: *Multi-antenna SAR tomography using superresolution techniques*, Proc. of EUSAR'00, May 2000.

[91] P. A. Rosen, S. Hensley, I. R. Joughin, F. K. Li, S. N. Madsen, E. Rodriguez, and R. M. Goldstein: *Synthetic Aperture Radar Interferometry*, Proceedings of the IEEE, vol. 88, no. 3, pp. 333-382, March 2000.

[92] L. Sagués, J. M. Lopez-Sanchez, J. Fortuny, X. Fàbregas, A. Broquetas, A. J. Sieber, *Indoor Experiments on Polarimetric SAR Interferometry* IEEE Trans. Geosci. Remote Sensing, vol. 38, no. 2, pp. 671-684, March 2000.

[93] L. Sagués, J. M. Lopez-Sanchez, J. Fortuny, X. Fàbregas, A. Broquetas, A. J. Sieber, *Polarimetric Radar Interferometry for Improved Mine Detection and Surface Clutter Rejection* IEEE Trans. Geosci. Remote Sensing, vol. 39, no. 6, pp. 1271-1278, June 2001.

[94] S. Sauer, L. Ferro-Famil, A. Reigber, E. Pottier: *Analysing Urban Areas using Multiple Track POL-InSAR Data at L-Band*, Proceedings of EUSAR'06, May 2006.

[95] S. Sauer, L. Ferro-Famil, A. Reigber, E. Pottier: *Estimation of Built-up Area Characteristics from Polarimetric Interferometric Multiple Track L-Band SAR Data*, Proceedings of IGARSS'06, August 2006.

[96] S. Sauer, L. Ferro-Famil, A. Reigber, E. Pottier: *Multibaseline POL-InSAR Analysis of Urban Scenes at L-Band*, Proceedings of POLINSAR'07, Jan. 2007.

[97] S. Sauer, L. Ferro-Famil, A. Reigber, E. Pottier: *3D Visualisation and Physical Feature Extraction of Urban Areas using Multibaseline POL-InSAR Data at L-Band*, Proceedings of URBAN'07, April 2007.

[98] S. Sauer, L. Ferro-Famil, A. Reigber, E. Pottier: *Multibaseline POL-InSAR Analysis of Urban Scenes for 3D Modeling and Physical Feature Retrieval at L-Band*, Proceedings of IGARSS'07, June 2007.

[99] S. Sauer, L. Ferro-Famil, A. Reigber, E. Pottier: *Physical Parameter Extraction over Urban Areas using L-Band POLSAR Data and Interferometric Baseline Diversity*, Proceedings of IGARSS'07, June 2007.

[100] R. O. Schmidt: *Multiple Emitter Location and Signal Parameter Estimation*, Proc. RADC Estimation Workshop, Rome Air Development Center, N.Y., Oct. 1979.

[101] G. Schwartz: *Estimating the dimension of a model*, Ann. Stat., vol. 6, pp. 461-464, 1978.

[102] G. Strang: *Linear Algebra and its Application*, Third edition, Wellesley Cambridge, 2003.

[103] G. A. Showman, W. L. Melvin, M. Belenkii: *Performance Evaluation of Two Polarimetric STAP Architectures*, Proceedings IEEE Radar Conference, 2003.

[104] P. Stoica, A. Nehorai: *MUSIC, Maximum Likelihood, and Cramér-Rao Bound*, IEEE Trans. Acoustics, Speech, and Signal Processing, vol 37, pp. 720-741, May 1989.

[105] P. Stoica, K. C. Sharman: *Maximum likelihood methods for direction-of-arrival estimation*, IEEE Trans. Acoustics, Speech, and Signal Processing, vol 38, pp. 1132-1143, July 1990.

[106] P. Stoica, A. Nehorai: *MUSIC, Maximum Likelihood, and Cramér-Rao Bound: Further Results and Comparisons*, IEEE Trans. Acoustics, Speech, and Signal Processing, vol 38, pp. 2140-2150, Dec. 1990.

[107] P. Stoica, R. Moses: *Introduction to Spectral Analysis*, Prentice Hall, 1997.

[108] R. Touzi, F. Charbonneau: *Characterization of target symmetric scattering using polarimetric SARs*, IEEE Trans. Geosci. Remote Sensing, vol. 40, no. 11, pp. 2507-2516, November 2002.

[109] F. T. Ulaby, C. Elachi (editors): *Radar Polarimetry for Geoscience Applications*, Artech House, 1990.

[110] M. Wax, T. Kailath: *Detection of Signals by Information Theoretic Criteria*, IEEE Trans. on Acoustics, Speech, and Signal Processing, vol. 33, pp. 387-392, April 1985.

[111] M. Wax, I. Ziskind: *On unique localization of multiple sources in passive sensor arrays*, IEEE Trans. on Acoustics, Speech, and Signal Proc., vol. 37, pp. 996-1000, July 1989.

[112] M. Wax, I. Ziskind: *Detection of the number of coherent and noncoherent signals by the MDL principle*, IEEE Trans. on Acoustics, Speech, and Signal Proc., vol. 37, pp. 1190-1196, Aug. 1989.

[113] M. Wax: *Detection and Localization of Multiple Sources Via the Stochastic Signals Model*, IEEE Trans. on Signal Processing, vol. 39, pp. 2450-2456, Nov. 1991.

[114] H. Yamada, Y. Yamaguchi, Y. Kim, E. Rodriguez, and W.-M. Boerner: *Polarimetric SAR Interferometry for Forest Analysis Based on the ESPRIT Algorithm*, IEICE Trans. Electron., vol. E84-C, pp. 1917-1924, Dec. 2001.

[115] H. A. Zebker, J. Villasenor: *Decorrelation in Interferometric Radar Echos*, IEEE Transactions on Geoscience and Remote Sensing, vol. 30, no. 5, pp. 950-959, 1992.

[116] L. C. Zhao, P. R. Krishnaiah, Z. D. Bai: *On detection of the number of signals in presence of white noise*, Journal of Multivariate Analysis, vol. 20, no. 1, pp. 1-25, 1986.

[117] I. Ziskind, M. Wax: *Maximum Likelihood Localization of Multiple Sources by Alternating Projection*, IEEE Trans. on Acoustics, Speech, and Signal Proc., vol. 36, pp. 1553-1560, Oct. 1988.

[118] I. Ziskind, M. Wax: *Maximum Likelihood Localization of Diversely Polarized Sources by Simulated Annealing*, IEEE Trans. on Antennas and Propagation, vol. 38, pp. 1111-1114, July 1990.

Résumé

Dans cette thèse, des techniques d'analyse spectrale sont généralisées afin de traiter des données polarimétriques SAR interférométriques multi-bases. Ces algorithmes polarimétriques de traitement multi-capteurs sont décrits d'une manière mathématique rigoureuse et appliqués aux zones urbaines. Ils permettent d'estimer la hauteur des diffuseurs, le mécanisme de rétrodiffusion et la réflectivité polarimétrique. A partir des observations mono-base POL-InSAR, un modèle numérique d'élévation d'une zone urbaine est généré en déterminant les mécanismes de rétrodiffusion. L'utilisation des données bi-base POL-InSAR permet de résoudre le problème de déversement et de réaliser des images SAR en trois dimensions en indiquant les types de réflexion.

Mots clefs: SAR, télédétection, interférométrie, polarimétrie, traitement du signal, environnements urbains.

Abstract

In this thesis, spectral analysis techniques are generalized to process polarimetric multibaseline interferometric SAR data. These polarimetric array signal processing algorithms are described in a rigorous mathematical way and applied to urban areas. They permit the estimation of the reflector height, the scattering mechanism, and the polarimetric reflectivity. From single-baseline POL-InSAR observations, a digital elevation model of an urban scene is generated including the scattering types. Using polarimetric dual-baseline InSAR data, the building layover problem is resolved and three-dimensional SAR images are produced that reveal the reflection mechanisms.

Keywords: SAR, remote sensing, interferometry, polarimetry, signal processing, urban environments